

UNDERSTANDING THE SOLID/SOLID AND LIQUID/SOLID INTERFACE PHENOMENA  
FOR ALTERNATIVE ENERGY APPLICATIONS

By

Thanaphong Phongpreecha

A DISSERTATION

Submitted to  
Michigan State University  
in partial fulfillment of the requirements  
for the degree of

Chemical Engineering – Doctor of Philosophy

2018

## ABSTRACT

### UNDERSTANDING THE SOLID/SOLID AND LIQUID/SOLID INTERFACE PHENOMENA FOR ALTERNATIVE ENERGY APPLICATIONS

By

Thanaphong Phongpreecha

In many alternative energy technologies, interfacial phenomena are critical in determining process efficiency and feasibility. Previously, a complete application of density functional theory (DFT) as a tool to study interfaces has not only led to fundamental insights into the system, but also predictive models and recommendations for materials that were experimentally validated. In this thesis, it is first demonstrated that such an approach can also be used to solve a well-characterized interface problems related to sustainable energy technologies. This first problem is a solid/solid interface between the solid oxide fuel cell (SOFC) and its sealant, specifically an interface between SOFC's exposed electrolyte, which is typically made of yttria-stabilized zirconia (YSZ), and the commercial Ag-CuO sealing braze. The current material, CuO, which helps molten Ag to wet on YSZ surfaces and later adhere once the Ag is solidified, has been previously characterized to form a CuO-rich layer between Ag and YSZ. However, over time it is reduced by the SOFC's reductive conditions and results in formation of pores. Therefore, alternative oxides are needed that are thermodynamically stable in SOFC's high operating temperatures and also provide similar adhesion properties to CuO. To that end, this thesis has identified two mechanisms that enable only CuO to work so far. First, it was found that, unlike most other Ag/oxides, the Ag/CuO interface has a particularly strong adhesion – five times that of Ag/YSZ. Second, the dissolved oxygen in molten Ag from air during the brazing process diffuses to the interface and partially improves adhesion. The high adhesion of Ag/CuO was proposed to be from CuO's unique atomic structure. Therefore, a descriptor based on the oxide's structural and chemical features was

developed to predict Ag/oxide adhesion. The descriptor expedites screening of new oxides as no expensive calculation is needed, leading to several recommendations such as  $\text{CuAlO}_2$  and  $\text{Cu}_3\text{TiO}_4$ .

In the second problem, a more complex and less well-characterized interface in sustainable energy technologies is investigated. It should be noted that due to the complexity, the screening model cannot be developed yet. This second interface is a liquid/solid interface between solvated lignin and its catalyst. Lignin is a highly heterogeneous polymer in lignocellulosic biomass with many functional groups. Its valorization is essential to the economic feasibility of biorefinery, and its catalytic hydrogenolysis in a liquid phase is well-studied technology route to add value to the lignin. Many experiments have shown that solvent choice can have large impacts on product types and yields. However, the solvent effect on the reaction is still unclear. An understanding of the solvated lignin/catalyst interface would be valuable. For this, we are interested in the adsorption. To achieve this, spectroscopic and wet chemistry techniques are first used to help characterize the system by identifying that the quantity of ether linkages in lignin is the most critical functional group that determines the hydrogenolysis yields. Using a lignin dimer that contains a characteristic ether linkage, DFT shows that, in vacuum, the adsorption of the dimer is much stronger on Ni(111) than Cu(111). Upon solvation with ethanol, it was found that the dimer-metal interactions weaken so significantly that for Cu(111), it no longer adsorbs onto the metal surface. This implies that Cu may not provide high catalytic activity, which agrees with hydrogenolysis experiments performed in this thesis, although there could be other contributing factors. Lastly, to circumvent large DFT calculations, a model based on a thermodynamic cycle was developed to predict adsorption energy of a solvated lignin dimer for a given pair of solvent and catalyst. Although the model is not suitable for screening purposes, it provides a valuable, quantitative insight to the solvent effects.

Copyright by  
THANAPHONG PHONGPREECHA  
2018

## ACKNOWLEDGEMENTS

Through a series of events, I have been fortunate to meet a number of smart, inspiring, and supportive people throughout my Ph.D. study, whose help I tremendously appreciate. First of all, I would like to thank my two principal investigators, Dr. David Hodge and Dr. Yue Qi, who have graciously taken me into their groups, are always open to discussions, and have provided support and guidance without reservation. I would also like to thank my committee members, Dr. Dennis Miller and Dr. James Jackson, who always welcomed me to their office, were happy to give me technical guidance, and also allowed me to use their precious laboratories. And last but not least, thank you Dr. Eric Hegg and Dr. Jason Nicholas for your support in my Ph.D. study.

To my family, thank you Mom and Dad (Vilai Phongpreecha and Siripot Phongpreecha), for all of your sacrifices since the day I was born. You always love me, believe in me, support me, and encourage me to go one step further. Of course, you too, Supreeya Phongpreecha and Suchawadee Phongpreecha, my little sisters, for taking care of Mom and Dad while I'm away and for your moral support.

To my friends, my Ph.D. life would have been so arduous and lonely without you guys. First of all, I would like to thank my former Hodge-lab mates, Jacob Crowe, Ryan Stoklosa, Lisaura Maldonado-Pereira, Muyang Li, and Glen Li for all the knowledge you passed to me and the fun times in the lab. Thank you my 2014 Chemical Engineering student crew, Aritra Chakraborty, Eric Straley, Jake Claes, Preetum Giri, Sayli Bote, and Kirti Bhardwaj for sticking through the first couple years of graduate school together. My Chinese squad (赞焖屋个), Jialin Liu, Pengchao Hao, Zhongyu Zhang, and Xinting Lin for not only helping me with my lab

struggles, but also for all the good times we had at Sichuan. My Hegg-lab mates, Aditya Bhalla, Namita Bhalla, Gracielou Klinger, Julius Campeciño, Elise Rivett, and Clarisse Mebane for teaching me biochemistry techniques and all the laughter you gave me. My Jackson-lab mates Benjamin Appiagyei and Tayeb Kakeshpour for always willing to help me with my poor chemistry. My Qi-lab mates Tridip Das, Hongkang Tian, Christine James, Kwangjin Kim, Yunsong Li, and Yuxiao Lin for the fun activities and teaching me theoretical works. My lab manager friends Cliff Foster, Dr. Dan Holmes, Dr. Li Xie, and Phillip Hill for all the good talks, helping out with using equipment, and not killing me when I broke it. My undergraduate friends, Nicholas Hool and Kendall Christy, I thank you for your hard work and sincerity, and I am happy to see your professional life taking off. For my Thai friends, I would like to first thank my undergraduate advisors who inspired and supported me to pursue a Ph.D. study Dr. Siwarutt Boonyarattanakalin, Dr. Wanwipa Siritwatwetchakul, and Dr. Apichit Svangariyaskul. My Thai cook landlords, Ekkarach Thaweerak, Sorawit meejinda, and Pronthep promna, who fed me countless number of meals. Also, my Thai friends who have not abandoned me and always kept me in company Sittipol Puarattana-aroonkorn, Charkrid Patamatamkul, Suwat Phinhongthong, Sathika Jariyatamkitti, Sudaporn Gunnaleka, Tonnam Balankura, Nattaya Siritrai, Will Wongsirikul, Woranit Muangmala, and many others who I may have failed to mention. Lastly, thank you Isaac Sarver for proof reading my English for this thesis. Thank you all for making this journey a relishing ride. I wish you all the best.

## TABLE OF CONTENTS

<b>LIST OF TABLES .....</b>	<b>x</b>
<b>LIST OF FIGURES .....</b>	<b>xi</b>
<b>CHAPTER 1 Background and Motivations .....</b>	<b>1</b>
1.1 Selected Interfaces in Solid Oxide Fuel Cell and Biorefinery & Problem Identification .....	1
1.1.1 Interfaces are Key Components in Energy Conversion and Storage Devices.....	1
1.1.2 Sealing of the Electrolyte in SOFC .....	5
1.1.3 Catalytic Hydrogenolysis of Lignin in Liquid Phase .....	7
1.2 Contributions of DFT Calculations to the Understanding of Interface Interactions .....	11
1.2.1 Contributions to the Gas/Solid Interface Interactions .....	13
1.2.2 Contributions to the Solid/Solid Interface Interactions .....	15
1.2.3 Contributions to the Liquid/Solid Interface Interactions.....	18
1.3 Current Studies on Adhesion at Metal-Zirconia Interfaces & the Challenges for Ag/Oxides Interface for the Sealing of the SOFC .....	20
1.3.1 Adhesion at the YSZ Electrolyte Surface.....	20
1.3.2 Trends and Correlation in Adhesion Energy .....	23
1.4 Current Computational Studies on Liquid/Metal Interface of Catalysts & the Challenges for Lignin Decomposition Processes .....	26
1.4.1 Characteristics of Solvent and Metal at the Interface.....	27
1.4.2 The Effect of Solvent on the Adsorption of Aromatics on Catalyst Surfaces.....	29
1.5 Motivation and Thesis Outline .....	30
<b>CHAPTER 2 Designing Metal Oxides to Enhance Adhesion of Silver Brazes on YSZ .....</b>	<b>33</b>
2.1 Summary .....	33
2.2 Introduction .....	33
2.3 Methods .....	36
2.3.1 Geometry optimization .....	36
2.3.2 Slab Models for Surfaces and Interfaces .....	38
2.3.3 <i>Ab Initio</i> Molecular Dynamics .....	41
2.4 The Role of the Oxygen at the Ag( <i>l</i> )/YSZ interface during Brazing Process.....	42
2.5 Enhancement of Interface Adhesion by CuO.....	45
2.6 Identification of Other Potential Oxide-Forming Alloying Elements.....	47
2.6.1 Formulation of a Descriptor Using $\gamma_{12}$ and $W_{adh}$ in a Predictive Model.....	47
2.6.2 Descriptor-Based Prediction of Interface Energy and $W_{adh}$ .....	50
2.6.3 Identification of Complex Oxides and Ternary Braze Alloy Design.....	53
2.7 Conclusion.....	56
<b>CHAPTER 3 Experimental Identification of the Yields Determining Functional Groups in Lignins.....</b>	<b>58</b>
3.1 Summary .....	58
3.2 Introduction .....	59

3.3 Methods .....	63
3.3.1 Lignin Fractionation .....	63
3.3.2 Lignin Extraction from Birch .....	63
3.3.3 Lignin Acetylation .....	64
3.3.4 NMR Analysis of Lignin .....	64
3.3.5 Gel Permeation Chromatography .....	66
3.3.6 Thioacidolysis Depolymerization of Lignin .....	66
3.3.7 Catalytic Oxidative Cleavage of Lignin .....	66
3.3.8 Catalytic Hydrogenolysis of Lignin .....	67
3.3.9 Yield Prediction Model Development .....	68
3.4. Lignin Fractionation Process and Recovery .....	69
3.5 Trends in Properties of Fractionated Lignins .....	70
3.6 Trends in Monomer Yields from Depolymerization of Fractionated Lignins .....	73
3.7 Correlating Lignin Properties and Monomer Yields for Fractionated Alkali Lignins .....	76
3.8 Prediction of Monomer Yields from $\beta$ -O-4 Content .....	79
3.9 Conclusion .....	85
<b>CHAPTER 4 Adsorption of the Yield Determining Lignin Dimer on Catalyst Surfaces ....</b>	<b>86</b>
4.1 Summary .....	86
4.2 Introduction .....	87
4.3 Computational Methods .....	91
4.3.1 Adsorption of Lignin Dimer and Monomers from DFT Calculations .....	91
4.3.2 Solvation Energy of Lignin Dimer by DFT Implicit and Explicit Model .....	94
4.3.3 Additional Classical Molecular Dynamics .....	96
4.4. Development of Computational Approaches .....	96
4.4.1 The Significance of van der Waals Correction on Adsorption of Aromatics .....	96
4.4.2 Determining Preferable Adsorption Site using Guaiacol .....	98
4.4.3 Representing Polymeric Lignin Structure with a Dimer .....	99
4.4.4 Identifying the most Stable Dimer Adsorption Conformation in Gas Phase .....	101
4.5 Adsorption Energy of Lignin in Solvated Environments .....	105
4.5.1 Comparison of the Implicit and Explicit Model for Solvated Lignin Adsorption .....	105
4.5.2 Calculation of Solvated Lignin Adsorption Energy from a Thermodynamic Cycle ..	108
4.6 Conclusion .....	111
<b>CHAPTER 5 Catalytic Hydrogenolysis of Lignin to Aromatic Monomers .....</b>	<b>113</b>
5.1 Summary .....	113
5.2 Introduction .....	114
5.3 Experimental Methods .....	118
5.3.1 Biomass and Lignin Compositions .....	118
5.3.2 Catalytic Hydrogenolysis of Lignin and Biomass .....	119
5.3.3 Enzymatic Hydrolysis .....	120
5.4. Monomer Yields from Native Lignin in Biomass Using Different Catalysts .....	121
5.5 Lower Monomer Yields from Low Quality Lignin .....	125
5.6 Characteristics of the Pretreated Biomass and Enzymatic Hydrolysis .....	127
5.7 Conclusion .....	130

<b>CHAPTER 6 Summary and Outlook.....</b>	<b>131</b>
<b>APPENDICES .....</b>	<b>135</b>
APPENDIX A: Supplementary Materials for Chapter 2.....	136
APPENDIX B: Supplementary Materials for Chapter 3.....	148
APPENDIX C: Supplementary Materials for Chapter 4.....	151
<b>BIBLIOGRAPHY .....</b>	<b>152</b>

## LIST OF TABLES

Table 1.1. Major products from selective hydrogenolysis reaction of lignin showing a wide range of possible products depending on reaction conditions and catalysts.....	9
Table 2.1. The parametric detail of the interface cells with their corresponding $k$ -points used in the present study. ....	38
Table 2.2. The average interface distance ( $\Delta d$ ), work of adhesion ( $W_{adh}$ ), calculated wetting angles ( $\theta^{cal}$ ), and experimental ( $\theta^{exp}$ ) for Ni/YSZ interface and systems involved in Ag–CuO/YSZ braze. ....	44
Table 2.3. The surface and interface energy involved in Ni[110](111)  YSZ[110](111) interface. ....	45
Table 3.1. Percent recovery of each fraction through CO <sub>2</sub> acidification at room temperature and at 115 °C (SLRP <sup>TM</sup> ). The pH 2 fraction was obtained by acidification with H <sub>2</sub> SO <sub>4</sub> .....	70
Table 4.1. Calculated adsorption energies (eV) of benzene on close-packed metal surfaces with different calculation methodology and comparison to the existing literature.....	97
Table 4.2. Adsorption energy in eV and average aryl carbon atoms distance to metal surface ( $\Delta d$ ) in Å for different adsorption conformations of the <i>threo</i> -dimer (shown in Figure 4.4) and conditions on Ni(111) and Cu(111) surfaces. ....	104
Table 4.3. Adsorption energy ( $\Delta E_{ads}^g$ ) in eV and average aryl carbon atoms distance to Ni(111) surface ( $\Delta d$ ) in Å for the two different adsorption conformations of the <i>erythro</i> -dimer (shown in Figure 4.5).....	105
Table 4.4. Comparison of solvation energy ( $\Delta E_{sol}$ ) of similar aromatic molecules in alcohol solvents using different implicit models, an explicit model, and from experiments. ....	107
Table A1. List of all the studied metals and oxides, including their crystal structures, lattice constants, surface energies from the present work, along with comparisons to experiment values, and the calculated values for the descriptor ( $\chi_{MO}$ ) as shown in Eqn. 2.4. All computational values are based on LDA functional unless otherwise stated.....	136
Table B1. The Summary of quantified lignin properties and monomer yields.....	148
Table C1. Comparison between density calculated from NPT dynamics using COMPASS II force field and experimental density of compounds similar to the dimer.....	151

## LIST OF FIGURES

Figure 1.1. Schematic diagram of SOFC in Nissan vehicle using bio-ethanol as a fuel (adapted from <sup>6</sup> ).	2
Figure 1.2. Schematic diagram of a single SOFC with a solid oxide-ion conducting electrolyte (A, adapted from <sup>11</sup> with permission), and of stacked SOFC showing sealing in each unit which is in contact with the SOFC's electrolyte (B, adapted from <sup>12</sup> ).	3
Figure 1.3. The hypothetical biorefinery concept with an examples on how each component of the lignocellulosic biomass (cellulose, hemicellulose, and lignin) can be catalytically converted to useful fuels and chemicals (adapted from <sup>14</sup> with permission).	4
Figure 1.4. Hypothetical structure of softwood and hardwood lignin. Bonds abundance is obtained from Adler. <sup>27</sup>	7
Figure 1.5. Examples of changes in lignin functionalities at the $\beta$ -O-4 linkage after going through different types of lignocellulosic biomass pretreatment (adapted from <sup>14</sup> with permission).	8
Figure 1.6. Experimental, theoretical and computational tools plotted over their respective time and length scale domain of applicability with examples in the characterization and modeling of deformation and failure of biological protein materials (adapted from <sup>46</sup> with permission).	12
Figure 1.7. DFT calculated scaling relations for adsorption energies of $\text{CH}_x$ species plotted against the adsorption energy of C for a number of different transition metals (adapted from <sup>51</sup> with permission).	13
Figure 1.8. DFT-calculated scaling relation between CO dissociative adsorption energy and an activation energy of C-O bond dissociation for methanation reaction (A). Experimentally measured rate as a function of the Fe/Ni content in catalysts (B) (adapted from <sup>55</sup> with permission).	15
Figure 1.9. Universal scaling relation for adhesion energy of different metal interfaces (adapted from <sup>69,70</sup> with permission).	17
Figure 1.10. The equation of state for different metals predicted by the scaling relation with results from experiments (adapted from <sup>72</sup> with permission).	18
Figure 1.11. The schematic diagram of Winterbottom analysis for calculation of interface energy and the high angle annular dark field micrographs of Ni particle on YSZ surface captured by HRTEM (A). The Ni(111)/YSZ(111) obtained from HRTEM (B) (adapted from <sup>64</sup> with permission).	21
Figure 1.12. The surface and Ni/ $\text{ZrO}_2$ interface termination of $\text{ZrO}_2(111)$ at different oxygen chemical potentials (A, adapted from <sup>95</sup> with permission). The oxygen chemical potential at each side and in electrolyte of an operating SOFC at 1000 °C (B, adapted from <sup>96</sup> with permission). Together, these indicate that $\text{ZrO}_2(111)$ is terminated with O layer at the interface.	22

Figure 1.13. The relationship between the work of adhesion ( $W_{adh}$ ) of metals/ $\alpha$ - $Al_2O_3$ (0001) and the metals' oxide formation energy energy (A, adapted from <sup>65</sup> with permission) and the relationship between $W_{adh}$ of metals on several oxides and the metals' oxide formation energy per unit surface area (B, adapted from <sup>101</sup> with permission).....	23
Figure 1.14. The relationship between the work of adhesion ( $W_{adh}$ ) of metals on various oxides as a function of oxide's formation energy or its band gap energy (adapted from <sup>103</sup> with permission). .....	25
Figure 1.15. Illustration of solvent simulation in an explicit (A) and an implicit model (B) (adapted from <sup>118</sup> with permission).....	26
Figure 1.16. The average number of hydrogen bond along the z-coordinate (A, adapted from <sup>124</sup> with permission). The water structure at a water/Pt interface. The water molecule with blue ball represents watA, and the water molecules with red balls are of watB. The HOMO of the interface is partially located on watA, as represented with pink and cyan isosurfaces. The dashed lines indicate the hydrogen bonds formed between water molecules with the number showing the vibrational frequencies (B, adapted from <sup>125</sup> with permission).....	28
Figure 1.17. Difference in adsorption energies between in vacuum and solvated of molecules on Pt(111) surface using a PCM model to represent water medium. The changes are classified in color by nature of the adsorbates (adapted from <sup>126</sup> with permission).....	29
Figure 2.1. Hypothetical mechanisms of how Ag-CuO braze enables wetting starting from the solid phase (left) to melting and wetting (right) during the heating process in air. While the wetting angle of Ag on YSZ $> 90^\circ$ , Ag-O clusters in Ag(l) solution may alter interfacial energy ( <i>Mechanism I</i> ), or addition of Cu may facilitate formation of CuO interlayer on YSZ surface ( <i>Mechanism II</i> ) leading to reduction of the wetting angle. The SEM images used for representation of stainless steel and YSZ microstructure was taken from literature. <sup>147</sup> .....	35
Figure 2.2. The relaxed interface structures for investigation of Ag-CuO/YSZ brazes. These include Ag(l)/YSZ (a), Ag/YSZ (b), Ag/CuO (c), and CuO/YSZ (d). Only the top half of the sandwich model of the solid/solid interface is shown due to symmetry.....	39
Figure 2.3. Ag(l)/YSZ interface structures with dissolved oxygen atoms at the beginning and end of 3 ps AIMD simulations at 1000 °C. Three initial positions of Ag-O clusters were investigated, including in the bulk Ag(l), at the free surface of the Ag(l), and at the Ag(l)/YSZ interface. The Ag-O at the interface is the most favorable structure.....	42
Figure 2.4. Side view and top view of surface and interface structures to illustrate the formulation of the descriptor, $\chi_{MO}$ , in Eqn. 2.3. The $N_M$ and $N_O$ were demonstrated for a) an unrelaxed rock salt CaO {100} surface, where $f=1$ is used and b) an unrelaxed corundum oxide surface structure represented by the $\alpha$ - $Al_2O_3$ (0001). The relaxed interfaces of Ag/corundum-oxide demonstrate that b) in $\alpha$ - $Al_2O_3$ and other corundum-oxides $f=2$ is used as the protruded cation, $Al^{3+}$ , weakens Ag-O interfacial bonding, except c) in $Fe_2O_3$ , whose cation, $Fe^{3+}$ , submerges beneath the oxygen layer after relaxation so it does not interfere with the Ag-O bonds ( $f=1$ ). The yellow arrows pinpoint the same cation in all the corundum oxides. ....	48

Figure 2.5. The correlation a) between of the interface energy ( $\gamma_{12}^{\text{DFT}}$ ) of Ag/oxides and the descriptor ( $\chi_{\text{MO}}$ ), which followed a logarithmic function, and b) between the predicted work of adhesion ( $W_{\text{adh}}^{\text{pred}}$ ) at the Ag/oxides interface and the DFT calculated ones ( $W_{\text{adh}}^{\text{pred}}$ )..... 51

Figure 2.6. The relaxed structure of the Ag/CuAlO<sub>2</sub> by LDA functional showing an interface gap of 1.95 Å (a), and the PDOS of the no-contact (10 Å apart) and interface positions showing large shift in the oxygen's *p*-states. This indicates strong interactions between Ag and CuAlO<sub>2</sub> (b).... 56

Figure 3.1. 2D <sup>1</sup>H -<sup>13</sup>C HSQC NMR spectra showing lignin fraction SLRP-1 composition and linkages. The contours in aliphatic region (left) are used to quantify the fraction of inter-unit linkages, while those in the aromatic region (right) are used for S/G ratios. .... 72

Figure 3.2. Trends in monomer yields from different depolymerization techniques, including (A) Cu-catalyzed oxidation, (B) quantitative thioacidolysis, and (C) Ni/C-catalyzed hydrogenolysis. .... 74

Figure 3.3. Correlation map for fractionated alkali lignin properties and monomer yields demonstrating strong correlations between most lignin properties and its susceptibility to depolymerization *via* β-O-4 cleavage. .... 77

Figure 3.4. Selected linear correlation between fractionated lignin properties and monomer yields, demonstrating that (A) β-O-4 content is directly correlated to molecular weight and inversely correlated to phenolic hydroxyl content, that (B) monomer yields from thioacidolysis (g/g) were associated to lignin's S/G ratios and β-O-4 contents, and that (C) as well as molecular weight and phenolic hydroxyl contents. .... 78

Figure 3.5. Lignin chain model of chain length *n* used for formulating prediction rationale. The *i*<sup>th</sup> monomer unit, *n*<sup>th</sup> linkages of lignin are represented by *m<sub>i</sub>* and *d<sub>n</sub>*. A triad is composed of three monomer units. .... 80

Figure 3.6. Predicted monomer yields as a function of β-O-4 content for lignin polymer populations of chain length of 100 monomers (left) and 25 monomers (right) with results from quantitative thioacidolysis of fractionated poplar lignin and native birch biomass included for validation..... 82

Figure 3.7. Model predictions of monomer yields from lignin polymer populations of different chain lengths versus monomer yields from thioacidolysis, oxidation, and hydrogenolysis of fractionated lignin. .... 83

Figure 3.8. Predicted yield distributions for monomers, dimers, and oligomers from the cleavage of β-O-4 in a population model of lignin polymers of *n* = 100 over a range of β-O-4 contents. . 84

Figure 4.1. Thermodynamic adsorption energy cycle of lignin dimer (lig) in solvated (A and B) with ethanol (EtOH) and vacuum (C and D) state. It should be noted that, by definition, the  $\Delta E_{\text{ads}}^l$  from state A to B is intended to encompass both partial loss in lignin solvation energy and ethanol adsorption energy. The  $\delta$  is fraction of solvation energy retained when dimer adsorbs relative to full solvation. The  $\theta$  is fraction of the surface area covered by adsorbed dimer. .... 93

Figure 4.2. Adsorption energy ( $\Delta E_{\text{ads}}$ ) of guaiacol at four different sites, top, bridge, FCC, and HCP, with two orientations, 0° and 30° with respect to the hexagonal ring formed by of nickel atoms on the top layer of the slab. .... 98

Figure 4.3. Top view and side view of relaxed hypothetical lignin of 10 G-units with only  $\beta$ -O-4 linkages and possible adsorption conformations of the polymer on metal surfaces (A). The approximated adsorption energy of the polymer ( $\Delta E_{\text{ads}}^g$  (polymer)) for a given number of units adsorbed on Ni and Cu and conformation energy ( $\Delta E_{\text{conf}}$ ) for a given number of unit fixed to lie horizontal (B). ..... 99

Figure 4.4. Relaxed adsorption conformations of lignin *threo*-dimer where in A) and B) both rings adsorb to the surface with both aryl rings completely planar, C) only one ring is completely planar, D) and E) only one ring adsorbs. The change in angles between the aromatic ring to the atoms next to it in conformation A and B compared to relaxed free dimer is shown in the enlarged images. The distances (Å) from the surface to all oxygen atoms in the molecule are also shown for conformation A and B. .... 103

Figure 4.5. Relaxed adsorption conformations of lignin *erythro*-dimer where both rings adsorbed on the Ni(111) with one conformation yielding an ethyl oxygen atom away from the surface (I) and the other adsorbed onto the surface (II) with distances from the surfaces to all oxygen atoms in the molecule and some bond distances within the molecule. .... 105

Figure 4.6. The values for solvent accessible surface area (SASA) using a 1.25 Å probe radius (grey mesh), the number of neighboring atoms (enlarged solvent atoms), and the number of bonds within a 2.5 Å radius before and after adsorption for relaxed A and D conformation from Table 4.2 in ethanol. The average  $\delta$  value is shown in parentheses. .... 108

Figure 5.1. Monomer yields from hydrogenolysis reaction at 200 °C (patterned) and 220 °C using different metal/C catalysts with whole biomass. The results are arranged according to group and period in the periodic table. The column “None” refers to no catalysts added. The products are, from left to right, 4-propylguaiacol (4-PG), 4-propylsyringol (4-PS), 4-propenylguaiacol (4-PnylG), 4-propenylsyringol (4-PnylS), 4-ethylguaiacol (4-EG), 4-ethylsyringol (4-ES). The very small green color in Pd corresponds to syringol. .... 121

Figure 5.2. Monomer yields from hydrogenolysis reactions of lignin dimer (guaiacylglycerol-beta-guaiacyl ether) using Pd/C in ethanol with and without presence of H<sub>2</sub> gas. The 4-vinylG and 4-PnylG refer to 4-vinylguaiacol and 4-propenylguaiacol, respectively. .... 124

Figure 5.3. Monomer yields from hydrogenolysis reaction using Ni/C and ethanol at 220 °C of alkali lignin that was sequentially precipitated through CO<sub>2</sub> acidification. The S refers to syringol. .... 126

Figure 5.4. Images of raw birch biomass (A), and after pretreatment at 220 °C in ethanol with no catalyst (B), and with Co/C catalyst (C). .... 127

Figure 5.5. Percent recovery of glucan, xylan, and lignin after pretreatment at 200 (dotted line) and 220 °C in ethanol with different metal/C catalysts (A). The correlation between total monomeric yields and lignin removal (100 – lignin recovery) (B). .... 128

Figure 5.6. Enzymatic hydrolysis yields of the biomass after the reaction at 200 (dotted line) and 220 °C in ethanol with different metal/C catalysts (A). The sugar yields are based on the untreated biomass compositions. The correlation between lignin removal and glucose yields (B). .... 129

Figure 6.1. Lignin dimer adsorption on Pd (111) with 0 and 0.33 ML hydrogen coverage. .... 132

Figure 6.2. <i>Ab initio</i> shows alcohol decomposition leads to H and ethoxy adsorbing species on Ni(111).....	133
Figure A1. The relaxed bulk structure of CuAlO <sub>2</sub> (a) and its (0001) <sub>O</sub> surface (b). The relaxed bulk structure of TiCu <sub>3</sub> O <sub>4</sub> (c) and its (010) <sub>O</sub> surface (d).....	139
Figure A2. Pair radial distribution function of Ag-Ag in liquid Ag with 2 O atoms dissolved showing the nearest Ag-Ag distance of 2.8 Å, which is the same to the experimental value of pure silver measured in reducing atmosphere.....	143
Figure A3. Projected density of states (PDOS) of interface atoms in Ni/YSZ, Ag/YSZ, and Ag/CuO in their no-contact positions (slabs were 10 Å apart) and in their interface position as calculated by LDA functional.....	144
Figure A4. Projected density of states (PDOS) of CuO(111) surface with stretched lattice parameters to match that of the metals in the interface. It exhibited a bandgap of 0.25 eV.....	145
Figure A5. Surface structures showing the difference between the position of the terminated metallic atom of most corundum oxides (represented by Al <sub>2</sub> O <sub>3</sub> ) and the Fe <sub>2</sub> O <sub>3</sub> . These are (0001) surface of initial Al <sub>2</sub> O <sub>3</sub> slab (a), relaxed Al <sub>2</sub> O <sub>3</sub> slab (b), initial Fe <sub>2</sub> O <sub>3</sub> slab (c), relaxed Fe <sub>2</sub> O <sub>3</sub> slab (d), relaxed Ag(111)  Al <sub>2</sub> O <sub>3</sub> (0001) interface (e), and relaxed Ag(111)  Fe <sub>2</sub> O <sub>3</sub> (0001) interface (f). .....	147
Figure A6. The correlation between $W_{adh}$ and the oxide formation energy of (0001) surface corundum type oxide and {001} rock salt type oxide. Note that Fe <sub>2</sub> O <sub>3</sub> was not included for the reason that its geometry was unlike other corundum oxides after surface relaxation. ....	147
Figure B1. Trends of phenolic hydroxyl contents (black) in fractionated lignin showing lower values in fractions precipitated at higher pH, while aliphatic hydroxyl content (red) do not show any specific trend.....	149
Figure B2. Trends of S/G ratios in fractionated lignin by HSQC NMR (red) and thioacidolysis (black) showing higher S/G values in fractions precipitated at higher pH and SLRP samples..	149
Figure B3. Trends of β-O-4 content (black) as measured by <sup>13</sup> C-NMR and molecular weight among fractionated lignin showing similar increasing trend in fractions precipitated at higher pH and SLRP samples. ....	149
Figure B4. Kinetics of Cu-catalyzed oxidation reactions of lignin sample SLRP-2 showing time for optimal yield at the study condition is at 7 minutes.....	150
Figure C1. The change in fraction of surface accessible surface area (SASA) of the dimer in solvated adsorb in reference to fully solvated state ( $\delta$ ) as estimated by SASA as a function of probe radius.....	151

## **CHAPTER 1 Background and Motivations**

### **1.1 Selected Interfaces in Solid Oxide Fuel Cell and Biorefinery & Problem Identification**

#### **1.1.1 Interfaces are Key Components in Energy Conversion and Storage Devices**

To decrease our dependence on fossil fuels, there has been a surge in development and deployment of alternative energy in the past decade. From 2008 to 2017, the generation of non-hydro renewable energy in the U.S. has more than tripled,<sup>1</sup> most of which can be contributed to the wind and solar energy sector. However, these technologies alone would not suffice because of, first, the intermittent nature of the energy source and, second, limited land-based transmission infrastructure in certain regions.<sup>2</sup> In light of the first shortcoming, battery and fuel cells have emerged as the solution for energy storage/conversion device. Additionally, both of them can also be used for transportation applications supported by alternative fuels. The second shortcoming can be addressed by other renewable energy sources, particularly lignocellulosic biorefinery, which produces liquid fuels that can leverage existing pipeline networks. Together, these technologies could expand the usage and applications of renewable resources, and hence, reduce our reliance on petroleum.

Two of the renewable energy technologies that are of the interest in this thesis are the solid oxide fuel cell (SOFC) and the lignocellulosic biorefinery. A SOFC is an electrochemical conversion device that produces electricity directly from oxidizing fuels such as methane or syngas using ceramic or oxide electrolytes. Lignocellulosic biorefinery is a process of chemical conversion and separation of biofuels and chemicals from non-food woody biomass, such as poplar or switchgrass, both of which have great potentials. For SOFC, it has been praised for fuel flexibility, low emissions, the highest efficiency (60-90%) of any hydrocarbon-based electricity generation technology, and most importantly, the highest gravimetric and volumetric power

densities of any energy conversion technology.<sup>3</sup> This makes SOFC suitable for applications such as offsetting intermittent renewable power sources.<sup>4</sup> On the other hand, lignocellulosic biorefinery offers not just energy from biofuels, such as ethanol, but also a platform for renewable chemicals.<sup>5</sup> As an example of how these technologies could expand the use of alternative fuels, bioethanol can also be integrated with SOFC as an energy storage in a vehicle as currently deployed by Nissan e-NV200 (Figure 1.1).<sup>6,7</sup> Together, they provide an alternative to battery-based electric vehicles, while also leveraging the existing petroleum infrastructure.<sup>8</sup>

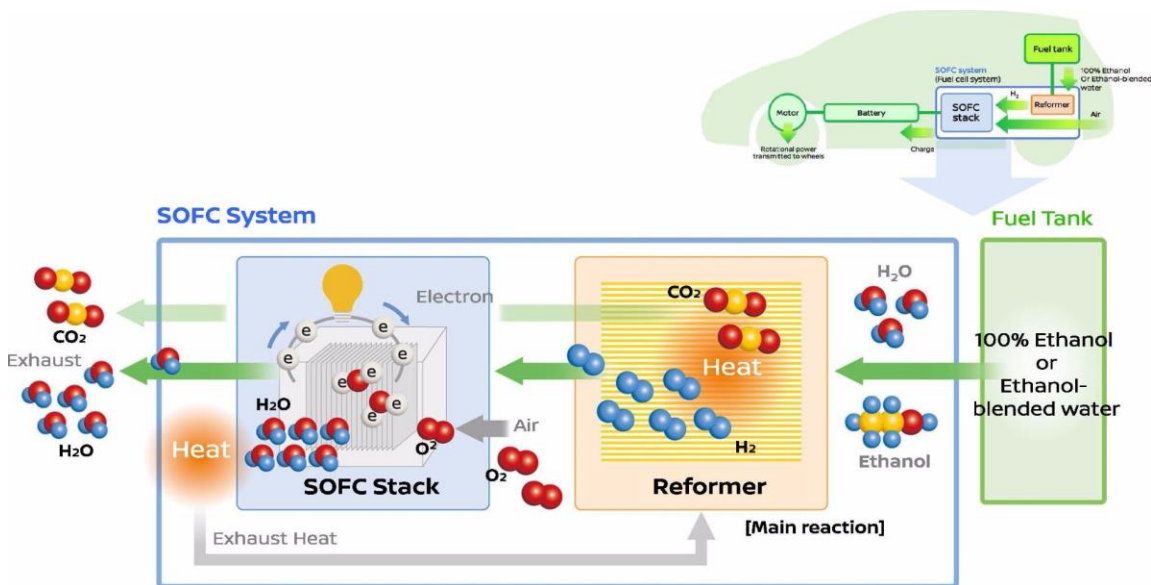


Figure 1.1. Schematic diagram of SOFC in Nissan vehicle using bio-ethanol as a fuel (adapted from <sup>6</sup>).

A diagram of a SOFC shown in Figure 1.2A shows that it is composed of anode, cathode, and a solid electrolyte, which are usually made up of nickel, lanthanum strontium manganite (LSM), yttria-stabilized zirconia (YSZ), respectively. An SOFC generates electricity through oxidation of fuels on the anode side. The oxygen is supplied from the cathode side, transporting through the solid electrolyte. This is possible through the high ionic conductivity of YSZ or other electrolyte materials at higher temperatures.<sup>9,10</sup> In practice, each SOFC is sealed and stacked

together to provide more power, where sealing is applied in between each unit and is in contact with its electrolyte, and the cell frame, which is typically made out of stainless steel (Figure 1.2B). Therefore, it is crucial that the sealant has a strong binding to both YSZ and stainless steel.

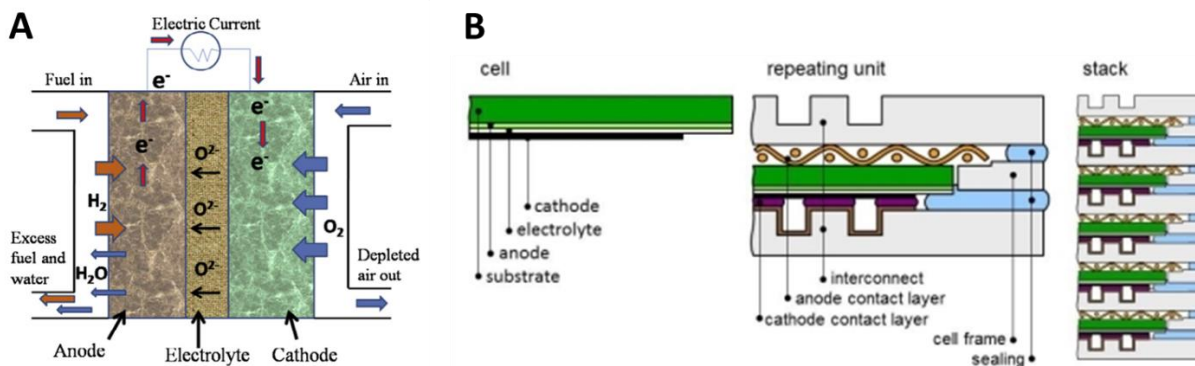


Figure 1.2. Schematic diagram of a single SOFC with a solid oxide-ion conducting electrolyte (A, adapted from <sup>11</sup> with permission), and of stacked SOFC showing sealing in each unit which is in contact with the SOFC's electrolyte (B, adapted from <sup>12</sup>).

The biofuel used in Fig 1.1, such as ethanol, can be generated from lignocellulosic biomass through biorefinery. Lignocellulosic biomass is mainly composed of cellulose, hemicellulose, and lignin. Biorefinery is a sustainable processing of these biomasses into a spectrum of marketable products. Beyond ethanol, Figure 1.3 shows these products, catalytic conversion methods, and which part of the biomass it came from. In practice, lignin is the only part that is still underutilized because it is cheaply burned at-site for energy production. As lignin accounts up to up to ~30% of plant's mass and is one of a few potential natural sources of aromatics,<sup>13</sup> its valorization represents a vital improvement in the economic viability of cellulosic biorefineries. In literature, numbers of studies have achieved this through either liquid-phase catalytic oxidative or reductive approaches (Figure 1.3). Therefore, an understanding of how lignin valorization reactions proceed on the catalyst surface is important for catalyst and solvent design to improve yields, selectivity, and other desired catalyst properties.

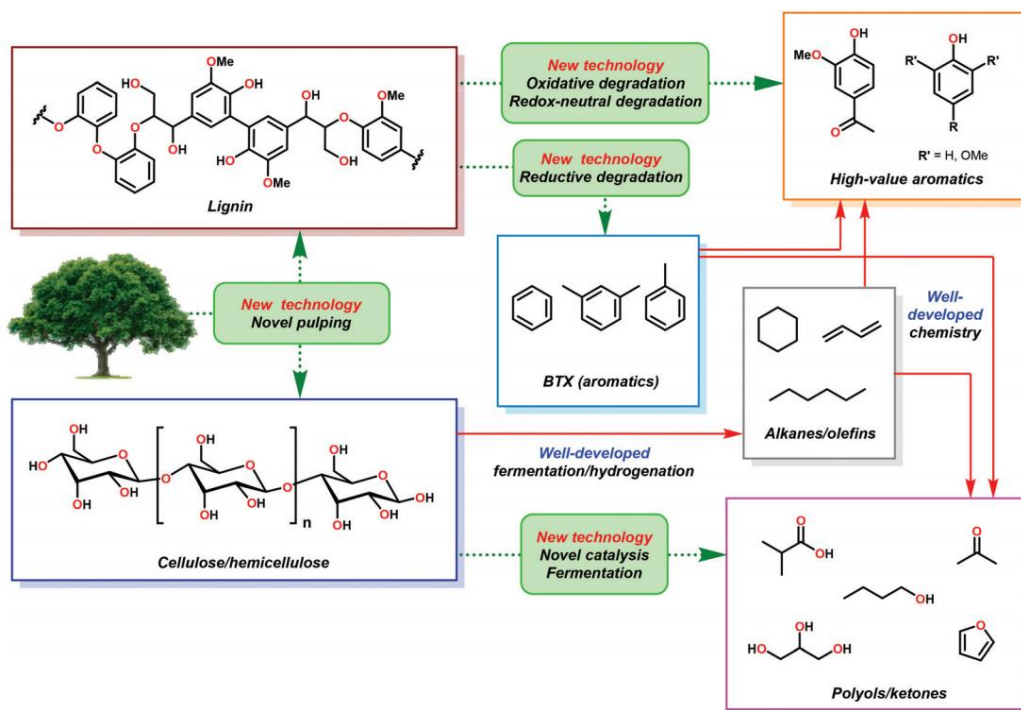


Figure 1.3. The hypothetical biorefinery concept with an examples on how each component of the lignocellulosic biomass (cellulose, hemicellulose, and lignin) can be catalytically converted to useful fuels and chemicals (adapted from <sup>14</sup> with permission).

In both of these technologies, a number of interfaces are involved and are critical in determining the feasibility and efficiency of the technologies. Interface is a boundary between two spatial regions occupied by different matter, at which material properties differ from the bulk phase. Fundamental to the operation of SOFC, the oxygen gas is reduced ( $\frac{1}{2} \text{O}_2(\text{g}) + 2\text{e}^- \rightarrow \text{O}^{2-}$ ) and diffuse into the cathode (LSM) surface through its oxygen vacancies, then through the electrolyte, and finally to the anode surface (Ni cermet/YSZ) where it is used for catalytic oxidation of  $\text{H}_2$  ( $\text{H}_2(\text{g}) + \text{O}^{2-} \rightarrow \text{H}_2\text{O} + 2\text{e}^-$ ).<sup>15</sup> To prevent these gases from leaking, a sealant is applied between the device's exposed surfaces and the stainless steel frame. Therefore, the adhesion at the SOFC/sealant/frame interface determines the strength of the seal. In lignocellulosic biorefinery, catalytic process is at the heart of its depolymerization process for all major components. For

example, efficient conversion of carbohydrates in biomass to furfurals, which are valuable feedstock for chemicals production, was conducted in organic solvents and typically with zeolite catalysts.<sup>16-18</sup> For lignin, its hydrogenolysis to aromatic monomers are usually conducted in liquid phase with various metal-supported catalysts such as Ni, Pd, and Pt.<sup>5,19</sup> These reactions occur at the liquid/solid interface of the solvated adsorbate with the catalyst. Therefore, their interactions at the interface largely determine the type of products, yields, and selectivity.

Two specific interfaces among these are of particular interest in this thesis. The first interface is the seal between the SOFC and the stainless steel frame, particularly at the interface between SOFC's electrolyte and its sealant, which currently inhibits the SOFC shelf life because of its early degradation. The other interface is the liquid/solid interface between solvated lignin and metal surfaces. This interface is critical in understanding of the effect of solvent on adsorbate-surface interactions, particularly in a context of catalytic reaction pathways.

### **1.1.2 Sealing of the Electrolyte in SOFC**

For SOFC, the interface problem of an interest is the adhesion between the device's electrolyte and its sealant. Currently, due to the extreme operating conditions of SOFC, its sealant microstructure degrades prematurely, inhibiting a long shelf life of SOFC. However, finding new replacement materials that would exhibit similarly strong adhesion to the electrolyte, and hence seal it, has proven to be a challenging task. This is because the sealing material has to be able to withstand extreme temperature (~800-1000 °C), and a highly oxidizing and reducing environments for prolonged period of time. Apart from these, the material needs to adsorb mechanical stress and the differences in thermal expansion.<sup>11</sup> Most importantly, it also needs to have strong binding to YSZ so that the seal can be hermetic.

Current technology employs a Ag-CuO braze to seal the exposed YSZ surface and mechanically supported by ferritic stainless steel frame.<sup>20</sup> Ag is used because of its many desirable braze characteristics including stability in air above 160 °C<sup>21</sup> and sufficient braze strength and ductility to withstand stress from expansion mismatch with YSZ.<sup>22</sup> Because liquid Ag used in the initial stages of the air brazing process needs to completely wet, *i.e.* spread on, on YSZ surface in order to form a coherent surface upon solidification, a small amount of Cu or CuO is added to promote its wettability. The wettability can be measured by contact angle, with an angle of more than 90° considered non-wetting. The contact angle of Ag on YSZ in air is 110 °C,<sup>23</sup> while adding just 4 wt% of CuO, which forms a CuO-rich layer between Ag and YSZ (SEM micrograph),<sup>24</sup> reduces it to 45° and keeps it adhered strongly upon solidification.<sup>25</sup>

However, overtime the high hydrogen diffusivity in Ag ( $8 \times 10^{-5}$  at 750 °C)<sup>21</sup> leads to reduction of CuO, and hence, formation of pores in the braze, limiting the lifespan of SOFC. Replacing CuO with many other common monovalent metal oxides did not lead to similar Ag wetting effect.<sup>26</sup> This emphasizes the need to find alternative oxides that could be more chemically complicated. However, currently it is not well understood how CuO helps Ag wet on YSZ. Having such understanding would be useful in facilitating materials discovery. **Therefore, the objectives of Chapter 2 of this thesis are to identify what are the underlying mechanisms of Ag-CuO/YSZ and to leverage the insight for designing new materials.**

### 1.1.3 Catalytic Hydrogenolysis of Lignin in Liquid Phase

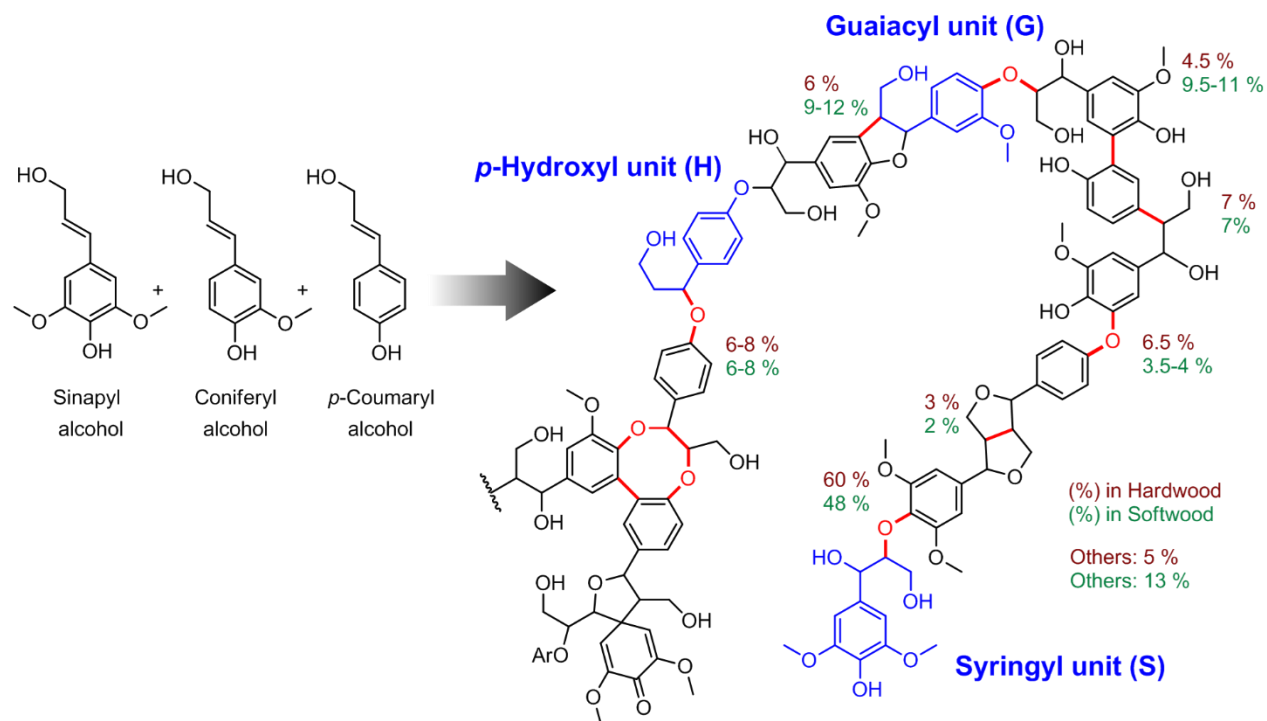


Figure 1.4. Hypothetical structure of softwood and hardwood lignin. Bonds abundance is obtained from Adler.<sup>27</sup>

For lignocellulosic biorefinery, the interface of interest is the adsorption of solvated lignin on metal surfaces. This represents an interface during lignin catalytic depolymerization to valuable chemicals (henceforth referred to as lignin upgrade/valorization), which is crucial to the economic feasibility of lignocellulosic biorefinery. Despite most upgrading reactions being performed in a liquid phase, there is still limited understanding of the solvent effect on surface adsorption mechanisms. Understanding this more could aid in catalyst and solvent design.

It is very challenging to understand and model the extremely complicated lignin upgrade topic, both from the perspective of lignin structure and its upgrade. This is because, first, lignin is a complex phenylpropanyl polymers synthesized in plant from three monomeric precursors, namely *p*-coumaryl, coniferyl, and sinapyl alcohol, which lead to its three monolignol units of *p*-

hydroxyphenyl, guaiacyl, and syringyl, respectively (Figure 1.4). Different types of plants have different proportions of these units in lignin. These units are then randomly connected by several types of ether and carbon cross-linkages shown in red in Figure 1.4. Secondly, isolation processes of lignin from biomass further induce more changes to its natural structure, mostly either introducing undesirable functionalization (Figure 1.5) or degrading it by forming more recalcitrant C–C linkages. These resulted in even more complex functionalities in lignin, including but not limited to variable changes in amounts of methoxyl groups, phenolic and aliphatic hydroxyl groups, polymer chain length, and linkages depending on the process. Each of these functionalization has been reported to affect depolymerization products and yields, especially the abundance of C–O linkages, which are the primary target as they are the most easily cleaved.<sup>28–31</sup>

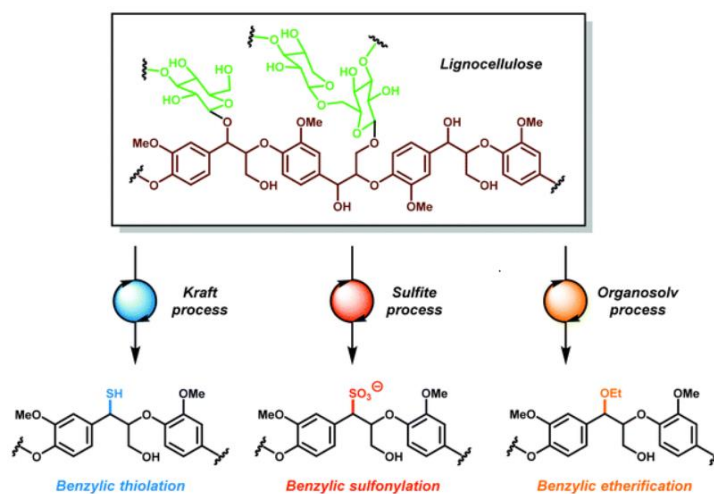


Figure 1.5. Examples of changes in lignin functionalities at the  $\beta$ -O-4 linkage after going through different types of lignocellulosic biomass pretreatment (adapted from <sup>14</sup> with permission).

Despite a number of reports on the effect from each functional group, quantitative relationships that relate these groups collectively with product yields have not been fully demonstrated yet. For modeling of the liquid/solid interface in the present study, this knowledge is vital in confirming that the section of lignin selected for atomistic modeling, which will be

limited in number of atoms, contains all the major yield-deciding functionality. Additionally, for the general lignin community, the understanding of this relationship would be useful for benchmarking the quality of lignin from different sources. **Therefore, prior to modeling lignin adsorption, Chapter 3 of this thesis will employ a number of experimental techniques (spectroscopies and wet chemistries) to characterize how lignin's functionalities relate to its monomer yields.**

Table 1.1. Major products from selective hydrogenolysis reaction of lignin showing a wide range of possible products depending on reaction conditions and catalysts.

Catalyst	T(°C), H <sub>2</sub> (bars)	Solvent						
			<i>P1</i>	<i>P2</i>	<i>P3</i>	<i>P4</i>	<i>P5</i>	<i>P7</i>
Ni/C*	200-200 °C, 0 MPa	C <sub>2</sub> H <sub>5</sub> OH		●	●			
Ni/C <sup>32</sup>	220 °C, 2 MPa	Dioxane		●			●	
Ni/Al <sub>2</sub> O <sub>3</sub> <sup>33</sup>	250 °C, 3 MPa	CH <sub>3</sub> OH		●			●	
Raney Ni <sup>34</sup>	200 °C, 0 MPa	CH <sub>3</sub> OH		●	●	●		
Pd/C*	200-200 °C, 0 MPa	C <sub>2</sub> H <sub>5</sub> OH	●	●	●			
Pd/C <sup>35</sup>	225 °C, 3.4 MPa	CH <sub>3</sub> OH		●			●	
Pd/C, Ru/C <sup>36</sup>	200-200 °C, 2 MPa	C <sub>2</sub> H <sub>5</sub> OH+ H <sub>2</sub> O	●					
PdZn/C <sup>37</sup>	225 °C, 3.4 MPa	CH <sub>3</sub> OH		●				
Ni <sub>7</sub> Au <sub>3</sub> <sup>38</sup>	130-160 °C, 1 MPa	Alkali H <sub>2</sub> O	●	●			●	
CuPMO <sup>39</sup>	180-220 °C, 4 MPa	CH <sub>3</sub> OH		●			●	●

\*Reactions done in the present thesis (See Chapter 6).

Catalytic depolymerization of lignin yields a mixture of valuable aromatic chemicals and degraded compounds. Particularly, liquid-phase hydrogenolysis will be the focus of the present thesis as it has been studied extensively recently. Apart from the lignin chemistry, catalytic hydrogenolysis of lignin would not only result in different yields, but could vary significantly in types of products as shown in Table 1.1. These differences could stem from the choice of catalyst, H<sub>2</sub> pressure, and solvent. For the last factor, as can be seen in the case of Pd/C in Table 1.1 where reaction temperature and H<sub>2</sub> pressure are similar, with different solvents, products could differ. In the present thesis, the effect of solvent will be highlighted.

Currently, the understanding of the solvent effects primarily comes from experimental approaches. By varying solvent choice and using Ni catalyst, it was suggested that in low temperatures (<100 °C), aprotic non-polar solvents, such as decalin and n-heptane, result in the highest yields with complete conversion to hydrogenated products. Through a thorough discussion, it was proposed that other solvents, including methanol, ethanol, and 1,4-dioxane, among others, result in low conversions because of strong interactions with the Ni surface. However, these solvents are also very commonly used for lignin reactions due to their high solubility.<sup>40</sup> Therefore, the paper highlighted a very interesting question quote: *“Is a compromise between catalytic activity and substrate solubility required for the efficient conversion of lignin?”*. Certainly, one of the solutions is to heat the reaction up significantly (>200 °C), which shows that alcohols can give similar yields. This is in agreement with the fact that most hydrogenolysis studies employ alcohols and Ni catalysts, which requires high temperatures.<sup>5,19</sup> Note that in many cases high reaction temperatures also lead to undesirable products and lower selectivity.<sup>41,42</sup> However, high yields from alcohol solvents at high temperatures are not necessarily true to all catalysts as a separate study comparing solvents at 300 °C using zeolite based catalysts suggests that other solvents,

including methyl isobutyl ketone and acetone, resulted in higher yields than alcohols.<sup>43</sup> There are several possible causes to the discrepancy, and one of which relates back to the effect of solvent, *i.e.* the change in the adsorption of lignin and its reaction intermediates could vary significantly depending on a specific combination of catalyst and solvent.

To answer the aforementioned question, hypothetically, there may exist a combination of solvent and catalyst that can dissolve lignin, and not at the cost of catalytic activity because of its interaction with the surface. To find (or design) that solvent, how these solvents affect the lignin-metal interactions at the surface needs to be understood first. However, studies on how the  $\beta$ -O-4 lignin dimer adsorbs on the surface even in a gas state is scarce and still inconclusive. More importantly, it was reported that different isomers of the model yielded different adsorption conformations on Ni surface, which subsequently leads to different reaction paths.<sup>44</sup> This stresses the significance of identifying adsorption structure, and particularly, how it changes when solvated. **Therefore, Chapter 4 of this thesis aims to clarify how lignin adsorbs on metal surfaces, and demonstrates how it changes with the effect of solvents, using a representative section of lignin. Additionally, the effect of these changes between different catalysts will be briefly compared to experiments through catalytic hydrogenolysis in Chapter 5.**

## **1.2 Contributions of DFT Calculations to the Understanding of Interface Interactions**

The use of multi-scale modeling and simulation methods has become a widely accepted strategy for furthering our understanding in essentially all fields of chemistry, biochemistry, condensed matter physics, and materials science.<sup>45</sup> Different modeling methods have different strengths, shortcomings, and hence, various suitable applications. In theory, material properties and reaction mechanisms can be describable by quantum mechanics (QM). However, as shown in Figure 1.6, simulation of large system size or long dynamics time, such as modeling of materials

crack propagation or nanoparticles sintering, are proven to be impractical for QM due to computational expense.<sup>46</sup> This was addressed by using approximations and simpler equations as shown in the higher scale at the expense of energy and force description accuracy. In this thesis, density functional theory (DFT) calculations, which is one of the flavors of QM, will be the primary computational tool for study of the interfaces. DFT is a method of obtaining an approximate solution to the Schrödinger equation of a ground-state many-body system. In DFT, the interacting system of fermions is described as a function of density, instead of its many-body wavefunctions. This allows the system to depend on spatial coordinates, instead of a number of electrons in a system. It should be noted that the energetics term derived from DFT does not include a contribution from entropy from translation and rotational modes.<sup>47</sup> In this section, general concepts and applications that DFT calculations can contribute to different types of interfaces will be discussed. These will also include energetic terms that will frequently be brought up.

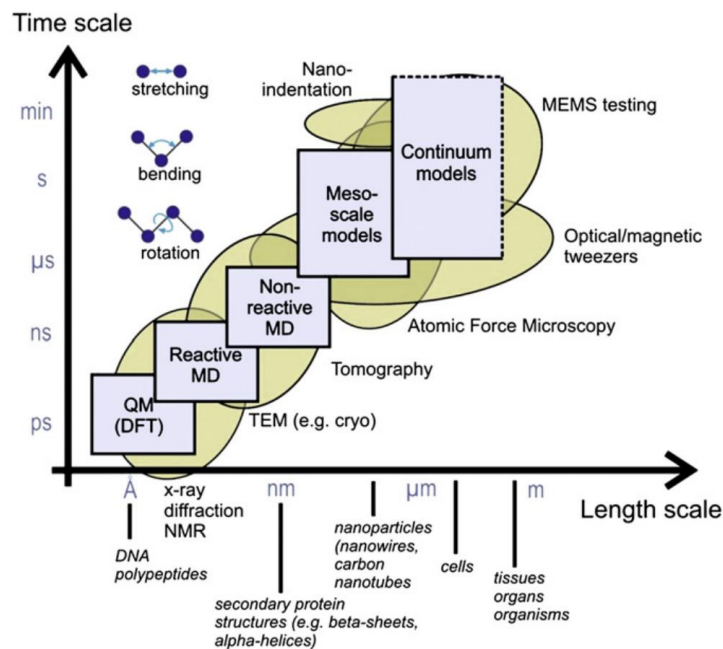


Figure 1.6. Experimental, theoretical and computational tools plotted over their respective time and length scale domain of applicability with examples in the characterization and modeling of deformation and failure of biological protein materials (adapted from <sup>46</sup> with permission).

### 1.2.1 Contributions to the Gas/Solid Interface Interactions

For gas/solid interfaces, DFT calculations are regularly used for the understanding of molecular adsorption and reaction on catalyst surface. DFT is selected in these applications to provide insights at the interface including geometry, energy, electronic structure, and more. Particularly, the adsorption energy of gas phase molecule ( $E_{\text{ads}}^g$ ), which is a measurement of the interaction between adsorbate and surface, was also measured, and is typically calculated in DFT by:

$$E_{\text{ads}}^g = E[\text{Adsorbate} \cdots \text{Metal}] - (E[\text{Adsorbate}] + E[\text{Metal}]) \quad \text{Eqn. (1.1)}$$

where  $E[\text{Adsorbate} \cdots \text{Metal}]$  is the energy of the cell with adsorbate on metal surface and  $E[\text{Adsorbate}]$  and  $E[\text{Metal}]$  are cells with individual adsorbate molecule and metal surface, respectively. Therefore, negative  $E_{\text{ads}}^g$  means it is an exothermic adsorption (the system gains energy). Using this concept, DFT calculations have shown accurate description of  $E_{\text{ads}}^g$  for many systems, including aromatics on metal surfaces, compared to experimental methods.<sup>48-50</sup>

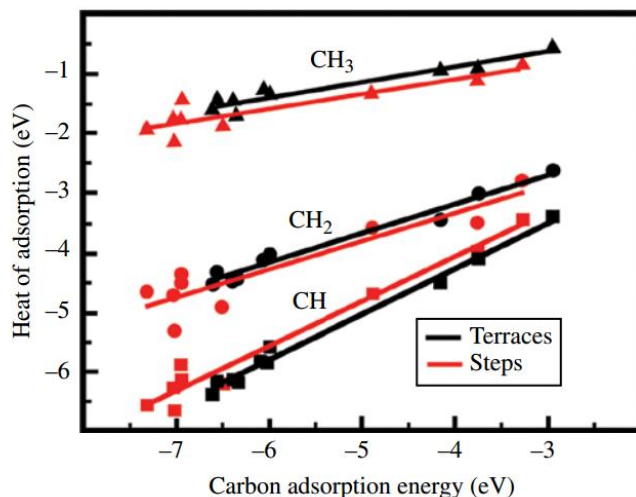


Figure 1.7. DFT calculated scaling relations for adsorption energies of  $\text{CH}_x$  species plotted against the adsorption energy of C for a number of different transition metals (adapted from <sup>51</sup> with permission).

With analyses of and faster access to the energetics at gas/solid interface, DFT has revealed several universal adsorption trends with fundamental insight and can be used for materials search, particularly in catalytic context. For example, scaling relations were developed to show that  $E_{\text{ads}}^g$  of different surface intermediates that bind to the surface through the same atom(s) scale with each other. An example of the relation is shown in Figure 1.7 for simple  $\text{CH}_x$  species on various metal surfaces.<sup>51</sup> With electronic structure analyses, it was demonstrated that the trend originating from that adsorption strength can be approximated by metal's  $d$  electrons, and is independent of their  $sp$  electrons. Given that the variations in adsorption energies and transition state energies are governed by the same basic physics, it is not surprising that the relation can also be used to relate with transition state energy, which can be used for calculation of reaction rate, leading to significantly faster catalyst screening and design. The approach has a wide impact over catalyst search for numbers of reactions, such as ammonia synthesis,<sup>52,53</sup> alcohol synthesis,<sup>54</sup> methanation,<sup>55</sup> hydrogen evolution,<sup>56</sup> acetylene hydrogenation,<sup>57</sup> ethanol decomposition,<sup>58</sup> and many more.<sup>59,60</sup> An example of this is shown for methanation ( $\text{CO} + 3\text{H}_2 \rightarrow \text{CH}_4 + \text{H}_2\text{O}$ ), where C-O dissociation was found to be the rate-limiting step. In Figure 1.8A, it is shown that the activation energy for C-O dissociation scaled with the dissociative adsorption energy of CO. The activation energy can then be used to quickly approximate activity using microkinetic models.<sup>61</sup> The result shown in Figure 1.8A indicated that Co and Ru should have the high activity; however, due to their high price, DFT calculations also suggest that alternatives such as Fe-Ni alloys with the composition between FeNi and FeNi<sub>3</sub> should yield similar activities.<sup>55</sup> The design was then confirmed by experiments where FeNi and FeNi<sub>3</sub> showed the highest activity (at different metal loading, Figure 1.8B) when alloy composition was varied, and were reportedly close to Co. These examples show that DFT has proven to be an efficient tool for exploration of gas/solid interface,

starting from accurate adsorption energy, to energy barrier determination, and finally to development of strategies for materials design. Therefore, DFT would be a suitable tool to provide insights to lignin/metals interactions in the present thesis.

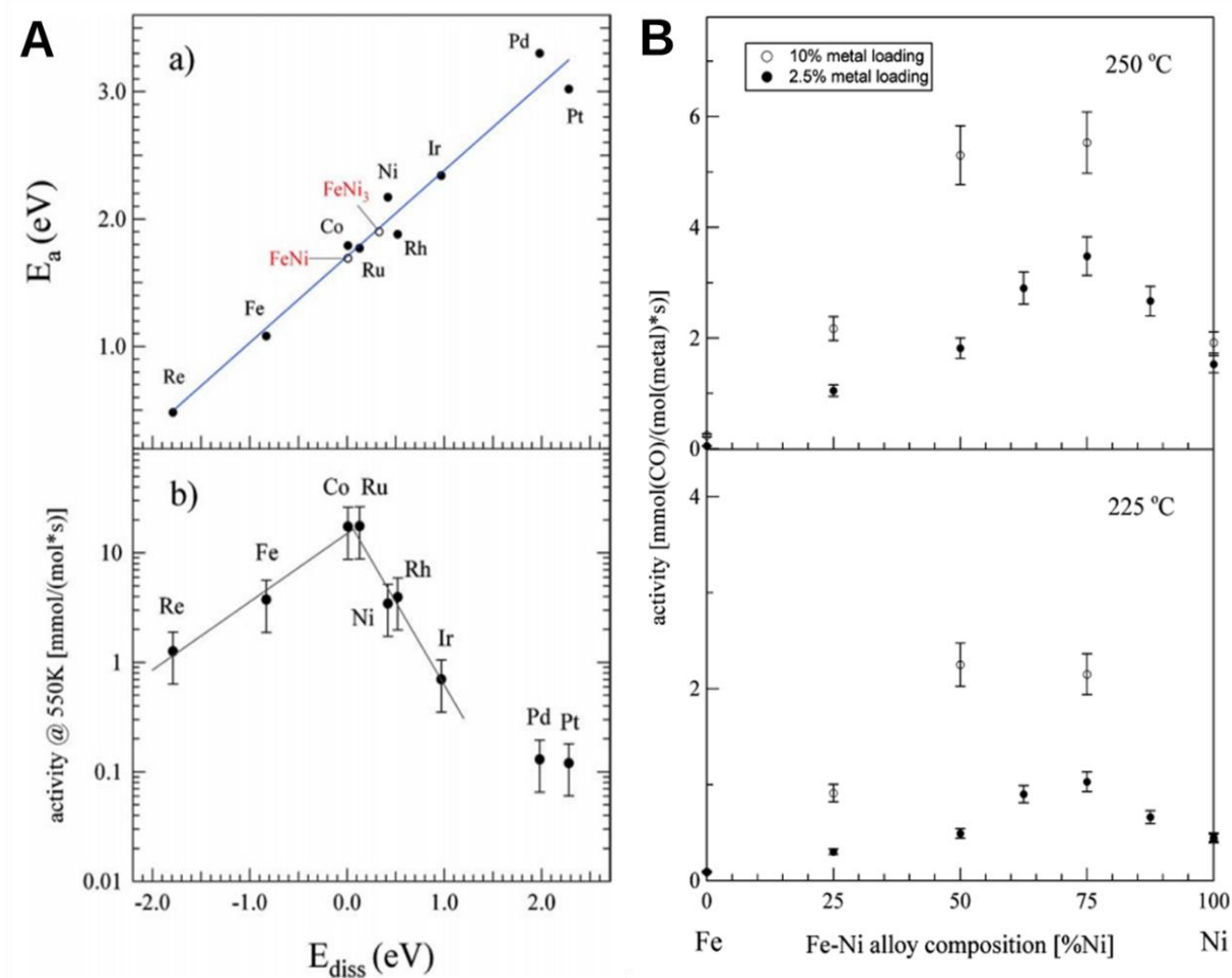


Figure 1.8. DFT-calculated scaling relation between CO dissociative adsorption energy and an activation energy of C-O bond dissociation for methanation reaction (A). Experimentally measured rate as a function of the Fe/Ni content in catalysts (B) (adapted from <sup>55</sup> with permission).

### 1.2.2 Contributions to the Solid/Solid Interface Interactions

At the solid/solid interface, materials of different phases adhere together, and the strength can be measured by several methods, such as scratch testing<sup>62</sup> and direct pull-off.<sup>63</sup> Measurement

from these methods, however, would also depend on macroscopic properties, such as cracks, grain boundaries, and other defects, apart from the chemistry of the materials.<sup>63</sup> To exclude interferences from these macroscopic features, analyses of images such as the ones from HRTEM were used to quantify pure interface adhesion that only depends on surface chemistry and atomic geometry.<sup>64</sup> This microscopic adhesion insight is useful in many applications, such as determining deposited nanoparticle coarsening. However, the procedure is significantly more complicated as it involves sample preparation such as deposition, annealing, and equilibration of metals under electron microscope,<sup>64</sup> making the amount of data in the literature limited. Conveniently, the adhesion in this level is also describable using DFT calculations, with an appropriate setup and a well-defined scope.

DFT has been used extensively to measure microscopic work of adhesion between two materials. Herein, the work of adhesion ( $W_{\text{adh}}$ ) is defined as the reversible thermodynamic work required to separate the interface from the equilibrium state of two phases to a separation distance of infinity. and could be calculated from DFT by:

$$W_{\text{adh}} \equiv (\gamma_1 + \gamma_2) - \gamma_{12} = (E_1 + E_2) - E_{12} \quad \text{Eqn. (1.2)}$$

where  $\gamma_1$  is the surface energy of material 1,  $\gamma_{12}$  is the interface energy at the boundary of material 1 and 2,  $E_1$  is the energy of the cell of slab 1 and  $E_{12}$  is the energy of the interface cell. Note that by definition, surface energy is the amount of work per area required to create a surface. Similarly, the amount of work per area required to increase that interface area is called interface energy. From Eqn. 1.2, the higher positive  $W_{\text{adh}}$  is, the stronger the interface adhesion. Using this setup, previous studies have demonstrated accurate  $W_{\text{adh}}$ , including that of metal/oxide, compared to experiments.<sup>65–68</sup>

## Scaling Relations

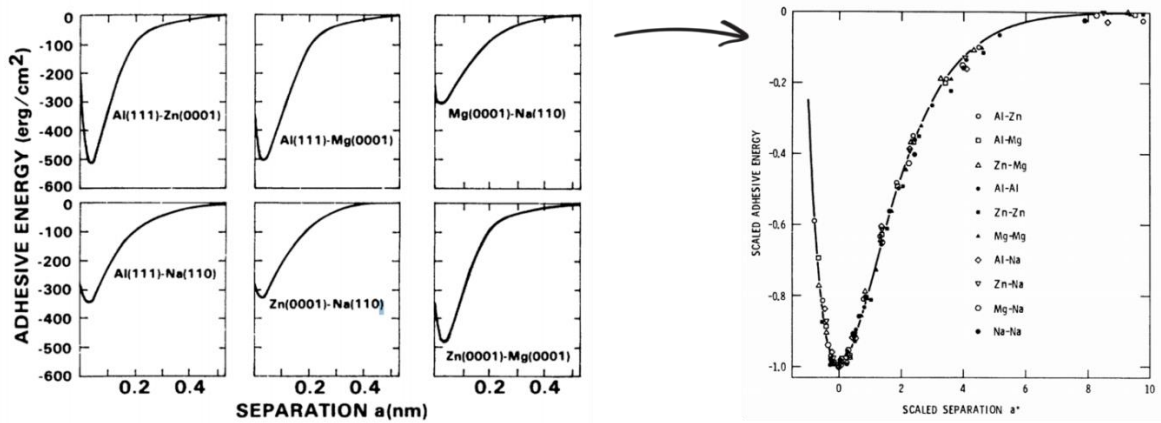


Figure 1.9. Universal scaling relation for adhesion energy of different metal interfaces (adapted from <sup>69,70</sup> with permission).

With the ability to focus on just the effect from surface chemistry and geometry, DFT has contributed many valuable insights and predictive capability to the field of solid/solid adhesion. For example, it was used to construct the universal binding-energy relation (UBER).<sup>69,70</sup> This relation describes the relationships between atomic separation and binding energy, or adhesion in this case, using just two parameters – the equilibrium adhesion energy and the equilibrium interstitial electron density – to fit a universal scale curve as shown in Figure 1.9. The equilibrium interstitial electron density is used for calculation of scaled distance ( $a^*$ ), which one could think of this as an analogy to scaling a length unit to a dimensionless parameter. The origin of this scaling behavior was identified to be the exponential decay of electron density into a vacuum from surfaces or interstitial sites.<sup>71</sup> This relation has an impact in many fields since it is essentially based on interatomic interactions. For example, by describing the interface of the same materials (*i.e.* cohesive energy), this relation has been used to derive an equation of state (EOS) for metals.<sup>72</sup> The predicted EOS compared to experimental data are shown in Fig 1.10. This has a significant impact in predicting materials properties. The universal relation itself has also been used as a foundation

in many other solid/solid relations, such as predicting crack growth,<sup>73,74</sup> predicting bulk modulus,<sup>75</sup> thermal expansion,<sup>76</sup> and melting temperatures.<sup>76,77</sup> Therefore, these examples show that DFT is an efficient tool for exploration of solid/solid interface that does not only give reliable interface adhesion, but also facilitates in development of prediction models.

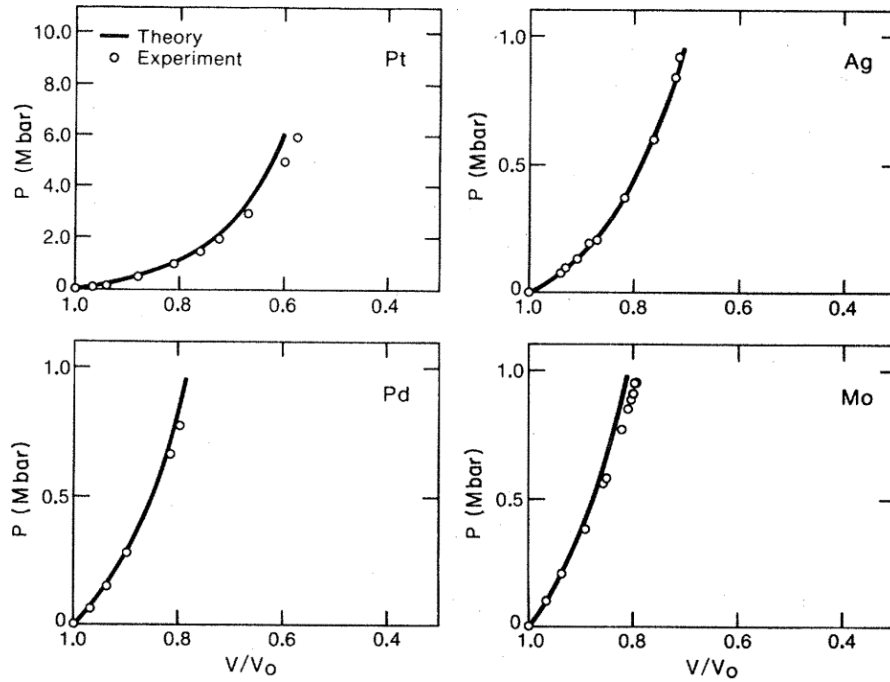


Figure 1.10. The equation of state for different metals predicted by the scaling relation with results from experiments (adapted from <sup>72</sup> with permission).

### 1.2.3 Contributions to the Liquid/Solid Interface Interactions

In liquid/solid interfaces, most of the works were contributed to pure liquid, *i.e.* no solute. Particularly, DFT has been useful in estimating wetting angle that result only from microscopic interactions.<sup>26,78,79</sup> In macro scale, wetting angle could be affected by several factors such as surface roughness.<sup>80</sup> However, in a microscopic level, the contact angle ( $\theta$ ) can be directly estimated from DFT-calculable  $W_{adh}$  defined in Eqn. 1.2 using the Young's equation,

$$W_{adh} = \sigma_l(1 + \cos\theta) \quad \text{Eqn. (1.3)}$$

where  $\sigma_l$  is the liquid surface energy, which will be approximated using DFT-calculated solid surface energy. The details of effects from this estimation are discussed in Section 2.3.2. Using this approximation, studies have been able to predict wetting angle of Pd and Pt on  $\text{ZrO}_2$  for  $125^\circ$  and  $120^\circ$  compared to  $100^\circ$  and  $95^\circ$  measured in experiments.<sup>79,81</sup> This may not be absolutely accurate, but given that the current thesis focuses on one metal, Ag, the order in the trend of the wetting angles of Ag/oxides should not change, and hence DFT calculations with this estimation will be employed with additional comparison to experiments when available.

For simulation of solute-solvent system at the interface, one of the applications of DFT is to measure the adsorption energy of the solvated adsorbate. Experimentally, the adsorption energy data is much more limited compared to gas phase adsorption, which could be due to that traditional instrument, such as TPD, is not compatible and specific experimental setup is required.<sup>82</sup> Even for DFT, it is still challenging to model solvent effects as there are many methods with different pros and cons, and it is still an actively developing field. The detail to these methods will be discussed in Section 1.4. In the past, studies mostly used DFT for calculation of adsorption energy of solvated small molecules on surfaces. For example, adsorption of CO or  $\text{H}_2$  on  $\text{Cu}_2\text{O}(111)$ , which is of an interest for catalytic synthesis applications.<sup>83,84</sup> shows that  $\text{H}_2$  does not adsorb on the surface when solvated with polar solvents such as water or methanol. This indicates stronger interactions of  $\text{H}_2$  with the solvents than the oxide surface. However, due to limited amounts of literature on adsorption energy in liquid phase, studies comparing calculated and experimental adsorption energy were not found. To this end, validation of the system has been mostly relied on comparing the solute-solvent interaction, *i.e.* solvation energy, and past studies have shown several successes in calculating accurate solvation energy of molecules compared to experiment,<sup>85,86</sup> for example methanol in water, which is -0.21 computationally and -0.22 experimentally.<sup>85</sup> Nonetheless, with

metal atoms included and many other pairs of solute-solvent unexplored, more procedures on solvation and methods to validate this for our thesis is required to ensure reliability of the calculation.

### **1.3 Current Studies on Adhesion at Metal-Zirconia Interfaces & the Challenges for Ag/Oxides Interface for the Sealing of the SOFC**

As discussed in Section 1.1.1, during the sealing process where Ag is brazed on yttrium-stabilized zirconia (YSZ), which is an SOFC electrolyte, two types of interfaces are involved – liquid/solid and solid/solid. Liquid Ag (with small amount of CuO) is initially wet on YSZ, then it forms a seal upon solidification. Because eventually all components are solid and during actual SOFC operations, the strength of the braze/YSZ interface is determined by the adhesion of these interfaces, the following sections will introduce current literature on the solid/solid adhesion of metals with the YSZ surface, and, to aid in formulating adhesion prediction, the trends in adhesion among metal/oxide interfaces.

#### **1.3.1 Adhesion at the YSZ Electrolyte Surface**

In an SOFC sealant, pure Ag adhesion on zirconia is so weak that it requires addition of CuO.<sup>87</sup> This is partly due to the surface nature of zirconia, and learning why is as important as identifying other oxides that it would strongly adhere to. Simulation of oxide surface and interface is challenging and requires multifaceted information because adhesion with it can change depending on surface terminations, defects, and environments. Therefore, to learn about zirconia characteristics at the interface and potentially apply them to the current thesis, this section reviews the nature of zirconia surfaces and interfaces, along with what can affect its adhesion. It should be noted that due to limited literature on Ag/ZrO<sub>2</sub> (and YSZ), the focus will be on Ni/ZrO<sub>2</sub> which has been studied most extensively due to its broad technological applications, including steam

reforming anode catalysts,<sup>88</sup> coatings,<sup>89</sup> and electrolysis.<sup>90</sup> Since both Ag and Ni are face-centered cubic (FCC) metals, it is expected that most of the insight from previous studies are applicable to the work in this thesis.

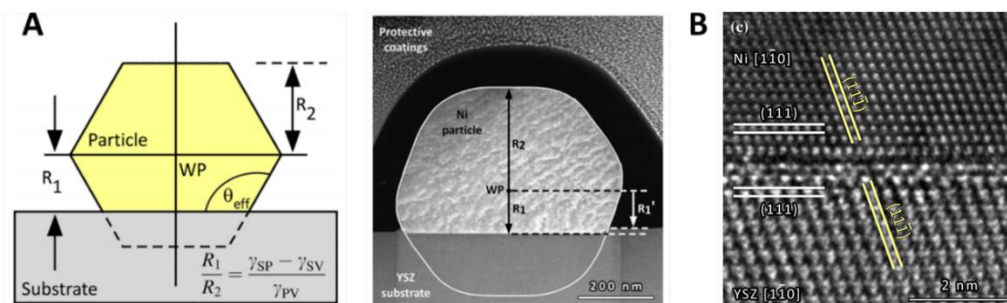


Figure 1.11. The schematic diagram of Winterbottom analysis for calculation of interface energy and the high angle annular dark field micrographs of Ni particle on YSZ surface captured by HRTEM (A). The Ni(111)/YSZ(111) obtained from HRTEM (B) (adapted from <sup>64</sup> with permission).

The type of surface that is exposed at the interface from the metal and oxide has a huge impact on the adhesion. Previous experiments using high-resolution transmission electron microscopy (HRTEM) have shown that both Ni and YSZ expose their (111) surface at the interface.<sup>64,91</sup> Furthermore, when the image was combined with the Winterbottom Analysis<sup>92</sup> of Ni particle on a YSZ substrate (Figure 1.11), a solid/solid interface energy was determined to be  $1.8 \text{ J/m}^2$ .<sup>64</sup> With the knowledge of YSZ and Ni surface energies,<sup>93,94</sup> this yields the  $W_{\text{adh}}$  of  $1.48 \text{ J/m}^2$ . This is 3 times higher than that of the Ag/YSZ interface computed in the present thesis. Additionally, this number will also be useful for benchmarking purposes in computational studies.

Computationally, studies have shown that  $\text{ZrO}_2(111)$  has an O-terminated surface (henceforth referred to as  $\text{ZrO}_2(111)_\text{O}$ ) in the SOFC operating conditions and maintained this even after forming an interface with Ni. Using DFT calculations, it was shown that  $\text{ZrO}_2(111)_\text{O}$  is preferred across a wide range of oxygen chemical potentials (Figure 1.12A).<sup>95</sup> Nevertheless, when

forming an interface with Ni(111), the region with oxygen chemical potential below -8.25 eV can favor Zr-terminated  $\text{ZrO}_2(111)$  instead. However, this is significantly below the SOFC operating condition of 0 (cathode side) to -2 eV (anode side, Figure 1.12B),<sup>96</sup> With the O termination, the bonding characteristic of Ni and O at the interface was shown to be site-dependent according to the charge distribution analysis. Ni atoms on top of  $\text{ZrO}_2$ 's terminal oxygen atom tend to have strong covalent bond characteristics, whereas Ni atoms at the hollow position and other positions form an ionic bond.<sup>95</sup>

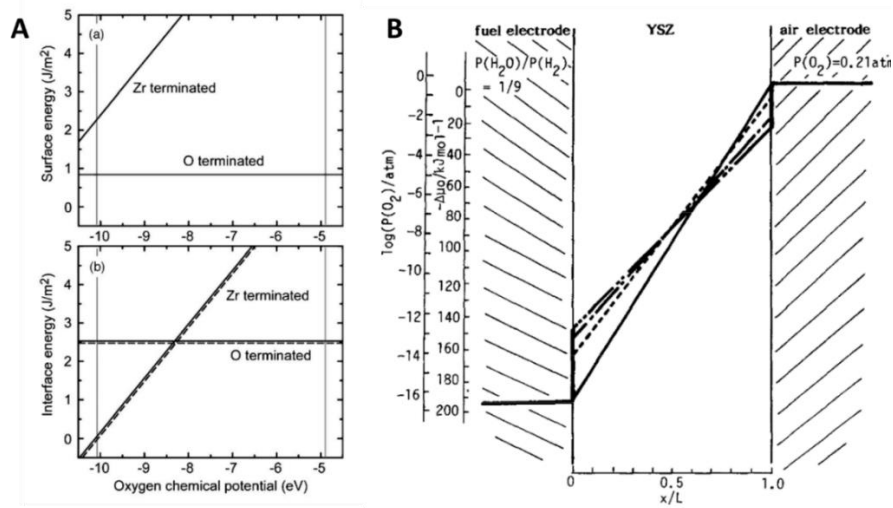


Figure 1.12. The surface and Ni/  $\text{ZrO}_2$  interface termination of  $\text{ZrO}_2(111)$  at different oxygen chemical potentials (A, adapted from <sup>95</sup> with permission). The oxygen chemical potential at each side and in electrolyte of an operating SOFC at 1000 °C (B, adapted from <sup>96</sup> with permission). Together, these indicate that  $\text{ZrO}_2(111)$  is terminated with O layer at the interface.

The position of oxygen vacancy, a natural point defect in oxides, was previously shown to decrease the  $W_{\text{adh}}$  of Ni/ $\text{ZrO}_2$  and Ni(YSZ).<sup>97,98</sup> The decrease was reportedly significantly larger in case of Ni/  $\text{ZrO}_2(111)_\text{O}$  as the oxygen vacancy was found through its formation energy to prefer to be at the outer most layer of the interface.<sup>99</sup> This was explained by the weaker Ni-O bond compared to Zr-O. A separate study also suggested similarly as first principles tensile tests indicate

fracture at the Ni-O interface.<sup>95</sup> In contrast, for YSZ(111), it was suggested that the effect from oxygen vacancy should be negligible as its vacancy prefers to be at the subsurface of the oxide's first multilayer.<sup>100</sup> Additionally, it was also found that as the simulated surface depth increases, calculations indicated more stability if the positions of the oxygen vacancy locate as a mixture of at subsurface and deeper multilayers.<sup>15</sup>

### 1.3.2 Trends and Correlation in Adhesion Energy

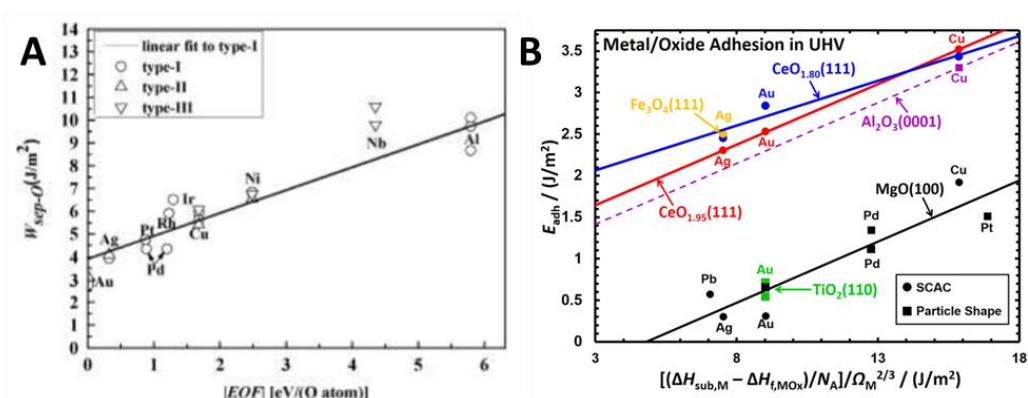


Figure 1.13. The relationship between the work of adhesion ( $W_{adh}$ ) of metals/ $\alpha$ - $Al_2O_3$  (0001) and the metals' oxide formation energy energy (A, adapted from <sup>65</sup> with permission) and the relationship between  $W_{adh}$  of metals on several oxides and the metals' oxide formation energy per unit surface area (B, adapted from <sup>101</sup> with permission).

For the challenges in the SOFC sealant, identifying what properties of the metal oxides could correlate with the interfacial energy or adhesion has an important implication in identifying oxides, apart from  $CuO$ , that would allow  $Ag$  to wet on. However, this does not exist for the  $Ag/oxides$  system yet, at least not a reliable one. Therefore, a brief history of how trends in metal/oxides adhesion which was developed and applied over the years will be discussed in this section.

Multiple studies have been able to relate  $W_{adh}$  of metal/oxides to several properties of the adhering metals themselves. By correlating the  $W_{adh}$  to either the metal's or the metal oxide's

properties, one could circumvent the experimental measurement or expensive DFT interface calculations, and hence, expedite the material design process. Metals' plasmon energy, the photon energy with frequency equals to the metals' plasma frequency, has been used to correlate with their  $W_{\text{adh}}$  on  $\text{SiO}_2$ , in which metals with higher plasmon energy such as Fe and Ni yield more adhesion.<sup>102</sup> Similarly, a correlation between  $W_{\text{adh}}$  and electron density at the boundary of the Wigner-Seitz cells of the corresponding metals also suggests Fe and Ni, which have higher electron density, to yield higher  $W_{\text{adh}}$  than other metals such as Pb or Sn.<sup>103,104</sup> Although not for purely predictive purposes, DFT calculations also indicate that the  $W_{\text{adh}}$  of  $\text{HfO}_2$  and  $\text{ZrO}_2(001)$  with various metals are positively correlated with the bond overlap population (BOP) at the interface.<sup>105</sup> Generally, it was found that metals with *sp* valence bands tend to have higher BOP due to the localized nature of the *d* band. Lastly, perhaps the most common correlation studied is between the  $W_{\text{adh}}$  and the metals' corresponding oxide formation energy.<sup>65,101,106–108</sup> For example, using DFT calculations, it was found that metals with higher corresponding oxide formation energy display higher  $W_{\text{adh}}$  on the  $\alpha\text{-Al}_2\text{O}_3(0001)$  surface (Figure 1.13A).<sup>65</sup> A recent experimental study further confirms the trend with several more oxides (Figure 1.13B), although the relationship is based on oxide formation energy per area.<sup>101</sup> This relies on the assumption that the strength of adhesion is related to the metal's oxophilicity. This could be applicable in most cases where the metal oxide surfaces are terminated with full or partial oxygen layers, which may not be true depending on oxygen chemical potential in a given condition.<sup>109</sup> Nonetheless, leveraging this adhesion relationship, studies have been able to understand and design metal oxide-supported catalysts that have higher thermal stability.<sup>110</sup> This knowledge has also become useful in many other fields such as for finding appropriate metallic interconnects in a semiconductor technology.<sup>111–114</sup>

Up to this point, it has been shown that there is a significant body of work on  $W_{adh}$  correlations with variation of metals on a single metal oxide surface. However, studies from a reversed point of view, *i.e.*  $W_{adh}$  correlations from a particular metal on various oxide substrates, is scarce. This could be due to the heterogeneity of different types of oxide surfaces. To the best of our knowledge, only two studies were dedicated to identifying such a relationship.<sup>102,103</sup> The first study is based on a collection of numbers of previous experimental results, which showed a linear correlation between higher  $W_{adh}$  of Ni, Fe, and Co with wider band gaps of the oxide substrates as well as higher formation energy of oxides (Figure 1.14).<sup>103</sup> The relationship was proposed to originate from the electronic charge transfer capability of the oxide. This prediction has been useful in many applications, such as designing alloys for composite steels by screening for metal oxides that Fe and Ni could wet on, among other criteria.<sup>115</sup> However, a separate study employing dielectric continuum theory suggests that the correlations between  $W_{adh}$  of Ag/oxides and the band gap of oxides is weak ( $R^2 \sim 0.6$ ).<sup>102</sup> This conclusion is similar to the one obtained from DFT calculations performed in the present thesis (results not shown). Therefore, this stresses the need to find a new descriptor that can describe Ag/oxides adhesion more accurately.

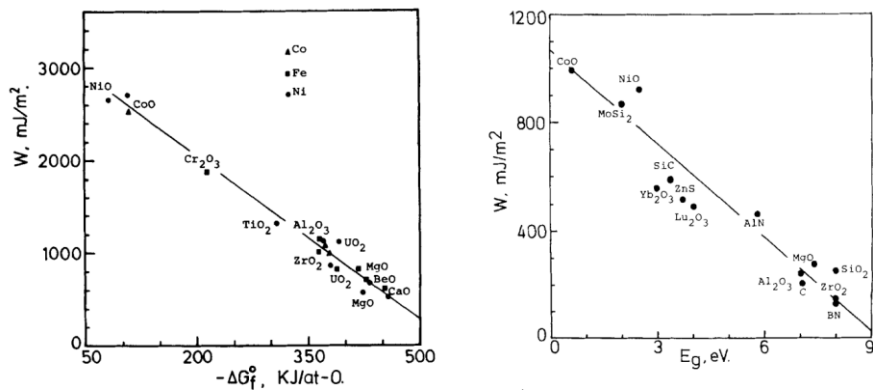


Figure 1.14. The relationship between the work of adhesion ( $W_{adh}$ ) of metals on various oxides as a function of oxide's formation energy or its band gap energy (adapted from <sup>103</sup> with permission).

## 1.4 Current Computational Studies on Liquid/Metal Interface of Catalysts & the Challenges for Lignin Decomposition Processes

Despite the fact that almost all lignin hydrogenolysis studies were done in a liquid phase, there is a very limited number of studies at the interface, with only a few of these studies being solvated. A number of existing computational studies suggests that solvents can affect the properties of metal at the interface, and hence the metal's activity, in many other reductive reactions such as phenol hydrogenation<sup>116</sup> and hydrodeoxygenation.<sup>117</sup> Therefore, in this section, an overview of methods to simulate liquid in DFT, and how those solvents change surface and interface properties with aromatic compounds, will be discussed.

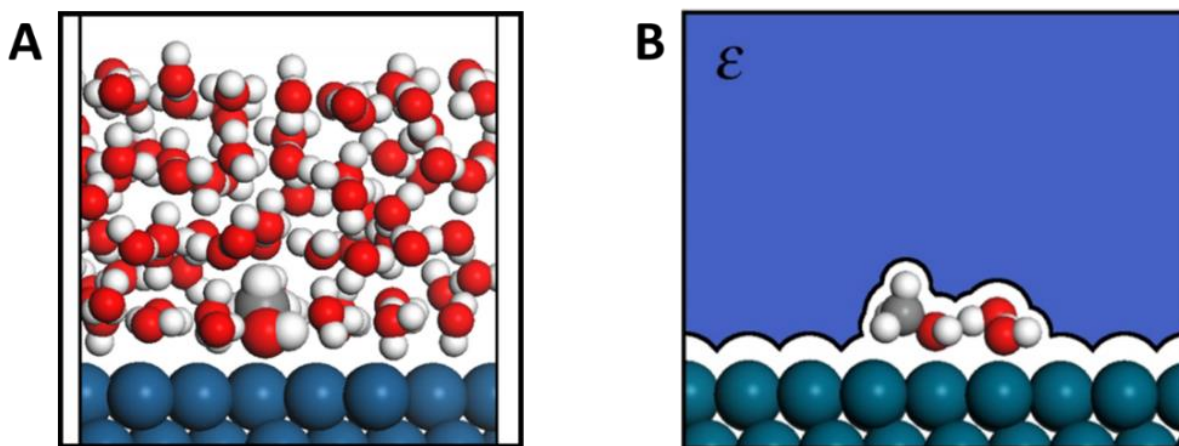


Figure 1.15. Illustration of solvent simulation in an explicit (A) and an implicit model (B) (adapted from <sup>118</sup> with permission).

In *ab-initio* calculations, solvent effects can be simulated by 3 means: an explicit model, an implicit model, and a hybrid model. Explicit models consider molecular details of each solvent molecule, while implicit models treat solvents as a continuous medium with a fixed dielectric constant where solutes are placed inside the cavity in the medium, ultimately allowing the calculation to be significantly faster. These two models are illustrated in Figure 1.15. Hybrid

models treat the first (and second) solvation sphere explicitly while the rest is treated implicitly.

The free energy of solvation can be defined by:

$$\Delta G_{\text{solv}} = \Delta G_{\text{cav}} + \Delta G_{\text{disp}} + \Delta G_{\text{elec}} + \Delta G_{\text{H-bonding}} \quad \text{Eqn. (1.4)}$$

where  $\Delta G_{\text{cav}}$  is the free energy required to form the solute cavity,  $\Delta G_{\text{disp}}$  is the van der Waals interaction,  $\Delta G_{\text{elec}}$  is the electrostatic interaction between solute and solvent, and  $\Delta G_{\text{H-bonding}}$  is the hydrogen bonding term.<sup>119</sup> By treating each of these terms differently, solvation energy from the explicit model and even from different flavors of implicit models can be significantly different. For example, in implicit models, a polarizable continuum model (PCM) calculated the cavity of the solute by overlapping van der Waals spheres,<sup>120</sup> whereas in a conductor-like screening model (COSMO) cavity is calculated based on the solvent accessible area.<sup>121</sup> With this in mind, the difference in results from the following literature should be expected.

#### 1.4.1 Characteristics of Solvent and Metal at the Interface

Challenges in solvation of the lignin dimer model adsorbed on metal surfaces in DFT simulations depends on the method used for simulation, which in itself is also a challenge. Due to the relatively large size of the lignin dimer, explicit solvation would be very expensive, whereas implicit solvation may not accurately describe the interaction. To learn of the past performances and effects from each method, the present section and Section 1.4.2 summarize relevant works on these with and without the presence of an adsorbate.

Using an explicit model, a study found that upon solvation with water molecules, Pt and Ni electron density at the interface is redistributed toward the subsurface layer.<sup>116</sup> This was shown to lower the metal work function, and subsequently, make the liquid-covered metal a higher chemical reduction strength. On the other hand, by testing various implicit solvation models, it

was found that most continuum models undersolvate metal surfaces, and underestimate the surface charge as a function of applied potential compared to experiments.<sup>122</sup> This is most likely because their parameterizations were fit to molecular solvation energies, with no ions or metallic surfaces included in the datasets.<sup>123</sup>

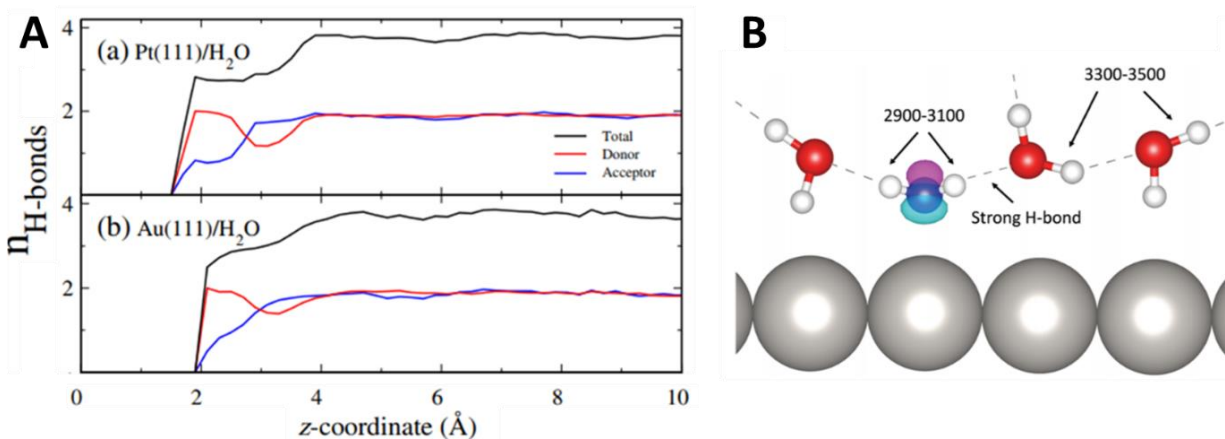


Figure 1.16. The average number of hydrogen bond along the  $z$ -coordinate (A, adapted from <sup>124</sup> with permission). The water structure at a water/Pt interface. The water molecule with blue ball represents watA, and the water molecules with red balls are of watB. The HOMO of the interface is partially located on watA, as represented with pink and cyan isosurfaces. The dashed lines indicate the hydrogen bonds formed between water molecules with the number showing the vibrational frequencies (B, adapted from <sup>125</sup> with permission).

On the solvent side, representation of water molecules on the Pt(111) surface explicitly has shown their different characteristics compared to their bulk. First, there is about one fewer number of average hydrogen bonds among water within a 1 Å thick layer above the interface compared to the bulk as shown in Figure 1.16A. This is a result of interaction with the metal surface.<sup>124</sup> However, it is shown that this interface characteristic is significantly dependent on the metal. As shown in Figure 1.16A, the number of hydrogen bonds at the interface layer with Au, which is a rather inert surface, recovers much quicker than that of Pt. Furthermore, it was also observed that some of the hydrogen bonds at the interface actually became stronger as evidenced by lower

vibrational frequencies shown in the interaction of watA (blue) compared to watB water molecules in Figure 1.16B.<sup>125</sup>

### 1.4.2 The Effect of Solvent on the Adsorption of Aromatics on Catalyst Surfaces

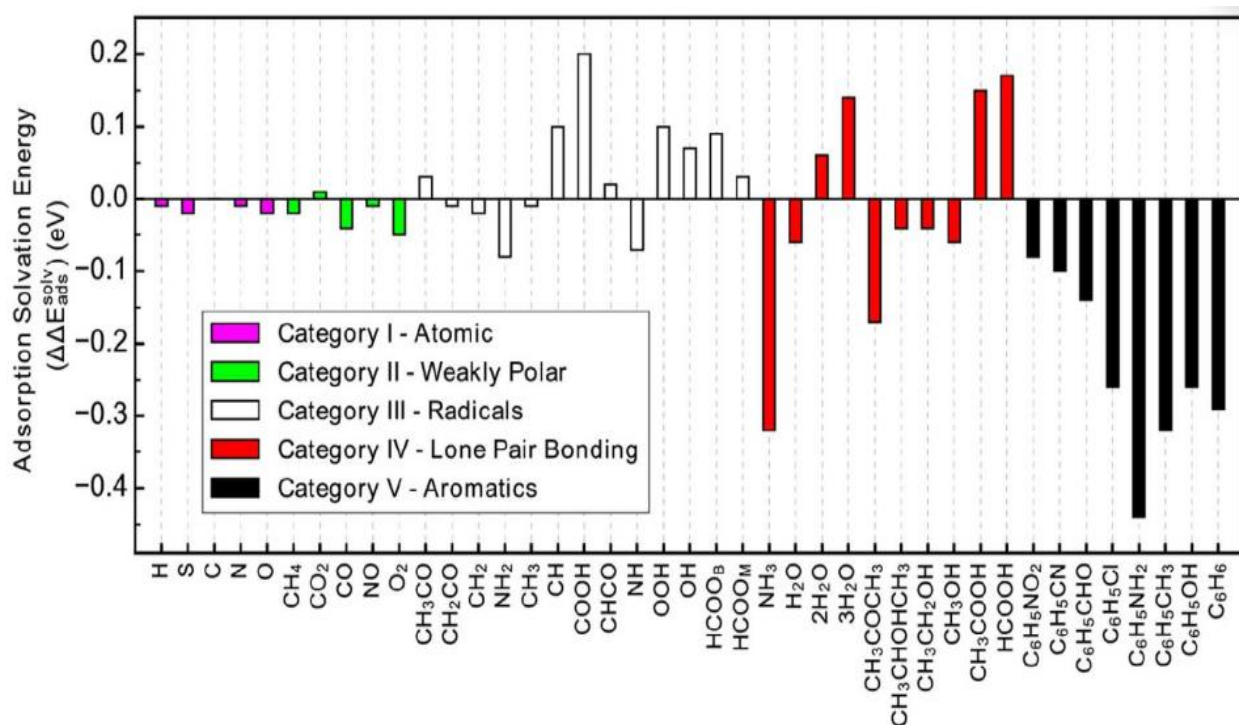


Figure 1.17. Difference in adsorption energies between in vacuum and solvated of molecules on Pt(111) surface using a PCM model to represent water medium. The changes are classified in color by nature of the adsorbates (adapted from <sup>126</sup> with permission).

Using a PCM method, it was reported that among different types of molecules that were solvated in water while adsorbing on Pt(111), the change in adsorption energy in aromatic compounds was the largest. Among the five categories of molecules, aromatics are on average the most affected with adsorption energy in a solvated state increased by ~0.3 eV compared to the value in a vacuum state (Figure 1.17).<sup>126</sup> These results imply that the hydrophobic, aromatic rings drive these molecules to adhere more strongly to the surface. Noted that the effect from interaction with water was amplified by the larger cavity sizes these aromatic adsorbates occupied. However,

a separate study modeling phenol adsorption on Ni(111) under explicit representation of water molecules suggested differently that the adsorption energy of phenol actually decreased by 0.11 eV when solvated.<sup>116</sup> On the other hand, a recent study has also attempted to incorporate the effect of solvation using ethylene glycol as a solvent to a lignin dimer model surface reaction. The study employed PCM method with thermodynamic cycle, and reported that the adsorption energy of the dimer decreased over 91%. These existing discrepancies in results and methods from previous studies pose a challenge in accurately modeling the solvated lignin dimer and stress the importance of careful defining and benchmarking solvation for this thesis.

### **1.5 Motivation and Thesis Outline**

Similar to the examples of DFT contribution in Section 1.2, where a complete usage of DFT builds from desired energetics, to fundamental insights, to prediction models, and finally to candidate suggestions, which could then be experimentally tested, the present thesis aims to use this approach to solve SOFC sealing interface problem. Therefore, it would encompass adhesion values, the mechanism of how Ag-CuO adhere strongly on YSZ surface, and predicting alternative oxides that are ready to be experimented on. For solvated lignin adsorption problem, a similar approach will be used but only up to getting the insight of how solvation affects lignin adsorption due to the complexity of liquid simulation and of the lignin itself. Because of the limit of DFT simulation size compared to the complexity of lignin, experimental identification of the most important functional group in lignins on their monomer yields will be conducted and serve as a basis for the simulated lignin section. Lastly, catalytic hydrogenolysis of lignin using the investigated metal surfaces will be conducted to observe the agreement between computational and experimental, although it should be noted that future works are required to investigate other contributing factors. In pursuing these goals, the chapters are outlined as follows:

## Chapter 2: Designing Metal Oxides to Enhance Adhesion of Silver Brazes on YSZ

This chapter explains the underlying mechanisms that allow the Ag-CuO system to adhere on YSZ surfaces and presents a descriptor for prediction of Ag/metal oxide adhesion. The effect of diffused oxygen in Ag on the adhesion was first investigated. The microscopic adhesion of Ag on all related metal oxide surfaces were then extensively studied. Based on the analyses of their structures and results, the descriptor was proposed and validated.

## Chapter 3: Identification of the Yield Determining Functional Groups in Lignin

This chapter explicates the correlations among the complex functionalities of technical lignin as well as their relationship to depolymerization yields from various reactions. Almost all functionalities of lignins, including polymer chain length, amount of aliphatic and phenolic hydroxyl contents, methoxyl content, and  $\beta$ -O-4 linkages, will be experimentally quantified and correlated. The lignin was also subjected to multiple types of reactions, and a model relating the lignin's functionality to reaction yields was developed and validated.

## Chapter 4: Adsorption of the Yield Determining Lignin Dimer on Catalyst Surfaces

This chapter examines the adsorption of the lignin dimer with the  $\beta$ -O-4 linkage, which was previously shown to be the primary yield determining factor, on Cu and Ni surfaces in vacuum and solvated states. First, the dimer's adsorption site and its conformation were identified. Ethanol was then added to the simulation to examine its effect on the adsorption conformation and energy. From these results, a thermodynamic model was then developed to connect the adsorption energy in vacuum and solvated states. This model highlights the importance of solvent selection and can be used for lignin dimer's solvated adsorption energy prediction.

## Chapter 5: Catalytic Hydrogenolysis of Lignin to Aromatic Monomers

This chapter explores the hydrogenolysis of lignin using ethanol as a solvent with a number of metal-supported catalysts. Using lignins directly from whole biomass, the product yields and selectivities from hydrogenolysis and hydrodeoxygenation were quantified. Lignin removal from the pretreated biomass was also investigated. By performing enzymatic hydrolysis on these biomasses, the correlation between lignin removal, aromatic monomer yields, and sugar yields were developed.

## Chapter 6: Summary and Outlook

This chapter exhibits a summary of the works performed in this thesis and discusses possible future research directions.

## CHAPTER 2 Designing Metal Oxides to Enhance Adhesion of Silver Brazes on YSZ

### 2.1 Summary

Ag-CuO is a broadly used reactive air brazing (RAB) system for effectively bonding ceramics and metal interfaces, especially for sealing yttria stabilized zirconia (YSZ) to metals in solid-oxide fuel cells (SOFCs). To understand the superior performance of this braze, density functional theory (DFT) calculations were employed to investigate two mechanisms that can potentially increase the work of adhesion ( $W_{adh}$ ) and hence reduce the wetting angle of Ag on YSZ. It was found while the formation of Ag-dissolved O clusters at the Ag-YSZ interface can promote wetting, a much greater wetting angle reduction comes from the formation of CuO interlayers between Ag and YSZ. Further, the  $W_{adh}$  of an Ag/CuO and CuO/YSZ interface was found to be significantly higher than that of an Ag/YSZ interface. Based on simulation obtained-insights into metal to oxide bond formation, a simple descriptor was developed to predict Ag/oxide interface energies, predict Ag/oxide  $W_{adh}$ , and search for potential oxide interlayers capable of promoting the wetting and adhesion of Ag on YSZ. Many simple metal oxides (single cation) were examined, however their  $W_{adh}$  with Ag was less than that of an Ag/CuO interface. Expanding the search to multi-cation oxides led to several promising candidates, such as CuAlO<sub>2</sub>, CuGaO<sub>2</sub>, and Cu<sub>3</sub>TiO<sub>4</sub>; all of which are also stable in the reducing SOFC conditions. Depending upon their solubility in molten Ag, these newly-identified oxides could either be pre-applied as wetting promoting interlayers or directly incorporated into Ag to form new reactive air brazes.

### 2.2 Introduction

Adhesive metal/metal-oxide interface bonds are critical in a variety of applications including the formation of durable passivation coatings, oxide-supported catalysts, solders, and brazes.<sup>127</sup> For instance, silver-based brazes have been used to separate the fuel (i.e. anode) and

oxidant (i.e. cathode) chambers in solid oxide fuel cells due to their superior toughness and gas impermeability compared to glass or mica seals.<sup>128–132</sup> In this application, sealing is accomplished by brazing a yttria-stabilized zirconia (YSZ) electrolyte layer to a stainless steel (SS) support. Unfortunately, wetting and adhesion problems of conventional silver or copper based brazes often result in braze joint manufacturing defects (pores) and as-produced joint failure at the braze-YSZ interface.<sup>23,87,133</sup>

To help overcome the poor wetting and adhesion issues of Ag on YSZ, a technique called reactive air brazing (RAB) has recently been developed.<sup>25,134,135</sup> Reactive air brazing is performed in air, and the braze alloy is intentionally designed to contain minor elements (such as Cu) that oxidize during brazing to promote wetting and adhesion. In fact, the addition of as little as 4 wt% CuO reduces the wetting angle of Ag on YSZ from 110° to ~45°.<sup>22,128,136,137</sup> Further, the fact that brazing can be done in the air prevents mechanical and electrochemical degradation of the oxygen-partial-pressure-sensitive SOFC cathode materials during brazing.<sup>138–140</sup> Lastly, Ag-CuO reactive air brazes have also shown an ability to bond metals to a variety of oxides including alumina, lanthanum strontium cobalt iron oxide, etc.<sup>24,141–144</sup>

As depicted in Figure 2.1, two mechanisms have been suggested to facilitate the wetting and adhesion of Ag–CuO reactive air brazes on oxide surfaces. In *Mechanism I*, the presence of oxygen dissolved in molten Ag is hypothesized to cause a 20°–35° drop in Ag on oxide wetting angles when brazing is performed in the air instead of inert atmospheres.<sup>145</sup> (Note, unlike most molten metals at elevated temperatures in air, Ag is thermodynamically more stable than AgO under brazing conditions,<sup>146</sup> suggesting that wetting improvements via the formation of crystalline AgO are unlikely). In *Mechanism II*, CuO is hypothesized to improve wetting and adhesion by forming a CuO-rich phase between the Ag and YSZ.<sup>24</sup>

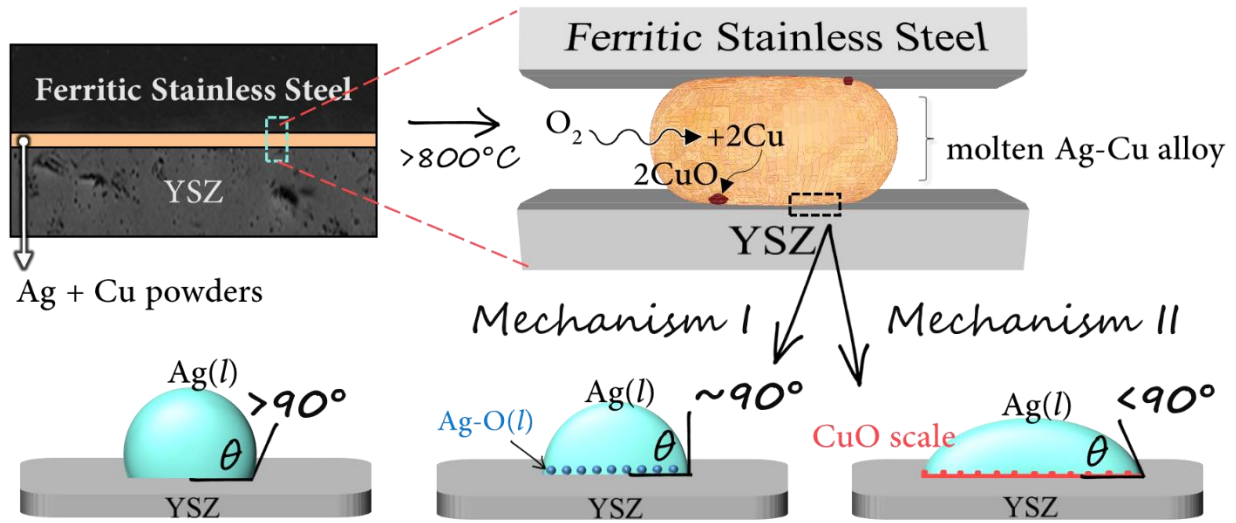


Figure 2.1. Hypothetical mechanisms of how Ag-CuO braze enables wetting starting from the solid phase (left) to melting and wetting (right) during the heating process in air. While the wetting angle of Ag on YSZ  $> 90^{\circ}$ , Ag-O clusters in Ag(l) solution may alter interfacial energy (*Mechanism I*), or addition of Cu may facilitate formation of CuO interlayer on YSZ surface (*Mechanism II*) leading to reduction of the wetting angle. The SEM images used for representation of stainless steel and YSZ microstructure was taken from literature.<sup>147</sup>

In the first half of the present study, the primary objective is to use atomistic modeling to determine, without interference from other factors, the extent to which these two mechanisms occur. We consider this is the basic step toward materials design. To examine *Mechanism I*, *Ab Initio* Molecular Dynamics (AIMD) was used to track the evolution of dissolved  $\text{O}_2$  in liquid Ag near the Ag(l)/YSZ interface in Section 3.1. In addition,  $\text{O}_2$  was initially placed at the Ag(l) surface, the Ag(l)/YSZ interface, or the Ag(l) center to determine if the dissolved oxygen lowered the wetting angle by altering either the Ag liquid/vapor surface energy ( $\gamma_{\text{LV}}$ ), the solid/liquid interfacial energy ( $\gamma_{\text{SL}}$ ), or both. To examine *Mechanism II* and determine the effect of a CuO interlayer between Ag and YSZ, DFT simulations were performed in Section 3.2 to calculate the work of adhesion,  $W_{\text{adh}}$ , of the Ag/YSZ, Ag/CuO, and Ag/YSZ interfaces. Ag wetting angles were then calculated from the computed surface and interface energies. Previous DFT-based surface studies have laid essential groundwork on the surface structures of these materials. Combined DFT

and thermodynamic calculations have identified the lowest energy facets for CuO to be the stoichiometric (111) for the entire O chemical potential region where CuO is stable.<sup>148,149</sup> For YSZ, which has a cubic ZrO<sub>2</sub> (c-ZrO<sub>2</sub>) structure, the O-terminated-(111) surface was shown to be the most stable in the entire oxygen chemical potential range encountered in a SOFC.<sup>150,151</sup> This is in accordance with the experimental HRTEM images of Ni/YSZ interfaces.<sup>91</sup> The surface structure of 9%-Y-doped YSZ (111),<sup>15,100,152</sup> which is shown experimentally to be in cubic phase at room temperature, has also been modeled via DFT and will be used as a basis for the present study.<sup>153</sup>

In the second half of the present work (Section 3.4.3), the objective was to use the conclusion gained from previous sections (Section 3.4.1 and 3.4.2) that *Mechanism II* is the dominant one to develop a simple descriptor to predict Ag/oxide interface energies, predict Ag/oxide  $W_{\text{adh}}$ , and search for new oxide interlayers capable of promoting the wetting and adhesion of Ag on YSZ, while maintaining stability in reducing environments. Although many theoretical and DFT studies have shown that for a given oxide surface, metals with lower  $d$ -band occupancy (particularly *bcc* metals) can induce higher metal-O charge transfer, and hence higher  $W_{\text{adh}}$ <sup>105,154–156</sup>, studies of the reverse relationship, *i.e.* identifying the oxides yielding a higher  $W_{\text{adh}}$  on a given metal (such as Ag), are scarce.<sup>103,105</sup> New brazing materials with other oxides are needed because the reduction of CuO on the anode side of Ag/CuO SOFC braze joints (CuO is thermodynamically unstable in the water-hydrogen mixtures found under SOFC operation)<sup>146</sup> induces pores that mechanically weaken the joint and limit joint lifetimes.<sup>157–160</sup>

## 2.3 Methods

### 2.3.1 Geometry optimization

All calculations in this study were performed using the plane wave DFT implemented in Vienna *Ab Initio* Simulation Package (VASP). The exchange correlations were treated with both

the Local Density Approximation (LDA) and the Generalized Gradient Approximation (GGA) by the Perdew–Burke–Ernzerhof (PBE) functional, for comparison.<sup>161,162</sup> Projector augmented wave (PAW) potentials were used to represent the effective electron-core interaction.<sup>163</sup> The electronic convergence was achieved self-consistently with a plane-wave cutoff energy of 500 eV. The two convergence criteria were  $10^{-5}$  eV for the total energy, and  $0.03 \text{ eV}\text{\AA}^{-1}$  for forces during structural relaxation via conjugate gradient minimization. The  $k$ -spacing and  $k$ -point with the details of the cell dimensions for the main interfaces are shown in Table 2.1 (the rest is shown in Table A1 in the appendix). Essentially, a  $k$ -spacing of studied interfaces are set at around  $0.04 \text{ \AA}^{-1}$  or below. Given that the interface dimensions are different in each interface, this constraint on the  $k$ -spacing resulted in various  $k$ -points, *i.e.* the longer dimension results in lower  $k$ -point as  $k$ -space is a reciprocal space. This spacing allows us to achieve an energy convergence of 1-2 meV/atom compared to the energy calculated by higher  $k$ -points. Gaussian smearing was employed with a sigma of 0.02 to achieve less than 1 meV/atom contribution from entropy. A spin-polarized calculation was performed with dipole moment correction along the perpendicular direction of the slabs. For strongly correlated transitional metal oxide, on-site coulomb interaction as introduced by Dudarev ( $+U_{\text{eff}}$ ) was employed.<sup>164</sup> The values of  $U_{\text{eff}}$  were taken from previous studies that employed LDA functional. These were 3.20,<sup>165</sup> 4.30,<sup>165</sup> 2.80,<sup>166</sup> 5.00,<sup>167</sup> 6.00,<sup>168</sup> 7.50,<sup>169</sup> and 7.50<sup>169</sup> eV for the transition metals in  $\alpha\text{-Cr}_2\text{O}_3$ ,  $\alpha\text{-Fe}_2\text{O}_3$ ,  $\text{Rh}_2\text{O}_3$ , NiO, c-CeO<sub>2</sub>, CuO, and Cu<sub>2</sub>O, respectively. In the case for GGA-PBE functional calculation of both CuO and Cu<sub>2</sub>O,  $U_{\text{eff}}$  of 8.50 eV was used.<sup>170</sup> The details of these oxides, including surface termination, lattice constants, and surface energies are tabulated in the appendix (Table A2).

Table 2.1. The parametric detail of the interface cells with their corresponding  $k$ -points used in the present study.

Interface	a, b, c (Å)		$\alpha, \beta, \gamma$	$k$ -points
	LDA	PBE	PBE&LDA	
Ag/YSZ	7.37, 7.37, 58.91	7.49, 7.49, 61.70	90°, 90°, 120°	4×4×1
Ag/CuO	12.31, 2.84, 53.98	13.96, 2.97, 54.29	90°, 90°, 60°	2×9×1
CuO/YSZ	11.56, 7.26, 50.57	12.20, 7.31, 51.14	90°, 90°, 95°	2×3×1

### 2.3.2 Slab Models for Surfaces and Interfaces

Slab models were constructed to compute surface energies. The surface orientation of each oxide used in this study was the lowest energy identified in the literature (See Appendix A). All the oxide surfaces were stoichiometric in this study except the delafossite oxides and  $\text{Cu}_3\text{TiO}_4$ , as detailed in Table A2. Particularly for the O-terminated (111) slab of YSZ, which adopts a cubic  $\text{ZrO}_2$  structure at SOFC operating and brazing temperatures,<sup>171</sup> the surface structure was taken from previous computational studies using  $(\text{Y}_2\text{O}_3)_{0.09}(\text{ZrO}_2)_{0.91}$  with the most preferable sites for Y and oxygen vacancies ( $V_{\text{O}}^{\bullet\bullet}$ ) identified.<sup>15,100</sup> Specifically, the  $V_{\text{O}}^{\bullet\bullet}$  was found to be at the subsurface of the first YSZ multilayer with Y substituting for Zr at the second nearest neighbors positions (2NN), in the first and second multilayers.<sup>100</sup> This is in agreement with experimental observation that Y tends to segregate to the surface.<sup>172,173</sup> The minimum number of layers in each slab was determined to give converged surface energy,  $\gamma_{iV}$ , within  $\pm 0.02 \text{ J/m}^2$ ; six layers for both Ag and Ni slabs, whereas for certain oxides, such as  $\text{ZrO}_2$ , NiO, and CuO, three layers were sufficient, and oxides of corundum type usually required five layers, while  $\text{Cu}_2\text{O}$  needed four.



identify the most preferable position. All sandwich models were constructed to have at least inversion symmetry to ensure that the two interfaces were identical, less affected by the dipole moment, and that the interface energy,  $\gamma_{12}$ , was uniquely defined.

The average interface width ( $\Delta d$ ) was defined as the z-distance between the averaged z-positions of the atoms in the first layer of each side of the interface. For YSZ and CuO, only oxygen atoms of the outermost layer were taken into account. For liquid Ag, only atoms within  $\pm 0.5 \text{ \AA}$  range from the bottom most atoms were used to compute the average.

The work of adhesion of the system was defined and calculated using the equation:

$$W_{\text{adh}} \equiv (\gamma_{1V} + \gamma_{2V}) - \gamma_{12} = (E_1 + E_2 - E_{12})/2A \quad \text{Eqn. (2.1)}$$

where  $\gamma_{iV}$  is the surface energy of the slab  $i$ ,  $\gamma_{12}$  is the solid/solid interface energy,  $E_i$  is the calculated energy of the slab  $i$ ,  $E_{12}$  is the calculated total energy of the interface system with slab 1 and 2, and  $A$  is the model interface area. Therefore,  $W_{\text{adh}}$  was computed based on the energy difference between a simulation cell with slab 1 and slab 2 far apart and where slab 1 and 2 shared an interface. Then, the interface energy was computed using the relationship  $\gamma_{12} = \gamma_{1V} + \gamma_{2V} - W_{\text{adh}}$ .

The wetting angle corresponding to the  $W_{\text{adh}}$  was calculated based on Young's equation:

$$\cos(\theta_{\text{cal}}) = \frac{\gamma_{\text{SV,oxide}} - \gamma_{12}}{\gamma_{\text{SV,metal}}} = \frac{W_{\text{adh}}}{\gamma_{\text{SV,metal}}} - 1 \quad \text{Eqn. (2.2)}$$

where  $\gamma_{\text{SV,oxide}}$  is the solid oxide surface energy from DFT calculation reported in Table A2,  $\gamma_{12}$  is the DFT calculated solid/solid interface energy from Eqn. 2.1,  $\gamma_{\text{SV,metal}}$  is the solid metal surface energy calculated by DFT listed in Table A2, and  $\theta_{\text{cal}}$  is the estimated contact angle. Except for one liquid Ag on YSZ interface calculation, all the other interfaces were solid/solid interfaces. It

should be noted that although the absolute magnitude of the  $\theta_{\text{cal}}$  values obtained from the solid/solid interface calculations, instead of liquid/solid, may be overestimated due to the higher surface energy of a solid compared to its liquid,<sup>174</sup> but the calculated trends in wettability are expected to hold at brazing temperatures.

### 2.3.3 *Ab Initio* Molecular Dynamics

*Ab-initio* molecular dynamics (AIMD) was used to determine the adsorption and wetting behavior of Ag(*l*), with and without dissolved oxygen, on YSZ. At a brazing temperature of 1000 °C, the solubility of O<sub>2</sub> in Ag is 1.93 mL, which translates to approximately 2 atoms of oxygen per 200 Ag atoms.<sup>175</sup> Hence, in these AIMD simulations, the Ag(*l*)/YSZ system was modeled as a ~1 nm thick molten Ag layer containing two oxygen atoms (for a total of 102 atoms) supported on a YSZ slab three unit cells thick. The basal plane YSZ atoms were fixed in position, the YSZ had a surface area of 181.44 Å<sup>2</sup>, and a vacuum gap of 13 Å was placed above the liquid surface in the initial structure. This initial structure corresponds to the experimentally measured density of 9.30 g/mL for Ag(*l*) at 1000 °C.<sup>176</sup> As shown in Figure 2.3, three different initial structures were generated by inserting the two oxygen atoms at either the YSZ interface, within the bulk of the Ag(*l*), or at the free surface of the molten Ag. Although the dissolved oxygen concentration used here was double the experimentally observed amount due to computational limitations, the calculated energy trends with oxygen position should still be applicable to real-world systems.

Both the molten Ag and the Ag(*l*)/YSZ interfaces were initially relaxed using classical MD with a COMPASS force field (Ag = ag\_m, O in Ag = o\_ag, Y = y3o, Zr = zr4o, and O in YSZ = o2z) implemented in Material Studio.<sup>177,178</sup> The force field was previously shown to give a melting temperature of metal closer to first-principle calculations than embedded atom model (EAM) method.<sup>179</sup> The evolution of these initial structures was simulated by constant-temperature,

constant-volume ensemble (NVT) AIMD using spin-polarized DFT calculations with GGA-PBE functional. The AIMD calculations were performed at the  $\Gamma$ -point  $k$ -point. The constant temperature was controlled at 1280K by the Nosé–Hoover thermostat and the integration time step is 1 fs for a total of 3 ps. The average energy for the  $W_{adh}$  calculation was then obtained by sampling and minimizing 3 frames from the last 0.5 ps of the AIMD run using  $(2 \times 2 \times 1)$   $k$ -points.

#### 2.4 The Role of the Oxygen at the Ag(*l*)/YSZ interface during Brazing Process

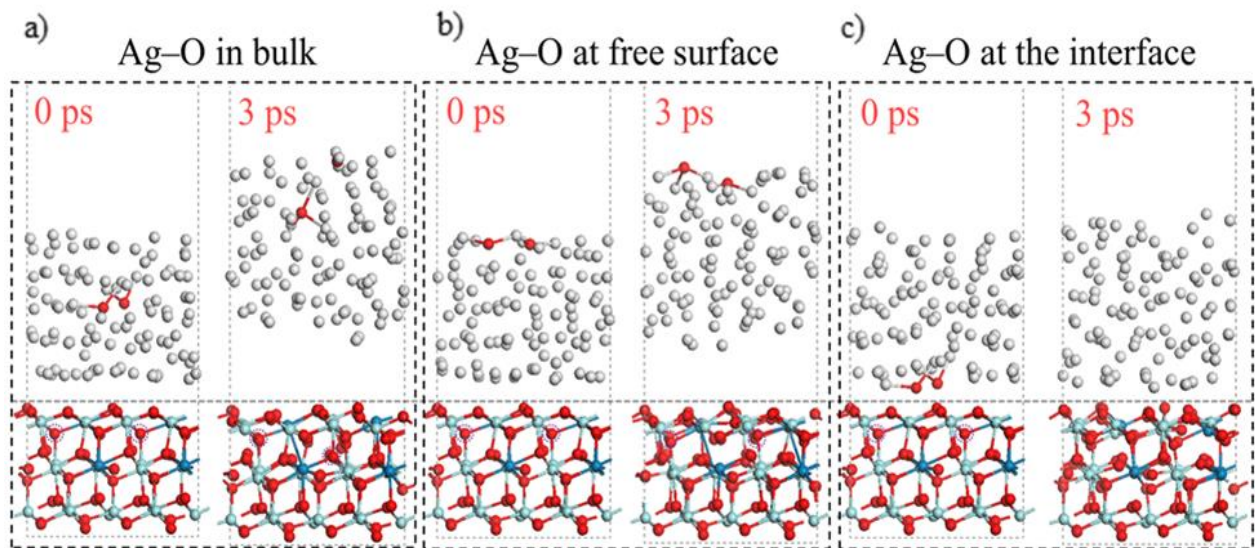


Figure 2.3. Ag(*l*)/YSZ interface structures with dissolved oxygen atoms at the beginning and end of 3 ps AIMD simulations at 1000 °C. Three initial positions of Ag–O clusters were investigated, including in the bulk Ag(*l*), at the free surface of the Ag(*l*), and at the Ag(*l*)/YSZ interface. The Ag–O at the interface is the most favorable structure.

AIMD was employed to investigate the energetics in Ag(*l*)/YSZ interface in order to examine the mechanism of dissolved O<sub>2</sub> in enhancing wettability, *i.e.* *Mechanism I* in Figure 2.1. AIMD was first performed to investigate dissolved O<sub>2</sub> in bulk liquid Ag. Dissociation of O<sub>2</sub> into Ag–O clusters was promptly observed, where O atoms formed 2.2–2.3 Å bonds with the Ag atoms surrounding them. This bond length is 5~10% longer than the Ag–O bond length in crystalline Ag<sub>2</sub>O (2.08 Å in GGA-PBE relaxed structure), a reasonable increase for the liquid phase. Analysis

of the system by pair radial distribution (RDF) shown in Figure A2 revealed that the nearest Ag-Ag distance peak was  $\sim 2.8 \text{ \AA}$ , in accordance with experimental measurements of pure Ag in a reducing atmosphere at  $1050^\circ\text{C}$ .<sup>180</sup> This indicated that the dilute concentration of oxygen in the Ag did not significantly alter the bulk behavior of the Ag.

Figure 2.3 shows three possible sites for Ag-O clusters to be at, including in the bulk (a), at the surface of molten silver (b), or at the interface of liquid Ag/YSZ (c). Although not the objective of the present work, oxygen vacancies in all these initial positions were observed to move around within the YSZ slab during the AIMD simulations. Figure 2.3a and 2.3b show that Ag with Ag-O clusters in the bulk of the Ag or placed at the Ag-free surface drifted away from the YSZ (yielding a GGA-calculated  $W_{\text{adh}} \sim 0 \text{ J/m}^2$  that may be a low considering the fact that GGA tends to underestimate binding energies). In contrast, Figure 2.3c shows that Ag with Ag-O clusters at the Ag(l)/YSZ interface remained attached to the YSZ with a GGA-calculated  $W_{\text{adh}} = 0.43 \pm 0.01 \text{ J/m}^2$ . The arrangement in Figure 2.3c, denoted henceforth as {Ag(l)+2O}/YSZ, had a lower overall energy than those in Figure 2.3a and 2.3b, indicating that changes in the Ag(l)/YSZ interface, and not changes in the Ag free surface energy, are responsible for the Ag wetting enhancements experimentally observed when switching from inert Ag/YSZ brazing atmospheres to air.<sup>25,87</sup>

Without the dissolved  $\text{O}_2$ , the pure liquid Ag has an average  $W_{\text{adh}}$  (on YSZ from GGA-PBE functional) of only  $0.11 \pm 0.01 \text{ J/m}^2$ , resulting in a contact angle of  $149^\circ$  (Table 2.2). This is consistent with experimental observations showing that liquid Ag does not wet YSZ.<sup>87</sup> Although the results from GGA may be overestimated, the trend and the relative change of the wetting angles are expected to be reliable as will be shown in the next section. As shown in Table 2.2, the {Ag(l)+2O}/YSZ wetting angle was  $38^\circ$  less than that for pure Ag(l)/YSZ, in agreement with a  $30^\circ$  drop observed experimentally<sup>25,87</sup> (Table 2.2 also shows that the binding energy

underestimated by the GGA-PBE method resulted in wetting angle predictions that were  $\sim 25^\circ$  higher than those observed experimentally). Figure 2.3c also shows that the two oxygen atoms originally dissolved in the Ag near the Ag/YSZ interface hopped into the YSZ substrate, filling two YSZ oxygen vacancies in the process. The resulting increase in the YSZ surface oxygen vacancy concentration likely contributed to the increased  $W_{\text{adh}}$  by providing additional sites for Ag-O bonding across the interface. Together, these results confirm *Mechanism I* (the hypothesis that oxygen dissolved in molten Ag is responsible for the  $\sim 20^\circ$ - $35^\circ$  drop in Ag on oxide wetting angles when brazing is performed in air instead of inert atmospheres).

Table 2.2. The average interface distance ( $\Delta d$ ), work of adhesion ( $W_{\text{adh}}$ ), calculated wetting angles ( $\theta_{\text{cal}}$ ), and experimental ( $\theta_{\text{exp}}$ ) for Ni/YSZ interface and systems involved in Ag-CuO/YSZ braze.

Interface Systems	XC	$\Delta d$ (Å)	$W_{\text{adh}}$ (J/m <sup>2</sup> )	$\theta_{\text{cal}}$	$\theta_{\text{exp}}$
Ni[1 $\bar{1}$ 0](111)  YSZ[1 $\bar{1}$ 0](111)	GGA	2.03	0.49	138°	120° <sup>87</sup>
	LDA	2.01	1.42	118°	
Ag(l)/YSZ(1 1 1) <sup>‡</sup>	GGA	2.41±0.02	0.11±0.01	149°	120° <sup>87</sup>
{Ag(l)+2O}/YSZ(1 1 1) <sup>†</sup>	GGA	2.17±0.04	0.43±0.01	111°	90° <sup>181†</sup>
Ag[ $\bar{3}$ 2 1](1 1 1)  YSZ[ $\bar{1}$ 1 0](1 1 1)	GGA	2.68	0.10	150°	120° <sup>87</sup>
	LDA	2.43	0.53	121°	
Ag[1 $\bar{1}$ 0](1 1 1)  CuO[ $\bar{1}$ 1 0](1 1 1)	GGA	2.26	0.48	112°	10° <sup>25‡</sup>
	LDA	2.11	1.43	73°	
CuO[1 $\bar{3}$ 2](1 1 1)  YSZ[0 $\bar{1}$ 1](1 1 1)	GGA	1.76	0.65	96°	—
	LDA	1.71	1.11	92°	

<sup>‡</sup>An interface without dissolved oxygen atoms.

<sup>†</sup>An interface with dissolved oxygen atoms located initially at the interface.

<sup>‡</sup>Sessile drop tests performed in air, and the contact angle of Ag/CuO was taken from the test of Ag-CuO system on both YSZ at high concentration of CuO, until the contact angle converged with respect to the amount of CuO.

## 2.5 Enhancement of Interface Adhesion by CuO

Table 2.3. The surface and interface energy involved in Ni[1 $\bar{1}$ 0](111)||YSZ[1 $\bar{1}$ 0](111) interface.

		$\gamma_{\text{Ni}(111)}$	$\gamma_{\text{YSZ}(111)}$	$\gamma_{\text{Ni-YSZ}}$	$W_{\text{adh}}$
<b>DFT</b>	<b>GGA-PBE</b>	1.94	0.70	2.26	0.49
<b>computed</b>	<b>LDA</b>	2.68	1.42 <sup>‡</sup>	2.68	1.42 <sup>‡</sup>
<b>Experiment</b> <sup>64</sup>		2.05 <sup>93</sup>	1.23 <sup>94</sup>	1.8±0.1	1.48

<sup>‡</sup>Because the obtained  $W_{\text{adh}}$  is coincidentally close to the surface energy of YSZ (based on LDA calculations), the derived interface energy of Ni/YSZ is the same as the Ni surface energy, following Eqn. 2.1.

Before studying these solid interfaces, the accuracy and reliability of the results were evaluated. A Ni/YSZ interface was employed because of abundant existing computations and detailed experimental results, in contrast to limited studies of Ag adhesion on YSZ or ZrO<sub>2</sub>. Table 2.3 shows the surface energy, interface energy, and  $W_{\text{adh}}$  from GGA and LDA functionals for Ni[1 $\bar{1}$ 0](111)||YSZ[1 $\bar{1}$ 0](111) interface shown in Figure A3. The  $W_{\text{adh}}$  agreed well with the experimentally measured values. In fact, the LDA-predicted  $W_{\text{adh}}$  of 1.42 J/m<sup>2</sup> was within 5% of the 1.48 J/m<sup>2</sup> value obtained by converting Nahor *et al.*'s experimentally measured Ni[1 $\bar{1}$ 0](111)||YSZ[1 $\bar{1}$ 0](111) interface energy and surface energies. The interface energy was measured from Winterbottom analysis of the same Ni[1 $\bar{1}$ 0](111)||YSZ[1 $\bar{1}$ 0](111) interface, equilibrated by annealing at 1350 °C in high-purity inert gas and H<sub>2</sub> ( $P_{\text{O}_2} = 10^{-20}$ ).<sup>64,92</sup> As  $W_{\text{adh}}$  is the primary focus of the subsequent sections, LDA functional was considered to give comparable results to the experiments. Further discussion on validation of the model and comparison to previous computational studies of related interfaces can be found in the appendix.

To evaluate *Mechanism II* (the hypothesis that CuO interlayers atop YSZ promote Ag wetting and adhesion),  $W_{\text{adh}}$  values for Ag(s)/YSZ, Ag/CuO, and CuO/YSZ were calculated using the solid/solid interfaces shown in Figure 2.2a-d. Solid interfaces were used because components

are eventually solidified and during actual SOFC operations, the strength of braze/YSZ interface was then determined by the adhesion of the two interfaces of Ag(s)/CuO/YSZ. Also, the work of adhesion with liquid Ag is likely to follow the same trend with solid Ag.

As shown in Table 2.2, the trend of the results from both LDA and GGA-PBE exchange correlations functionals agreed that the presence of CuO leads to a more adherent braze. The closer interface distances shown in Figure 2.2 and the  $\Delta d$  values of Table 2.2 also correlated well with the increased  $W_{adh}$ . The higher  $W_{adh}$  resulted in reduction of wetting angle of  $\sim 48^\circ$  when replacing Ag/YSZ with Ag/CuO. Particularly from the prediction by LDA functional, the increment in  $W_{adh}$  alone would theoretically be substantial enough to make Ag wettable on CuO ( $<90^\circ$ ). On the other hand, the high  $W_{adh}$  for CuO/YSZ indicates that CuO can firmly adhere to YSZ.

While the liquid/solid interface mimics the braze processing condition and the solid/solid interface represents the solidified braze during SOFC operation, the adhesion and wetting angle between solid/solid and liquid/solid are directly related. Hence the results from one can be translated to the other. Even though these simulations were performed on solid/solid interfaces, these conclusions should hold for a system with molten Ag for the following reasons: 1) both experimental measurements<sup>174</sup> and thermodynamic derivation<sup>182</sup> have shown that solid Ag surface energies are systematically higher by  $\sim 20\text{-}33\%$  of those of liquid Ag, the computed  $W_{adh}$  on different interfaces should follow the same trend for liquid and solid Ag. 2) Wetting angles of many liquid metals are known to be a very weak function of temperature (for example, the  $W_{adh}$  of Ag(*l*) on ZrO<sub>2</sub> only changes by 0.05 J/m<sup>2</sup> from 1000 to 1300°C).<sup>23,133,183</sup> Thus, the absolute values of the  $W_{adh}$  and  $\theta_{cal}$  obtained from the solid/solid interface will be overestimated due to the higher surface energy of a solid compared to its liquid,<sup>174</sup> but the calculated trends in both values are expected to hold at brazing temperatures.

It should be noted that the experimental wetting angles of Ag/CuO listed in Table 2.2 were not taken from pristine experiments like that of Ni[1 $\bar{1}$ 0](111)||YSZ[1 $\bar{1}$ 0](111) interface.<sup>64</sup> The contact angle of Ag/CuO was taken from the test of liquid Ag droplet in the air on YSZ with a high concentration of CuO, until the contact angle converged with respect to the amount of CuO. Thus, in practice, the experimental result has a combined effect from *Mechanism I* and *II*. Nevertheless, these experiments show similar contact angle change that can be interpreted from the present study. We have shown that in *Mechanism I*, the presence of oxygen in Ag/YSZ can reduce the contact angle by  $\sim 38^\circ$ , and forming CuO on YSZ will further reduce the contact angle by  $\sim 48^\circ$  from *Mechanism II*, yielding an overall  $\sim 86^\circ$  reduction in contact angle when brazing in the air. This is consistent with the experimentally observed  $110^\circ$  drop in contact angle (from  $120^\circ$  to  $10^\circ$ ).<sup>25</sup> The rest of the discrepancy can be attributed to the use of solid/solid interface in the simulation and liquid/solid interface in experiments.

## 2.6 Identification of Other Potential Oxide-Forming Alloying Elements

A descriptor that correlates a simple interface structure and bond strength to interface energy at the Ag/oxide interfaces was identified to facilitate the search for potential oxides. The descriptor was based on the results from the projected density of states (PDOS, Figure A4), which is discussed in the Appendix A and indicates that interfacial bonding occurred primarily from the metal-oxygen bonds. The calculations pertaining to descriptors were performed using LDA functional only as results from previous sections indicate comparable  $W_{adh}$  to experiments.

### 2.6.1 Formulation of a Descriptor Using $\gamma_{12}$ and $W_{adh}$ in a Predictive Model

The aforementioned descriptor was developed based on the definition of the interface energy, *i.e.* the excess energy introduced by the interface compared to the bulk structure. The first assumption used in this descriptor was that no new Ag-oxide phases formed during brazing. Since

the Ag-Ag bond strength is much lower than that of metal-oxide bonds, the descriptor was simplified to only account for 1) the number of unsaturated cation and anion bonds per unit surface area, and 2) the energy changes per unit surface area caused when a portion of the oxygen dangling bonds on a surface was replaced with the newly formed Ag-O bonds across the oxide-Ag interface. This leads to the newly formulated the descriptor ( $\chi_{MO}$ ):

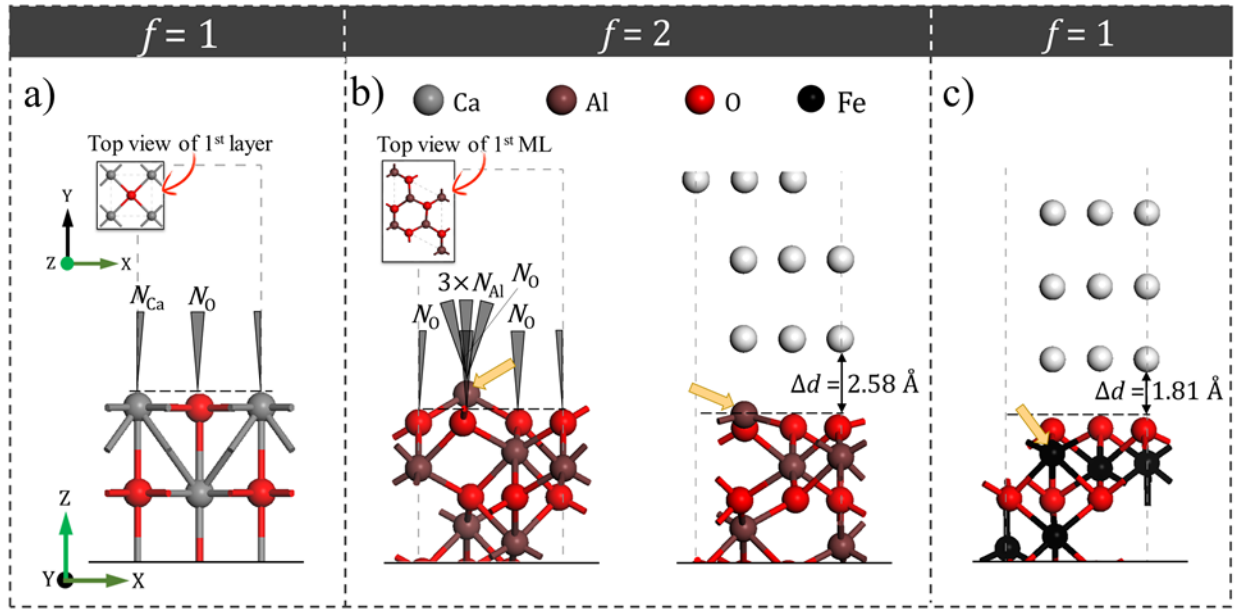


Figure 2.4. Side view and top view of surface and interface structures to illustrate the formulation of the descriptor,  $\chi_{MO}$ , in Eqn. 2.3. The  $N_M$  and  $N_O$  were demonstrated for a) an unrelaxed rock salt CaO {100} surface, where  $f=1$  is used and b) an unrelaxed corundum oxide surface structure represented by the  $\alpha$ -Al<sub>2</sub>O<sub>3</sub> (0001). The relaxed interfaces of Ag/corundum-oxide demonstrate that b) in  $\alpha$ -Al<sub>2</sub>O<sub>3</sub> and other corundum-oxides  $f=2$  is used as the protruded cation, Al<sup>3+</sup>, weakens Ag-O interfacial bonding, except c) in Fe<sub>2</sub>O<sub>3</sub>, whose cation, Fe<sup>3+</sup>, submerges beneath the oxygen layer after relaxation so it does not interfere with the Ag-O bonds ( $f=1$ ). The yellow arrows pinpoint the same cation in all the corundum oxides.

$$\chi_{MO} = \frac{f((N_M+N_O) \times |E_{M-O}|) - (N_O \times |E_{Ag-O}|)}{A_{MO}} \quad \text{Eqn. (2.3)}$$

where  $N_M$  and  $N_O$  were the number of dangling bonds on the surface cation and oxygen atoms, respectively, in an oxide surface unit cell,  $E_{M-O}$  was the bond enthalpy of the oxide as defined by oxide formation enthalpy ( $\Delta H_{f,MO}$ ) divided by the number of bonds in a unit cell,  $E_{Ag-O}$  was the

bond enthalpy of silver oxide ( $\text{Ag}_2\text{O}$ ), and  $A_{\text{MO}}$  was the surface area of an oxide unit surface.  $f$  was an empirical structure factor assigned to be 1 for all studied oxides, except most of the corundum oxides such as  $\text{Al}_2\text{O}_3$ ,  $\text{Cr}_2\text{O}_3$  and  $\text{In}_2\text{O}_3$  which, as highlighted in Figure 2.4b, contained protruding surface cations necessitating the use of  $f=2$  (further explained in the next paragraph).

Figure 2.4 shows the surface and interface structures used to calculate the descriptors for three sample oxides:  $\text{CaO}$ ,  $\alpha\text{-Al}_2\text{O}_3$ , and  $\text{Fe}_2\text{O}_3$ . Figure 2.4a shows that on the  $\{100\}$  surface of  $\text{CaO}$ , both Ca and O have one dangling bond (resulting in  $N_{\text{Ca}} = 1$  and  $N_{\text{O}} = 1$ ). Dividing an LDA-calculated  $\Delta H_{f,\text{CaO}} = -6.78$  eV (which is comparable to  $-6.39$  eV obtained by extrapolating NIST database data down to 0 K), by the 6 Ca-O bonds per unit cell yields  $E_{\text{Ca-O}} = \frac{-6.78}{6} = -1.13$  eV/bond. In a similar fashion, LDA calculated the relaxed structure  $E_{\text{Ag-O}}$  to be  $-0.14$  eV/bond. The relaxed  $\text{CaO}$   $\{100\}$  surface has  $A_{\text{CaO}}$  of  $11.14 \text{ \AA}^2$ . Together with  $f=1$ , this yielded a  $\chi_{\text{CaO}}$  of  $0.19 \text{ eV/\AA}^3$ . Figure 2.4b shows the surface structure of corundum-type oxides, represented by  $\text{Al}_2\text{O}_3$  (0001) and its relaxed interface with Ag. It has a  $N_{\text{Al}} = 3$ , a  $N_{\text{O}} = 3$ , a LDA calculated relaxed structure  $A_{\text{Al}_2\text{O}_3} = 19.40 \text{ \AA}^2$ , and a LDA calculated relaxed structure  $\Delta H_{f,\text{AlO}_3} = -17.42$  eV which resulted in a  $E_{\text{Al-O}} = -\frac{17.42}{12} = -1.45$  eV, with an  $f$  factor of 2, this yielded a  $\chi_{\text{Al}_2\text{O}_3}$  of  $0.85 \text{ eV/\AA}^3$ . Among all the corundum oxides tested, namely  $\text{Al}_2\text{O}_3$ ,  $\text{Cr}_2\text{O}_3$ ,  $\text{In}_2\text{O}_3$ , and  $\text{Rh}_2\text{O}_3$  all have protruding (0001) surface cation (pointed out by the yellow arrow in Figure 2.4). The protruded cation prevents the silver slab to get closer to the oxygen layer (Figure 2.4b), where the  $\Delta d$  of  $\text{Ag/Al}_2\text{O}_3$  is  $2.58 \text{ \AA}$  compared to  $1.81 \text{ \AA}$  in  $\text{Ag/Fe}_2\text{O}_3$  (Fig 2.4c). This behavior may account for the weak  $\text{Ag/Al}_2\text{O}_3$  bonding reported in the literature.<sup>184</sup> Consequently, to account for the increase in interfacial energy,  $f=2$  is used for most of the corundum oxides with protruded cations. It is interesting to note that all the corundum type oxides studied here, except  $\text{Fe}_2\text{O}_3$ , had protruding

(0001) surface cations that necessitated the use of  $f = 2$ . In  $\text{Fe}_2\text{O}_3$ , whose cation,  $\text{Fe}^{3+}$ , submerges beneath the oxygen layer after the relaxation so it does not interfere the Ag-O bonds (Figure 2.4c). This means that there is no need to increase the structure factor, so the calculation of  $\chi_{\text{MO}}$  for  $\text{Fe}_2\text{O}_3$  follows the similar manner as  $\text{Al}_2\text{O}_3$  but with  $f=1$  for the smooth top O layer. Table A2 in the appendix summarizes all the descriptor calculations performed in the present work.

The unique behavior of  $\text{Fe}_2\text{O}_3$  may be due to its strong  $3d$  electron interaction with the oxygen polyhedron. In  $\text{M}_2\text{O}_3$  corundum oxides bulk structure, the cation  $\text{M}^{3+}$  occupies 2/3 of the oxygen octahedral sites. On the  $\text{M}^{3+}$  terminated surface, the protruding  $\text{M}^{3+}$  without unpaired electrons will relax toward the oxygen due to electrostatic interactions, as for  $\text{Al}_2\text{O}_3$  and  $\text{In}_2\text{O}_3$ . Comparing  $\text{Fe}^{3+}(3d^5)$ ,  $\text{Rh}^{3+}(4d^6)$ , and  $\text{Cr}^{3+}(3d^3)$  in  $\text{Cr}_2\text{O}_3$ ,  $\text{Rh}_2\text{O}_3$ , and  $\text{Fe}_2\text{O}_3$ , respectively, the interaction between the oxygen octahedral may attract  $\text{Fe}^{3+}(3d^5)$ , which has the most unpaired  $d$ -electrons to move underneath the top oxygen layer. Due to the complexity of computing strong correlated  $d$ -electrons in transition metal oxides, more research is warranted.

It should be noted that the use of surface energetics, classical view of charge transfer, and metal-oxide formation energies, to formulate a descriptor to relate directly to interface energy  $\gamma_{12}$  and work of adhesion  $W_{\text{adh}}$  for Ag/oxide interface has been tried, but we did not find no strong correlation.

### 2.6.2 Descriptor-Based Prediction of Interface Energy and $W_{\text{adh}}$

Figure 2.5a shows the DFT computed interface energy and its relationship with  $\sigma_{\text{MO}}$  in various types of oxides. The interface energy monotonically increases with the descriptor. The simple descriptor defined in Eqn. 2.3 enables assessment of oxide properties that will lead to high or low interface energy. Two factors can affect the interface energy; one is the oxide bond energy ( $|E_{\text{M-O}}|$ ), which has a chemical nature. The other is the density of the dangling bonds, which

depends on the geometry of the surface. The increase in either of these would increase the value of descriptor, and hence the interface energy.

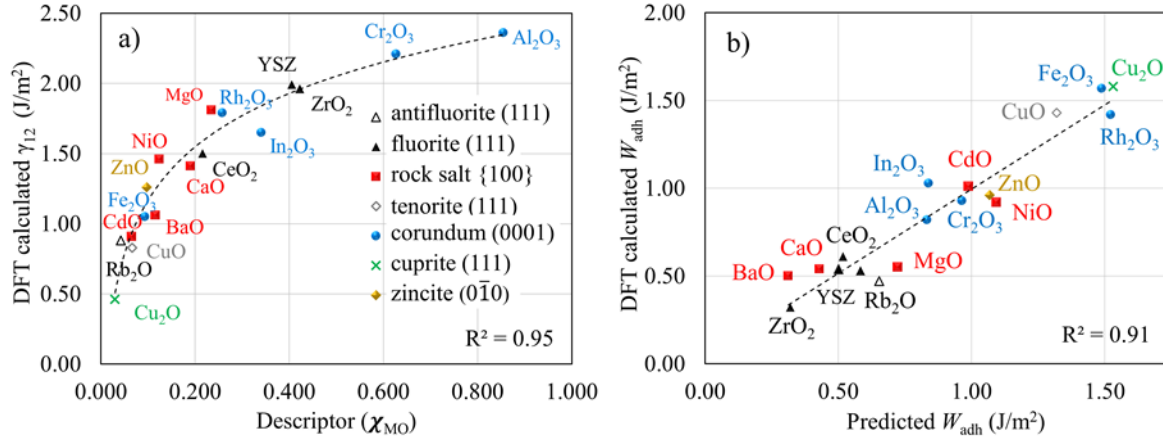


Figure 2.5. The correlation a) between of the interface energy ( $\gamma_{12}^{\text{DFT}}$ ) of Ag/oxides and the descriptor ( $\chi_{\text{MO}}$ ), which followed a logarithmic function, and b) between the predicted work of adhesion ( $W_{\text{adh}}^{\text{pred}}$ ) at the Ag/oxides interface and the DFT calculated ones ( $W_{\text{adh}}^{\text{DFT}}$ ).

In Figure 2.5a, the interplay between these two factors is evident. For example,  $\text{ZrO}_2$ , which has the highest bond energy among oxides in this study (-2.39 eV/bond), did not show the highest interface energy.  $\text{Al}_2\text{O}_3$  has the highest interface energy, although its bond energy of -1.45 eV/bond is not as large as  $\text{ZrO}_2$ . This is due to a different surface geometry, as  $\text{Al}_2\text{O}_3$  contains 1.7 times larger surface dangling bond density than  $\text{ZrO}_2$ . In fact, the oxides with higher interface energy with Ag (Fig 2.5a) was dominated by corundum type oxides. On the other hand, in the lower region of interface energy, although  $\text{Rb}_2\text{O}$  and  $\text{CdO}$  both had similarly low bond energy of -0.46 and -0.43 eV/bond, respectively,  $\text{Cu}_2\text{O}$  with the bond energy of -0.51 eV/bond exhibited much lower interface energy due to its low dangling bond density of  $0.07 \text{ bonds}/\text{\AA}^2$ , compared to  $0.11$  and  $0.18 \text{ bonds}/\text{\AA}^2$  of  $\text{Rb}_2\text{O}$  and  $\text{CdO}$ . This simple descriptor also means that if oxides of interest possessed the same surface geometry, and likely the same crystal structures, the descriptor could be approximated by just the chemical feature – the bond formation energy, or equivalently oxide

formation energy. This trend can be seen in Fig 2.5, as different crystalline structures were labeled with different symbols. Therefore, for oxides within the same crystalline family, both interface energy and  $W_{\text{adh}}$  can be simplified to correlate with their formation energies as shown in Figure A6 for corundum and rock salt oxides and suggested by Li *et al.*<sup>103</sup>

The results plotted in Fig 2.5a demonstrated that the descriptor is well-correlated with the DFT calculated interface energy, which increases with the descriptor. A fitting equation:

$$\gamma_{12}^{\text{pred}} = 0.55 \ln(\chi_{\text{MO}}) + 2.43 \quad \text{Eqn. (2.4)}$$

was obtained with a coefficient of determination  $R^2 = 0.95$ . Hence, this equation can be used to estimate interface energy ( $\gamma_{12}^{\text{pred}}$ ) solely based on the descriptor. The predicted interface energy was then used to predict  $W_{\text{adh}}^{\text{pred}}$  as defined by Eqn. 2.1, with tabulated surface energies, which is easier compute with DFT calculations. In this study, the surfaces of these oxides were selected based upon a criterion of being the lowest surface energy. The individual surface energy of these oxides is tabulated in Table A2 and discussed in Appendix A.

The predicted  $W_{\text{adh}}^{\text{pred}}$  was plotted against the DFT-calculated  $W_{\text{adh}}$  in Fig 2.5b, which also demonstrates satisfactory accuracy (Figure 2.5b). The conclusion obtained from the two ends of the  $W_{\text{adh}}$  plot indicated that  $\text{ZrO}_2$  as well as YSZ were among the most difficult oxides for Ag to be wetted. On the other hand, while both  $\text{Fe}_2\text{O}_3$  and  $\text{Rh}_2\text{O}_3$  provided high adhesion, like CuO, both of them are not stable under SOFC reducing environment ( $\text{Fe}_2\text{O}_3$  would be reduced at temperature above 587 °C). Within Figure 2.5b, a candidate with the highest  $W_{\text{adh}}$  that would be stable in a reducing environment is  $\text{In}_2\text{O}_3$ , but its  $W_{\text{adh}}$  is only 1.03 J/m<sup>2</sup>, 0.4 J/m<sup>2</sup> lower than CuO.

The descriptor was also employed to screen more single cation oxides but, among those, none gave a higher  $W_{\text{adh}}$  with Ag than CuO. For example, a rutile  $\text{SnO}_2$  (110) was predicted based

on the descriptor to have  $W_{\text{adh}}$  of 1.23 J/m<sup>2</sup>. For validation purposes, the DFT-calculation gave  $W_{\text{adh}} = 1.10$  J/m<sup>2</sup>, using a half-sandwich interface model. The  $W_{\text{adh}}$  translated to a borderline wetting contact angle of 90°, which when combined with the effect from dissolved oxygen in Ag(*l*) could enable Ag wetting, although it would not be as good as CuO. In addition, SnO<sub>2</sub> is a bit more resistant to the reduction environment, as it is expected to be stable up to 647 °C according to Ellingham Diagram. It has been suggested that V<sub>2</sub>O<sub>5</sub> could be another potential oxide;<sup>24</sup> however, due to the step-like structure of the (010) surface, a smooth surface of Ag used in the present descriptor model could not accurately determine  $W_{\text{adh}}$  of this interface. In conclusion, our screening of monocation oxides could not identify a candidate that would yield similar or higher  $W_{\text{adh}}$  than CuO, while not being cost-prohibitive or reduced in SOFC operating conditions.

### 2.6.3 Identification of Complex Oxides and Ternary Braze Alloy Design

Since the simple oxide search did not predict many candidates that could potentially be 1) better than CuO in enhancing  $W_{\text{adh}}$  and 2) stable in a reducing SOFC environment, the descriptor was used to search for potential multi-cation oxides. First, the descriptor was used to explore multi-cation oxides with lower descriptor values that lead to lower interface energy (since a low interface energy is a necessary but not sufficient condition for a high work of adhesion). Then, the surface energies were computed by DFT. The stable surface for all delafossite oxides was chosen to be O-terminated (0001) surfaces, based on experimental and computational evidence.<sup>185–187</sup> Predicting the interface energy  $\gamma_{12}^{\text{pred}}$  from the descriptor using Eqn. 2.4, and the DFT computed surface energies, the  $W_{\text{adh}}$  was first predicted before the DFT interface model was constructed. From this, it was found that several oxides with a delafossite structure could exhibit strong adhesion due to their high surface energy relative to a low predicted interface energy (Table 2.4). For comparison, CuO is listed as well. While some delafossite oxides exhibited low adhesion  $\sim 0.7$  J/m<sup>2</sup> with Ag,

such as  $\text{CuCrO}_2$  and  $\text{CuFeO}_2$ , several delafossite oxides,  $\text{CuAlO}_2$ ,  $\text{CuGaO}_2$ , and  $\text{CuInO}_2$ , showed higher predicted  $W_{\text{adh}}$  (2.3~2.6  $\text{J/m}^2$ ) with Ag than CuO (1.43  $\text{J/m}^2$ ).

$\text{Cu}_3\text{TiO}_4(010)$  also yielded a predicted  $W_{\text{adh}}$  of 2.12  $\text{J/m}^2$ , which is higher than that of CuO.  $\text{Cu}_3\text{TiO}_4$  has a similar structure to delafossite, and its (010) surface is equivalent to the (0001) surface of delafossite oxides. The increase of  $W_{\text{adh}}$  on  $\text{Cu}_3\text{TiO}_4$  surface could also explain the observed enhanced braze wettability when  $\text{TiO}_2$  is added to the Ag–CuO system.<sup>136</sup>  $\text{TiO}_2$  itself is not the likely cause of wettability enhancement, as predictions for both the rutile  $\text{TiO}_2(110)$  and anatase  $\text{TiO}_2(101)$  structures yielded  $W_{\text{adh}}$  of only 0.40 and 0.56  $\text{J/m}^2$ , respectively. However,  $\text{TiO}_2$  could react with CuO or  $\text{Cu}_2\text{O}$  to form  $\text{Cu}_3\text{TiO}_4$ .<sup>188,189</sup> Therefore, the addition of Cu and Ti to Ag, with modification of brazing gas environment and temperature conditions to purposely generate  $\text{Cu}_3\text{TiO}_4$  on the YSZ surface could also further enhance the wetting of Ag. Also, as indicated by its formation energy (-13.12 eV) on the Ellingham diagram,  $\text{Cu}_3\text{TiO}_4$  will be stable in a reducing SOFC environment.

Another interesting oxide is  $\text{CuAlO}_2$ . The formation of  $\text{CuAlO}_2$  would be favorable in certain conditions as the  $\text{CuAlO}_2$  formation energy was calculated to be -9.70 eV, which is comparable to -9.74 eV for  $\frac{1}{2}(\text{Al}_2\text{O}_3 + \text{Cu}_2\text{O})$ . Experimental phase diagrams indicate that  $\text{CuAlO}_2$  is stable at high temperature, especially in the brazing and SOFC operating temperature range<sup>190</sup>. Putting the calculated formation energy of  $\text{CuAlO}_2$  on the Ellingham diagram shows that it is stable in a reducing environment. To further investigate this promising oxide and also obtain the accurate  $W_{\text{adh}}$ , DFT calculations were performed (Figure 2.6a). The DFT-calculated  $W_{\text{adh}}$  of Ag/ $\text{CuAlO}_2$  is 3.04  $\text{J/m}^2$ , almost twice of that at the Ag/CuO interface. The changes in PDOS through formation of this interface shown in Figure 2.6b correspond well to its high  $W_{\text{adh}}$ , where oxygen *p*-states moved from high-energy antibonding (-2 to 0 eV) to bonding states at energies below the metal *d*-

states ( $\sim -8$  eV). This high adhesion will lead to complete wetting ( $0^\circ$ ). Moreover, DFT calculation using half-sandwich model also indicate strong adhesion ( $W_{\text{adh}} = 2.04$  J/m<sup>2</sup>) between CuAlO<sub>2</sub> and YSZ. Overall, this is in accordance with reports that the greater extent of CuAlO<sub>2</sub> formed from the unintended reaction of CuO with Al<sub>2</sub>O<sub>3</sub>, the lower contact angle of Ag.<sup>145</sup>

The other delafossites, CuGaO<sub>2</sub> and CuInO<sub>2</sub>, and Cu<sub>3</sub>TiO<sub>4</sub> were predicted to yield similarly high  $W_{\text{adh}}$  are therefore are expected to yield similar results. However, the formation energy of CuInO<sub>2</sub>, which is the highest among investigated delafossites ( $-5.70$  eV), was only  $-0.52$  eV below the hydrogen line in Ellingham diagram. Given that LDA tends to overestimate bonding energy, it is more prudent to assume that CuInO<sub>2</sub> would not be stable in a reducing SOFC environment.

Therefore, several oxide interlayers, CuAl(or Ga)O<sub>2</sub> or Cu<sub>3</sub>TiO<sub>4</sub>, that could improve the interfacial strength were identified via our computational search. In order to form these oxide layers, the complex oxide could either be pre-sputtered or coated on the YSZ surface before brazing or be directly added to Ag, as similar methods have been used for Ag-CuO system.<sup>145,191</sup> Alternatively, alloying Ag with a mixture of Cu and Al (or Ga, Ti) and fine tuning the brazing gas environment and temperature conditions to intentionally maximize the formation of CuAl(or Ga)O<sub>2</sub> or Cu<sub>3</sub>TiO<sub>4</sub> could also improve the interfacial strength. It should be noted that, according to the original definition, in order to be classified as a RAB component, the oxides formed by the secondary metals in air must be at least be partially soluble in Ag<sup>192</sup> in order to avoid forming thick oxide scale on the liquid surface to inhibit wetting. The oxide solubility, the impact of these alloy or oxide additions on the melting temperature, can be considered in follow-up studies. Nevertheless, these examples suggest that ternary alloy systems may offer many more possibilities. The discovery of potential oxides can be expanded beyond the examples given here.

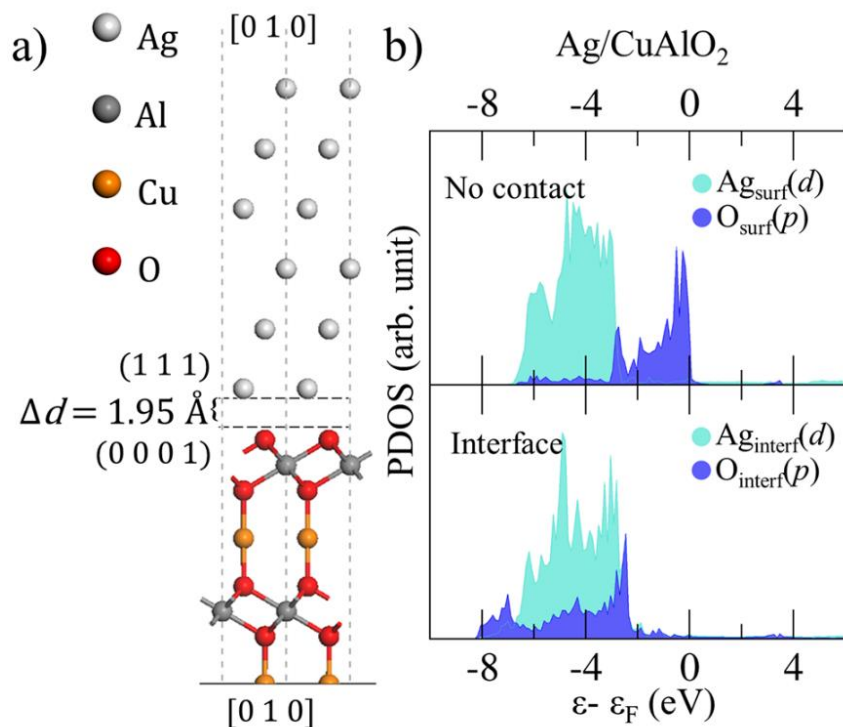


Figure 2.6. The relaxed structure of the Ag/CuAlO<sub>2</sub> by LDA functional showing an interface gap of 1.95 Å (a), and the PDOS of the no-contact (10 Å apart) and interface positions showing large shift in the oxygen's *p*-states. This indicates strong interactions between Ag and CuAlO<sub>2</sub> (b).

## 2.7 Conclusion

The RAB process is a promising solution to solve wetting and adhesion problem of Ag on an YSZ surface for sealing applications as well as providing practicality for industrial settings. As the current Ag-CuO system has a short-coming due to pore formation from reduction of CuO to Cu, there are alternative approaches of other oxide interlayer design that may be effective. Using DFT calculations and interface models, the present paper has identified the two primary mechanisms that enabled Ag to wet on YSZ surfaces, including 1) formation of Ag–O clusters at the Ag/YSZ interface from the oxygen in solution (*Mechanism I*), and 2) enhanced  $W_{\text{adh}}$  by formation of a CuO scale on top of the YSZ (*Mechanism II*). *Mechanism I* reduces the wetting angle by 20~25°, which is a smaller effect than the second mechanism, as the CuO scale can reduce

the wetting angle by  $\sim 45^\circ$ , changing the metal from non-wetting to wetting. The electronic analysis of the involved interfaces shows that interactions between Ag and oxygen atoms of the oxide dominates the interfacial bonding. With this knowledge, a simple descriptor for calculation of interface energy was developed to reduce the dependence on expensive interface calculations. With known surface energy, which is much more easily calculated, the descriptor can also be used for prediction of  $W_{\text{adh}}$ . Several single cation metal oxides were considered, but the number of those with  $W_{\text{adh}}$  comparable to CuO and tolerant of a reducing environment were few. For example, none of the investigated metal oxides, with crystalline structures of rock salt, fluorite, and anti-fluorite, showed high  $W_{\text{adh}}$ . However, by expanding the search to multi-cation oxides, several promising candidates in oxides with delafossite structure, such as  $\text{CuAlO}_2$ ,  $\text{CuGaO}_2$ , and  $\text{Cu}_3\text{TiO}_4$ , were discovered to double the work of adhesion of CuO with Ag. The study provides insight to geometry and bonding energy of metal-oxide interfaces with implications beyond just Ag and YSZ interfaces. The convenient search also opens new pathways to develop potential ternary Ag-oxide braze alloys with enhanced adhesion and wetting on YSZ.

## **CHAPTER 3 Experimental Identification of the Yields Determining Functional Groups in Lignins**

### **3.1 Summary**

Lignin depolymerization to aromatic monomers with high yields and selectivity is essential for the economic feasibility of many lignin-valorization strategies within integrated biorefining processes. Importantly, the functional groups (henceforth referred to as properties) of the lignin source play an essential role in impacting the conversion chemistry, yet this relationship between lignin properties and lignin susceptibility to depolymerization is not well established. In this study, we quantitatively demonstrate how the detrimental effect of a pretreatment process on the properties of lignins, particularly  $\beta$ -O-4 content, limit high yields of aromatic monomers using three lignin depolymerization approaches: thioacidolysis, hydrogenolysis, and oxidation. Through pH-based fractionation of alkali-solubilized lignin from hybrid poplar, this study demonstrates that the properties of lignin, namely  $\beta$ -O-4 linkages, phenolic hydroxyl groups, molecular weight, and S/G ratios exhibit strong correlations with each other even after pretreatment. Furthermore, the differences in these properties lead to discernible trends in aromatic monomer yields using the three depolymerization techniques. Based on the interdependency of alkali lignin properties and its susceptibility to depolymerization, a model for the prediction of monomer yields was developed and validated for depolymerization by quantitative thioacidolysis. These results highlight the importance of the lignin properties for their suitability for an ether-cleaving depolymerization process, since the theoretical monomer yields grows as a second order function of the  $\beta$ -O-4 content. Therefore, this research encourages and provides a reference tool for future studies to identify new methods for lignin-first biomass pretreatment and lignin valorization that emphasize

preservation of lignin qualities, apart from focusing on optimization of reaction conditions and catalyst selection.

### **3.2 Introduction**

Technologies for the conversion of renewable, non-food plant biomass to fuels, chemicals, polymers, and materials have the potential to displace fossil sources of carbon while simultaneously contributing to rural agricultural economies and lowering CO<sub>2</sub> emissions.<sup>193</sup> While technologies for the production of cellulosic biofuels are beginning to be commercialized in the U.S., Europe, and Brazil, substantial technical, logistical, and economic challenges still remain.<sup>194</sup> In particular, one economic challenge is that current processes produce low-value, high-volume biofuels that require substantially higher capital costs per unit of biofuel produced relative to starch- or sucrose-derived biofuels. This is a consequence of plant cell wall recalcitrance, whereby the polysaccharides that may serve as the feedstock for biological conversion to biofuels are embedded in the plant cell wall matrix. This cell wall matrix can be considered as a composite material comprising polysaccharides (cellulose and hemicelluloses) and lignin that presents a challenge for “deconstruction” and conversion.<sup>195</sup>

Diversifying the product portfolio of lignocellulose-to-biofuels processes to include renewable, bio-based chemicals is widely recognized as an opportunity both to improve the economics of these processes and to buffer against market fluctuations. Thus, there is an obvious and compelling need to develop integrated processing approaches that enable multi-product biorefineries. Despite comprising a substantial portion of plant cell walls (as much as one third of the mass of lignocellulosic biomass) and representing the second-most abundant naturally occurring biopolymer after cellulose, the chemical functionality in lignins remains largely unutilized as a source of renewable carbon for the production of bio-based chemicals, polymers,

and materials. As such, there is an opportunity for technologies that can be integrated with conversion processes employing a biomass pretreatment/fractionation strategy, whereby it may be possible to utilize all or a fraction of the process-modified lignins for purposes other than as a low-value solid fuel.<sup>196</sup> Commercialization of co-products from wood lignins derived from Kraft pulping have long proved challenging, but it should be understood that lignin origin (*e.g.*, hardwood, softwood, or grass) and processing history (*e.g.*, alkaline pulping, organosolv pulping, sulfite pulping, dilute-acid pretreatment, *etc.*) have an enormous impact on the structure, properties, and suitability of the lignin for a target application, which this work will investigate.

Although lignin valorization has increasingly been the subject of substantial research, significant challenges still remain.<sup>197,198</sup> General strategies for lignin utilization include thermochemical conversion to heat and power or syngas, utilization of (potentially modified) polymeric lignins in applications such as resins for application as adhesives or coatings,<sup>199</sup> and lignin depolymerization to generate sets of aromatic compounds that can serve as bio-based alternatives to petroleum-derived aromatic platform chemicals.<sup>200</sup> Notably, a recent DOE report has highlighted the critical need for utilizing lignin-derived compounds as potential platform chemicals as well as the challenge in achieving this due to the difficulty of generating a limited range of aromatic compounds from lignin at high yields and selectivities that can act as renewable aromatic monomer cognates to existing petrochemicals.<sup>201</sup> This challenge is derived both from the random nature of the lignin polymer as a consequence of its synthesis via free radical-mediated oxidation and its propensity for modification during conversion or extraction processes. Strategies for the depolymerization of lignin include catalytic cracking/pyrolysis,<sup>202,203</sup> oxidation<sup>204</sup> and hydrogenolysis-hydrodeoxygenation,<sup>205,206</sup> and base-catalyzed depolymerization.<sup>207</sup> As examples, the depolymerization of lignin using solid acid-catalyzed hydrolysis has been reported to yield

primarily 4-propenyl guaiacol/syringol products, while base-catalyzed depolymerization can yield additional aromatic products.<sup>207,208</sup> Oxidative cleavage of lignin in many studies aims to achieve a defined set of products including vanillin, vanillic acids, and their syringyl counterparts.<sup>209–211</sup> A number of studies have investigated molecular oxygen or hydrogen peroxide as an oxidant in the presence of a transition metal-based homogeneous catalysts including Cu, Fe, or V.<sup>212–215</sup> Other oxidative approaches include using a combination of formic acid and TEMPO catalysts, or polyoxometalates.<sup>216,217</sup> Lignosulfonates derived from sulfite pulping of wood have been utilized commercially as a feedstock for the production of vanillin since the 1940's using catalyzed and/or uncatalyzed alkaline oxidation with vanillin yields of up to 15% reported.<sup>204,218,219</sup> Vanillin production from Kraft lignin using these approaches has been extensively explored, although yields are typically lower compared to lignosulfonates since Kraft lignins may be more condensed.<sup>220</sup> Approaches for reductive cleavage, particularly hydrogenolysis, have received substantial recent attention, and a number of heterogeneous catalysts have been proposed including ligand-less Ni,<sup>221</sup> Ni alloys,<sup>222</sup> NiAu,<sup>223</sup> Ni/SiO<sub>2</sub>,<sup>224</sup> or Pd/C.<sup>225</sup> The products differ depending on reaction conditions. A mild liquid reaction of range ~200 °C will predominantly produce guaiacol or syringol with the alkyl side chain intact at the 4-position. The amount of substitution of this alkyl side chain with hydroxyl groups can vary depending on reaction conditions and catalyst.<sup>226,227</sup> Under more severe conditions, ring hydrogenation and hydrodemethoxylation can occur to yield saturated compounds such as 4-propylcyclohexanol or 4-propylcyclohexane, which are suitable for fuel applications.<sup>228,229</sup>

For many depolymerization approaches, enormous effort has been invested in the study of reaction conditions, particularly selection of catalysts and solvents.<sup>40,230–232</sup> More importantly, these conditions were also often used as a benchmark to determine the effectiveness of the

depolymerization approach. On the other hand, the structural features of lignin used in the reaction are often not considered, despite several studies reporting significantly lower yields when the same methods performed on lignin dimer models were applied to real lignin.<sup>222,233</sup> Specifically, there has not been conclusive evidence demonstrating how these structural features are fundamentally related, especially after lignin-modifying extraction or pretreatment, and how it would affect lignin's susceptibility towards depolymerization. Previous studies have suggested that native lignin in biomass with higher syringyl/guaiacyl unit ratios (S/G ratios) give higher monomer yields from quantitative thioacidolysis, which is due to the higher natural  $\beta$ -O-4 content.<sup>234,235</sup> Many lignin-modifying pretreatments have been investigated,<sup>236-238</sup> with each of these imparting changes to the physical and chemical properties of lignin through different mechanisms (for example by the cleavage of C-O bonds). However, many of these pretreatments can also result in the formation of new C-C linkages which hinder approaches to generate aromatic monomers.<sup>239-241</sup> Knowledge of how these changes impact a lignin's susceptibility to depolymerization could help in the integration of strategies for lignin conversion into biorefining processes.

Therefore, the objective of this study is to develop a better understanding of the relationship between lignin properties and to model their effect on lignin susceptibility to depolymerization through cleavage of ether linkages. This will be achieved through solubility-based fractionation of a hardwood lignin from an alkaline pretreatment liquor in order to generate lignin fractions exhibiting diverse properties. These fractions will be characterized and subjected to three depolymerization approaches. Correlations amongst the lignin properties and between obtained yields will be established in order to develop a methodology for assessing lignin quality for its suitability for depolymerization.

### 3.3 Methods

#### 3.3.1 Lignin Fractionation

Pretreatment was performed in an M/K Systems, Inc. (Peabody, MA, USA) single vessel pulp digester with a capacity of 10 L using debarked wood chips of 20-year old hybrid poplar (*Populus nigra x maximowiczii* cv. NM6) obtained from Dr. Raymond Miller (Michigan State University Forest Biomass Innovation Center, Escanaba, Michigan). Pretreatment was performed at a liquor-to-wood ratio of 4:1 using conditions identical to those in our previous work for an H-factor of 166.<sup>242</sup> These mild pretreatment conditions were utilized to preserve solubilized lignin quality. Lignin was fractionally precipitated from this liquor through two sequential pH reduction approaches. The first one employed sequential acidification and precipitation at using CO<sub>2</sub> at room temperature and atmospheric pressure. For room temperature fractionation, pH was decreased stepwise as shown in Table 3.1 until a pH of 9.0 was achieved and yielding 4 fractions. A final fraction was generated by further acidification to a pH of 2 by addition of 1 M H<sub>2</sub>SO<sub>4</sub>. The second lignin fractionation approach employed the Sequential Liquid-Lignin Recovery and Purification (SLRP) process using CO<sub>2</sub> acidification at elevated temperature (115 °C) and pressure (6.2 bar) as reported in our previous work.<sup>243</sup> For this, the SLRP fractions represent the lignin recovered by acidification between a pH of 11.0 of 10.5 (SLRP-1) and the pH increment of 10.5 to 10.0 (SLRP-2) as shown in Table 3.1. The Klason lignin content of each pH fractions, as determined by NREL standard procedure (NREL/TP-510-42618), was used as a basis for subsequent characterization and monomer yield determination.

#### 3.3.2 Lignin Extraction from Birch

To assess the impact of lignin depolymerization on a “native” lignin, lignin was extracted from debarked silver birch (*Betula pendula* Roth.) grown in northern Sweden and supplied Curt

Lindström (Smurfit-Kappa Kraftliner AB, Piteå, Sweden). The lignin extraction was performed according to the method proposed by Gu et al.<sup>244</sup> In short, the biomass was cryogenically ball-milled in a TissueLyser II (Qiagen, Hilden, Germany) for a total of 4 hr with 15 min interval for cooling in liquid nitrogen. The ball-milled sample was dissolved in 8% LiCl/DMSO at a concentration of 5% by weight and stirred at 25 °C for 48 hr then at 50 °C for 24 hr. The biomass was precipitated as a gel by dropwise addition of the LiCl/DMSO solution into deionized water. This gel was thoroughly washed with deionized water until no Cl remained in the gel as determined by addition of AgNO<sub>3</sub>. The decrystallized biomass sample was then lyophilized before undergoing enzymatic hydrolysis for 72 hrs (20 mg protein / g biomass; CTec II and HTec II from Novozymes in a 2:1 ratio at 50°C with in pH 5.25, using 0.05 M Na-citrate buffer). Next, the sample was washed with excess water and lyophilized again. The solid residue was then subjected to dioxane extraction for 6 hr with 50 mL 96% aqueous (v/v) dioxane.

### **3.3.3 Lignin Acetylation**

Acetylated lignin samples were used for <sup>1</sup>H NMR and GPC analyses. The procedure was adopted from previous study with slight modification.<sup>245</sup> Essentially, 12.5 g/L of lignin solution in 1:1 pyridine/acetic anhydride was prepared. Fractions that were harder to solubilize were subjected to sonication for 10-20 min. The completely dissolved solutions were left in an incubator at room temperature and 180 rpm for 24 hr before applying washing steps as in the previous study.

### **3.3.4 NMR Analysis of Lignin**

<sup>1</sup>H-NMR spectra were acquired on a 500 MHz NMR spectrometer (Agilent 500/54) equipped with a OneNMR probe. Acetylated lignin was dissolved in CHCl<sub>3</sub>-d<sub>6</sub> at a concentration of 44 mg/mL. Pentafluorobenzaldehyde (PFB) was used as an internal standard with tetramethylsilane (TMS) as a peak reference. The spectra were acquired from -2 to 14 ppm with a

30° pulse, a recycle delay of 4 s, and a total of 800 scans. Aliphatic and aromatic hydroxyl content were determined on a per aromatic basis (mol/mol) by using the methoxyl content corrected for the thioacidolysis-determined S/G ratio. <sup>13</sup>C-NMR spectra were acquired on a 500 MHz NMR spectrometer (Varian Inova) equipped with a double-resonance broadband probe. Proton decoupling was applied only during acquisition period (*i.e.*, decoupling-NOE). A sample of lignin (300 mg) was dissolved in 0.6 mL DMSO-*d*<sub>6</sub> along with 2.0 mg chromium(III) acetylacetonate as a relaxation reagent. Sonication was used to facilitate dissolution. The spectra were acquired from -15 to 235 ppm with a 90° pulse, a recycle delay of 1.7 s, and an acquisition time of 1.2 s. A total of 10,000 scans were collected. Peak assignments were based on the previous literature.<sup>246,247</sup> The β-O-4 content was determined on a per 100 aromatic monomer basis (mol/mol) by using the methoxyl content corrected for the thioacidolysis-determined S/G ratio. The gradient 2D <sup>13</sup>C-<sup>1</sup>H-correlation (HSQC) experiments (Bruker standard pulse sequence ‘hsqcedetgpcisp2.2’; phase-sensitive ge-2D multiplicity-edited HSQC using PEP and adiabatic inversion and refocusing pulses with gradients in back-inept) were performed on a 900 MHz NMR spectrometer (Bruker Avance) equipped with a TCI triple-resonance inverse detection cryoprobe. A sample of lignin (100 mg) was dissolved in 0.6 mL DMSO-*d*<sub>6</sub>. The solvent peak ( $\delta_C$  39.5,  $\delta_H$  2.49 ppm) is used as an internal reference. The spectra were acquired from 0 to 9 ppm in F<sub>2</sub> (<sup>1</sup>H) dimension by using 3234 data points for an acquisition time (AQ) of 200 ms, and from -15 to 155 ppm in F<sub>1</sub> (<sup>13</sup>C) dimension by using 512 increments (AQ of 6.66 ms). The number of scans per t1 increment was 32, and the recycle delay was 1 s. The total experimental time was 337 min. Peak assignments were based on the prior literature.<sup>217,248–251,25,87–90</sup>

### **3.3.5 Gel Permeation Chromatography**

Gel permeation chromatography (GPC) was performed as in our previous work.<sup>245</sup> Briefly, acetylated lignin (2 mg/mL) was dissolved in THF. The samples were analyzed by HPLC (Agilent 1100) equipped with a Waters Styragel HR 4 column (Milford, MA, USA) at a flow rate of 0.5 mL/min, temperature of 40 °C, and detection by UV absorbance at 280 nm. Polystyrene standards of molecular weight 1, 10, 50, 100, 200 kDa were used for calibration.

### **3.3.6 Thioacidolysis Depolymerization of Lignin**

Quantitative thioacidolysis utilizing derivatized monolignol standards was performed as described in our previous work.<sup>234</sup> For this, three 2-mg replicates of dried and isolated lignin sample were weighed into glass vials and heated with a mixture of dioxane, ethanethiol, and boron trifluoride diethyl etherate to liberate the lignin monomers. The extracted thioether derivatized monomers were subsequently silylated with N,O-bis-trimethylsilyl-acetamide (BSA) and quantitated using GC-MS analysis (Agilent 7890A / 5975C MS).

### **3.3.7 Catalytic Oxidative Cleavage of Lignin**

The catalytic oxidation method was adapted from the literature.<sup>209</sup> For this, 10 mg of each lignin sample and 5 % (w/w) CuSO<sub>4</sub> were dissolved in 5 mL of 2 M NaOH. Samples were sonicated for 10 min to ensure complete dissolution. The solution was then poured into a 50-mL passivated stainless steel reactor and pressurized to 10 bars with O<sub>2</sub> gas (>99.99% purity, Airgas) following evacuation of the reactor headspace by vacuum. The reactors were submerged in a fluidized sand bath (Techne, Cole-Palmer) preheated to 160 °C for a specific period of time. When the reaction was complete, the reactor was submerged in an ice bath for 10 min. The pH of the final solution was reduced to 2.0 by addition of 6 M HCl and centrifuged to isolate the solid residue. The products in the liquid fraction were extracted four times by chloroform. The solution

was then evaporated under vacuum at 40 °C and re-dissolved in 10 mL of 1:1 methanol/water with 1% (v/v) formic acid. Quantification of the products was performed by HPLC (Agilent 1100) using 1:4 methanol/water with 1% formic acid as a mobile phase and a C18 column (Atlantis T3 100 Å, 3 µm, 3.0 mm x 150 mm; Waters). Standards for product quantification included vanillin, vanillic acid, acetovanillone, syringaldehyde, syringic acid, acetosyringone, 4-hydroxybenzaldehyde, and 4-hydroxybenzoic acid. All standards were purchased from Sigma Aldrich and monomer yields were determined on a per mass Klason lignin basis.

### 3.3.8 Catalytic Hydrogenolysis of Lignin

Catalytic hydrogenolysis of lignin was performed according to previous work.<sup>230</sup> In short, 10% metal loading Ni/C was synthesized by incipient wetness. Typically, 2.76 g of Ni(NO<sub>3</sub>)<sub>2</sub>·6H<sub>2</sub>O (Sigma-Aldrich) was added to 8 g deionized water and stirred until well mixed. The solution was then added dropwise to 5 g of activated carbon (Darco<sup>®</sup> G-60, Aldrich, water absorption capacity of 2.1 mL/g). The mixture was kept wet at room temperature for 24 h before drying overnight at 100 °C. Then it was calcined at 400 °C under nitrogen atmosphere for 4 hr, and reduced at 400 °C under 10% H<sub>2</sub> in an Ar atmosphere, both of which used at a temperature ramp of 6.25 °C/min. The finished catalysts were stored and weighed in an anaerobic glove box. For the hydrogenolysis reaction, 40 mg of lignin, 30 mg of catalyst, and 4 mL of ethanol were charged to a 10 mL passivated stainless steel reactor while in the anaerobic glove box. Reactors were submerged into a fluidized sand bath set at 220 °C for 6 hr. The resulting liquid was collected, filtered, and injected into GC/MS (Agilent 7890A / 5975C) using Agilent DB-WAXETR column (30 m x 0.250 mm x 0.25 µm) with 1:1000 split for product. The temperature program holds at 60 °C for 3 min before ramping up at 40 °C/min to 260 °C and held for 2.5 min. Standards were run for quantification. Yields were determined as mass products per mass Klason lignin using

standard curves constructed from pure monomers including 4-propyl guaiacol, 4-propyl syringol, 4-ethyl guaiacol, 4-ethyl syringol, and syringol. All standards were purchased from Sigma Aldrich except 4-propyl syringol, which was synthesized according to Parsell et al.,<sup>37</sup> and 4-ethyl syringol, which was estimated using the same response factor as 4-propyl syringol. These products comprise all peaks that were detected.

### 3.3.9 Yield Prediction Model Development

Computational prediction of monomer yields was performed in MATLAB (MathWorks, Inc., Natick, MA). For this approach, populations of lignin polymers of length  $n$  with  $n-1$  bonds between the  $n$  monomers were generated over a range of expected values for  $\beta$ -O-4 contents (See Section 3.4.5). The assignment of the identity of each of the  $n-1$  bonds between dyads as a  $\beta$ -aryl ether was made by choosing a threshold value corresponding to the expected value for  $\beta$ -O-4 content for a given population using the '*randn*' function in MATLAB. This was done to generate populations of lignin polymers of constant chain length with randomly distributed  $\beta$ -O-4 bonds at a set average content of  $\beta$ -O-4 bonds. This methodology was applied to determine monomer yields from populations of 5000 polymers of desired chain length  $n$  over a range of 0 to 100% over 2500 intervals for the probability that any bond is a  $\beta$ -O-4 bond, where a monomer can be generated only from two adjacent  $\beta$ -O-4 bonds within a triad or a  $\beta$ -O-4 bond at a chain end. This methodology assumes that lignin is a linear polymer and that no cross-linking or aryl-aryl bonds are present in the polymer. For comparing calculated theoretical yields to quantified yields, the experimental yields by thioacidolysis, hydrogenolysis, and oxidation were converted to a mol/mol yield by assuming a molar mass of 196 g/mol for a guaiacyl monomer and 226 g/mol syringyl monomer within the lignin polymer.

### 3.4. Lignin Fractionation Process and Recovery

The lignins used in the first part of this study were obtained from the fractional precipitation of pretreatment liquors following the mild alkali pretreatment of hybrid poplar at a final temperature of 150 °C at a total time of 3 hr as performed in our previous work in order to minimize lignin modification and to maximize xylan retention in the pretreated biomass.<sup>242</sup> Both native and process-modified lignin are highly heterogeneous which hinders accurate characterization and may limit their value for applications requiring a homogeneous, well-defined starting material. For this work, alkali-solubilized lignins are subjected to fractionation in order to both obtain more homogeneous lignin fractions and to enrich or deplete these fractions in certain properties that can yield insight into property differences that impact the conversion process chemistry.

A number of approaches for the recovery and fractionation of lignin from alkaline pulping or pretreatment liquors have been explored in the past. These approaches include ultrafiltration or approaches based on precipitation due to altering the properties of the solvent by acidification with a weak or strong acid and the use of organic solvents.<sup>252–255</sup> Of these approaches, CO<sub>2</sub> acidification has been employed in a number of recent commercial or pilot studies, including LignoBoost™, LignoForce™, and of particular interest to this study, Sequential Liquid Recovery and Purification™ (SLRP™) process.<sup>256–258</sup> This pH-based fractionation by CO<sub>2</sub> has previously shown the ability to generate lignin fractions with different properties from Kraft black liquor of softwood biomass.<sup>245</sup> For the present work, lignin fractionation was performed using two approaches to sequentially acidify and fractionally recover lignins from this alkaline pretreatment liquor. The first approach utilized sequential acidification and precipitation with CO<sub>2</sub> at room temperature and atmospheric pressure, while the other (*i.e.*, the SLRP™ process) was performed at elevated temperature and pressure as in our previous work.<sup>245</sup> The mass yields for the lignin fractions

obtained from these processes are presented in Table 3.1. This shows that for recovery at the same pH range, the room temperature recoveries were more than double from the SLRP<sup>TM</sup> process. This may be due to the higher solubility of the lignin at higher temperature. These fractions, hereafter, will be referred to as named in Table 3.1 throughout the study. Furthermore, it should be understood that these fractions do not represent 100% of the recoverable lignin, but were generated in order to better understand how diversity in lignin properties impact depolymerization aromatic monomer yields.

Table 3.1. Percent recovery of each fraction through CO<sub>2</sub> acidification at room temperature and at 115 °C (SLRP<sup>TM</sup>). The pH 2 fraction was obtained by acidification with H<sub>2</sub>SO<sub>4</sub>.

<b>Room Temperature (RT) Fractionation</b>		
<b>Precipitation pH</b>	<b>Fraction name</b>	<b>Percent Recovery</b>
11	RT-1	8.42
10.6	RT-2	20.79
10	RT-3	13.95
9	RT-4	12.59
2	RT-5	26.07
<b>Sequential Liquid-Lignin Recovery and Purification (SLRP)</b>		
10.5	SLRP-1	4.05
10	SLRP-2	7.95

### 3.5 Trends in Properties of Fractionated Lignins

Next, we characterized the properties of the different lignin fractions by applying a number of characterization techniques. These techniques included determination of S/G ratios as measured by both 2D <sup>1</sup>H-<sup>13</sup>C-correlated HSQC NMR and quantitative thioacidolysis, the fraction of linkages between monolignols by HSQC NMR, the β-O-4 contents by quantitative <sup>13</sup>C-NMR, the phenolic and aliphatic hydroxyl content as determined by <sup>1</sup>H-NMR, and the molecular weight using gel

permeation chromatography (GPC). All results are available in the Appendix B. It was found that all of these properties, with the exception of the aliphatic hydroxyl content, exhibited obvious trends across the various fractions obtained by pH-based lignin fractionation.

The HSQC spectra of fraction SLRP-1 is shown in Figure 3.1 as a representative spectrum. From this, it can be observed that in the aromatic region a minor fraction (3%) of the syringyl units are oxidized (S'). Also, it can be observed that there is no significant increase in the peak corresponding to *p*-hydroxyphenyl, which implies that there was no or negligible demethoxylation occurring during the alkali pretreatment and fractionation process. The S/G ratios from the HSQC spectra were determined as the relative integration areas of the S<sub>2,6</sub> and S'<sub>2,6</sub> peaks to the G<sub>2</sub> peak. The results (Figure B1 in appendix) indicate a distinct trend that lignin precipitated at higher pH, particularly from the SLRP process, showed higher values of S/G ratios with the highest (S/G = 1.99) from fraction SLRP-1 and lowest (S/G = 1.80) at pH 2 (RT-5). It should be noted that the SLRP fractions exhibit higher S/G ratios relative to room-temperature fractions. This trend is in a good agreement with S/G ratios obtained from thioacidolysis, which are all slightly lower than those from HSQC, ranging from 1.95 in SLRP-1 fraction down to 1.73 in sample RT-5.

Three types of linkages in the aliphatic region from HSQC spectra were detected, including  $\beta$ -O-4,  $\beta$ -5 and  $\beta$ - $\beta$  (Figure 3.1). From both regions of the spectra, no other peaks corresponding to possible linkages from alkali pretreatment, such as stilbene and diarylmethane, were detected. It should be noted that there could be some linkages as a result of condensation that would not be detectable through HSQC NMR such as 5-5' linkage. Therefore, the assessment of linkages from HSQC NMR was semi-quantitative, *i.e.* percentage of detected linkages. The percentage trend of linkages is obvious and is shown in Figure B3, which indicates that lignin at higher pH fractions, particularly SLRP fractions, contained a higher proportion of the  $\beta$ -O-4 and  $\beta$ -5 linkages, while

the relative abundance of the  $\beta$ - $\beta$  linkage increases as recovery pH decreases. It should be noted that adding standards for absolute quantification was not performed due to several prohibitive factors that originate from the lignin; primarily the error caused by varying  $T_2$  relaxation and resonance offsets in HSQC NMR which affect the signal intensity.<sup>259</sup> Instead, quantitative  $^{13}\text{C}$ -NMR was used to directly determine the amount of  $\beta$ -O-4 linkages per 100 aryl units. A similar trend was observed, in which the fractions recovered at higher pH contained higher  $\beta$ -O-4, and the increase was particularly pronounced in SLRP fractions (Figure B1). Notably the fraction with highest  $\beta$ -O-4 content, SLRP-1, was shown to have double the  $\beta$ -O-4 content relative to the lowest.

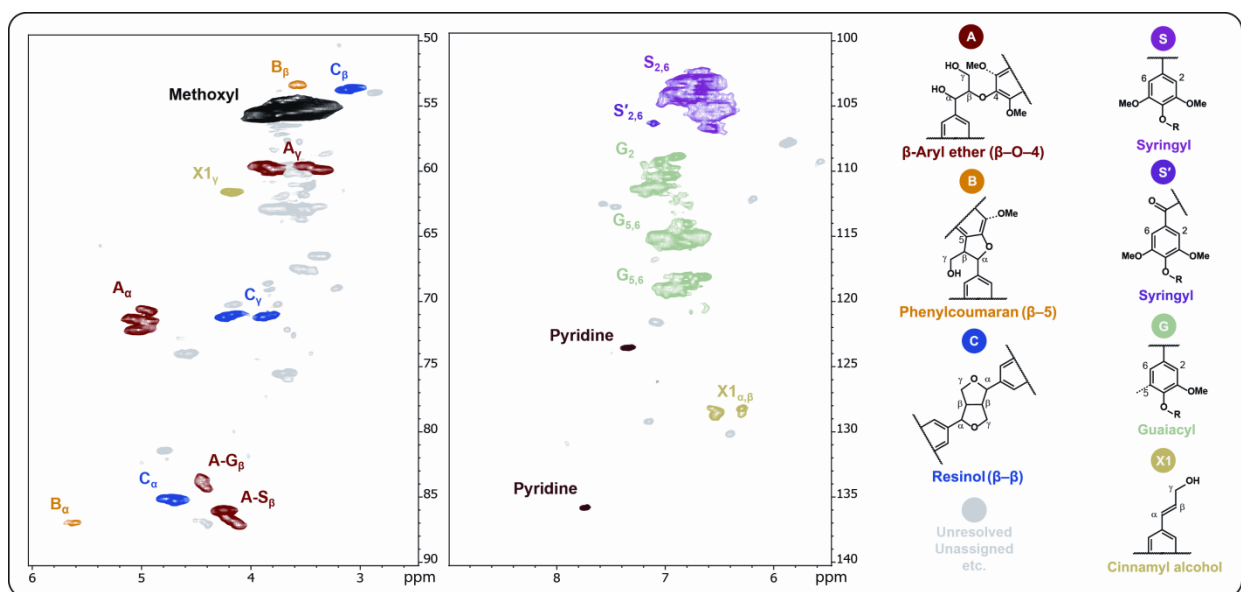


Figure 3.1. 2D  $^1\text{H}$ - $^{13}\text{C}$  HSQC NMR spectra showing lignin fraction SLRP-1 composition and linkages. The contours in aliphatic region (left) are used to quantify the fraction of inter-unit linkages, while those in the aromatic region (right) are used for S/G ratios.

Next, we investigated the amount of phenolic and aliphatic hydroxyl groups by application of  $^1\text{H}$ -NMR of the acetylated lignin fractions. The results indicated that the amounts of aliphatic hydroxyl groups remain nearly constant across all fractions with the exception of the pH 2 fraction (Figure B2). The amount of phenolic hydroxyl groups, on the other hand, demonstrated a clear trend in which higher pH fractions, especially the SLRP fractions, had a lower content of phenolic

hydroxyl groups. We have previously identified this same trend in SLRP-fractionated lignins derived from a softwood Kraft black liquor.<sup>242</sup> Lastly, the results from GPC for molecular weight also demonstrated a trend across the fractions with the high-pH fractions exhibiting the highest molecular weights (Figure B3).

In summary, we identified trends in almost all properties of lignin except aliphatic hydroxyl group. Higher values for  $\beta$ -O-4 content, S/G ratios, and molecular weight were observed in higher pH fractions with the effect more pronounced in SLRP fractions. The phenolic hydroxyl group showed an opposite trend where its amount is lower in higher pH fraction and increases as pH fraction decreases. Apart from S/G ratios, these trends from the hardwood used in this study are similar to those reported earlier from softwood by Stoklosa et al.<sup>245</sup>

### **3.6 Trends in Monomer Yields from Depolymerization of Fractionated Lignins**

As it was shown that there are trends in structural features corresponding to precipitated pH, this section aims to investigate how the difference in these features affects their susceptibility to depolymerization. This was examined by quantifying yields of monomers generated from lignin following depolymerization utilizing three different conversion chemistries. These included catalytic oxidation utilizing molecular oxygen and a homogeneous copper catalyst under alkaline conditions and elevated temperature. This approach is comparable to what has been employed commercially in the past to produce vanillin from liginosulfonates.<sup>260</sup> The second approach employed hydrogenolysis using ethanol as both a solvent and a hydrogen source catalyzed by Ni on an inert support at elevated temperature and pressure. The third approach employed quantitative thioacidolysis. Although each approach shows different monomer-product distributions, we chose to focus on the total yields (Figure 3.2). Similar to the lignin properties across the different fractions, clear trends were observed for monomer yields following depolymerization. We must

stress that the yields, by necessity, must be based on the total content of lignin. There is not a clear consensus on how aromatic monomer yields from lignin should be defined, especially lignin that has been chemically modified where its composition may be altered beyond definition of lignin.<sup>261</sup> Therefore in order to be consistent, the present study has reported all yields from these reactions on a basis of Klason lignin, which does not consider acid-soluble lignin and may contain contaminants such as proteins.<sup>262</sup>

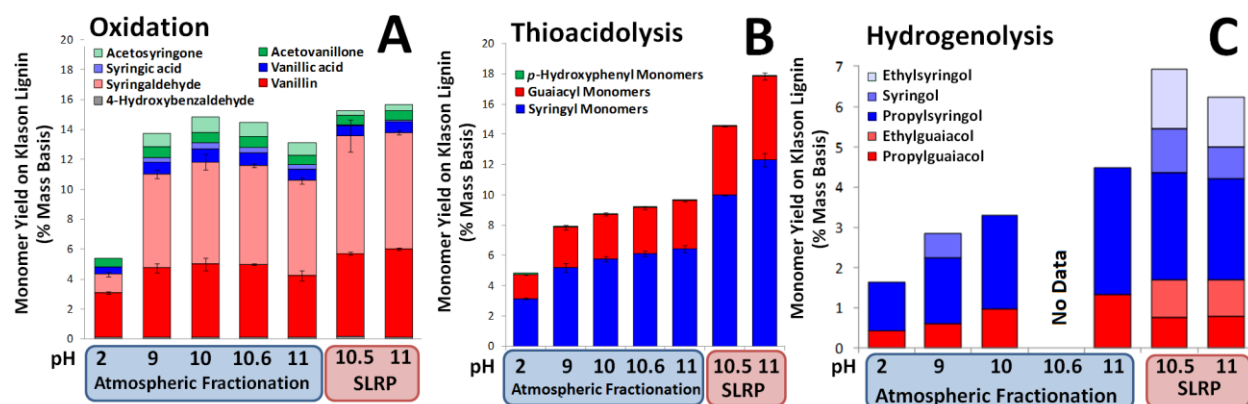


Figure 3.2. Trends in monomer yields from different depolymerization techniques, including (A) Cu-catalyzed oxidation, (B) quantitative thioacidolysis, and (C) Ni/C-catalyzed hydrogenolysis.

Prior to performing oxidation on the different lignin fractions, a kinetic study of monomer yields and selectivities was performed on SLRP-2 (Figure B4) in order to determine optimal reaction conditions since oxidation products have been reported to repolymerize under these conditions.<sup>263</sup> Although optimal yields may differ from fraction to fraction, the optimal yields for sample SLRP-2 were obtained at 7 min which was chosen as the reaction time used for all other pH fractions. The results show that monomer yields from oxidation generally increased as the recovery pH increased (Figure 3.2A). It should be noted that previous work using alkali poplar lignins for Cu-catalyzed oxidation were able to achieve yields of around 10%, which is roughly an average of all the RT samples combined.<sup>213</sup> The differences in yields were not apparent, especially in fractions recovered at higher pH. There was also a discrepancy in sample RT-1 and RT-2, which

fell out of trend. The ambiguity in trends is likely due to the intrinsic mechanism of oxidative cleavage in alkali solution, wherein depolymerization and condensation reactions share similar intermediates.<sup>264</sup> Moreover, the desired product itself, vanillin, was previously shown to be able to condense to form dimers.<sup>263</sup> The concurrence of these reactions makes the trend of lignin-monomer yields through oxidation not as obvious as we would expect compared to the trend from quantified properties.

We next employed quantitative thioacidolysis to assess the yields across the lignin fractions. Thioacidolysis cleaves exclusively ether linkages within lignin and yields stable products. The results from quantitative thioacidolysis show a clear trend whereby fractions recovered at higher pH demonstrated higher yields (Figure 3.2B). Similar to the trends observed for lignin properties, the results from the SLRP fractions are particularly notable when compared to the fractions recovered at ambient temperatures and pressures. Additionally, lower yields were observed for these fractions than were obtained from oxidation, which may be attributed to the less selective nature of oxidation reaction, which was shown to also cleave certain C-C linkages, in addition to ether linkages in presence of  $\text{Cu}^{2+}$  or other catalysts to yield aldehydes and ketones.<sup>214,215,265</sup> The results were not entirely unexpected as both  $^{13}\text{C}$ -NMR and HSQC NMR show that higher pH fractions contain more  $\beta$ -O-4 linkages, which is the target for thioacidolysis. However, the monomer yields have demonstrated how differences in  $\beta$ -O-4 content affect lignin depolymerization. From Figure 3.2B a five-fold difference in yields can be observed between the two extreme fractions that correspond to a two-fold difference in  $\beta$ -O-4. The topic of how  $\beta$ -O-4 content can be related to these depolymerization yields will be investigated in subsequent sections.

Lastly, the lignin fractions were screened for monomer yield by hydrogenolysis catalyzed by carbon-supported Ni. This approach has been used in many recent studies<sup>37,226,230,266</sup> as it has

been demonstrated to produce high monomer yields (>40%) with excellent selectivity.<sup>267</sup> It was also shown by HSQC NMR to selectively cleave only ether linkages at a reaction temperature of 200 °C in ethanol.<sup>227</sup> When subjected to hydrogenolysis the fractionated alkali lignins, however, showed that the highest yield achieved was 7% (Figure 3.2C). Unlike the approach using oxidation, the monomer products are stable under the conditions used for hydrolysis and a clear trend can be observed within the fractions from alkali-pretreated lignin. The samples from higher pH fractions, particularly SLRP, produced more monomers.

We have shown that lignin properties have a strong impact on its susceptibility toward cleavage of ether linkages. Particularly, the trends are clear in thioacidolysis and hydrogenolysis as it was not complicated by other side reactions that may have occurred during oxidation. Nonetheless, general trends from any of the depolymerization techniques point toward higher monomer generations in the fractions recovered at higher pH, notably in the SLRP fractions, with significant gaps as high as four times the yield from thioacidolysis between the highest pH SLRP fractions and the lowest pH atmospheric fraction. Therefore, lignin properties can greatly affect the outcome of depolymerization reactions.

### **3.7 Correlating Lignin Properties and Monomer Yields for Fractionated Alkali Lignins**

Several obvious trends were identified among the fractionated alkali lignins, namely that properties of lignin co-vary and that these properties can be linked to the potential for generation of aromatic monomers from lignin. In this section, these results are correlated in order to gain deeper insight into how these trends are connected. The trends among almost all properties from the previous section imply that the properties of lignin, even after the alkali pretreatment, were still fundamentally related. Correlations among some of the quantified properties, as summarized by the Pearson's Correlation Coefficient (R), are presented in Figure 3.3. This shows that a number

of strong correlations can be observed between many properties. Importantly, S/G ratios, molecular weight, phenolic hydroxyl groups, and  $\beta$ -O-4 content, were all found to have R values of greater than 0.95, with the exception of the correlation between S/G and  $\beta$ -O-4 content, which is still above 0.9. It has been shown that in native lignin, S/G ratios are correlated with  $\beta$ -O-4 content as high S/G ratios result in more  $\beta$ -O-4 linkages as the extra methoxyl group in syringyl monomers prevents formation of C-C linkages at the 5-C position during lignin biosynthesis.<sup>235</sup> In our pretreated lignin fractions, this same correlation still exists.

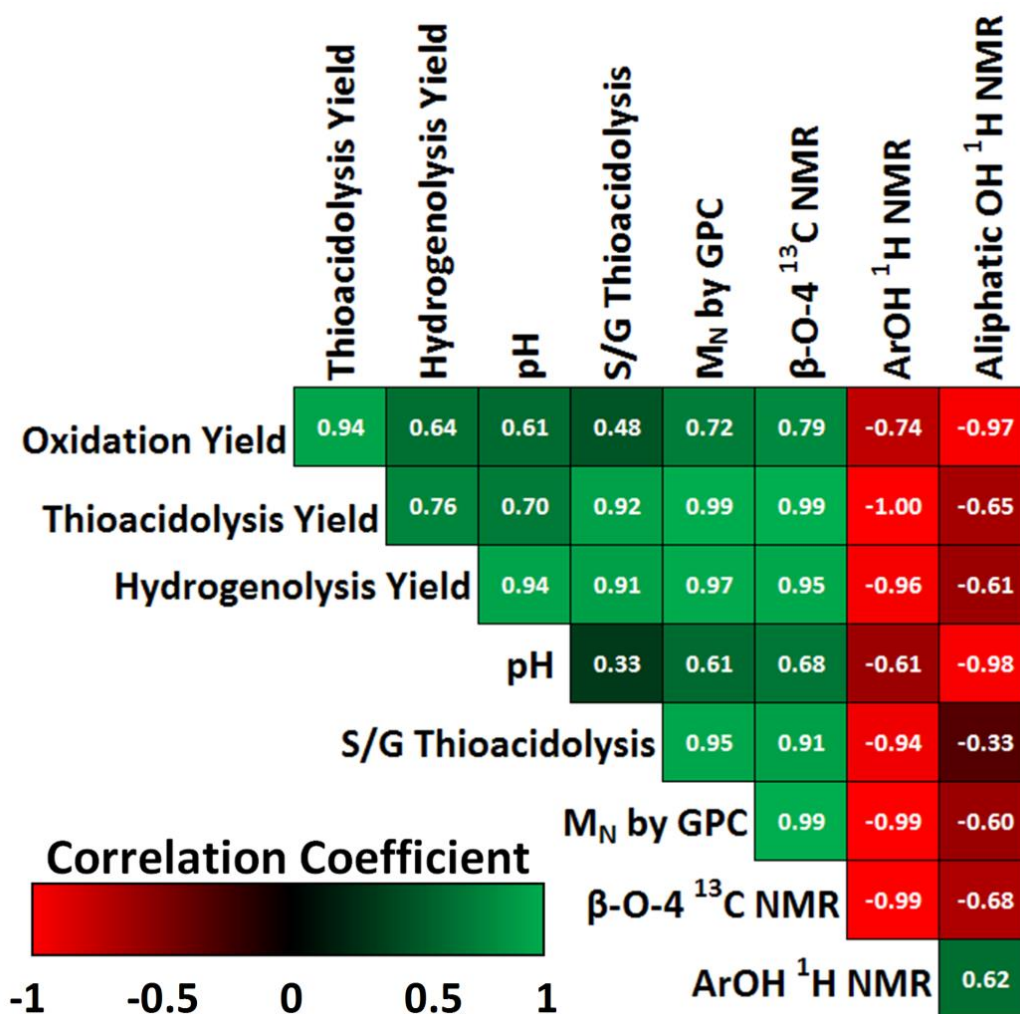


Figure 3.3. Correlation map for fractionated alkali lignin properties and monomer yields demonstrating strong correlations between most lignin properties and its susceptibility to depolymerization *via*  $\beta$ -O-4 cleavage.

Given that the original native lignin possesses the highest  $\beta$ -O-4 content and that during pretreatment these linkages are broken, the fractions depleted in  $\beta$ -O-4 content signify more cleavage and are correlated to lower molecular weight. Cleavage of the  $\beta$ -O-4 linkages then result in the formation of new phenolic hydroxyl groups giving negative correlations between phenolic hydroxyl groups,  $\beta$ -O-4 linkages, and molecular weight (Figure 3.4A). The difference in the amount of phenolic hydroxyl groups is likely the factor that allows fractionation based on pH in this study to be possible because in alkaline solutions one of the factors that promotes lignin solubility is the deprotonation of phenolic hydroxyl groups.<sup>268</sup>

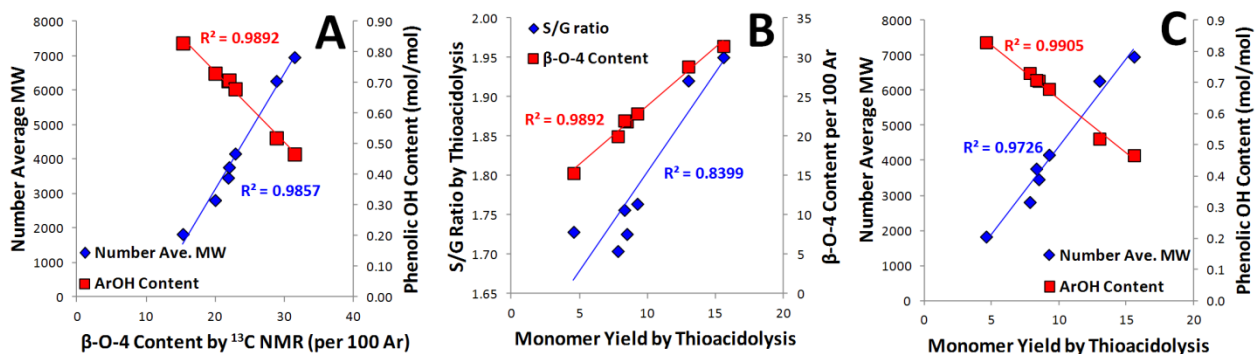


Figure 3.4. Selected linear correlation between fractionated lignin properties and monomer yields, demonstrating that (A)  $\beta$ -O-4 content is directly correlated to molecular weight and inversely correlated to phenolic hydroxyl content, that (B) monomer yields from thioacidolysis (g/g) were associated to lignin's S/G ratios and  $\beta$ -O-4 contents, and that (C) as well as molecular weight and phenolic hydroxyl contents.

Similar to the trends observed among the lignin properties, trends can be observed across these lignin fractions subjected to depolymerization with different techniques. Monomer yields from thioacidolysis and hydrogenolysis exhibited strong correlations to a number of lignin properties, while oxidation yields were much less strongly correlated (Figure 3.3). Specifically, thioacidolysis yields showed a linear correlation for many of the lignin properties (Figure 3.4B & C). However, it should be noted that this linearity could be the result of the small range of  $\beta$ -O-4 content inherent in processed lignin. It may not be extrapolated to a wider range of  $\beta$ -O-4 content

as will be shown in later sections. Nonetheless, the results indicate that the diverse structural properties of the lignin are fundamentally correlated and affect the depolymerization reaction accordingly. Consequently, a single property can be used as a descriptor of lignin susceptibility to depolymerization.

### 3.8 Prediction of Monomer Yields from $\beta$ -O-4 Content

We have established that lignin properties, even after the alkaline pretreatment performed in this work, are still fundamentally inter-dependent and they also correlate well with the yield of monomers generated by three different catalytic depolymerization chemistries. This section aims to further analyze the effect of lignin properties beyond just correlation. We aim to validate a generalizable prediction model based on a quantifiable lignin property. This would yield a tool to assess the potential of lignin to yield aromatic monomers. Since most of these properties are related, this implies that a single property can be selected to represent the other properties, and serve as a descriptor for the depolymerization of lignin utilizing approaches that target inter-unit ether linkages. To do so, we chose the amount of  $\beta$ -O-4 content as a property to predict lignin susceptibility to depolymerization, *i.e.* maximum possible yields, because it is relatively easy to establish a rationale for the predicting formula.

For a monomer to be generated from the cleavage of  $\beta$ -O-4 linkages, a unit in a triad as shown in Figure 3.5 must either have two adjacent  $\beta$ -O-4 linkages or be at the chain end connected by a  $\beta$ -O-4 linkage. For example, if  $m_2$  in Figure 3.5 were to become a monomer, both  $d_1$  and  $d_2$  must be  $\beta$ -O-4 linkages because otherwise a dimer or oligomer would be generated instead if one of the connecting linkages was a C-C bond. Likewise, for a monomer to be generated from  $m_1$ ,  $d_1$  must be an ether linkage. As a lignin polymer is assumed to be synthesized by the free radical mediated oxidative polymerization mechanism, the distribution of linkages throughout the

polymer can be assumed to be random. Therefore, the quantified content of a lignin property, such as  $\beta$ -O-4 content, can be considered to represent the probability that linkage within the polymer is a  $\beta$ -O-4. With this assumption, the prior rationale can be applied to yield an expression predicting the probability that any monomer within the lignin polymer can be released by cleaving a  $\beta$ -O-4 bond as:

$$P(A \cap B) = P(A) P(B) \quad \text{Eqn. (3.1)}$$

where  $P(A)$  is the probability of a  $\beta$ -O-4 linkage existing on one end of a triad and  $P(B)$  is the probability of a  $\beta$ -O-4 linkage occurring at the other end of the triad. Likewise, the probability that a monomer will be released from a polymer chain end can be considered as  $P(C)$ , represents the probability of a  $\beta$ -O-4 linkage occurring as the terminal linkage at the end of a polymer chain. This methodology is based on the simplification that lignin is a linear polymer without branches or crosslinks between polymers. Recent work has provided evidence that at least some native lignins may be primarily linear oligomers.<sup>269,270</sup> Based on this rationale and assuming that any of the monomer-yielding events are mutually exclusive, the monomer yield can be estimated based on the expected values of  $\beta$ -O-4 content, which is:

$$E[\text{Yield}] = \frac{1}{n} \sum_{i=1}^{n-2} E[P(A_i)P(B_i)] + \sum_{i=1}^2 E[P(C_i)] \quad \text{Eqn. (3.2)}$$

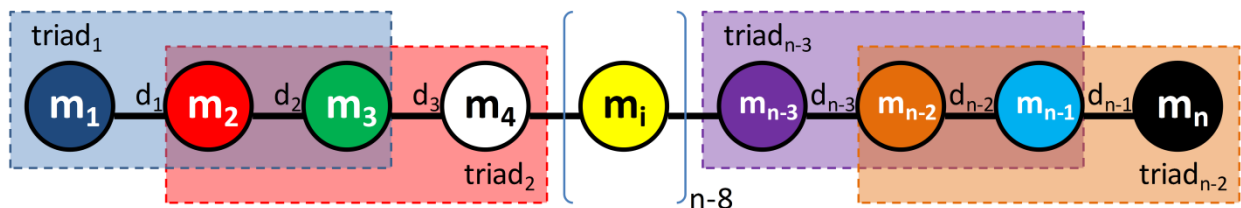


Figure 3.5. Lignin chain model of chain length  $n$  used for formulating prediction rationale. The  $i^{\text{th}}$  monomer unit,  $n^{\text{th}}$  linkages of lignin are represented by  $m_i$  and  $d_n$ . A triad is composed of three monomer units.

Assuming the  $\beta$ -O-4 content is randomly distributed throughout the polymer chain (i.e., the probabilities that any bond is a  $\beta$ -O-4 bond are equal), this expression simplifies to:

$$E[\text{Yield}] = \frac{(n-2) \times (\beta\text{-O-4 Content})^2}{n} + \frac{2 \times (\beta\text{-O-4 Content})}{n} \quad \text{Eqn. (3.3)}$$

where  $n$  is the number of monomers within the chain. The general form of this same equation has been previously derived for predicting distributions of polymer depolymerization products by Montroll and Simha in 1940.<sup>271</sup> For the case where the lignin chain is very long (i.e.,  $n \gg 100$ ), Eqn. 3.3 can also be truncated to:

$$E[\text{Yield}] = (\beta\text{-O-4 Content})^2 \quad \text{Eqn. (3.4)}$$

This simplified model relating  $\beta$ -O-4 content to monomer yields was first proposed in the work of Yan et al.<sup>267</sup>

Based on Eqn. 3.3, the predicted trends for monomer yield versus  $\beta$ -O-4 content for a lignin with a chain length of 100 and 25 units with the  $\beta$ -O-4 content exhibiting a Gaussian distribution were generated (Figure 3.6). It can be observed that the trends do not vary significantly within this window of chain length indicating that the difference in number of end units is still relatively insignificant.<sup>272</sup> In Figure 3.6, the red circles represent thioacidolysis yields from different alkali-pretreated fractions. These yields followed the predicted trend very well, where twice the amount of  $\beta$ -O-4 content in the fraction SLRP-1 produced almost three times the monomer amount compared to RT-5. However, the range of  $\beta$ -O-4 content within these fractions are still limited. Therefore, a lignin from dioxane extraction was generated with a 38% extraction yield. Application of <sup>13</sup>C-NMR and quantitative thioacidolysis to this lignin showed a  $\beta$ -O-4 content of 65% and 38% monomer yield (Figure 3.6, green square). The results conformed to the predicted trend as well as

asserting the importance of obtaining a lignin enriched in  $\beta$ -O-4 content if the goal is to generate high monomer yields.

Theoretically, if the  $\beta$ -O-4 content is reduced during alkali pretreatment, this should not cause its thioacidolysis yields to be inferior to those from extracted lignin as the loss in ether linkages would be compensated by an increase in end-chain units. However, the fact that the monomer yields from alkali lignin fractions are significantly lower could be derived from two factors. Namely, the potential formation of C-C bonds by condensation reactions during the pretreatment, and, second, that  $\beta$ -O-4 units cleaved during pretreatment yield monomers and short chain oligomers that were not recovered during lignin recovery by pH fractionation.

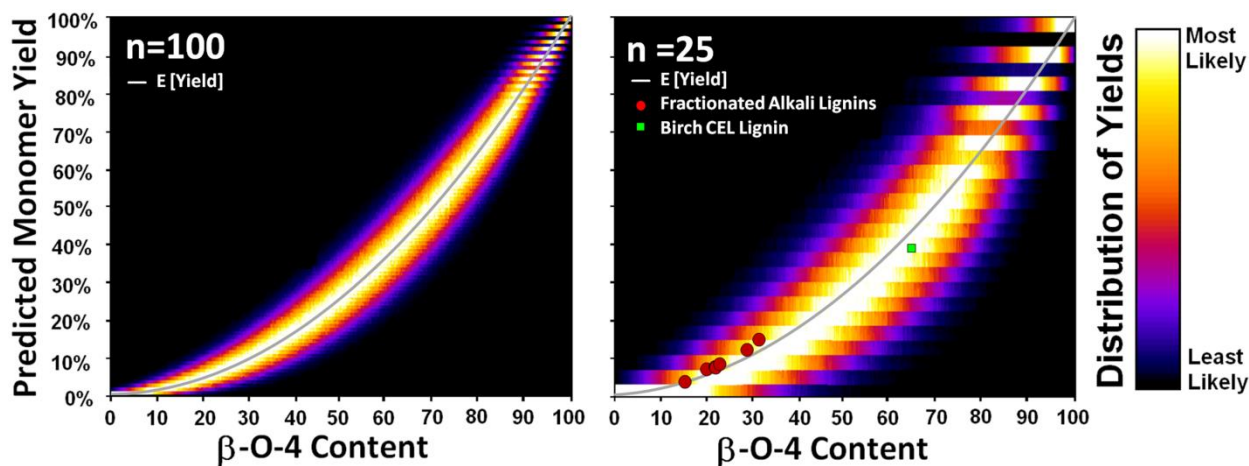


Figure 3.6. Predicted monomer yields as a function of  $\beta$ -O-4 content for lignin polymer populations of chain length of 100 monomers (left) and 25 monomers (right) with results from quantitative thioacidolysis of fractionated poplar lignin and native birch biomass included for validation.

A closer look to the prediction results further emphasizes the significance of the quality of lignin. With lower  $\beta$ -O-4 contents in the pretreated biomass, regardless of reaction optimization or catalyst selection, high monomer yields are not achievable from these lignins. The correlation in Eqn. 3.4 not only explains the low yields from the alkali lignin fractions in this study, it also provides justification for performing lignin depolymerization prior to significant lignin

modification. For example, certain studies employed catalytic reductive cleavage of lignin using whole biomass as a substrate with the reaction conditions and solvents chosen to limit undesirable condensation reactions.<sup>273,274</sup> With high quality lignin substrate and limited condensation, yields have been demonstrated in the range 20-50% from a variety of catalysts and biomass sources for  $\beta$ -O-4 contents that were expected to range from 50–70%,<sup>226,266,275,276</sup> while a high-syringyl content transgenic poplar containing primarily  $\beta$ -O-4 bonds could achieve monomer yields as high as 78% monomers.<sup>277</sup> Likewise, high monomer yields were also observed in oxidative cleavage approaches that used isolated lignin and mild reaction conditions.<sup>30</sup> Therefore, from the predicted results and mentioned examples, it was clear that lignin quality was crucial for achieving high monomer yields. This can be contrasted to the hydrogenolysis yields obtained from alkali hardwood lignin in this study, which used similar reaction conditions (Figure 3.2).

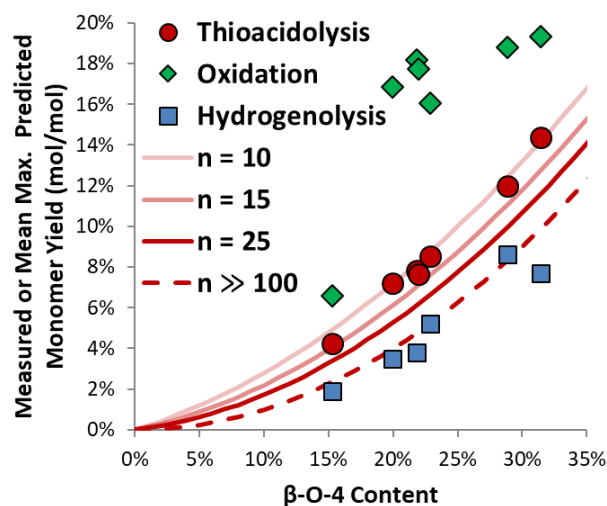


Figure 3.7. Model predictions of monomer yields from lignin polymer populations of different chain lengths versus monomer yields from thioacidolysis, oxidation, and hydrogenolysis of fractionated lignin.

Monomer yields of pretreatment-derived lignins from oxidation and hydrogenolysis are also plotted against the prediction model (Figure 3.7) and show that unlike the yields from thioacidolysis that show good agreement with the model prediction, the yields from the oxidation

reaction do not. As the model prediction is based solely on the cleavage of  $\beta$ -O-4 bonds, this discrepancy can be hypothesized to be due to the less selective nature of the oxidation reaction as well as potentially condensation of the monomer products. The yields for hydrogenolysis, on the other hand, seem to follow the trend. This should be expected as previous work has shown that only peaks corresponding to ether regions on HSQC NMR disappear after the hydrogenolysis reaction. Moreover, a hydrogenolysis reaction conducted on  $\beta$ -5 dimer did not produce any monomers.<sup>227</sup> However, it can be seen in Figure 3.7 that although the trend follows the prediction line, the values are lower than what is predicted for thioacidolysis. This could be due to a number of factors such as incomplete conversion for the reaction time used, or incomplete solubilization of the pretreatment-derived lignins in the solvent. Either of these assertions is supported by the finding that a considerable amount of lignin residue remained after the reaction; however, accurate measurement of the leftover residue was prohibited due to limited amount of available samples.

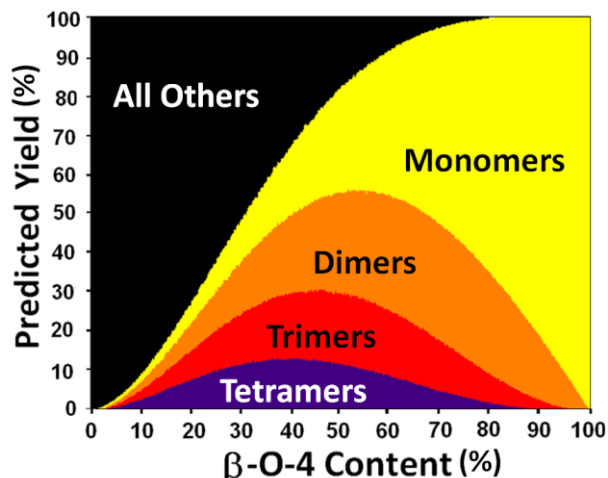


Figure 3.8. Predicted yield distributions for monomers, dimers, and oligomers from the cleavage of  $\beta$ -O-4 in a population model of lignin polymers of  $n = 100$  over a range of  $\beta$ -O-4 contents.

Besides monomer yields, this approach can be extended to predict the yield of oligomeric products by employing a similar rationale to that used for monomer generation. As an example, to

yield a dimer, three monomers must be linked by two non-adjacent  $\beta$ -O-4 linkages. These results, as shown in Figure 3.8 presented as cumulative yields, show that for a  $\beta$ -O-4 content of 50%, cleavage of all  $\beta$ -O-4 linkages would be predicted to yield approximately 10% tetramers, 17% trimers, 25% dimers, 27% monomers, and 21% all other oligomeric products. From this plot it can be observed that as  $\beta$ -O-4 content increases above ca. 55%, the yield of monomers dominates over other oligomeric products (Figure 3.8). Again, this emphasizes the importance of enhancing and preserving  $\beta$ -O-4 content of lignin, preferably above 55% or more, if high monomer yields are the goal. In fact, recent studies tried to achieve this through so called lignin-first biomass pretreatment and isolation processes.<sup>33,278,279</sup>

### 3.9 Conclusion

The present work has demonstrated through characterization of hardwood lignins generated by pH-based fractionation of alkaline pretreatment liquors that many lignin properties exhibited strong correlations with each other. Specifically, lignin fractions with higher S/G ratios were found to have higher  $\beta$ -O-4 contents and molecular weights with lower phenolic hydroxyl contents. More importantly, the differences in these properties among fractions, specifically  $\beta$ -O-4 content, were shown to greatly impact the achievable monomer yields through three different lignin depolymerization approaches. Furthermore, a model was developed to explain the correlation between  $\beta$ -O-4 content and monomer yield. The prediction model was validated experimentally by  $^{13}\text{C}$ -NMR quantified  $\beta$ -O-4 content and quantitative thioacidolysis yields from the fractionated lignins as well as “native” extracted hardwood lignin. As the model predicts that the maximum achievable yield is the  $\beta$ -O-4 content squared, it highlights the importance of preserving high  $\beta$ -O-4 contents in the lignins during pretreatment or isolation.

## **CHAPTER 4 Adsorption of the Yield Determining Lignin Dimer on Catalyst Surfaces**

### **4.1 Summary**

Lignin hydrogenolysis has recently been studied extensively as it was shown to result in high monomer yields. Most of these reactions were conducted in the liquid solvent, which has been shown to have large impacts on product types and yields. Since adsorption is the first step to any heterogeneous catalyst reactions, this work aims to understand how solvent affects lignin adsorption on Ni(111) and Cu(111) surfaces. To achieve so, density functional theory (DFT) calculations were employed to investigate  $\beta$ -O-4 lignin dimer (a model compound) adsorption conformations in both vacuum and liquid ethanol. In the vacuum, it was found that lignin prefers to adsorb strongly on Ni(111) and weakly on Cu(111) with both aromatic rings parallel to the surface. Solvated adsorption was modeled using both implicit and explicit models. It was found that an explicit model is required to accurately describe the lignin-solvent interactions. With the explicit solvation model, it was found that lignin dimer adsorbs on Ni(111) surface but not on Cu(111). Furthermore, to circumvent the expensive liquid interface calculations, a thermodynamic cycle method was developed to quickly estimate the solvated lignin dimer adsorption energy from the adsorption energy in a vacuum and the solvation energies. This model quantifies the effects from solvent on lignin dimer adsorption, including the contributions from the lignin-solvent and the solvent-metals interactions, and suggests how to design catalyst and solvent to tune lignin adsorption.

## 4.2 Introduction

Lignin is an aromatic polymer that can comprise a significant fraction of the mass (up to 30%) of lignocellulosic biomass,<sup>13</sup> but is currently underutilized. Its valorization is important for the economic feasibility of lignocellulosic biorefineries. Lignin is composed of primarily of 2 types of aromatic moieties syringyl (S) and guaiacyl (G), that differ in the number of methoxyl substitutions on the aromatic ring. These monomers are linked by various types of C-O and C-C bonds<sup>280</sup> with the  $\beta$ -aryl ether linkage (*i.e.*, the  $\beta$ -O-4 linkage) comprising the most abundant type of linkage at 50-80% of the inter-unit linkages in native lignins.<sup>279</sup> Lignin depolymerization to aromatic monomers and low molar mass oligomers is one route to generate renewable aromatic chemicals from lignin. Many approaches targeting the  $\beta$ -O-4 linkage offer the potential for achieving high yields and selectivities for a limited set of aromatic monomers.<sup>5,19,281</sup> Lignin hydrogenolysis and partial hydrodeoxygenation is one of these promising approaches to lignin depolymerization and has been reported using diverse catalysts such as NiAu,<sup>223</sup> Ni/C,<sup>226</sup> or Pd/C<sup>225</sup> in solvents that include short chain alcohols, dioxane, or alkali water.<sup>225,233,282,283</sup> As will be discussed in more detail, the selection of solvent was shown to have significant impacts on products yields and selectivities. However, how these solvents affect the lignin-metal interactions at the catalyst surface is still not well-understood. In fact, theoretical studies on how lignin model compounds (*e.g.*, a  $\beta$ -O-4 lignin dimer) are adsorbed onto catalyst surfaces, even in the vacuum state, is scarce and still inconclusive. The few existing studies only briefly explore the potential range of adsorption conformations considering the high degree of freedom in lignin's structure.<sup>31,44</sup> More importantly, it has been reported that different isomers of the model yielded different adsorption conformations on the Ni surface, which subsequently lead to different reaction pathways.<sup>44</sup> This stresses the significance of adsorption conformation as it is the first step in any

reaction. Therefore, this study aims to clarify how lignin adsorbs on metal surfaces and to characterize the impact of solvent on this adsorption.

Experimentally, the choice of solvent, among others, has been shown to significantly impact hydrogenolysis product selectivities and yields. One study assessed various solvents using Raney Ni as a catalyst and demonstrated that in a presence of H<sub>2</sub> gas, aprotic non-polar solvents, such as decalin and n-heptane, gave the highest yields at low temperature (90 °C); however, at high temperature (300 °C), alcohol solvents demonstrated comparable performance while also exhibiting high selectivity.<sup>40</sup> Furthermore, studies also point out that ethanol could give higher yields than methanol as it can act as a capping agent by alkylation and esterification with lignin's phenolic hydroxyl group, essentially limiting repolymerization.<sup>28,274</sup> Given this knowledge, it is not uncommon to encounter studies in literature where similar reaction conditions and catalysts were used, except for solvent choice, but different products and selectivities between products were obtained. On Ni/C, studies using dioxane as a solvent resulted in phenolic monomers with hydroxylated propyl side chains (*i.e.*, dihydrosinapyl and dihydroconiferyl alcohol),<sup>32,284</sup> whereas others using methanol as a solvent reported higher selectivities for products with deoxygenated side chains (*i.e.*, 4-propylsyringol and 4-propylguaiacol).<sup>226,285</sup> These are in agreement to a recent study suggesting that methanol can limit the product defunctionalization when compared to other alcohol solvents.<sup>34</sup> The effect was claimed to be due to the stronger chemisorption of methanol on the Ni surface. For other catalysts, such as Pd/C, a similar case can be found when comparing pure methanol versus methanol mixed with water as the solvent.<sup>35,36</sup> All of these examples strongly suggest the important role played by the solvent on the reaction pathway followed. However, the understanding of solvent impacts at surfaces, which could improve the process of catalyst and solvent selection, is still very limited. To address this shortcoming, density functional theory

(DFT) calculation is selected as the tool because, in addition to providing insights into adsorption energetics, it can yield insights into molecular geometry. In the present work, the  $\beta$ -O-4 bond within lignin is selected as the key feature of the model system as it is the prime target for hydrogenolysis and previous studies have shown it to be the primary yield-determining property in lignin.<sup>286</sup>

Computational methods have been used in the past to evaluate the impact of solvents on lignin solubility and conformation. In an ionic liquid, charge analysis also showed that dissolution of lignin dimer is facilitated primarily by H-bond interaction and  $\pi$ -stacking interactions.<sup>287,288</sup> For H-bonds, anions were found to have the strongest interaction at the  $\alpha$ -OH position of the dimer, while cations had the strongest interaction at the  $\gamma$ -OH position, whereas the cation contributed more to  $\pi$ -stacking interactions. The strength of the interaction could lead to changes in the structure of lignin. This was studied in detail for an aqueous solution using classical molecular dynamics (MD), where polymeric lignin was shown to form a compact globular structure minimizing the exposure of the surface to the solvent due to its natural hydrophobic interactions.<sup>282,289</sup> However, it was found that the structure exhibited more open conformations with increased temperature.<sup>290</sup> Interestingly, using DFT calculations combined with an implicit solvation model, such as the conductor-like screening model (COSMO)<sup>121</sup> to represent alkali water, it was found that the compact globular structure of lignin could also be opened up by oxidation of benzylic alcohol to form ketone.<sup>282</sup> The more open, accessible structure of the polymeric lignin was speculated to be the reason for higher monomer yields from oxidized lignin relative to natural lignin. This example demonstrates the importance of understanding the interfacial behavior of lignin.

To address the limited understanding of the adsorption behavior of model lignins on surfaces, particularly when the solvent is involved, the present work will conduct a thorough study of lignin *erythro* and *threo*  $\beta$ -O-4 dimer adsorption on metals in both vacuum and liquid environments. The goals of the study are to identify the most likely stable adsorption of lignin dimers and to identify the relationship between gas phase and liquid phase adsorption. Ultimately, we hope that the relationship can be leveraged for a quick estimation of adsorption energy in the solvated state. The selected metal surfaces are Ni(111) and Cu(111) to represent metals with strong and weak adsorptions. The solvent selected for the explicit model is ethanol as it is commonly used in hydrogenolysis reactions.<sup>28,226</sup> Particularly, the solvent will be modeled at a density corresponding to the temperature of 50 °C to accommodate experiments at low temperatures,<sup>222,291,292</sup> and therefore, the interactions at higher temperatures should lie between this and the simulation results for in a vacuum.

Selecting an appropriate  $\beta$ -O-4 dimer is important. Previous theoretical studies employed dimers with various functionalities included or neglected as representative of  $\beta$ -O-4 linkages within a lignin polymer. Lignin dimers composed of all functional groups present in the polymer are known to have a bond dissociation energy in a range of 2.6 to 3.0 eV.<sup>293</sup> However, simplifying the dimer model by eliminating either the phenolic hydroxyl or the aliphatic hydroxymethyl group can affect the bond breaking energy by approximately 10%, while the effect from methoxyl group could be negligible.<sup>294,295</sup> Considering that these functional groups can also affect adsorption geometries, the present study will use guaiacylglycerol-beta-guaiacyl ether as a representative  $\beta$ -O-4 dimer as it contains all functional groups an actual lignin polymer would have as well as allowing us to study the effect of lignin side chain chirality.

To achieve the aforementioned goals, the present manuscript will 1) validate the computational setup and suitability of the chosen lignin dimer as representative of polymeric lignin, 2) identify lignin's most stable adsorption conformation in the gas phase, 3) demonstrate the effects of solvation on adsorption, and 4) derive and validate the relationship between gas phase and liquid phase adsorption.

## 4.3 Computational Methods

### 4.3.1 Adsorption of Lignin Dimer and Monomers from DFT Calculations

Calculations of dimer adsorption in this study were performed through the implementation of plane wave DFT in Vienna *Ab Initio* Simulation Package (VASP). The exchange correlations were treated within the generalized gradient approximation (GGA) by Perdew-Burke-Ernzerhof (PBE) functional.<sup>161</sup> Projector augmented wave (PAW) potentials were used to represent the effective core radii.<sup>163</sup> The electronic optimization was achieved self-consistently with a cutoff energy of 500 eV. The electronic energy convergence was set at  $10^{-4}$  eV due to convergence difficulty of the surface when included van der Waals, the same criteria were used in previous studies with results validated with experimental data.<sup>48</sup> The convergence for forces during structural relaxation is set at  $0.03 \text{ eV}\text{\AA}^{-1}$ . A Monkhorst-Pack grid with  $14 \times 14 \times 1$  k-point sampling per  $(1 \times 1)$  cell was used for the calculation. A spin-polarized calculation was performed with dipole moment correction along the perpendicular direction. Methfessel-Paxton smearing was employed with a sigma of 0.20. The effect of van der Waals interaction was accounted for by introducing either correction coefficients from Grimme's method (DFT-D3)<sup>296,297</sup> or a non-local correlation functional through optB88-vdW.<sup>298,299</sup> The computed bulk lattice constants for Cu and Ni as relaxed by PBE functional with optB88-vdW are 3.635, 3.517 Å, respectively.

The  $\beta$ -O-4 model dimer selected for the present study is guaiacylglycerol-beta-guaiacyl ether as it has functionalities and stereochemistry representative of real lignin. The adsorption energy of the dimer in the gas phase ( $\Delta E_{\text{ads}}^g$ ) is calculated with simulation cells in vacuum by:

$$\Delta E_{\text{ads}}^g = E[\text{Metal} \cdots \text{Dimer}] - (E[\text{Metal}] + E[\text{Dimer}]) \quad \text{Eqn. (4.1)}$$

where  $E[\text{Metal} \cdots \text{Dimer}]$ ,  $E[\text{Metal}]$ , and  $E[\text{Dimer}]$  correspond to the energy of a dimer adsorbed on a metal slab, the metal slab only, and the dimer in gas phase. The [Metal] structure refers to a slab model with 4 layers of close-packed Cu(111) or Ni(111) at  $(7 \times 7)$  unit cells with a vacuum of 16 Å on top of the surface. The bottom two layers of the metal slab were constrained in all direction to emulate bulk characteristics. A negative  $\Delta E_{\text{ads}}^g$  denotes a gain in energy of the system (exothermic process).

The adsorption energy in the liquid phase calculated with the implicit model, where the solvent was represented as a homogeneous constant dielectric constant, was implemented with a polarizable continuum model (PCM) developed for VASP (VASPsol) by Mathew *et al.*<sup>300,301</sup> The model incorporates the dielectric screening due to permittivity of the solvent and the electrostatic shielding due to mobile ions in the electrolyte. The adsorption energy is calculated as:

$$\Delta E_{\text{ads}}^l(\text{implicit}) = E[\text{Metal} \cdots \text{Dimer}(\epsilon)] - (E[\text{Metal}(\epsilon)] + E[\text{Dimer}(\epsilon)]) \quad \text{Eqn. (4.2)}$$

where each simulation cell in the calculation was filled with solvent using an appropriate dielectric constant value ( $\epsilon$ ). A  $\epsilon$  of 21.04 was used for ethanol at 50 °C.

The adsorption of a lignin dimer in liquid is also simulated using an explicit solvation model with the adsorption energy from the model calculated as:

$$\Delta E_{\text{ads}}^l(\text{explicit}) = E[\text{Dimer Adsorbed}] - E[\text{Dimer Solvated}] \quad \text{Eqn. (4.3)}$$

where  $E[\text{Dimer Adsorbed}]$  is the energy of a lignin dimer in an adsorbed state on a metal surface with solvent molecules surrounding it (Figure 4.1B) and  $E[\text{Dimer Solvated}]$  is the energy where the dimer is fully solvated in the middle of the solvent slab, away from the metal surface (Figure 4.1A). For both Cu and Ni, 37 molecules of ethanol and a dimer were packed into a  $4152.91 \text{ \AA}^3$  volume (corresponding to  $0.80 \text{ g/cm}^3$ , See Section 2.2 for calculation details) between metal slabs. Noted that the height in z-direction of the metal slab surface ends at a distance corresponds to van der Waals radius of Cu ( $2.09 \text{ \AA}$ ) and Ni ( $1.97 \text{ \AA}$ ) from the atom center position.<sup>302</sup> This corresponds to solution density at a temperature of  $50 \text{ }^\circ\text{C}$ , and lignin dimer concentration of  $0.13 \text{ g/cm}^3$ . The concentration is slightly higher than a typical range of  $0.01$  to  $0.1 \text{ g/cm}^3$  used in lignin depolymerization studies, but is not expected to affect the conclusion.<sup>37,226</sup>

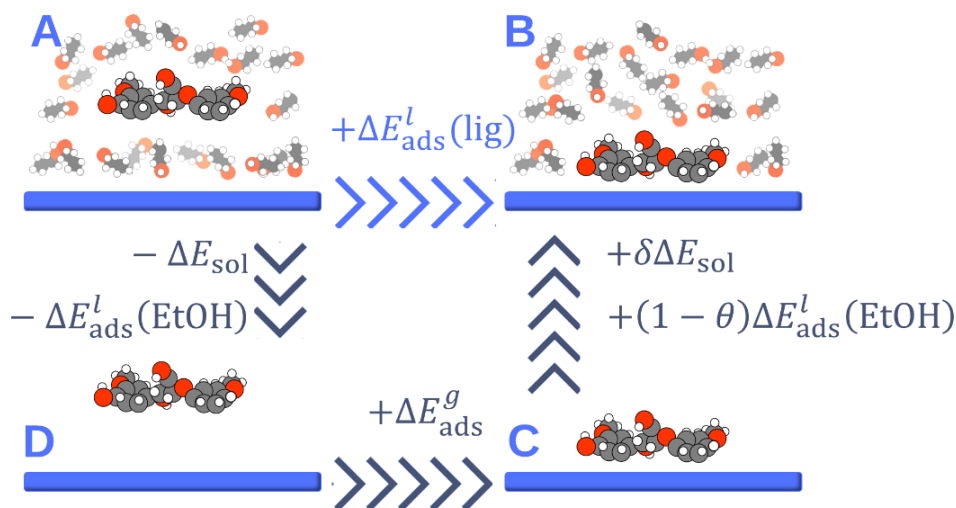


Figure 4.1. Thermodynamic adsorption energy cycle of lignin dimer (lig) in solvated (A and B) with ethanol (EtOH) and vacuum (C and D) state. It should be noted that, by definition, the  $\Delta E_{\text{ads}}^l$  from state A to B is intended to encompass both partial loss in lignin solvation energy and ethanol adsorption energy. The  $\delta$  is fraction of solvation energy retained when dimer adsorbs relative to full solvation. The  $\theta$  is fraction of the surface area covered by adsorbed dimer.

Alternatively, the liquid state adsorption energy could also be calculated using the gas phase adsorption energy and the solvation energy via a thermodynamic cycle shown in Figure 4.1.

Instead of going through pathway A to B as done in Eqn. 4.3, one could go from A to D to C to B to complete the thermodynamic cycle. Therefore, following the energy terms associated with the path, we can define that the liquid state adsorption energy of dimer from a thermodynamic cycle as:

$$\Delta E_{\text{ads}}^l(\text{thermo}) = \Delta E_{\text{ads}}^g - (1 - \delta)\Delta E_{\text{sol}} - \theta\Delta E_{\text{ads}}^l(\text{EtOH}) \quad \text{Eqn. (4.4)}$$

where  $\Delta E_{\text{sol}}$  is the solvation energy of lignin dimer (in EtOH for this study) and  $\Delta E_{\text{ads}}^l(\text{EtOH})$  is the adsorption energy of the bulk solvent on the metal surface. The  $\delta$  term is the estimated fraction (from 0 to 1) of solvation area retained after adsorption in the liquid phase compared to fully solvated in the solvent, which could be approximated in several ways as detailed in Section 3.2b. The  $\theta$  term is the fraction from 0 to 1 of the area of the surface projected on to it by adsorbed lignin dimer (with perimeter drawn by dimer atoms' van der Waals radii) over the entire area of metal surfaces (including the area from the top and bottom of metal surfaces due to periodic boundary condition). The  $\Delta E_{\text{ads}}^{\text{EtOH}}$  is calculated via an explicit interface model as:

$$\Delta E_{\text{ads}}^l(\text{EtOH}) = E[\text{Metal} \cdots \text{EtOH}] - (E[\text{Metal}] + E[\text{EtOH}]) \quad \text{Eqn. (4.5)}$$

where  $E[\text{Metal} \cdots \text{EtOH}]$  is the energy of the cell of 37 ethanol molecules packed into a 3735.55 Å<sup>3</sup> volume (corresponding to 0.76 g/cm<sup>3</sup> (see Section 2.2 for calculation details) between metal slabs with van der Waals radii taken into account,  $E[\text{Metal}]$  is the energy of the metal slab, and  $E[\text{EtOH}]$  is the energy of the ethanol slab by removing metals from  $E[\text{Metal} \cdots \text{EtOH}]$  without further relaxation to retain the same density.

#### 4.3.2 Solvation Energy of Lignin Dimer by DFT Implicit and Explicit Model

The liquid properties are more sensitive to the temperature change than those of solids. Although the DFT models in general ignored the entropy contribution from translation and

rotational modes, to capture the temperature effect on the solvent, the corresponding ethanol density and dielectric constants at the typical experimental temperature were considered for the following calculation setup.

Equation 4.4 requires the knowledge of the solvation energy, therefore it is computed from both implicit and explicit models. For an implicit model, the effect of solvation was simulated using VASPsol with appropriate dielectric constants ( $\epsilon$ ).<sup>303,304</sup> From which, the  $\Delta E_{\text{solv}}$  is obtained from:

$$\Delta E_{\text{solv}} = E[\text{Dimer}(\epsilon)] - E[\text{Dimer}] \quad \text{Eqn. (4.6)}$$

where  $E[\text{Dimer}(\epsilon)]$  is the energy of the dimer in an implicit model with a dielectric constant  $\epsilon$  and  $E[\text{Dimer}]$  is the energy of the dimer in vacuum. For ethanol at 50 °C, the  $\epsilon$  is set to 21.04.<sup>305</sup>

In an explicit model of solvation, the energy is calculated by:

$$\Delta E_{\text{solv}} = E[\text{EtOH} + \text{Dimer}] - (E[\text{EtOH}] + E[\text{Dimer}]) \quad \text{Eqn. (4.7)}$$

where an energy in each term was obtained from averaging DFT relaxed 5 initial structures generated from classical MD ran at 50 °C (Section 2.3). For the ethanol only cell, to achieve an ethanol density of 0.76 g/cm<sup>3</sup> (at 50 °C), 37 molecules of ethanol were packed into a cell volume of 3735.55 Å<sup>3</sup>. For a cell of ethanol with a dimer solute, the cell volume was increased to 4152.91 Å<sup>3</sup> to accommodate for the molar volume of lignin dimer. This approach allows the density of the bulk liquid phase to be kept approximately constant (0.04 g/cm<sup>3</sup> change). Due to the lack of experimental values, the density of the lignin dimer was approximated to be 1.28 g/cm<sup>3</sup> using COMPASS II force field isothermal isobaric ensemble (NPT) MD. The calculation detail and result validations with other similar known density molecules, which show 3-7% error from experiments, can be found at Table C1 in the Appendix C. It is acknowledged that the molar

volume of the dimer in ethanol could change; the molar volume of phenol in water decreases by 7%.<sup>306</sup> Therefore, additional tests for  $\Delta E_{\text{sol}}$  on several molecules were performed to assure sufficiently accurate results (Section 4.5.1).

### 4.3.3 Additional Classical Molecular Dynamics

The liquid structures are all first generated by classical MD methods. The same calculation approach is also used to evaluate the adsorption of a lignin polymer to confirm whether the lignin dimer selected for the present study is representative of polymeric lignin. These classical MD simulations were carried out in the Material Studio software package using the COMPASS II force field (type c3a, c43o, c4o, h1, h1o, o2e, and o2h) commonly used for study of organic polymers.<sup>178,307</sup> The simulation was performed at the required temperature for a duration of 200 ps (100 ps equilibration, 100 ps production) at a time step of 1 fs. Temperature coupling was performed with the Nose algorithm ( $Q = 0.01$ ). An accuracy of  $10^{-4}$  kcal/mol Edwald summation method was used for neighboring electrostatic calculations. The van der Waals interaction switch function was set at a cutoff distance of 15.5 Å.

## 4.4. Development of Computational Approaches

The model lignin dimer is a complicated molecule as it involves several degrees of freedom along the side chain. Moreover, there is currently no experimental data and very limited computational data for benchmarking purposes. Therefore, to ensure that the selected calculation methodologies are suitable and reliable, simpler aromatic and polymer models were first calculated and benchmarked in this section.

### 4.4.1 The Significance of van der Waals Correction on Adsorption of Aromatics

Although contributions from van der Waals interaction by definition should be relatively minimal, this was not the case for  $\pi$ -bond-metal interaction that dominated adsorptions.

The calculation of adsorption of smaller aromatics in this section was performed using a smaller ( $4 \times 4$ ) Ni super cell. Benzene was selected as a model to investigate selected choice of calculation methodology, particularly the importance of inclusion of appropriate van der Waals corrections, based on the abundant literature<sup>48,308</sup> for benzene and superficial structural resemblance to the lignin dimer. Van der Waals interactions were accounted for using optB88-vdW<sup>48,308</sup> and DFT-D3<sup>31,309</sup> functionals.

Table 4.1. Calculated adsorption energies (eV) of benzene on close-packed metal surfaces with different calculation methodology and comparison to the existing literature.

	Cu(111)		Ni(111)
<b>PBE/PAW</b>	-0.03		-1.02
<b>PBE + DFT-D3</b>	-0.99		-2.13
<b>PBE + optB88-vdW</b>	-0.72		-1.80
<b>Theoretical</b>	-0.68, <sup>48, a</sup>	-0.79, <sup>48, b</sup> -0.53 <sup>308, c</sup>	-1.79, <sup>308, a</sup>
<b>Experiment</b>	-0.62, <sup>310</sup>	-0.58, <sup>311</sup> -0.68 to -0.81 <sup>312</sup>	-1.95 <sup>50</sup>

References employing <sup>a</sup>PBE + optB88-vdW, <sup>b</sup>PBE + vdW<sup>surf</sup>.

The results in Table 4.1 show adsorption energies of benzene lying horizontally on Ni and Cu(111) bridge site, which was previously shown to be the most preferable by various metals.<sup>48</sup> The results indicate a systematic trend among investigated metals, wherein PBE alone substantially underestimates the adsorption energies, as the underbinding nature of GGA is well-established<sup>313</sup>. This can be addressed by incorporating van der Waals corrections. By correcting this using DFT-D3, the adsorption energies were all slightly over-compensated compared to experiments. This is in agreement with a previous study of benzene  $\Delta E_{\text{ads}}^g$  on Ag(111).<sup>314</sup> Using optB88-vdW the results are in closer agreement with experiment results on a Cu(111) and slightly underestimate for the case of Ni(111).<sup>315,316</sup> These indicate that optB88-vdW can suitably capture the  $\pi$ -bond interaction with *d*-electrons of the transition metal. Since coupling PBE with optB88-vdW results in the most accurate energy for this system, this combination will be employed throughout the present study.

#### 4.4.2 Determining Preferable Adsorption Site using Guaiacol

Where the lignin dimer adsorbs on the surface can significantly impact the adsorption energy. To locate the most preferable site, we employed guaiacol, which is structurally equivalent to a unit of the dimer. Figure 4.2 shows the adsorption of guaiacol at the different sites of Ni(111) with two orientations –  $0^\circ$  or  $30^\circ$  – with respect to the hexagonal ring formed by of nickel atoms. The results indicate that guaiacol oriented as  $30^\circ$  to the bridge site is the most stable site with a  $\Delta E_{\text{ads}}^g$  of -2.00 eV (Figure 4.2). This site and angle preference were in agreement with adsorption of phenol on Pd(111).<sup>31</sup> Therefore, adsorption of both aromatic rings of the lignin will be positioned to best fit the bridge sites.

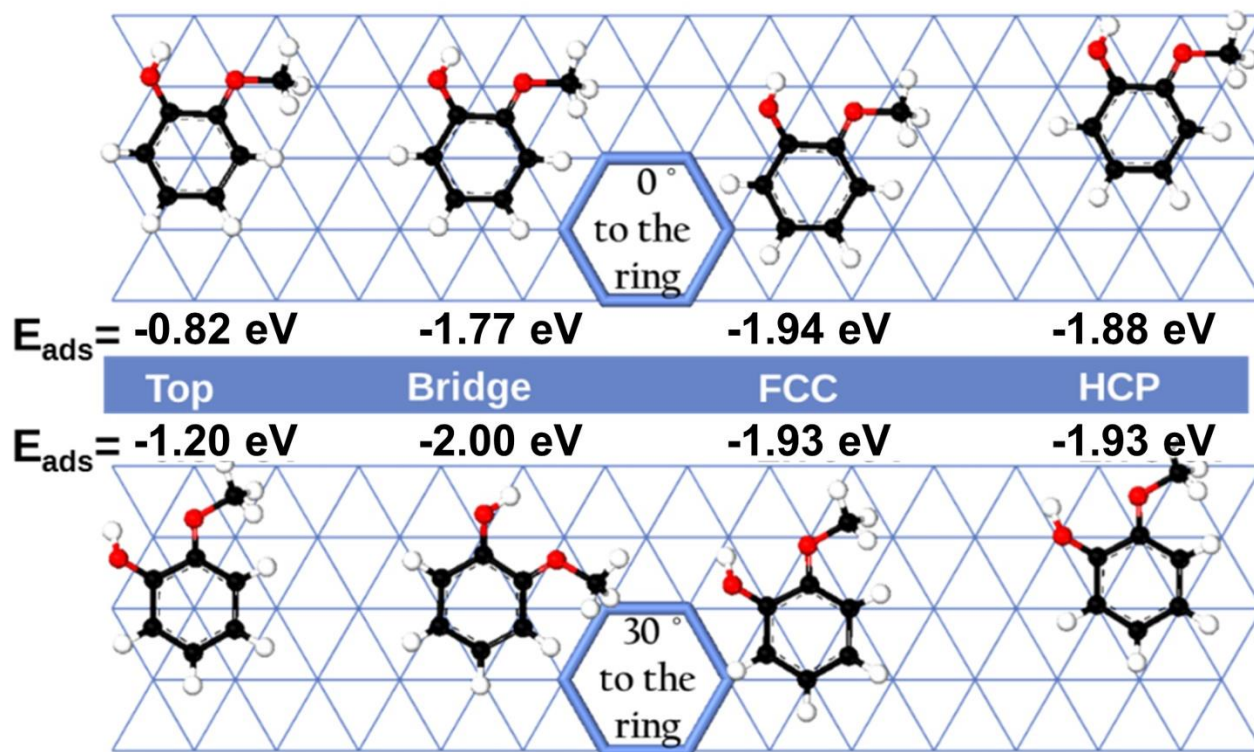


Figure 4.2. Adsorption energy ( $\Delta E_{\text{ads}}$ ) of guaiacol at four different sites, top, bridge, FCC, and HCP, with two orientations,  $0^\circ$  and  $30^\circ$  with respect to the hexagonal ring formed by of nickel atoms on the top layer of the slab.

It should be noted that the  $\Delta E_{\text{ads}}^g$  of guaiacol, which contains two more oxygenated functional group than benzene, on Ni only shows 0.08 eV higher  $\Delta E_{\text{ads}}$ . On a Cu(111), guaiacol  $\Delta E_{\text{ads}}^g$  is -1.04 eV (result not shown), 0.32 eV higher than benzene. These indicate that the functional groups could have different contributions to the  $\Delta E_{\text{ads}}^g$  on different metals. However, the major contribution to the  $\Delta E_{\text{ads}}^g$  was still from the interaction of  $\pi$ -bonds on the benzene ring with the metal surface. Hence, although the dimer model used in this study is a G unit of lignin, the results are expected to be extendable to S units of lignin as well.

#### 4.4.3 Representing Polymeric Lignin Structure with a Dimer

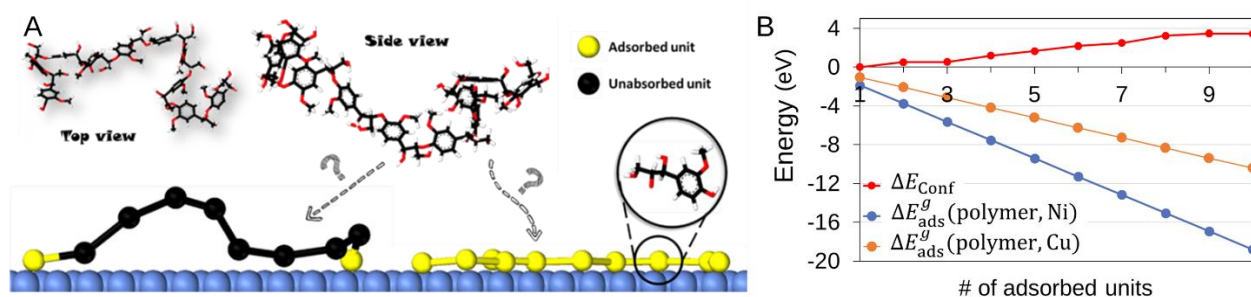


Figure 4.3. Top view and side view of relaxed hypothetical lignin of 10 G-units with only  $\beta$ -O-4 linkages and possible adsorption conformations of the polymer on metal surfaces (A). The approximated adsorption energy of the polymer ( $\Delta E_{\text{ads}}^g$  (polymer)) for a given number of units adsorbed on Ni and Cu and conformation energy ( $\Delta E_{\text{conf}}$ ) for a given number of unit fixed to lie horizontal (B).

In a natural state, the fully relaxed polymeric lignin is highly twisted and tend to self-aggregate (Figure 4.3A top). In contrast, the adsorption of lignin is assumed to require the aromatic rings to be flat and parallel to the surface to maximize  $\pi$ -bond-metal interaction. This would therefore exert constraints on parts of the lignin dimer. The energy cost to constrain the dimer is defined here as conformational energy ( $\Delta E_{\text{conf}}$ ). Unlike the lignin dimer that only has two units, the adsorbed conformation of a polymer chain can vary from an end-of-the-chain adsorption<sup>317</sup> to

a completely flat configuration (Figure 4.3A),<sup>318</sup> which is a tradeoff between the gain from adsorption energy and cost due to conformation energy.

Therefore, the objective of this subsection is to determine the adsorbed conformation of the polymer in vacuum and evaluate if that conformation could be modeled using a dimer. This is accomplished by first calculating the  $\Delta E_{\text{conf}}$  of a hypothetical 10-unit polymer comprised of only  $\beta$ -O-4 linkages using classical MD. The  $\Delta E_{\text{conf}}$  is the energy cost by constraining a certain number of lignin's benzene ring to be flat and horizontally parallel to an imaginary plane (as if they were in adsorbed state), which can be expressed by:

$$\Delta E_{\text{conf}} = E[\text{Polymer Constrained}] - E[\text{Polymer Free}] \quad \text{Eqn. (4.8)}$$

where  $E[\text{Polymer Constrained}]$  is the average energy (from 3 relaxed frames of NVT MD) of the polymer with a set number of monomer units constrained, and  $E[\text{Polymer Free}]$  is that of a fully relaxed polymer with no units constrained. The resulting  $\Delta E_{\text{conf}}$  is shown in Figure 4.3B. The  $\Delta E_{\text{conf}}$  increases from 0 eV up to 4 eV as more units in the polymer were constrained. To compare  $\Delta E_{\text{conf}}$  with the polymer's gain in adsorption energy, the  $\Delta E_{\text{ads}}^g$  of the polymer was estimated by:

$$\Delta E_{\text{ads}}^g(\text{polymer}) \approx \# \text{ of units adsorbed} \times \Delta E_{\text{ads}}^g(\text{unit}) \quad \text{Eqn. (4.9)}$$

where  $\Delta E_{\text{ads}}^g(\text{unit})$  is the DFT-calculated  $\Delta E_{\text{ads}}^g$  per unit. For the aromatic unit adsorption, the  $\Delta E_{\text{ads}}^g(\text{unit})$  is -0.72 eV for Cu and -1.80 for Ni. In both of these estimations, the  $\Delta E_{\text{ads}}^g$  outweighed the  $\Delta E_{\text{conf}}$  significantly, indicating that the lignin polymer preferred to adsorb entirely flat on Ni(111) and Cu(111), and hence the  $\beta$ -O-4 lignin dimer, presumably with both rings adsorb on the surface, can be used to represent the adsorption of the lignin polymer.

#### 4.4.4 Identifying the most Stable Dimer Adsorption Conformation in Gas Phase

Because a lignin dimer can exist in multiple conformations, the first task for this section is to identify the stable free lignin conformation. To achieve this, 15 conformations of a *threo*-lignin dimer were generated and compared with respect to energy. The image of the most stable conformation is shown in Figure 4.4 (free dimer). The relative energy difference between the least and the most stable conformation studied was 0.33 eV. The stability of the lignin conformation was found to be partially affected by the intramolecular hydrogen bonds. Focusing on just the propyl chain, stable conformations (~0.15 eV difference from the most stable one in this study) contain 2 to 3 hydrogen bonds from among the aliphatic hydroxyl groups, the  $\beta$ -O-4's oxygen, and the methoxyl group's oxygen, depending on the conformation (3 was the maximum). This is in agreement with previous reports suggesting that intramolecular hydrogen bonding play an important role for lignin conformation.<sup>319,320</sup> In addition, it should be noted that several other conformations exhibited energies close to the most stable one (~0.02 eV), suggesting there could be more than one solution. However, a common feature among all the studied free dimers is that the angle between the aromatic ring and the propyl chain atoms next to it is about 180°, which is to be expected of a free dimer.

Upon adsorption with aromatic rings completely parallel to the Ni(111), the angle of the *threo*-dimer was no longer 180° as in the case for the relaxed two-ring adsorbed conformation (conformation A and B) in Figure 4.4A and 4B. This supposedly results in an increase in conformation energy. Therefore, to ensure that the most likely stable conformation is identified, other conformations that are expected to exhibit less constraints were also investigated. These conformations are called one-ring conformations and include conformation C, D, and E in Figure

4.4. The common trait among these three conformations is that they allow one of the aromatic rings to be relatively free, while the other aromatic ring adsorbs onto the surface.

The resulting  $\Delta E_{\text{ads}}^g$  for each of these dimers is presented in Table 5.2. As the results show higher  $\Delta E_{\text{ads}}^g$  from both conformation A and B, it is clear that the interaction between the aromatic ring and the metal outweighs the conformation energy by having two rings completely adsorb on the surface. Furthermore, conformation A was shown to be statistically more stable than B. The bond lengths between these two are shown in Fig. 5.4 and are mostly similar. The main difference between these two is at the oxygen within the  $\beta$ -O-4 bond where, in one conformation, this oxygen atom is away from the surface (2.91 Å away, Fig. 5.4A), and the other closer to the surface (1.94 Å away, Fig. 5.4B). Conformation A is analogous to a previous study using 2-phenoxy-1-phenylethanol as a model dimer adsorbing on Pd(111).<sup>14</sup> On the other hand, conformation B is similar to what was used in a recent DFT study on reaction pathways during lignin hydrogenolysis.<sup>13</sup> Taking their reported adsorbing structure and relaxed using our setup resulted in  $\Delta E_{\text{ads}}^g$  of -3.33 eV, a similar value to the result for conformation B in the present study (-3.50 eV from Table 5.2). As conformation A is shown here to be more stable, this may affect subsequent reaction pathways. It should be noted that we have investigated changes within each conformation using at least 5 additional images, each with minor changes such as adjusting dihedral angles and alternating position of the methoxyl group, to determine how these perturbations impact  $\Delta E_{\text{ads}}^g$ . The results are presented as an average ( $\Delta \bar{E}_{\text{ads}}^g$ ) with standard deviation shown in Table 5.2. The image shown in Fig. 5.4 is of the most stable conformation with the atomic position of conformation A and B provided in the supporting materials.

Lastly, for lignin dimer adsorption on a Cu(111) surface, only conformations A and D were selected for comparison between two-ring and one-ring adsorption. Although the interaction between Cu and the dimer was weaker than that of Ni, as observed by the significantly lower  $\Delta E_{\text{ads}}$  (Table 5.2), the adsorption conformation A is still more favorable.

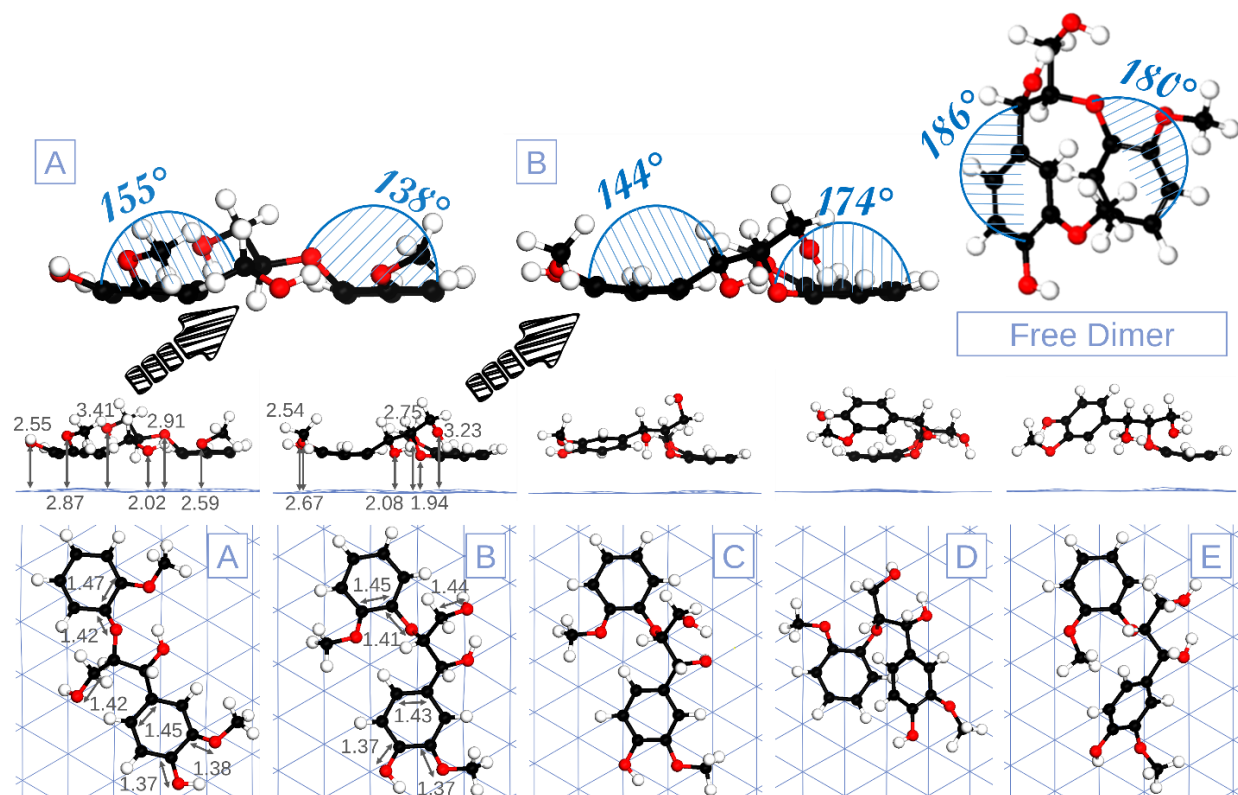


Figure 4.4. Relaxed adsorption conformations of lignin *threo*-dimer where in A) and B) both rings adsorb to the surface with both aryl rings completely planar, C) only one ring is completely planar, D) and E) only one ring adsorbs. The change in angles between the aromatic ring to the atoms next to it in conformation A and B compared to relaxed free dimer is shown in the enlarged images. The distances (Å) from the surface to all oxygen atoms in the molecule are also shown for conformation A and B.

To supplement the results on adsorption of the *threo*-isomer the adsorption of the *erythro*-isomer on Ni(111) using two conformations is next investigated. These two conformations are derivatives from *threo*-isomer in the Figs. 4.4A and 4.4B structures. To reserve conformation A

and B for *threo*-isomer and prevent confusion, these derived structures are called conformation I and II shown in Figure 4.5I and II, respectively. Unlike the *threo*-isomer, the results show that conformation II, where the oxygen atom of the  $\beta$ -O-4 is close to the surface, is now the most stable conformation (Table 3), and is in agreement with previously published literature.<sup>44</sup> The reason that the conformation in Fig.4.5I is not the most stable could be due to the strain at its ether oxygen atom that needs to be as high as 3.14 Å away from the surface compared to 2.91 Å for the conformation in Fig.4.4A to remain connected with the propyl chain of this isomer. This resulted in the  $\beta$ -O-4 bond angle of 130°, compared to 122° in both Figure 4.4A for the *threo*-isomer and for the free lignin (data not shown). Overall, the observed differences in adsorption conformation implies that *erythro*- and *threo*-isomer could undergo different reaction paths.

Table 4.2. Adsorption energy in eV and average aryl carbon atoms distance to metal surface ( $\Delta d$ ) in Å for different adsorption conformations of the *threo*-dimer (shown in Figure 4.4) and conditions on Ni(111) and Cu(111) surfaces.

Metal	Ni(111)					Cu(111)	
Conf.	A	B	C	D	E	A	D
<b>Vacuum</b>							
$\Delta E_{\text{ads}}^g$	-3.59	-3.50	-3.10	-2.48	-2.26	-1.99	-1.55
$\Delta \bar{E}_{\text{ads}}^g$	$-3.53 \pm 0.03$	$-3.33 \pm 0.10$	$-3.06 \pm 0.04$	-	-	-	-
$\Delta d$	1.98	2.00	1.98	1.97	1.99	2.97	2.77
<b>Implicit Solvent Model (<math>\epsilon_r = 21.04</math>) by Eqn. 4.2</b>							
$\Delta E_{\text{ads}}^l$ (implicit)	-3.55	-	-	-	-	-	-
$\Delta d$	1.97	-	-	-	-	-	-
<b>Implicit Solvent Model (<math>\epsilon_r = 80.00</math>) by Eqn. 2</b>							
$\Delta E_{\text{ads}}^l$ (implicit)	-3.52	-	-	-	-	-	-
$\Delta d$	1.98	-	-	-	-	-	-
<b>Explicit Solvent Model (<math>\rho = 0.76 \text{ g/cm}^3</math>) by Eqn. 3</b>							
$\Delta \bar{E}_{\text{ads}}^l$ (explicit)	$-0.58 \pm 0.55$	-	-	$0.46 \pm 0.54$	-	$0.35 \pm 1.16$	$0.76 \pm 1.05$
$\Delta d$	1.99	-	-	2.00	-	2.90	3.08
<b>Thermodynamics cycle by Eqn. 4.4</b>							
$\Delta \bar{E}_{\text{ads}}^l$ (thermo) <sup>(a)</sup>	$-0.58 \pm 0.20$	-	-	$0.24 \pm 0.18$	-	$0.46 \pm 0.14$	$0.69 \pm 0.10$
$\Delta \bar{E}_{\text{ads}}^l$ (thermo) <sup>(b)</sup>	$-1.09 \pm 0.50$	-	-	$0.03 \pm 0.37$	-	$0.40 \pm 0.33$	$0.60 \pm 0.44$
$\Delta \bar{E}_{\text{ads}}^l$ (thermo) <sup>(c)</sup>	$-1.21 \pm 0.53$	-	-	$-0.05 \pm 0.36$	-	$0.53 \pm 0.26$	$0.72 \pm 0.32$

<sup>(a)</sup> The  $\delta$  in Eqn. 4.4 was calculated based on solvent accessible surface area (SASA) using probe radius of 1.25 Å, <sup>(b)</sup> by the number of neighbor atoms within 2.5 Å distance, and <sup>(c)</sup> by number of bonds within the 2.5 Å distance.

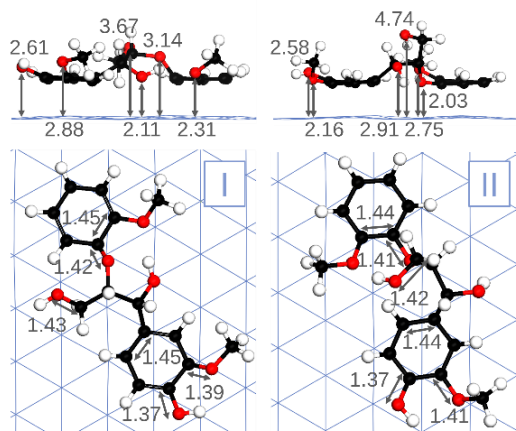


Figure 4.5. Relaxed adsorption conformations of lignin *erythro*-dimer where both rings adsorbed on the Ni(111) with one conformation yielding an ethyl oxygen atom away from the surface (I) and the other adsorbed onto the surface (II) with distances from the surfaces to all oxygen atoms in the molecule and some bond distances within the molecule.

Table 4.3. Adsorption energy ( $\Delta E_{\text{ads}}^g$ ) in eV and average aryl carbon atoms distance to Ni(111) surface ( $\Delta d$ ) in Å for the two different adsorption conformations of the *erythro*-dimer (shown in Figure 4.5).

Metal	Ni(111)	
Conf.	I	II
$\Delta E_{\text{ads}}^g$	-3.16	-3.73
$\Delta \bar{E}_{\text{ads}}^g$	$-3.16 \pm 0.00$	$-3.63 \pm 0.10$
$\Delta d$	1.98	1.96

## 4.5 Adsorption Energy of Lignin in Solvated Environments

### 4.5.1 Comparison of the Implicit and Explicit Model for Solvated Lignin Adsorption

The adsorption energies of a solvated lignin dimer from both implicit and explicit models are shown in Table 5.2, where the dimer's initial conformation for two-ring and one-ring adsorption was taken from the most stable *threo*-isomer adsorption in vacuum (*i.e.* the A and D conformation).

The explicit model and implicit models gave very different adsorption energies. In the implicit model,  $\Delta E_{\text{ads}}^l$  (implicit), it was found that by applying a  $\epsilon$  of 21.04 (equivalent to ethanol

at 50 °C) the adsorption energy change very slightly compared to that of the vacuum state. To examine the effect of  $\epsilon$  on  $\Delta E_{\text{ads}}^l$ , the  $\epsilon$  was increased to 80 (equivalent to water at 25 °C), but the change in  $\Delta E_{\text{ads}}$  remained minimal. In contrast, the explicit solvation model yielded an average  $\Delta E_{\text{ads}}^l(\text{explicit})$  of -0.58 eV for two-ring adsorption on a Ni(111), a 2.95 eV reduction compared to its vacuum counterpart (Table 5.2). Furthermore, on a Cu(111) the adsorption decreased so drastically that the  $\Delta E_{\text{ads}}^l(\text{explicit})$  is positive for both the one-ring and two-ring conformation, suggesting that the dimer no longer prefers to adsorb on the surface at this liquid density. It should be noted that the large standard deviations of the explicit model results are associated with the fluctuations in NVT MD from which the images were sampled, and are expected of liquid phase simulations. A test run using *ab initio* MD for 3 ps production run also yielded similar fluctuations (results not shown).

Apart from the energy, there are also differences in the relaxed geometry between the implicit and explicit model. In the results using the implicit model, there was virtually no change in either bond length or the distance of the dimer from the surface compared to the gas phase conformations (within 0.03 Å). However, noticeable structural changes can be observed from the explicit model. For the case of the two-ring adsorption conformation on a Ni(111), the entire hydroxymethyl group shifted away from the surface and closer to the solvent phase primarily due to the hydrogen bonding of the  $\gamma$ -hydroxyl group with ethanol. For example, the oxygen atom of the  $\gamma$ -hydroxyl became  $3.73 \pm 0.26$  Å away from the surface compared to 3.29 Å in the vacuum state as shown in Figure 4.5A. To a lesser extent, the effect is also observed on the  $\beta$ -O-4 ether oxygen atom, which drifted  $0.10 \pm 0.04$  Å away from the surface compared to its vacuum state. On the other hand, the change is almost negligible for the  $\alpha$ -hydroxyl group due to its structural proximity to the  $\beta$ -O-4 ether and methoxyl oxygen atoms, allowing the  $\alpha$ -hydroxyl group to form

intramolecular hydrogen bonds with these ether groups and less likely to interact with ethanol. Apart from these, no significant changes were observed among the aromatic atoms. On the Cu(111), similar changes were observed upon explicit solvation.

Table 4.4. Comparison of solvation energy ( $\Delta E_{\text{sol}}$ ) of similar aromatic molecules in alcohol solvents using different implicit models, an explicit model, and from experiments.

Solute	Conditions				Solvation Energy			
	Solvent	T°	Density (g/cm <sup>3</sup> )	$\epsilon$	VASP <sub>sol</sub>	COSMO	Explicit	Exp
Phenyl ethanol	EG	25 °C	1.11	40.00	-0.20	-0.36	-0.63 ± 0.38	-0.68 <sup>321</sup>
1,3-Dimethoxy benzene	2-PrOH	25 °C	0.79	20.18	-0.09	-0.30	-0.60 ± 0.52	-0.58 <sup>322</sup>
Benzoic acid	2-PrOH	25 °C	0.79	20.18	-0.20	-0.35	-0.78 ± 0.28	-0.76 <sup>322</sup>
Benzyl alcohol	EtOH	25 °C	0.79	24.50	-0.16	-0.35	-0.81 ± 1.04	-0.66 <sup>322</sup>
Dimer*	EtOH	50 °C	0.76	21.04	-0.63	-0.78	-1.53 ± 0.74	-

\* *threo*-guaiacylglycerol-beta-guaiacyl ether

To ensure that the description of the solute-solvent interactions by an explicit model is dependable, solvation energies of similar aromatic molecules in alcohols were calculated using implicit models and an explicit model and compared to experimentally determined values (Table 4). It should be noted that for this, another implicit model (COSMO) was also used for comparison purposes. The differences between VASP<sub>sol</sub> and COSMO include, but are not limited to, the method used for calculating cavity size and electrostatic interactions.<sup>119</sup> From the results, we can see that both implicit models consistently underestimated the solvation energy. This could be due to their limitations in describing site-specific interactions between solute and solvents (*e.g.* hydrogen bonding) as well as parametrization for the metal's cavity size.<sup>323</sup> In contrast, the explicit model showed promising results compared to experiments and support that the results from explicit solvation model are the most reliable in the present study. These results suggest the adsorption

energy difference between the implicit and explicit model is mainly due to the inaccurate description of lignin-solvent interaction in the implicit model.

#### 4.5.2 Calculation of Solvated Lignin Adsorption Energy from a Thermodynamic Cycle

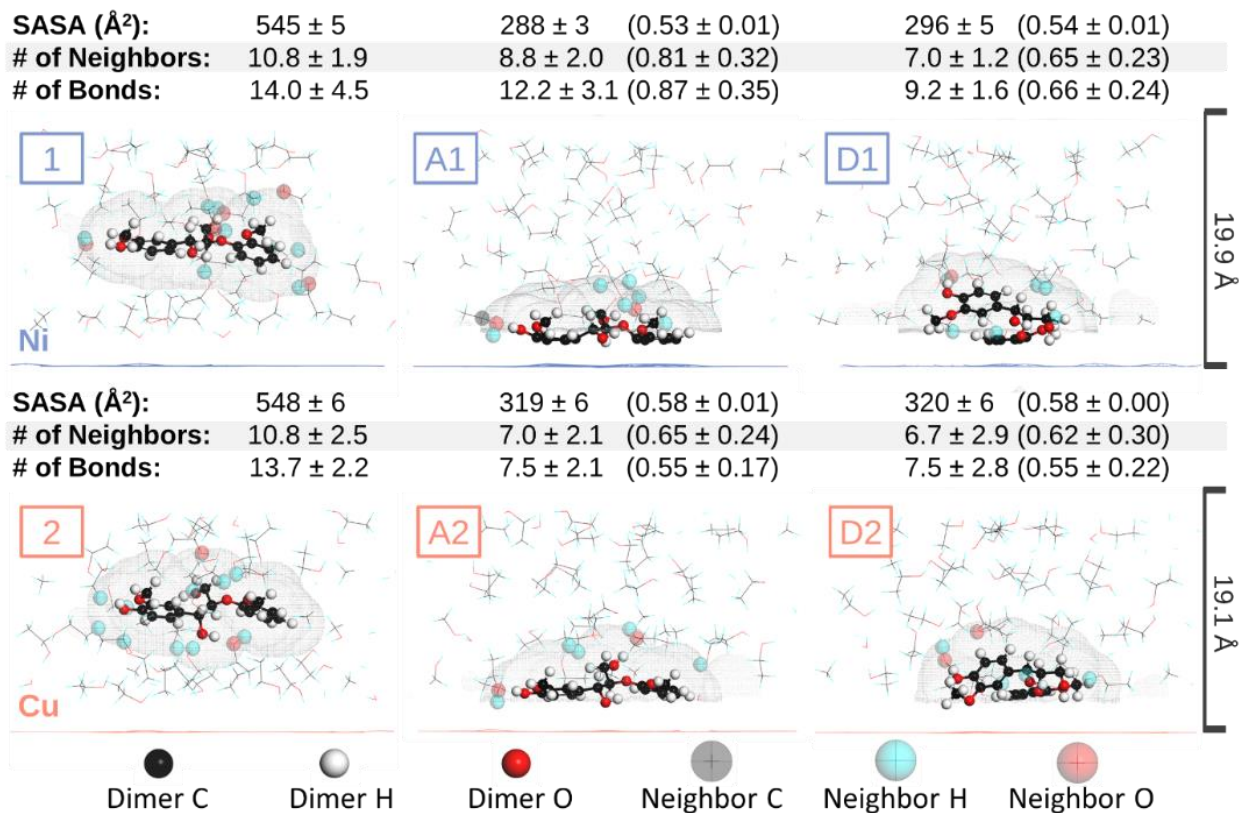


Figure 4.6. The values for solvent accessible surface area (SASA) using a  $1.25 \text{ \AA}$  probe radius (grey mesh), the number of neighboring atoms (enlarged solvent atoms), and the number of bonds within a  $2.5 \text{ \AA}$  radius before and after adsorption for relaxed A and D conformation from Table 4.2 in ethanol. The average  $\delta$  value is shown in parentheses.

Calculation of  $\Delta E_{\text{ads}}^l(\text{explicit})$  using Eqn. 4.3 is an expensive calculation and further scaling up of the cell size would be computationally prohibitive for most cases. In this section, we propose strategies to approximate adsorption energy in the solvated state using a thermodynamic cycle ( $\Delta E_{\text{ads}}^l(\text{thermo})$ ). As shown in Figure 4.1 and Eqn. 4.4, the  $\Delta E_{\text{ads}}^l(\text{thermo})$  can be calculated by leveraging known  $\Delta E_{\text{ads}}^g$  with calculated  $\Delta E_{\text{sol}}$  and bulk solvent adsorption energy

( $\Delta E_{\text{ads}}^{\text{EtOH}}$ ), all of which can be simulated with less expense than direct calculations. For example,  $\Delta E_{\text{sol}}$  does not include metal atoms and  $\Delta E_{\text{ads}}^{\text{EtOH}}$  can be calculated in smaller cell and scaled up as necessary using the work of adhesion concept,<sup>111</sup> *i.e.* adsorption per area. The fraction of the metal surface area covered by lignin dimer ( $\theta$ ) was assumed to be the same as in gas state. This leaves only the  $\delta$  parameter to be calculated, which is the fraction of solvation surface of the dimer in the solvated, adsorbed state (Figure 4.1C) relative to the fully solvated state (Figure 4.1B).

Here, we investigated three approaches to estimate the  $\delta$ , including surface accessible surface area (SASA), the number of bonds, and the number of neighboring atoms. The SASA is defined as the surface area of a molecule that is accessible to a solvent, and is typically used in biomolecule investigations. For these, we employed a cutoff radius of 2.5 Å for bond length and number of neighboring atoms. It should be noted that the number of neighbors is not equal to number of bonds because some neighbor atoms may form bonds with multiple dimer atoms. Correspondingly, the probe radius of the SASA is 1.25 Å. The cutoff was chosen based on the assumption that the solvation energy was mostly influenced by neighbor atoms and that 2.5 Å also represents a strong hydrogen bond distance. The values were calculated using Python scripts coupled with the PyMOL package.<sup>324</sup>

Figure 4.6 shows the results of these simulations for the SASA, the number of neighbor atoms, and the number of bonds. The SASA is represented with a grey mesh around the dimer whereas neighboring atoms are enlarged and translucent. Taking SASA as an example, from these we can see that in the bulk solvent, the lignin dimer has  $\sim 550 \text{ \AA}^2$  of SASA. As expected, the accessible area decreased upon adsorption to  $\sim 300 \text{ \AA}^2$  for Ni(111). The trend is similar using other criteria. It should be noted that there is not a significant difference between the SASA of the two-ring (Figure 4.6A) and the one-ring conformations (Figure 4.6D). Originally, it was anticipated

that the one-ring conformation may allow more interactions between the dimer and ethanol molecules. However, all three criteria suggested equivalent, or even less, interactions because the folded structure of the one-ring conformation limited the exposure of part of the dimer to solvent. Given these values for each criteria, the  $\delta$  value for each conformation is the ratio of the values from a selected criterion of that conformation to that of the dimer in the bulk solvent. For example, the  $\delta$  value for the adsorption conformation presented in image A1 of Figure 4.6B calculated by SASA is 0.53 and was obtained from 288 divided by 545. All  $\delta$ 's are shown in the parentheses in Figure 4.6.

Table 4.2 presents the results for the  $\Delta E_{\text{ads}}^l(\text{thermo})$  determined using the calculated  $\delta$  values in Eqn. 4.4. The results indicate that using the SASA for  $\delta$  yielded the closest approximation to  $\Delta E_{\text{ads}}^l(\text{explicit})$ , which typically show only  $\sim 0.1$  eV error and correctly predict that the dimer would not adsorb on Cu. More importantly, the SASA of vacuum and solvated states are almost identical. Calculating the SASA of two-ring adsorbed dimer in vacuum yielded  $285 \text{ \AA}^2$ , compared to  $288 \text{ \AA}^2$  for the solvated state. On a Cu(111), the SASA in vacuum state is  $315 \text{ \AA}^2$ , compared to  $319 \text{ \AA}^2$  in the solvent. This means that users would not be required to generate solvated structures, which could inherently be dependent on the type of methods used. Since the SASA is highlighted, it should be noted that SASA is also not sensitive to the chosen probe radius. As shown in Figure S1, the  $\delta$  value only changed by 0.1 in response to changing the probe radius from 0.5 to 1.5  $\text{\AA}$ .

For Cu, similar to the results from  $\Delta E_{\text{ads}}^l(\text{explicit})$ , estimation using  $\Delta E_{\text{ads}}^l(\text{thermo})$  with SASA indicates that the dimer does not prefer to adsorb at this density. Equation 4.4 implies that the use of a Cu catalyst with alcohol solvent for depolymerization of a lignin dimer would require high temperature to mitigate the solvation effect and allow lignin to adsorb. This is in agreement with the observed experimental conditions where Cu-based catalysts were typically found to be

used with these elevated temperatures.<sup>228,325</sup> On the other hand, it also explains why a majority of the successful depolymerization experiments, particularly those using more mild conditions, employ Ni-based catalysts which can maintain adsorption of dimer even in solvated conditions.<sup>222,226,291</sup>

Equation 4.4 highlights the effect of solvents on adsorption energy and suggests strategies to improve adsorption via either choosing solvent that has less interaction with the dimer (lower  $\Delta E_{\text{sol}}$ ), or choosing a solvent that has less interaction with the metal surface (lower  $\Delta E_{\text{ads}}^l(\text{solvent})$ ). Investigating the contribution from each term in Eqn. 4.4 shows that for both Ni(111) and Cu(111)

Given that the former is harder to tune (as solvation of lignin is required), it may be easier to find solvent that can dissolve lignin but has less interaction with the metal surface. This is in agreement with experiments which investigate the effect of solvents on hydrogenolysis of a lignin 4-O-5 model dimer and found that the highest yields were obtained in decaline and methylcyclohexane, both of which are expected to yield low  $\Delta E_{\text{ads}}^l(\text{solvent})$ , due to being relatively large molecules and completely hydrogenated.<sup>40</sup> Therefore, the use of Eqn. 4.4 can help approximate adsorption energy of dimer and aid in solvent selection for a particular catalyst.

## 4.6 Conclusion

The present study has provided a systematic investigation and analysis of the adsorption conformation of lignin dimers representing a vacuum and solvated state. First, it was demonstrated that a lignin  $\beta$ -O-4 dimer exhibited similar adsorption behavior to its polymer counterpart. The preferred adsorption conformation for both a *erythro*- and *threo*-isomer of the dimer was found to be with two aryl rings adsorbed on the surface. However, the *erythro*-isomer prefers the

conformation where its ether oxygen on the alkyl chain is close to the surface, whereas the *threo*-isomer favors the conformation where the ether oxygen is away from the surface. Adsorption energy of the dimer in vacuum on Ni(111) was also shown to be significantly higher than that on Cu(111) surface.

Upon solvation with ethanol using an explicit representation of the ethanol at a density corresponding to 50 °C, the adsorption energy was reduced significantly for all surfaces. While the dimer prefers adsorbing on Ni(111), the reduction in adsorption energy leads to endothermic adsorption for Cu(111). As implicit models were found to not be able to sufficiently describe solvent-solute interactions, and the explicit model is quite expensive computationally, an alternative, more computationally efficient approach to calculate the solvated adsorption energy was developed based on a thermodynamic cycle. The model resulted in errors on the scale of only ~0.1 eV relative to the explicit model and correctly predicted that the dimer would not adsorb on Cu in the studied condition. This finding would allow for future studies to be able to select the solvent for a particular metal catalyst more effectively relative to explicit solvation method. Moreover, these results emphasize the critical impact that the solvent plays on lignin adsorption during processes employing heterogeneous catalysts for lignin upgrading.

## CHAPTER 5 Catalytic Hydrogenolysis of Lignin to Aromatic Monomers

### 5.1 Summary

Lignin hydrogenolysis has been recently been studied extensively as it shows high yields and selectivities with limited condensation reaction. Moreover, the reaction can also exploit other hydrogen source apart from H<sub>2</sub> such as from ethanol, *i.e.* catalytic transfer hydrogenolysis. A number of studies have shown that several supported metal catalysts can be used for the reaction using biomass as a substrate. The reaction does not only serve as a lignin valorization method, but also biomass pretreatment. However, due to variable quality of lignin and biomass substrate, it is unknown how do these catalysts compare both in term of monomer yields, and the quality of pretreated biomass. In this study, a series of supported metal catalysts (metal/C) is used for catalytic transfer hydrogenolysis using birch biomass as a substrate and ethanol as a solvent at 200 and 220 °C. The catalysts were chosen based on previous report that it has been used for ethanol reforming. The results revealed that Co/C, Ni/C, Ru/C, and Pd/C can give high yields and selectivities, in a respective order. Particularly, Co/C has not been used previously for catalytic hydrogenolysis transfer of lignin before. It was also showed that, for this method, the amount of  $\beta$ -O-4 contents is the most critical functional group the reaction. In term of pretreatment efficacy, biomass resulted from these catalysts showed significant higher removal of xylan and lignin, compared to catalysts that give low yields and no catalyst at all. Moreover, in all cases glucan was almost perfectly retained. Significant improvement in glucose yields were observed from reactions with catalysts that gave high yields, particularly it was shown that the glucose yields were correlated to lignin removal. These show that catalytic hydrogen transfer, with an appropriate catalyst, is an effective method for both lignin monomer generation from lignin and pretreating biomass.

## 5.2 Introduction

The plant cell walls of lignocellulosic biomass are comprised primarily of the structural polymers cellulose, hemicellulose, and lignin. Among these, lignin is the most underutilized component where it is cheaply burned at site. Considering that it comprises 17-33% of the biomass,<sup>13</sup> there has been a significant effort in valorization of lignin. One of the methods is depolymerization of lignin to valuable products through hydrogenolysis, in which the products are typically followed by hydrodeoxygenation in the same reaction pot.<sup>5,281</sup> The methods have drawn significant attention in the past several years due to its ability to apply to whole biomass, *i.e.* the lignin valorization step has become pretreatment step in itself, showing limited condensation in certain conditions, and the compatibility with hydrogen transfer reactions, which allows it to leverage other hydrogen sources than pressurized gas.<sup>274,326</sup> A number of catalysts for the reaction has been proposed and shown to give high yields, such as Ni, Pd, and Ru-based catalysts.<sup>19</sup> However, different studies using different lignin sources, conditions, and catalysts have resulted in not just monomer yields and, sometimes, product types that are not comparable, but also the impact on the pretreated biomass. The lack of benchmarking standard hinders the process of catalyst selection and design. Therefore, the present study aims to fill this gap by determining the efficiency of different supported metal catalysts on both monomer yields and quality of the pretreated hardwood biomass by a mean of enzymatic hydrolysis. The reaction will be performed using hydrogen transfer from the selected solvent, which is ethanol in this work.

Early dedicated lignin hydrogenolysis studies were performed by Pepper *et al.*, where it was shown that using whole softwood biomass as a substrate, monomer yields as high as 22% could be achieved by using Raney Ni catalyst with water/dioxane (50:50) solvent.<sup>327,328</sup> Since then, there has been significant development in the process including identifying new catalysts, solvents,

and new hydrogen sources. Arguably, the reaction gains the most traction when it was demonstrated that using Ni/C with hardwood and alcohol solvents, lignin monomer as high as 50% were achieved with >90% selectivity.<sup>226</sup> Many other studies using similar conditions with Ni/C have shown similarly high yields ranging from 26% to similarly high depending on biomass type.<sup>275,283–285</sup> Other supported transition metal catalysts also have shown promising results, for example Pd/C, Ru/C, Pt/C, and many other transition metal alloys.<sup>35–37,223,233</sup> These indicate that there are many possible transition metals, possibly more that has not been investigated, that could efficiently perform lignin hydrogenolysis.

Many of the hydrogenolysis reactions did not use H<sub>2</sub> as a hydrogen source, but instead relies on the hydrogen transfer mechanism (catalytic transfer hydrogenolysis), such as from alcohols,<sup>200,226,229,326,329</sup> formic acid,<sup>330</sup> and dioxane,<sup>233</sup> each of which with different donating mechanisms. One of the advantages of the process is that it doesn't require excessively high pressure-rating vessels as one would do for molecular hydrogen. However, this also indicates that the efficacy of the reaction would also partly depend on the alcohol reforming activity of the catalyst. As alcohols are the most commonly used hydrogen donors and ethanol will be used in the present study, it is worth discussing about the capability of ethanol reforming of some of transition metal catalysts. Ethanol reforming is a process that convert ethanol to methane and other syngas and is typically conducted at very high temperature (600-800 °C).<sup>331,332</sup> Adsorbed hydrogen atom from the process could be the source for lignin hydrogenolysis. Mechanistically, ethanol reforming is a complex reaction process that involve several molecular decompositions, water activation, and oxidation of the adsorbed carbon species.<sup>331</sup> Metals that are typically used include, Ni, Co, Fe, Cu, Pt, Pd, and Rh.<sup>331–334</sup> Therefore, these metals could have potential for lignin hydrogenolysis. Particularly, to our knowledge, supported Co and Rh catalyst have not been previously used for

catalytic transfer hydrogenolysis. Nevertheless, it should be noted that some of the metals have different decomposition mechanism compared to others. For example, on Ni and Co, ethanol first loses the hydroxyl hydrogen, resulting in  $\text{CH}_3\text{CH}_2\text{O}\cdot$  adsorbing species, whereas on Pt and Pd, hydrogen abstraction first occurs at the  $\alpha$ -carbon position, resulting in  $\text{CH}_3\dot{\text{C}}\text{HOH}$  adsorbing species.<sup>330</sup> These adsorbing species are likely to have different affinities to the metal surface. Previous studies have proposed that adsorbing species, particularly one with stronger interactions with the catalyst, could block lignins from getting to the surface and hence results in lower hydrogenolysis yields.<sup>40</sup> Therefore, the low/high final monomer yields could be partly attributed to the catalyst's reforming reaction paths.

Regardless of catalysts and conditions, a common trait among all the examples that resulted in relatively high monomer yields is that a high-quality lignin, *i.e.* high amount of  $\beta$ -O-4, was used as a substrate. This is in agreement with studies indicating that C-O ether bonds in lignin are significantly more fragile than C-C bonds;<sup>295</sup> additionally, investigation of the reaction pathways from some of the catalysts (using moderate temperatures around 200 °C) point out that the products are primarily from cleavage of the  $\beta$ -O-4 bond.<sup>19,226</sup> High-quality lignins are mostly obtained *in situ* during the hydrogenolysis reaction of biomass, where lignin is extracted out by the solvents. This is because lignins isolated from biomass pretreated by traditional methods, such as dilute acid or kraft, typically has a degraded structure where  $\beta$ -O-4 amount is low and significant amount of C-C bonds was formed during the pretreatment.<sup>335,336</sup> However, it should be noted that with recent advances in pretreatment processes, high quality lignin could also be obtained from novel pretreatments such as Cu-catalyzed alkaline-oxidative (Cu-AHP)<sup>249,337,338</sup> and  $\gamma$ -valerolactone pretreatment,<sup>339</sup> where studies have shown that lignin retain high amount of its native  $\beta$ -O-4

contents.<sup>340</sup> In the present study, to ensure high quality of lignin, whole biomass will be used as a reaction substrate to maximize monomer yields.

Using biomass as a substrate implies that lignin valorization process has also become a pretreatment process in itself, which is also commonly known as lignin-first biorefinery.<sup>33,341,342</sup> As such, apart from the monomer yields, the process should also be subjected to criteria that are traditionally used to evaluate the efficacy of a pretreatment process. One of the common method is to measure how much the pretreatment has increase the accessibility to the carbohydrates. This is typically performed by enzymatic hydrolysis to produce sugar monomers. Some of the factors that could impact enzymatic hydrolysis yields include lignin content, hemicellulose content, and cell wall's porosity. Lignin inhibits enzyme accessibility and its removal is well known to be vital for enzymatic hydrolysis.<sup>343</sup> However, it should be noted that it is not in a linear relationship with sugar yields as certain biomass and pretreatment do not require high removals to obtain high sugars.<sup>344</sup> Similarly, hemicellulose was also reported to inhibit accessibility,<sup>344</sup> although this could be addressed by addition of xylanases.<sup>345</sup> Lignin re-deposition and other structural changes that occur during pretreatment, which ultimately change cell wall's porosity, has also been shown to affect sugar yields.<sup>346,347</sup> Without addition of catalysts, the lignin valorization process using biomass substrate would be similar to an organosolv pretreatment. Previous ethanol-based organosolv pretreatment is typically mixed with water and slight addition of acids to help remove hemicellulose.<sup>348,349</sup> The pretreatment were able to remove lignin down to just 5% depending on the severity. In the present thesis, no acid will be added, and hence the effect from catalyst on this process in term of enzymatic hydrolysis would be demonstrated.

In summary, previous studies have suggested that several transition metal catalysts can be used to perform lignin hydrogenolysis using whole biomass as a substrate, particularly through

hydrogen transfer reactions. However, due to diversity of lignin sources, pretreatments, and reaction conditions, it has been difficult in determining the efficiency of different supported metals catalysts, both on the criteria of monomer yields and as a pretreatment. Therefore, in the present study different metal/C catalysts, particularly those that have been shown to possess ethanol reforming capability, will be compared using the same source of lignin, from which monomer yields, characteristics of pretreated biomass, and enzymatic hydrolysis yields will be determined. The metals include Fe, Co, Ni, Cu, Zn, Ru, Pd, and Ag. Additionally, the same treatment will be performed on lignins obtained after alkali pretreatment to demonstrate the importance of the quality of the substrate.

## **5.3 Experimental Methods**

### **5.3.1 Biomass and Lignin Compositions**

The biomass used for the present thesis is silver birch (*Betula pendula* Roth.) grown in northern Sweden and supplied by Curt Lindström (Smurfit-Kappa Kraftliner AB, Piteå, Sweden). The biomass was characterized with S/G ratios and  $\beta$ -o-4 content of 3.2. The biomass was Wiley milled to 5 mm size. Following air-drying, all samples had moisture contents of 3-5%, and the composition for each feedstock was determined by NREL/TP 510-42618 with minor modifications.<sup>350</sup>

The lignin was obtained from alkaline pretreatment of debarked wood chips of 20-year old hybrid poplar (*Populus nigra x maximowiczii* cv. NM6) obtained from Dr. Raymond Miller (Michigan State University Forest Biomass Innovation Center, Escanaba, Michigan) at a liquor-to-wood ratio of 4:1 using conditions identical to those in our previous work for an H-factor of 166.<sup>242</sup> Lignin was obtained by fractionally precipitated from this liquor through two sequential pH reduction approaches. The first one employed sequential acidification and precipitation at using

CO<sub>2</sub> at room temperature and atmospheric pressure to stepwise decrease the pH. The lignin was collected at pH 11, 10.6, 10, 9, and by adding 1 M H<sub>2</sub>SO<sub>4</sub>, also at the pH 2. These samples are named RT-1, RT-2, RT-3, RT-4, and RT-5, respectively. The second lignin fractionation approach employed the Sequential Liquid-Lignin Recovery and Purification (SLRP) process using CO<sub>2</sub> acidification at elevated temperature (115 °C) and pressure (6.2 bar) as reported in our previous work.<sup>243</sup> For the SLRP fractions, the lignin was collected at pH 11 and 10.5 and named SLRP-1 and SLRP-2, respectively. The percent recovery from each pH fraction can be found in our previous work.<sup>286</sup>

For both biomass and lignin, the Klason lignin content as determined by NREL standard procedure (NREL/TP-510-42618) was used as a basis for subsequent characterization and monomer yield determination.

### **5.3.2 Catalytic Hydrogenolysis of Lignin and Biomass**

Catalytic hydrogenolysis of lignin was performed according to previous work.<sup>230</sup> In short, 10% metal loading metals/C was synthesized by incipient wetness where the metals were sourced from Fe(NO<sub>3</sub>)<sub>3</sub>·9H<sub>2</sub>O, Co(NO<sub>3</sub>)<sub>2</sub>·6H<sub>2</sub>O, Ni(NO<sub>3</sub>)<sub>2</sub>·6H<sub>2</sub>O, Cu(NO<sub>3</sub>)<sub>2</sub>·3H<sub>2</sub>O, Zn(NO<sub>3</sub>)<sub>2</sub>·6H<sub>2</sub>O, and Ag(NO<sub>3</sub>)<sub>3</sub>, and RuCl<sub>3</sub>·xH<sub>2</sub>O, where x is estimated as 0.5, which is an average degree of hydration reported for the product (Sigma-Aldrich). For example, 2.76 g of Ni(NO<sub>3</sub>)<sub>2</sub>·6H<sub>2</sub>O was added to 8 g deionized water and stirred until well mixed. The solution was then added dropwise to 5 g of activated carbon (Darco<sup>®</sup> G-60, Aldrich, water absorption capacity of 2.1 mL/g). The mixture was kept wet at room temperature for 24 h before drying overnight at 100 °C. Then it was calcined at 400 °C under nitrogen atmosphere for 4 hr, and reduced at 400 °C under 10% H<sub>2</sub> in an Ar atmosphere, both of which used at a temperature ramp of 6.25 °C/min. For Pd/C, it was purchased

from commercially available product (Sigma-Aldrich 205699). The finished catalysts were stored and weighed in an anaerobic glove box.

For the hydrogenolysis reaction, 200 mg of biomass (or 40 mg of alkali lignin), 30 mg of catalyst, and 4 mL of ethanol were charged to a 10 mL passivated stainless steel reactor while in the anaerobic glove box. Reactors were submerged into a fluidized sand bath set at 200 or 220 °C for 6 hr. The resulting liquid was collected, filtered, and injected into GC/MS (Agilent 7890A / 5975C) using Agilent DB-WAXETR column (30 m x 0.250 mm x 0.25 µm) with 1:1000 split for product. The temperature program holds at 60 °C for 3 min before ramping up at 40 °C/min to 260 °C and held for 2.5 min. Standards were run for quantification. Yields were determined as mass products per mass Klason lignin using standard curves constructed from pure monomers including 4-propyl guaiacol, 4-propyl syringol, 4-ethyl guaiacol, 4-ethyl syringol, and syringol. All standards were purchased from Sigma Aldrich except 4-propyl syringol, which was synthesized according to Parsell et al.,<sup>37</sup> and 4-ethyl syringol, which was estimated using the same response factor as 4-propyl syringol. After collecting the liquid, the leftover biomass was washed with excessing amount of water and left to dry at room temperature.

### **5.3.3 Enzymatic Hydrolysis**

Approximately  $10 \pm 0.3$  mg of the pretreated biomass was added to 1.5-mL Eppendorf® Safe-Lock microcentrifuge tubes. The hydrolysis was performed at a 5% (w/v) solid loading with the citric acid buffer at a concentration of 50 mM and pH around 5.5 was added based on the findings of Lan *et al.*<sup>351</sup>. To prevent bacterial contamination during hydrolysis, tetracycline and cycloheximide was added at a concentration of 40 µg/mL and 60 µg/mL, respectively. Enzyme cocktails consisted of Cellic CTec2 and HTec2 (Novozymes A/S, Bagsævard, Denmark) and were added at a ratio of 2:1, respectively. For all experiments, the total enzyme loading was 20 mg total

proteins per gram of glucan in the biomass sample. The reaction was performed in a shaking incubator at 50 °C at 160 rpm. After 72 hours, samples were collected and analyzed for glucose and xylose using HPLC with a method reported previously.<sup>352</sup> The amount of sugar yields are based on the fraction of glucose and xylose determined from composition analysis of the whole biomass from NREL standard method.

#### 5.4. Monomer Yields from Native Lignin in Biomass Using Different Catalysts

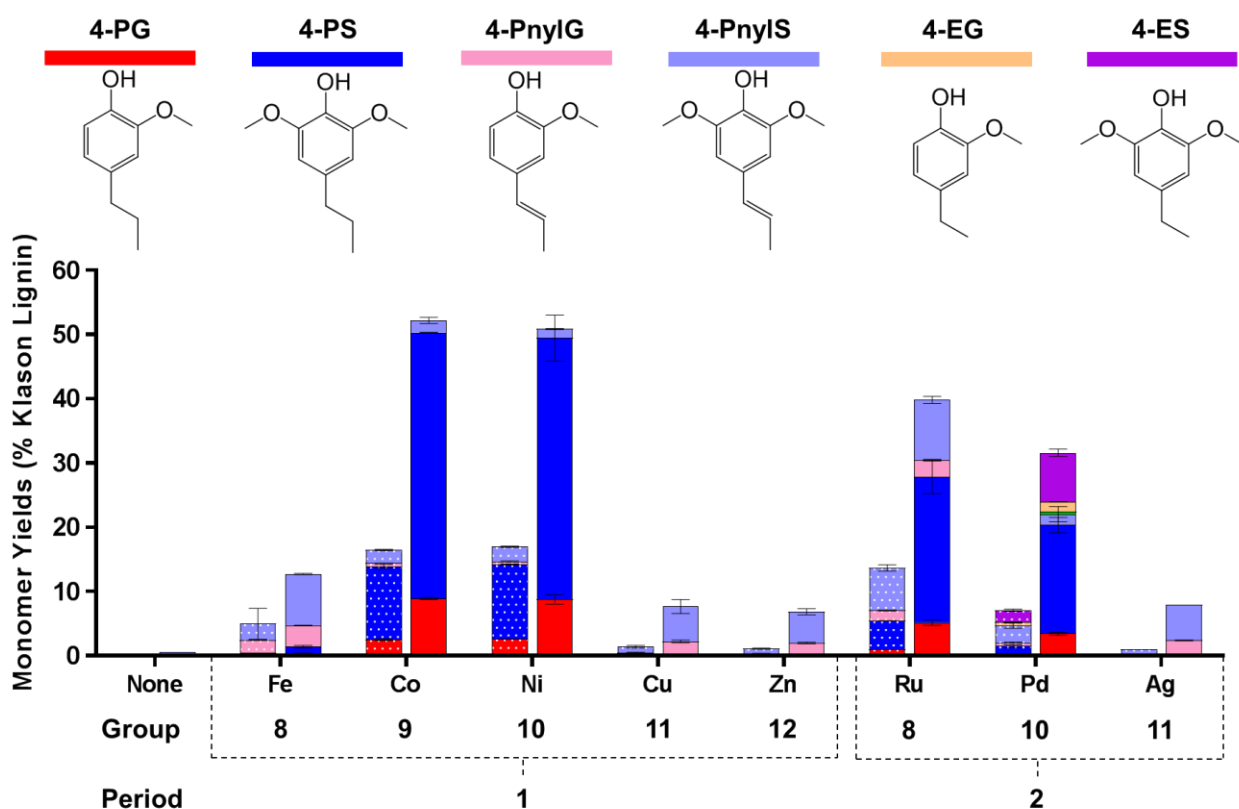


Figure 5.1. Monomer yields from hydrogenolysis reaction at 200 °C (patterned) and 220 °C using different metal/C catalysts with whole biomass. The results are arranged according to group and period in the periodic table. The column “None” refers to no catalysts added. The products are, from left to right, 4-propylguaiacol (4-PG), 4-propylsyringol (4-PS), 4-propenylguaiacol (4-PnylG), 4-propenylsyringol (4-PnylS), 4-ethylguaiacol (4-EG), 4-ethylsyringol (4-ES). The very small green color in Pd corresponds to syringol.

From a general observation of Figure 5.1, it can be seen that the highest monomer yields obtained by using whole biomass as a substrate were obtained from Co and Ni catalysts at ~50% with Ru and Pd also resulting in relatively high yields. Not using catalyst resulted in virtually zero monomers. Notably, there is a large difference between the temperature of 200 and 220 °C. This is likely due to that at 220 °C resulted in significantly higher ethanol reforming activity as there was noticeable more bubbles and pressure upon opening the reactors. Noted that by arranging the results according to groups in periodic table (Figure 5.1), a volcano-plot like shape could be observed, particularly for period 1 where a sufficient number of metals was investigated. This suggests that the energetics related to adsorption and desorption of species on Co and Ni resulted in optimal reactivity. Interestingly, Co-based catalyst was also shown to yield highest amount of H<sub>2</sub> during low temperature ethanol reforming (400 °C).<sup>332</sup>

From each of the catalyst in Figure 5.1, we can see that not all of the catalysts that were previously reported for ethanol reforming (all except Zn and Ag) are working well, including Fe and Cu. For Fe, the low yields were likely to be caused by the high affinity of Fe with oxygen. From a previous theoretical study on ethanol reforming mechanism at, it is likely that ethoxy adsorbing species was formed at the interface. At the temperatures in the present study (compared to 800°C, where H<sub>2</sub> formation from Fe was comparable to Co and Ni),<sup>332</sup> the adsorbing species are likely to stick to the Fe surface. On the other side of the volcano, the reason why Cu does not work is likely to be opposite that of Fe. Studies have suggested low adsorption energy of ethanol on Cu surfaces. Therefore, higher temperatures than the current study (800°C) were typically used for ethanol reforming with Cu to produce high amount of H<sub>2</sub> likely by improving kinetics and lowering the solvent-solvent interactions.<sup>332</sup> Apart from this, the interaction between lignin and the Cu itself was also low. It was even showed that lignin dimer solvated in ethanol at 50 °C did not adsorb on

Cu surface anymore.<sup>353</sup> Therefore, higher temperature should be used for Cu to reduce the solvent-solute interactions. In agreement with this analyses, in previous studies on catalytic transfer hydrogenolysis of lignin using Cu-based catalysts, studies have shown that a temperature of 300 °C was sufficient for Cu to generate significant H from methanol, resulting in almost complete conversion.<sup>228,354</sup> However, due to high temperatures, the products were also completely hydrogenated.

Apart from metals that were typically used for ethanol reforming, Zn and Ag were also investigated. It can be seen that both of which did performed hydrogenolysis as compared to no catalysts, they both resulted in ~7% monomer yields at 220 °C, similar to Cu (Figure 5.1). For Zn, it has been previously used as a co catalyst with Pd, where it was found through multiple characterization techniques that Zn deposited and form complex at activated carbon's -OH sites, where it was proposed to facilitate reaction either by help binding with hydroxyl groups of lignin or it could desorb from the surface as Zn<sup>2+</sup> ions from the reaction heat and deposited back upon cooling down. Nevertheless, in the present study, it is clear that not sufficient hydrogen was generated for both of these catalysts as evidenced by the low yields, and the products were virtually all composed of unsaturated propenyl side chain.

In the context of product types and distribution, it can be seen from Figure 5.1 that at 220 °C, the metal Co, Ni, Ru, and Pd resulted in mostly 4-propylguaiacol (4-PG) and 4-propylsyringol (4-PS). The catalyst Cu and Ni gave the highest amount of saturated products and also the highest selectivity based on the native lignin's units (>96 % for both catalysts). In the native lignin, there are primarily two units, *i.e.* syringyl and guaiacyl, where the former has two methoxyl groups on its aromatic ring and the latter has one. The monomer products from each of these groups are expected to retain its original methoxyl group(s). Given that the S/G ratio of the

birch used in this study is 3.2 but the S/G ratio of the products from Co and Ni catalysts is 4.83 on average, this implies that more of the lignin's syringyl units underwent hydrogenolysis, and ~4% products from guaiacyl units were lacking assuming that monomers from syringyl have reached maximum. This could be due to several reasons, for example, the guaiacyl units of lignin could be less susceptible to hydrogenolysis, or more likely, higher number of the guaiacyl units are not linked by  $\beta$ -O-4 from both sides. As the reaction primarily aims at cleaving  $\beta$ -O-4, to generate monomer it is required that both ends of the unit are  $\beta$ -O-4 linkage. This could be supported by well-studied topic that during lignin biosynthesis, more guaiacyl units leads to less  $\beta$ -O-4 bonds.<sup>235</sup> Apart from these, a major portion of monomers from catalysts that resulted in low yield is contributed to unsaturated products, including 4-propenylguaiacol (4-PnylS) and 4-propenylsyringol (4-PnylG). The same is applied for reaction at 200 °C. Both of these suggest the insufficient generation of hydrogen adatoms in those conditions.

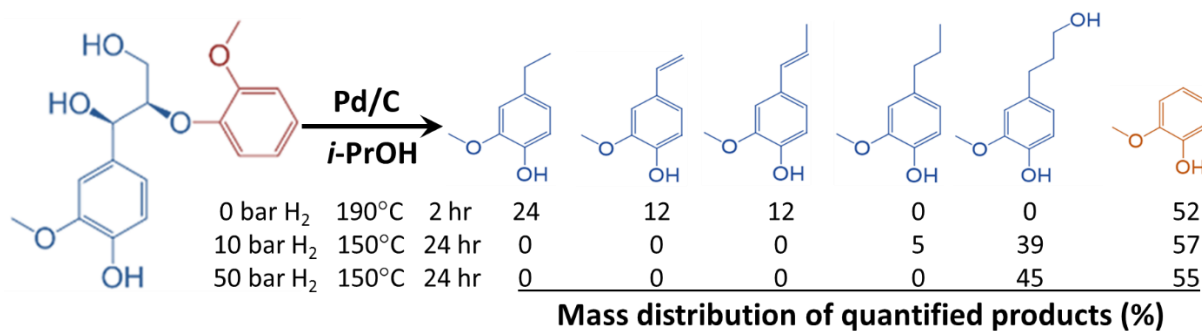


Figure 5.2. Monomer yields from hydrogenolysis reactions of lignin dimer (guaiacylglycerol-beta-guaiacyl ether) using Pd/C in ethanol with and without presence of H<sub>2</sub> gas. The 4-vinylG and 4-PnylG refer to 4-vinylguaiacol and 4-propenylguaiacol, respectively.

Among all of the catalysts, Pd is the only catalyst that gave unique products including 4-ethylguaiacol (4-EG), 4-ethylsyringol (4-ES), and a very tiny amount of syringol (result not shown in Figure 5.1 as it is visually too small). Additionally, unlike other catalysts that were reported to yield similar products whether there is with or without H<sub>2</sub> added such as Ni/C. The product 4-EG

and 4-ES were not reported in previous studies using that use Pd/C with H<sub>2</sub> gas. To ensure that our reactions and product identification is accurate, a lignin dimer (guaiacylglycerol-beta-guaiacyl ether) was employed for further investigation. Lignin dimer was used to eradicate any other possible side reactions or contributions from other linkages in real lignin.

Figure 2 shows the different products obtained from lignin dimer hydrogenolysis on Pd/C with and without presence of H<sub>2</sub> gas. Without hydrogen gas, a similar product profile to lignin was generated. However, addition of H<sub>2</sub> gas resulted in products (4-propanolguaiacol, 4-PnolG) that are similar to previous studies.<sup>266</sup> Specifically, if we look at difference H<sub>2</sub> pressure in Figure 5.2, we could see that at lower pressure, 4-PG was produced (possibly more if the pressure was ever lower). However, it totally disappears at high pressure. These suggest that lignin on Pd/C undergoes different reaction path in presence of H<sub>2</sub>, and was likely dependent of the hydrogen coverage at the metal-liquid interface. Future studies to probe into the effect of hydrogen coverage on different catalyst would make an interesting future study. Note that the results in Figure 5.2 are estimated from peak areas and were not quantified, therefore, yields were not reported. Additionally, the temperature of the one with H<sub>2</sub> gas was slightly lower due to reactor limits, while the other one needs to be at higher temperatures to ensure sufficient hydrogen is produced. The longer reaction time was used for the one with H<sub>2</sub> to see if the product would eventually change.

### **5.5 Lower Monomer Yields from Low Quality Lignin**

To elucidate the importance of using high quality lignin for hydrogenolysis, a similar reaction condition at 220 °C using Ni/C catalyst was performed lignin obtained from alkali pretreated black liquor and precipitated through CO<sub>2</sub> sequential acidification. Noted that it was shown in our previous work that fraction precipitated at higher pH, *e.g.* RT-1, and temperature,

*e.g.* SLRPs, tend to have higher  $\beta$ -O-4 content than those precipitated at lower pH.<sup>286</sup> In the present samples, the  $\beta$ -O-4 of alkali lignin ranges from 15 to 31%.

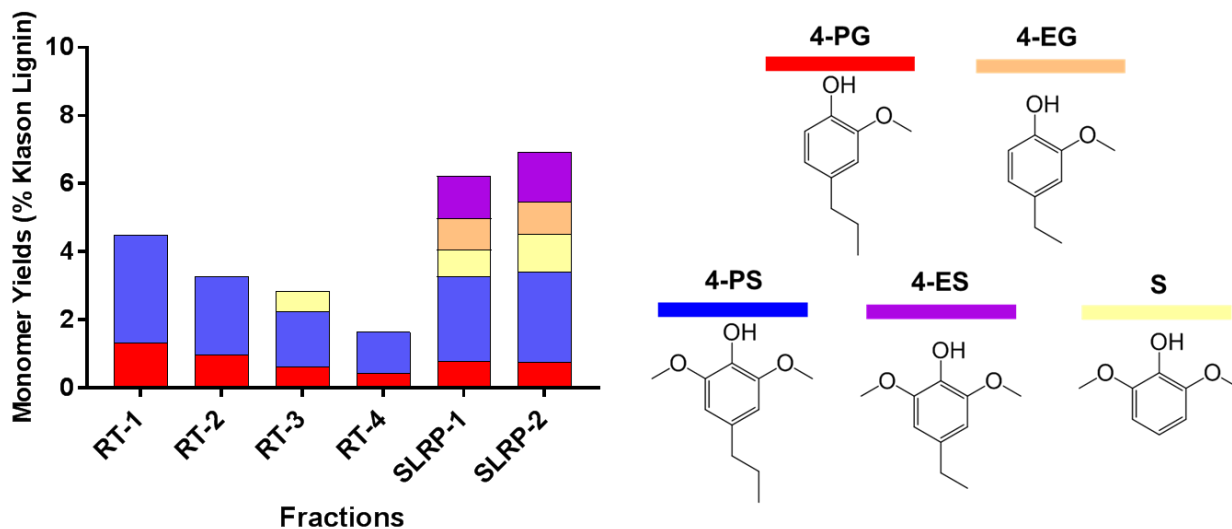


Figure 5.3. Monomer yields from hydrogenolysis reaction using Ni/C and ethanol at 220 °C of alkali lignin that was sequentially precipitated through CO<sub>2</sub> acidification. The S refers to syringol.

The hydrogenolysis yields from different fractions of alkali pretreatment show significantly lower monomer yields (Figure 5.3). Even the fraction precipitated at higher temperatures only resulted in ~7% yields compared to 50% when whole biomass is used. The 7% is close to yield approximation using  $\beta$ -O-4 content, *i.e.*  $0.3^2 = 0.09$ . This indicates that, similar to whole biomass, the hydrogenolysis reaction results in almost complete cleavage of  $\beta$ -O-4 linkages. However, the monomers from alkali lignin are different in that there are 4-EG and 4-ES that were only found from Pd/C previously. More importantly, significant amounts of syringol were produced. These indicate the capability of C-C cleavage of Ni/C that could be facilitated by certain functionality of alkali lignin that was induced from the acid precipitation, particularly SLRP. However, this is not within the scope of the present work and should be subject to future studies.

## 5.6 Characteristics of the Pretreated Biomass and Enzymatic Hydrolysis



Figure 5.4. Images of raw birch biomass (A), and after pretreatment at 220 °C in ethanol with no catalyst (B), and with Co/C catalyst (C).

After partial removal and hydrogenolysis, the biomass could now be considered pretreated. The physical color before and after pretreatment is shown in Figure 5.4. Comparing between before pretreatment (Figure 5.4A) and after pretreatment without catalysts (Figure 5.4B), it can be seen that biomass has become significantly darker, despite compositional analysis indicating that pretreatment without catalyst removes 42% of the lignin (Figure 5.5). This indicates that lignin was melted during the process and redeposited on biomass surface, which is a common phenomenon observed previously in dilute acid pretreatment and is expected to retard cellulose accessibility.<sup>355</sup> With addition of Co/C catalyst it is clear that the color becomes lighter (Figure 5.4C), suggesting of more lignin removal.

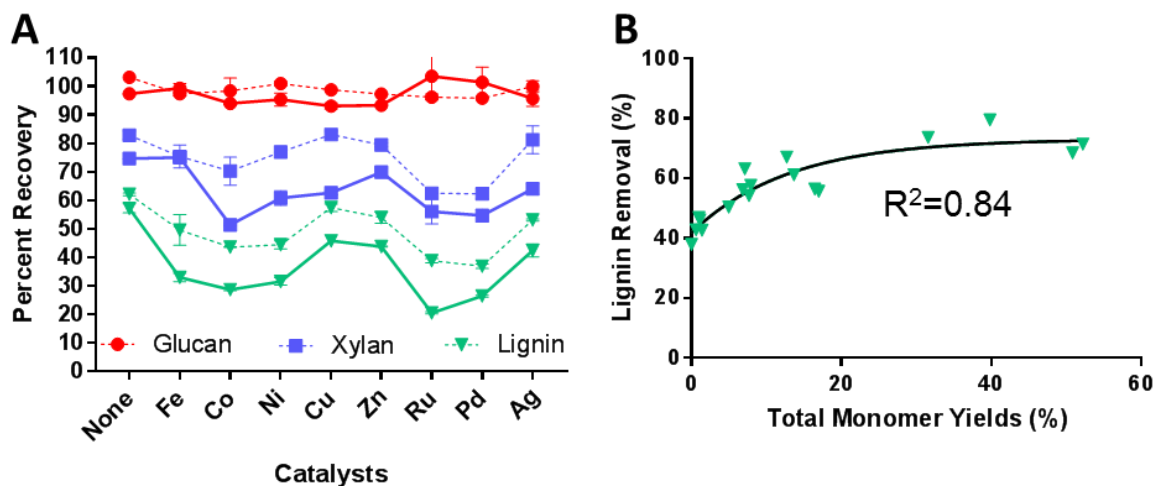


Figure 5.5. Percent recovery of glucan, xylan, and lignin after pretreatment at 200 (dotted line) and 220 °C in ethanol with different metal/C catalysts (A). The correlation between total monomeric yields and lignin removal (100 – lignin recovery) (B).

A summary of percent recovery of each main biomass component after pretreatment is shown in Figure 5.5A. Noted that untreated birch was characterized with 41% glucan, 20% xylan, and 20% lignin. Overall, it was shown that cellulose was successfully reserved even after the reaction at 220 °C. However, hemicellulose was partially lost particularly at the higher temperature. Catalysts seem to have some effect on the loss of hemicellulose, most likely through its hydrogenolysis. Hydrogenolysis of hemicellulose at similar conditions was previously reported to result in soluble sugars without further hydrogenations,<sup>37,226</sup> which should theoretically be recoverable from the liquid fraction. More noticeably, for lignin recovery there seems to be an inverse-shaped volcano plot, indicating that lignin removal could be correlated to monomer yields. The correlation is shown in Figure 5.5B, where it can be seen that the relationship is not entirely linear as it seems to flatten out in for higher monomer yields. This could be due to couple of reasons. First, the maximum amount of lignin removal was reached. Second, the dimers and other ethanol soluble products from some catalysts were not taken into consideration. These products

are not likely to redeposit on biomass, and hence higher lignin removal even though monomer yields were not as high.

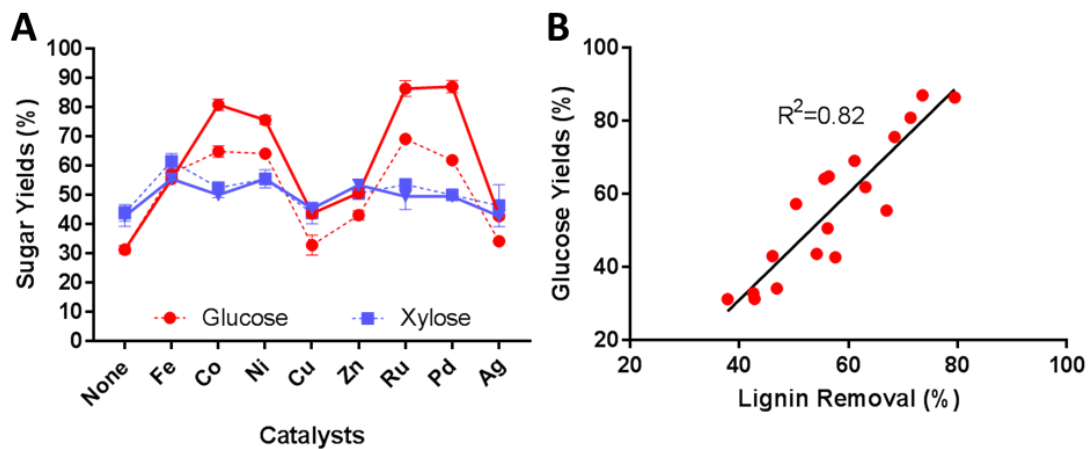


Figure 5.6. Enzymatic hydrolysis yields of the biomass after the reaction at 200 (dotted line) and 220 °C in ethanol with different metal/C catalysts (A). The sugar yields are based on the untreated biomass compositions. The correlation between lignin removal and glucose yields (B).

Lastly, effects from pretreatment on enzymatic hydrogenolysis is evaluated. Noticeably, there is also a volcano-plot like for the glucose yields (except from Cu to Zn, Figure 5.6). This reflects the effect from lignin and hemicellulose removals on hydrolysis yields. Without any catalyst, the glucose yields were only 31%, whereas the glucose yields >75% could be obtained from reactions that added Co/C, Ni/C, Ru/C, and Pd/C using a temperature of 220 °C. Noted that the slightly higher glucose yields from Pd and Ru catalysts was because they preserved slightly higher amount of glucose. For xylose yield, it does not exhibit a strong trend because those that could yield higher xylose, such as Co/C, also has higher loss of xylan after pretreatment. Overall, this indicates that adding catalysts, such as Co, Ni, Ru, and Pd catalysts did not only result in high monomers from lignin hydrogenolysis, but also significantly promote accessibility of enzymes to cellulose and hemicellulose.

## 5.7 Conclusion

The present study has conducted a comparison of lignin catalytic transfer hydrogenolysis from ethanol using different supported metal catalysts with the goal of demonstrating their effects on both aromatic monomer yields and pretreatment efficacy. Selecting catalysts that were previously used for study of ethanol reforming, we found that in term of total monomer yields at 220 °C, Co/C gave the highest amounts (52%) followed by Ni/C, Ru/C, and Pd/C. All of these catalysts also exhibited high selectivity, particularly for Co/C and Ni/C. Interestingly, Co/C is an promising candidate that has not been used for this purpose previously. It was also affirmed that hydrogenolysis at this condition relies heavily on the quality of the substrate, *i.e.*  $\beta$ -O-4 content, as evidenced by significantly lower yields (~7%) when using alkali.

Apart from lignin valorization, the reaction is also a pretreatment in itself. It was shown that after the reaction, cellulose was essentially preserved in all cases, whereas hemicellulose was lost. The loss tends to be higher with catalysts that generate higher monomer yields. This is similar to lignin, although more lignin is removed than hemicellulose (down to as low as 20% of the original). The evaluation of its efficacy as a pretreatment was determined by sugar yields from enzymatic hydrolysis. Similarly, it was found that catalysts that resulted in high monomer yields tend to also result in more glucose yields. This was likely because of higher lignin removal from those catalysts. Therefore, through comparison of different catalysts, our results suggest that addition of catalysts have a large impact not on just monomer yields, but also pretreatment aspect of the biomass. Therefore, selecting a proper catalyst for lignin-first approach is vital and further development, such as alloying or support modification, is needed for a robust and cost-effective catalyst.

## CHAPTER 6 Summary and Outlook

In the present thesis, a complete application of DFT has been used to get adhesion values, fundamental understanding of the solid/solid interface, predictive models, and recommendations for experiments. From the simulations at the SOFC's interface, it was found that unlike most other oxides, CuO has a strong interaction with Ag, and is almost 5 times stronger than that of YSZ. Moreover, during the brazing of the Ag in air, diffused oxygen in Ag also partially promotes the interfacial interactions. With these, the Ag-CuO system was able to wet and adhere strongly to the YSZ surface. The strong Ag/CuO adhesion was identified to be due to the CuO chemical properties and unique surface structure. Using this knowledge, a descriptor was formulated based on a combination of these factors and validated with a number of different oxides. Using this descriptor which allows quicker estimation of Ag/oxides adhesion for materials search, new multivalent oxides that will be stable in SOFC operating conditions while also providing strong adhesion with Ag were identified, such as  $\text{CuAlO}_2$  and  $\text{Cu}_3\text{TiO}_4$ . The descriptor can have wider impacts for materials search in Ag/oxide interfaces, such as thin film growth or coating applications.

Due to the complexity of the problem, in the liquid/solid interface, DFT was only employed to draw insight from a solvated lignin dimer on catalyst surfaces, and not for development of screening models. To reduce the complexity of lignin and render it small enough for DFT simulations, spectroscopic and wet chemistry methods showed that despite the variability and complexity of lignin polymer,  $\beta$ -O-4 linkage emerges as the primary functional group that determines the amount of monomer yields for hydrogenolysis. A model was also developed and validated to show that using this functionality alone was sufficient to predict theoretical maximum monomer yields. Therefore, a dimer containing just this linkage was used for DFT simulation. The

simulation of a  $\beta$ -O-4 dimer adsorption on Ni(111) and Cu(111) surface shows that, in a vacuum, the dimer prefers to adsorb on the metal surfaces with both aromatic rings parallel to the surfaces, where Ni(111) shows significantly higher adsorption energy. Upon solvation with an explicit model that represents ethanol with density at 50 °C, it was found that the lignin dimer still adsorbs on the Ni(111) surface with a similar conformation. However, it no longer adsorbs on the Cu(111) surface. This implies that Cu(111) may not be an effective catalyst, particularly at lower temperatures. It should be noted that representing solvation using implicit models could not describe the solvent-lignin interactions accurately. To circumvent the large liquid/solid interface calculations, a model based on a thermodynamic cycle was developed for prediction of dimer adsorption energy for a given solvent and catalyst. Although the model is not suitable for large screening, it facilitates understanding for solvent selection by providing quantification to the solvent effect. Performing catalytic hydrogen transfer reactions on lignin shows that using Ni-based catalysts did result in much larger yields than a Cu-based catalyst. This is partly due to low lignin-Cu interactions; however, it is also contributed by other factors, and among those is lower amount of hydrogen produced from ethanol in Cu(111).

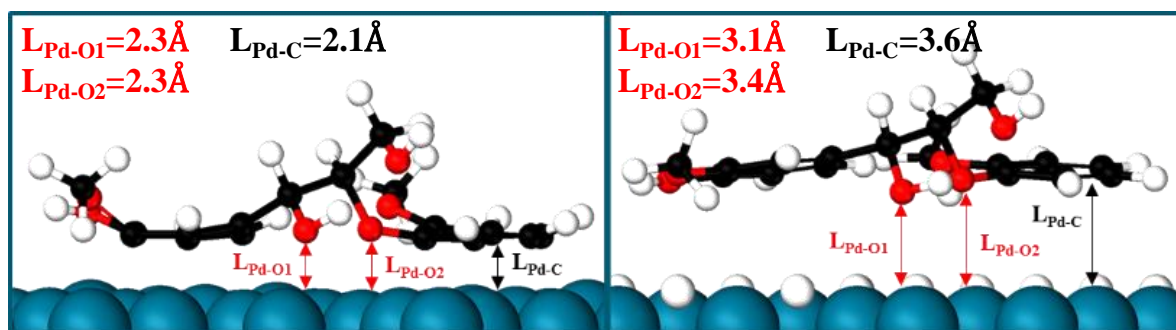


Figure 6.1. Lignin dimer adsorption on Pd (111) with 0 and 0.33 ML hydrogen coverage.

Although the present thesis has shed light the effect of solvent at the catalyst surface for lignin reactions, there remains many other phenomena at the interface that need to be explored in

order to fully comprehend the reaction and for catalyst design. Naturally, one of those is the solvent effect beyond adsorption, *i.e.* on the reaction pathways. Stabilization of the intermediates from different solvents may favor different reaction paths and different energy barriers.

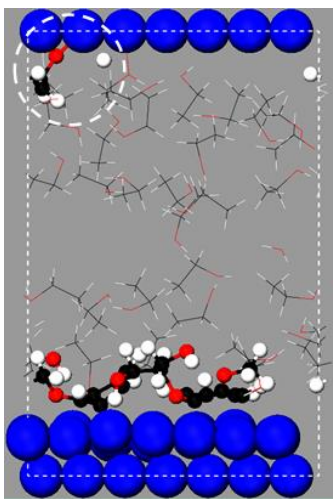


Figure 6.2. *Ab initio* shows alcohol decomposition leads to H and ethoxy adsorbing species on Ni(111).

Other phenomena that would affect lignin hydrogenolysis are the effects from other adsorbing species. For example, one of those is the effect of hydrogen coverage. As we have briefly discussed in Chapter 5, different hydrogen pressure could result in different products. Preliminary DFT calculations support the hypothesis by showing that on the Pd(111) surface, a hydrogen coverage of 0.33 ML on the surface leads to much weaker adsorption as shown by the distance between the dimer and surface shown in Figure 6.2. As many liquid and gas phase experiments used excessive H<sub>2</sub> gas, study on this topic may reveal that having higher H<sub>2</sub> does not necessarily always lead to higher catalytic activity. More importantly, it would provide valuable insight on how hydrogen coverage affects reaction energy barriers as well as reaction pathways.

The other type of surface coverage is that, instead of pressurizing with H<sub>2</sub> gas, it could be covered with other intermediates from solvents, such as when hydrogen is obtained through

catalytic hydrogen transfer from ethanol. This represents challenging simulations as it involves two concurrent reactions – ethanol decomposition and lignin hydrogenolysis. As detected in the preliminary *ab initio* molecular dynamics shown in Figure 6.1, ethanol decomposed to an ethoxy and hydrogen adatoms. While the hydrogen will be used for hydrogenolysis and its coverage is expected to be low, the ethoxy adatom could affect the reaction rate depending on its interaction with the catalyst. These topics will make an interesting subject for future studies as the understanding could have a wider impact on more than just lignin hydrogenolysis, particularly on other reductive reactions using different hydrogen sources and pressures.

## **APPENDICES**

## APPENDIX A: Supplementary Materials for Chapter 2

Table A1. List of all the studied metals and oxides, including their crystal structures, lattice constants, surface energies from the present work, along with comparisons to experiment values, and the calculated values for the descriptor ( $\chi_{MO}$ ) as shown in Eqn. 2.4. All computational values are based on LDA functional unless otherwise stated.

Structural Info.	Metal/Oxide	Lattice constants (Å)		$\gamma$ (J/m <sup>2</sup> )			$\Delta H_{f,MO}$ (ev)	$N_M, N_o$	$E_{M-O}$	$A_{MO}$	$\chi_{MO}$
		Present	Exp.*	Present	Others	Exp.					
Metallic <i>Fm-3m</i> (111)	Ag	4.1474 <sup>PBE</sup>	4.0857	0.77 <sup>PBE</sup>	0.75 <sup>356, PBE</sup>	1.24 <sup>182</sup>	-				
		4.0035		1.10	1.15 <sup>357</sup>						
	Ag(l)	-	-	0.77±0.01 <sup>PBE</sup>	-	0.93 <sup>358</sup>	-				
	Ag(l)	with O at surface		0.67±0.01 <sup>PBE</sup>	-	-	-				
Corundum <i>R-3c</i> (0001) <sub>M</sub>	$\alpha$ -Al <sub>2</sub> O <sub>3</sub>	4.7333, 4.7533, 12.9177	4.7590, 4.7590, 12.9910	2.08	2.13 <sup>361</sup>	1.69 <sup>362</sup>	-17.42	6, 3	-1.45	19.40	0.855
		4.9388, 4.9930, 25.9979									
	$\alpha$ -Fe <sub>2</sub> O <sub>3</sub>	5.0083, 5.0083, 13.5404	5.0350, 5.0350, 13.7200	1.52	1.60 <sup>365, ‡</sup>	1.90 <sup>366</sup>	-9.81	3, 3	-0.82	21.73	0.094
		In <sub>2</sub> O <sub>3</sub>	5.5042, 5.5042, 14.5231	5.4870, 5.4870, 14.5100	1.58	-	-	-9.78	6, 3	-0.81	26.24
Rock salt <i>Fm-3m</i> {100}	BaO	5.4803	5.5230	0.46	0.53 <sup>368</sup>	-	-5.64	2, 1	-0.94	15.02	0.116
	CaO	4.7203	4.8105	0.85	0.88 <sup>368</sup>	1.31 <sup>369</sup>	-6.78	2, 1	-1.13	11.14	0.190
	CdO	4.6546	4.6953	0.82	-	-	-2.57	2, 1	-0.43	11.01	0.065
	MgO	4.1457	4.2112	1.26	1.20 <sup>368</sup>	1.20 <sup>370</sup>	-6.40	2, 1	-1.07	8.50	0.235
	NiO	4.0600	4.1684	1.28	1.14 <sup>371</sup>	1.38 <sup>364</sup>	-3.48	2, 1	-0.58	8.24	0.124
Fluorite <i>Fm-3m</i> (111) <sub>O</sub>	c-CeO <sub>2</sub>	5.4151	5.4110	1.01	1.00 <sup>372</sup>	1.20 <sup>373</sup>	-11.54	2, 1	-1.44	12.70	0.216
	c-ZrO <sub>2</sub>	5.1175 <sup>PBE</sup>	5.0700	0.81 <sup>PBE</sup>	0.79 <sup>374, PBE</sup>	-	-19.09	2, 1	-2.39	10.96	0.423

Table A1 (cont'd)

		5.0320		1.18	–							
	c-YSZ <sup>†</sup>	7.2373, 7.2373, 15.3526	–	0.70 <sup>PBE</sup>	1.04 <sup>375, †</sup>	1.23 <sup>94</sup>	-421.77	8, 4	-2.29	43.86	0.405	
		7.1163, 7.1163, 15.0960	–	1.42								
Antifluorite <i>Fm-3m</i> (111) <sub>M</sub>	Rb <sub>2</sub> O	6.5600	6.7400	0.25	–	–	-3.72	2, 0	-0.46	18.62	0.025	
Tenorite <i>C2/c</i> (111)	CuO	4.6939, 3.4318, 5.1426 <sup>PBE</sup>	4.6530, 3.4100, 5.1080	0.72 <sup>PBE</sup>	0.74 <sup>148, PBE</sup>	–	-1.94	2, 1	-0.65	17.52	0.066	
		4.5359, 3.3422, 5.0054		1.16	–	–						
Tenorite <i>C2/c</i> (111)	Cu <sub>2</sub> O	4.2772	4.2696	0.65 <sup>PBE</sup>	0.67 <sup>376, PBE</sup>	–	-2.06	2, 1	-0.51	29.50	0.030	
		4.1271		0.94	–	–						
Zincite <i>P6<sub>3</sub>mc</i> (010)	ZnO	3.2044, 3.2044, 5.1373	3.2493, 3.2493, 5.2054	1.10	–	–	-3.45	2, 1	-0.86	28.51	0.097	
Rutile <i>P4<sub>2</sub>/mnm</i> (110)	SnO <sub>2</sub>	4.7309, 4.7309, 3.1958	4.7373, 4.7373, 3.1864	1.46	1.29 <sup>377</sup>	–	-6.33	3, 2	-1.05	21.38	0.135	
	TiO <sub>2</sub>	4.5716, 4.5716, 2.9269	4.5940, 4.5940, 2.9590	0.97	0.90 <sup>378</sup>	–	-10.03	3, 2	-1.67	18.92	0.250	
Anatase <i>I4<sub>1</sub>/amd</i> (101)	TiO <sub>2</sub>	3.7652, 3.7652, 9.4766	3.7760, 3.7760, 9.4860	0.82	0.52 <sup>379, PBE</sup>	–	-8.62	4, 2	-1.44	19.27	0.284	
Delafossite <i>P 63/mmc</i> (for CuAlO <sub>2</sub> ) or <i>R-3m</i> (0001) <sub>O</sub>	CuAlO <sub>2</sub>	2.8218, 2.8218, 11.1750	2.858, 2.858, 11.293 <sub>380</sub>	3.02	3.47 <sup>187, HF</sup>	–	-9.69	1, 1	-1.21	6.88	0.156	
	CuCrO <sub>2</sub>	2.9393, 2.9393, 16.7759	2.9734, 2.9734, 11.400 <sub>381</sub>	1.40	–	–	-10.11	1, 1	-1.26	7.48	0.150	
	CuFeO <sub>2</sub>	2.7498, 2.7498, 17.1314	3.035, 3.035, 11.449 <sub>382</sub>	1.08	–	–	-8.51	1, 1	-1.06	6.54	0.141	

Table A1 (cont'd)

	CuGaO <sub>2</sub>	2.9510, 2.9510, 17.0000	3.011, 3.011, 11.441 <sub>383</sub>	2.82	–	–	-6.76	1, 1	-0.85	7.54	0.094
	CuInO <sub>2</sub>	3.3052, 3.3052, 17.1665	3.3831, 3.3831, 11.551 <sub>383</sub>	2.54	–	–	-5.70	1, 1	-0.71	9.46	0.061
Cu <sub>3</sub> TiO <sub>4</sub> P2 <sub>1</sub> /c (010) <sub>o</sub>	Cu <sub>3</sub> TiO <sub>4</sub>	2.9188, 11.1783, 6.6167	3.090, 5.272, 11.552 <sub>384</sub>	1.76	–	–	-13.12	2, 2	-0.82	15.86	0.086

\*lattice constants were taken from the default structures in Material Studio unless cited,

<sup>PBE</sup> values from PBE functionals,

<sup>‡</sup> values from GGA with full-potential linearized augmented plane wave,

<sup>HF</sup> values from Hatree-Fock,

<sup>†</sup> lattice constants were supercell of ZrO<sub>2</sub> and substituted with Y to obtain 9%-doped yttria,

<sup>†</sup> 12.5%-doped yttria,  $\Delta H_{f,MO}$  is defined by  $\Delta H_{f,MO} = E_{oxide} - (n_M \cdot E_{metal} + n_O \cdot E_O)$ , where  $E_{oxide}$  is the energy of the oxide cell per formula,  $n_M/n_O$  is the number of metal/oxygen in the oxide structure,  $E_{metal}$  is the energy of metal per atom taken from its bulk structure, and  $E_O$  is the energy of atomic oxygen taken from half of the oxygen gas.

## A.1 Surface Energy Calculation

The surface energies for stoichiometric symmetric slabs were calculated from the formula,

$$\gamma = \frac{E_{slab} - nE_b}{2A}$$

, where  $\gamma$  is the surface energy,  $E_{slab}$  is the calculated energy of the slab,  $n$  is the molecular ratio between the slab to the bulk formula,  $E_b$  is energy of the bulk structure, and  $A$  is the surface area of the slab.

For stoichiometric asymmetric slabs, including in the delafossite and Cu<sub>3</sub>TiO<sub>4</sub>, the surface energies were estimated based on an average between both surface terminations as follow,

$$\gamma = \frac{\gamma_I + \gamma_{II}}{2} = \frac{E_{Slab}^I + E_{Slab}^{II} - nE_b}{4A}$$

, where  $E_{\text{Slab}}^{\text{I}}$  and  $E_{\text{Slab}}^{\text{II}}$  are the energy of the non-stoichiometric symmetric slabs of the two terminations present in the stoichiometric slab, and  $n$  is the molecular ratio between the combined slabs and the bulk formula.

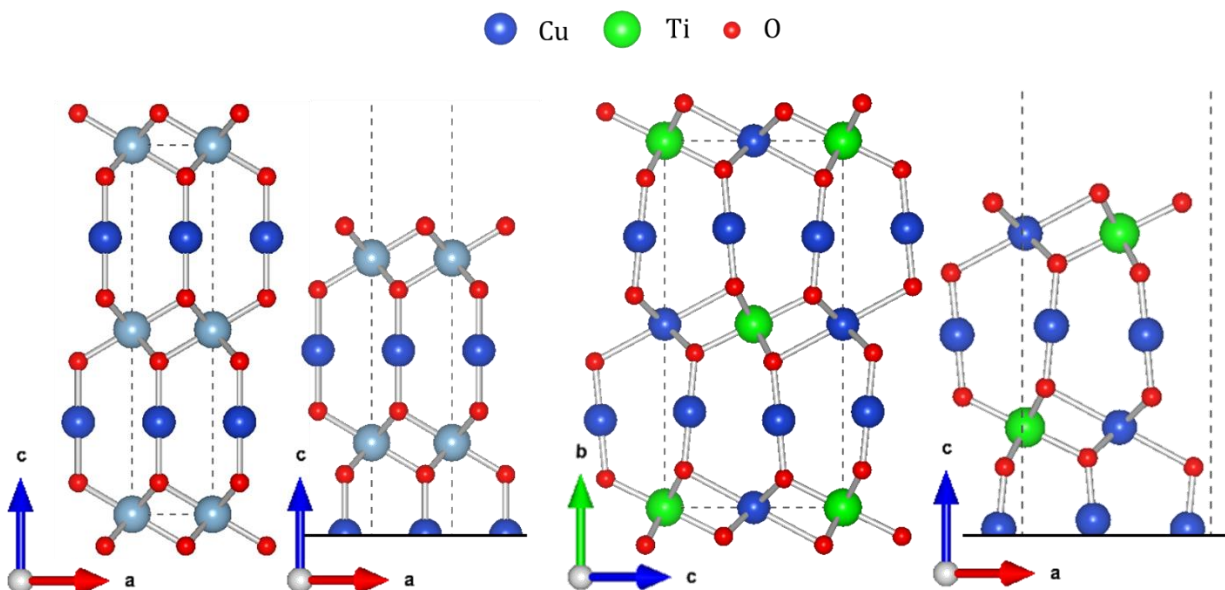


Figure A1. The relaxed bulk structure of  $\text{CuAlO}_2$  (a) and its  $(0001)_{\text{O}}$  surface (b). The relaxed bulk structure of  $\text{TiCu}_3\text{O}_4$  (c) and its  $(010)_{\text{O}}$  surface (d).

## A.2 Energetics and Orientations of the Individual Surfaces

In the present study, two metals and six types of oxide structure were investigated. The surface energies of these components are listed in Table A1 with some obtained by both PBE and LDA functionals for benchmarking purposes throughout the study. For individual surface energies, it was found that results from LDA functional, as obtained from metals,  $\text{ZrO}_2$ , and  $\text{CuO}$ , conformed better with experiments. Similar preference for LDA was also reported in a recent study where PAW potentials and GGA functional, which is typically regarded as a more superior one, were used for calculation of work functions, but particularly for surface energy, LDA was chosen for the reason that it yielded results closer to experiments.<sup>357</sup> Therefore, most of the results presented

in this study, including Table 2.1, will be based on LDA functional. Nonetheless, we expected that the trends of surface energy among oxides and metals will be the same for both functionals. Hereafter, mentions of metals/oxides surface in the present study are referred to the phase and surface presented in Table A1 unless otherwise stated.

For oxides of corundum structure, the stoichiometric surface (0001) with a single metal atom per unit cell at the surface termination was chosen for this study (Figure A5). It should be noted that in practice the surfaces of many corundum oxides could coexist in two forms, (0001) and ( $1\bar{1}02$ ) due to extremely close surface energies.<sup>367,385,386</sup> Previous studies have reported that for (0001) surface of  $\text{Al}_2\text{O}_3$ ,  $\text{Cr}_2\text{O}_3$ ,  $\text{Fe}_2\text{O}_3$ , and  $\text{Rh}_2\text{O}_3$ , the single metal atom termination was the most stable over a wide range of oxygen chemical potential.<sup>367,387–389</sup> No information was found for corundum  $\text{In}_2\text{O}_3$ , but it was expected to be the same. The (0001) surface used in this study was relaxed with more stringent criteria (force  $< 0.015$  eV and broken symmetry) because of potential surface reconstruction. Upon relaxation, all of the corundum oxide' surfaces investigated in the present study exhibited substantial change, wherein the top metal atom exhibited an inward relaxation toward the bulk (Figure A5). In relative to the bulk structure the position moved inward by 76, 58, 97, and 45% for  $\text{Al}_2\text{O}_3$ ,  $\text{Cr}_2\text{O}_3$ ,  $\text{In}_2\text{O}_3$ ,  $\text{Rh}_2\text{O}_3$ . Previous study on  $\text{Al}_2\text{O}_3$  using GGA functional and experiments also reported *ca.* 80% inward movement of an Al atom.<sup>390–392</sup> The inward movement of the top metallic atom was likely in order to minimize the energy from a numbers of dangling bonds at the metal atom. To an even greater extent, the inward movement of the surface Fe in  $\text{Fe}_2\text{O}_3$  was 163%, meaning it submerged into the sublayer (Figure A5d). This inward movement of the atom for  $\text{Fe}_2\text{O}_3$  was tested in both ferromagnetic and antiferromagnetic state, both of which yielded the same configuration. These changes were expected to affect adhesion properties, particularly in case of  $\text{Fe}_2\text{O}_3$ . The drastic change in the position of the metal

atom in  $\text{Fe}_2\text{O}_3$  and  $\text{In}_2\text{O}_3$  could contribute to their lower surface energy in relative to most other corundum oxides in Table A1.

Within fluorite structure, the surface energy of cubic  $\text{ZrO}_2$  was obtained by both LDA and PBE functionals as it represented a YSZ surface, which is one of the main components in SOFC-related interface that will be investigated in more detail. The results indicated that using PAW potential with PBE functional, like in cases of CuO and metals, tends to underestimate the surface energy. It should be noted that the selection of (111) surface was not only supported by it being the lowest surface energy, but also adhesion of YSZ with metal interfaces were shown to occur on this surface.<sup>91</sup>

Cupric oxide's structure is one-of-a-kind due to its unpaired *d* electron inducing Cu magnetic moments and a cubic-to-monoclinic structural distortion.<sup>393</sup> The structure's most stable surface was reportedly to be (111).<sup>148</sup> It should be noted that majority of previous studies in CuO's electronic structure, and catalysis, employed lower  $U_{\text{eff}}$  of 4-7 eV with regards to PBE functionals.<sup>148,149,394,395</sup> However, the difference between experimental and our CuO's lattice constants was significant when  $U_{\text{eff}}$  was 7 eV. Since lattice constants would be more important given the context of this study, we employed a lesser used  $U_{\text{eff}}$  of 8.50 for Cu. The discrepancy between our results and previous computational studies is likely due to the higher cutoff energy in this study – 500 eV, whereas previous studies used 400 eV or less. Additionally, similar reasonable lattice constants were achieved if we used the cutoff energy of 400 eV.

For cuprite structure, previous computational study reported that (111) surface exhibited the lowest energy, with a caveat that symmetry must be broken during surface relaxation to facilitate its reconstruction, and hence, lower surface energy.<sup>376,396</sup> As the study was performed in

PBE functional, Table 2.1 also includes results from PBE functional for  $\text{Cu}_2\text{O}$  to ensure the present computational setup enabled us to achieve the lowest surface energy possible.

For zincite structure, it was reported to mostly exposed  $(2\bar{1}0)$  and  $(0\bar{1}0)$  surfaces.<sup>397</sup> However, computationally, our calculated surface energy showed slightly higher surface energy of the  $(2\bar{1}0)$  surface ( $1.21 \text{ J/m}^2$ ) than the  $(0\bar{1}0)$  surface ( $1.10 \text{ J/m}^2$ ). Therefore, the prediction was based on  $(0\bar{1}0)$  surface, although it should be noted that the  $W_{\text{adh}}$  from the prediction based on  $(2\bar{1}0)$  doesn't differ much (results not shown). For rutile phase, many studies have demonstrated that the  $(110)$  surface is the most stable ones for both  $\text{SnO}_2$  and  $\text{TiO}_2$ .<sup>377,378</sup> In case of  $\text{TiO}_2$ , the other morphology that was investigated was that of anatase structure. Anatase  $\text{TiO}_2$  was also previously shown computationally to have the lowest surface energy being  $(101)$ , which was also one of the most exposed surfaces on its synthesized thin films.<sup>398,399</sup>

Lastly, in delafossite structure there was limited literature on their surfaces. However, detailed investigation was conducted on surfaces of  $\text{CuAlO}_2$ . By using XPS, studies suggested that thin film of  $\text{CuAlO}_2$  on alumina exposed almost solely  $(0001)$  surface<sup>185,186</sup>. The surface was also shown computationally to be O-terminated.<sup>187</sup> As the structure of  $\text{Cu}_3\text{TiO}_4$  is similar to delafossite oxides, and its  $(101)$  is equivalent to the  $(0001)$  surface of delafossite. Therefore, the  $(101)$  surface of  $\text{Cu}_3\text{TiO}_4$  was used in this study.

### A.3 AIMD Simulation of the Liquid Ag/YSZ Interface

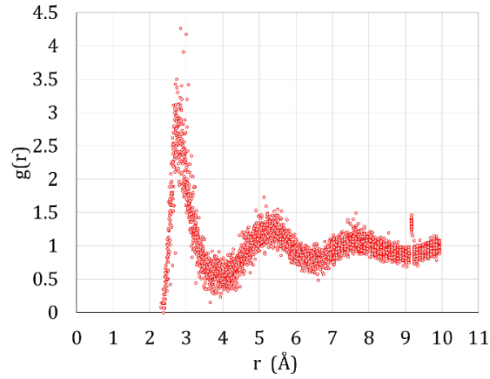


Figure A2. Pair radial distribution function of Ag-Ag in liquid Ag with 2 O atoms dissolved showing the nearest Ag-Ag distance of 2.8 Å, which is the same to the experimental value of pure silver measured in reducing atmosphere.

### A.4 Comparison to Previous Computational Study of Ni/ZrO<sub>2</sub>

The importance of using c-YSZ instead of c-ZrO<sub>2</sub> due to stability concerns was highlighted when comparing the  $W_{\text{adh}}$  with prior computational studies. Previous DFT studies of the Ni(111)/ZrO<sub>2</sub>(111) interface using the PBE functional with an ultrasoft pseudopotential indicated a  $W_{\text{adh}}$  of 1.00 J/m<sup>2</sup>.<sup>400</sup> Other studies using c-ZrO<sub>2</sub> also reported similar values at 1.12 and 1.28 J/m<sup>2</sup> when using the PBE functional with norm-conserving pseudopotential and linear combination of atomic orbital (LCAO) DFT.<sup>105,401</sup> All of these values are larger than the results of 0.49 J/m<sup>2</sup> from GGA-PBE functional in the present study on Ni(111)/YSZ interface. This is likely due to the phase instability of cubic ZrO<sub>2</sub>. Pure zirconia exists in a monoclinic phase at low temperature, tetragonal at 927 °C, and cubic at 2377 °C until its melting point.<sup>402,403</sup> To stabilize the cubic phase, 8%-40% yttria is necessary.<sup>153</sup>

Calculations on Ni(111)/c-ZrO<sub>2</sub>(111) interface calculations were performed with both GGA-PBE and LDA functionals. Upon relaxation, the cubic to tetragonal phase transition started from the interface region and propagated through the ZrO<sub>2</sub> slab. This led to an energy reduction of

the slab by 1.07 and 0.22 eV (54 and 11 meV per  $\text{ZrO}_2$  formula unit) for the GGA-PBE and LDA functionals, respectively. However, the cubic  $\text{ZrO}_2$  slab for surface energy calculations remained meta-stable cubic phase after minimization. Thus, according to Eqn. 2.1, the energy reduction of the interface slabs due to phase transformation would proportionally reduce the interface cell energy ( $E_{12}$ ), and consequently falsely increase the calculated  $W_{\text{adh}}$ . This might be the reason for the high  $W_{\text{adh}}$  at Ni(111)/c- $\text{ZrO}_2$ (111) interface in previous DFT studies.<sup>105,400,401</sup>

### A.5 Formation of Metal-Oxygen Bonds at the Interface

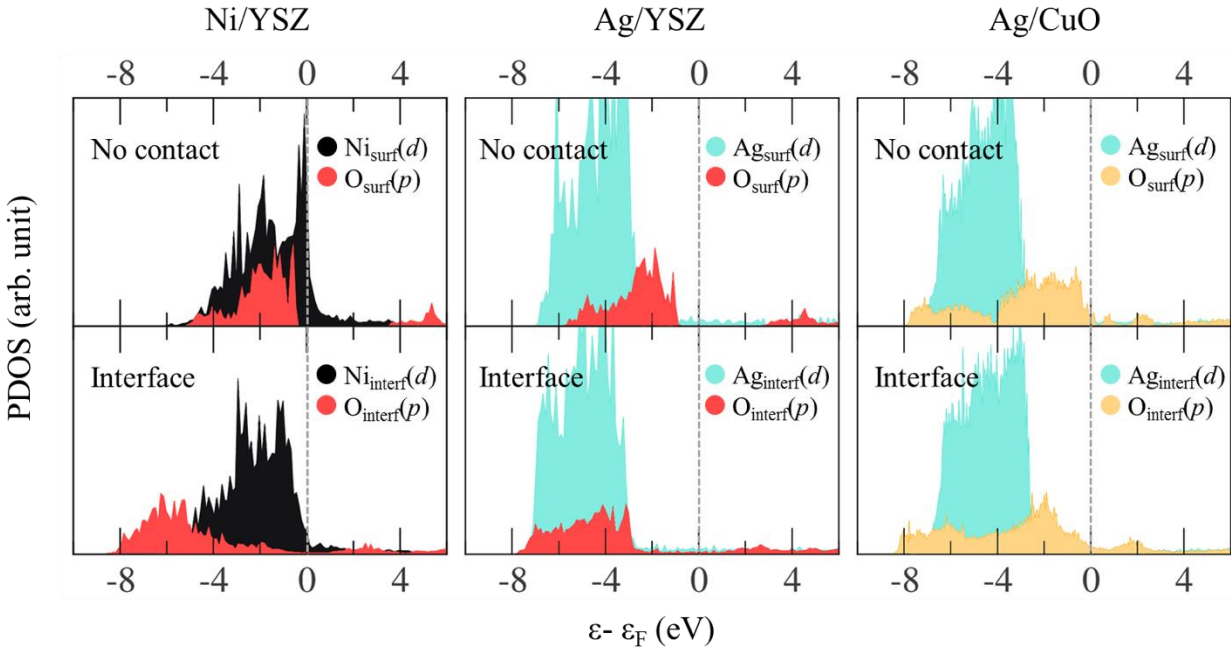


Figure A3. Projected density of states (PDOS) of interface atoms in Ni/YSZ, Ag/YSZ, and Ag/CuO in their no-contact positions (slabs were 10 Å apart) and in their interface position as calculated by LDA functional.

To obtain deeper insight into the nature of metal/oxide interface bonding, projected density of states (PDOS) calculations were generated for the interfaces shown in Figure A3. Firstly, before the slabs were put together to make the interfaces, PDOS calculations were performed on a no-contact configuration, where the metal and oxide slabs were separated by 10 Å. This serves as a

reference point as well as providing initial characteristics of individual slabs. Comparing the metals' PDOS in Figure A4, the range of energies of *d*-orbitals in Ni was wider than Ag and there a higher density of incompletely filled states evidenced by spilling across the Fermi level. This suggests an easier distribution of charges in Ni, and hence more polarizable than Ag. In the YSZ slab, a band gap in the O of 2.88 eV was observed. However, for CuO, the band gap was not very clear in the no-contact PDOS. This minor error was likely due to the disturbance of the CuO antiferromagnetic spins by the presence of Ag in spite of the 10 Å vacuum in between. A 0.28 eV band gap was obtained in (Figure A4) by removing the Ag slab and keeping the CuO slab in the same cell dimensions.

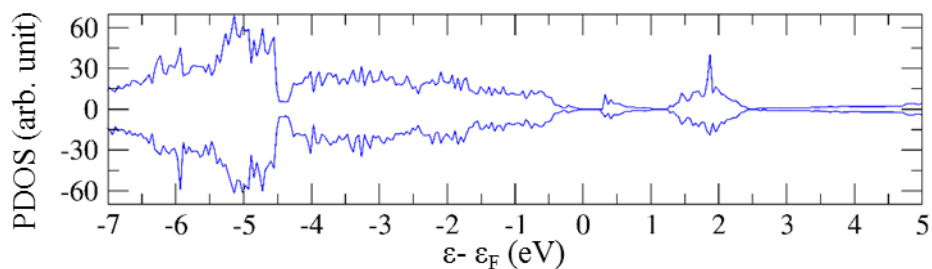


Figure A4. Projected density of states (PDOS) of CuO(111) surface with stretched lattice parameters to match that of the metals in the interface. It exhibited a bandgap of 0.25 eV.

Upon contact with the oxide surface, the noticeable feature of interface bonding observed in all three interfaces was the previously developed metal-induced gap states (MIGS) proposition, wherein the oxygen *p*-states spilled over into the band gap region (Figure A3).<sup>404</sup> This stemmed from the charge transfer at the interface in order to reach electrochemical potential equilibrium for electrons. Although the charge transfer, presumably from metals to the oxide oxygen atoms, would theoretically increase the energy of the oxide slabs, but the energy of the overall system was

reduced as a result of the charge transfer. This was manifested in the shift of the PDOS for both the metal and oxide toward lower energy states (Figure A4).

Principally, the strength of the bonds at the interface was attributed mostly by the appearance of bonding and anti-bonding states resulting from the coupling of the metal *d*-states and the oxygen *p*-states in the oxide, which are located below the oxide valence bands and above the metal *d*-bands, respectively.<sup>405</sup> It should be noted that non-bonding states could appear and mingle in between these two states. However, a definitive criterion separating these states cannot be drawn from PDOS diagrams due to complex deformation of dispersive bands.<sup>406</sup> Therefore, as an estimate, any occupied states whose energy was lowered corresponded to bond formation, whereas the opposite was observed for the anti-bonding.

The shifts in density of states shown in Figure A3 correspond well to the higher adhesion energy of Ni/YSZ than Ag/YSZ. In the Ni/YSZ interface, the formation of the bonding *p*-states below the metal *d*-states was noticeable as the majority of the *p* states at interface oxygen atoms shifted to under -5 eV, well below the oxygen valence bands in the no-contact states. The same phenomenon was observed in the Ag/YSZ interface, but to a much lesser extent. Lastly, for the Ag/CuO interface, the shift in *p*-states of the oxygen atoms was not as dramatic as those in YSZ structure. However, the trend was similar in that there is a lesser amount of the *p*-state in the anti-bonding region (~0 to -3 eV) and a higher population in the lower energy range of -4 to -8 eV. Overall, the PDOS showed several indications of the interaction between interface metal atoms and the oxygen atoms of the oxides.

## A.6 The Interface Energy and Work of Adhesion Descriptor

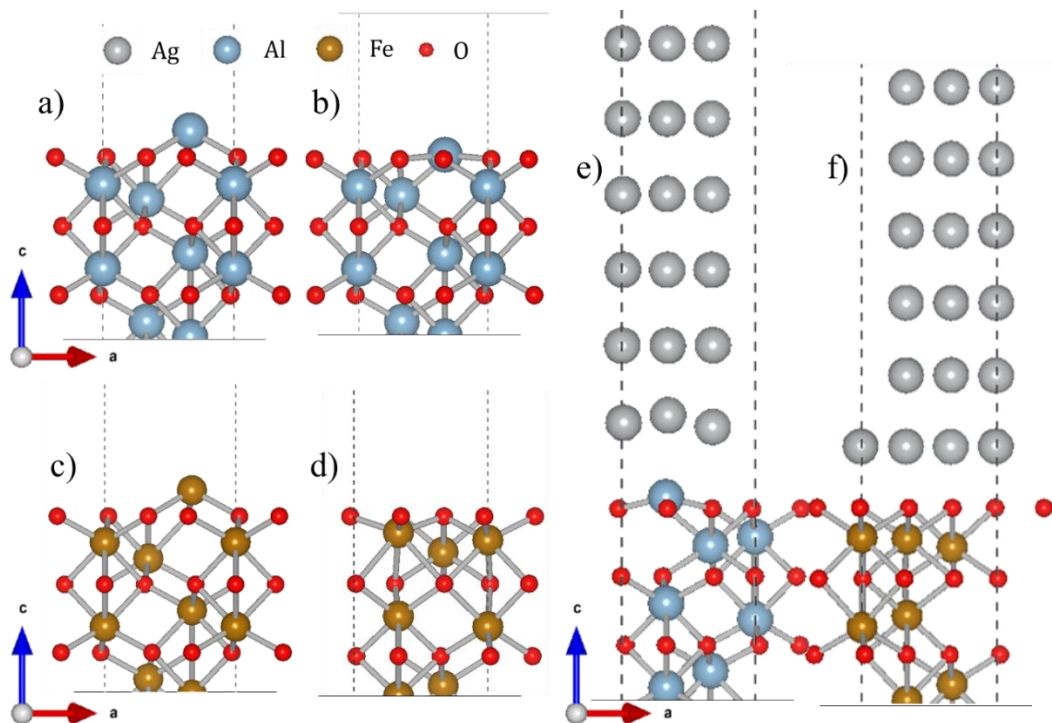


Figure A5. Surface structures showing the difference between the position of the terminated metallic atom of most corundum oxides (represented by Al<sub>2</sub>O<sub>3</sub>) and the Fe<sub>2</sub>O<sub>3</sub>. These are (0001) surface of initial Al<sub>2</sub>O<sub>3</sub> slab (a), relaxed Al<sub>2</sub>O<sub>3</sub> slab (b), initial Fe<sub>2</sub>O<sub>3</sub> slab (c), relaxed Fe<sub>2</sub>O<sub>3</sub> slab (d), relaxed Ag(111)||Al<sub>2</sub>O<sub>3</sub>(0001) interface (e), and relaxed Ag(111)||Fe<sub>2</sub>O<sub>3</sub>(0001) interface (f).

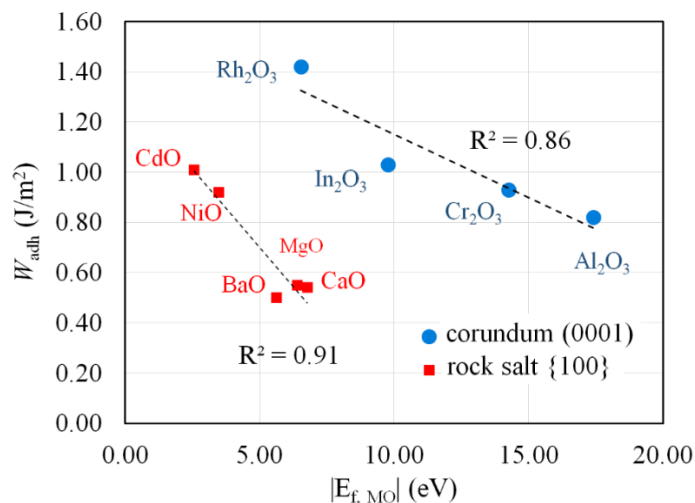


Figure A6. The correlation between  $W_{\text{adh}}$  and the oxide formation energy of (0001) surface corundum type oxide and {001} rock salt type oxide. Note that Fe<sub>2</sub>O<sub>3</sub> was not included for the reason that its geometry was unlike other corundum oxides after surface relaxation.

## APPENDIX B: Supplementary Materials for Chapter 3

Table B1. The Summary of quantified lignin properties and monomer yields.

Fraction	Klason Lignin	$\beta$ -O-4	$\beta$ -O-4	$\beta$ -5	$\beta$ - $\beta$	S/G	S/G	Mn	Mw	PhOH	AIOH
		<sup>13</sup> CNMR	HSQC	HSQC	HSQC	HSQC	Thio*				
RT-5	57.80	15.23	58.08	3.49	38.43	1.8	1.73	1825	7161	0.82	1.59
RT-4	69.46	20	58.27	4.98	36.75	1.8	1.70	2811	21558	0.73	1.27
RT-3	86.61	21.91	59.56	4.77	35.67	1.84	1.73	3461	28066	0.71	1.26
RT-2	68.25	21.92	59.88	5.48	34.64	1.86	1.76	3765	33923	0.71	1.27
RT-1	86.45	22.88	64.62	5.72	29.66	1.86	1.76	4161	30883	0.68	1.27
SLRP-2	78.50	28.66	67.67	8.53	23.79	1.95	1.92	6269	71216	0.52	1.25
SLRP-1	70.74	31.25	73.02	7.94	19.04	1.99	1.95	6960	15400	0.47	1.25

Fraction	Ni-catalyzed hydrogenolysis yields <sup>‡</sup> (%)						Quantitative thio* yields (%)			
	4-PG	4-PS	4-VG	4-VS	Sy	Total	S unit	G unit	H unit	Total
RT-5	0.44	1.2	0	0	0	1.64	2.99	1.52	0.07	4.58
RT-4	0.62	1.62	0	0	0.6	2.84	5.12	2.64	0.07	7.83
RT-3	0.98	2.31	0	0	0	3.29	5.59	2.84	0.05	8.48
RT-2	0	0	0	0	0	0	5.50	2.75	0.06	8.31
RT-1	1.32	3.17	0	0	0	4.49	6.14	3.05	0.06	9.25
SLRP-2	0.76	2.65	0.95	1.48	1.1	6.92	8.88	4.06	0.06	13.00
SLRP-1	0.77	2.51	0.92	1.24	0.78	6.23	10.70	4.81	0.06	15.57

Fraction	Cu-catalyzed oxidation yields <sup>†</sup> (%)						
	V	S	VA	SA	AceV	AceS	Total
RT-5	2.97 ± 0.05	1.23 ± 0.14	0.51 ± 0.08	0.08 ± 0.04	0.57 ± 0.04	0.00 ± 0.00	5.40 ± 0.18
RT-4	4.63 ± 0.30	6.29 ± 0.26	0.78 ± 0.01	0.01 ± 0.19	0.70 ± 0.02	0.91 ± 0.05	13.41 ± 0.40
RT-3	4.88 ± 0.44	6.83 ± 0.51	0.85 ± 0.12	0.12 ± 0.06	0.71 ± 0.06	1.04 ± 0.16	14.42 ± 0.73
RT-2	4.87 ± 0.05	6.62 ± 0.13	0.84 ± 0.05	0.05 ± 0.06	0.75 ± 0.02	0.91 ± 0.11	14.11 ± 0.19
RT-1	4.14 ± 0.35	6.34 ± 0.21	0.77 ± 0.03	0.03 ± 0.06	0.63 ± 0.02	0.81 ± 0.09	12.80 ± 0.42
SLRP-2	5.58 ± 0.09	7.85 ± 1.06	0.68 ± 0.01	0.01 ± 0.06	0.63 ± 0.06	0.33 ± 0.04	15.21 ± 1.07
SLRP-1	5.91 ± 0.08	7.76 ± 0.12	0.72 ± 0.03	0.03 ± 0.11	0.62 ± 0.01	0.44 ± 0.08	15.57 ± 0.20

\* thio = thioacidolysis

‡ 4-PG = 4-propylguaiacol, 4-PS = 4-propylsyringol, 4-VG = 4-vinylguaiacol, 4-SG = 4-vinylsyringol, Sy = Syringol

† V = Vanillin, S = Syringaldehyde, VA = Vanillic Acid, SA = Syringic Acid, AceV = Acetovanillone, AceS = Acetosyringone

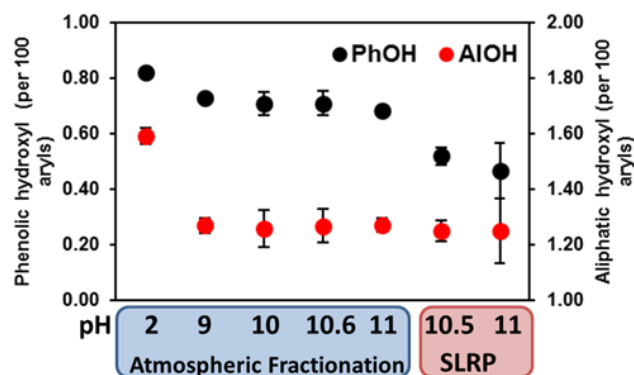


Figure B1. Trends of phenolic hydroxyl contents (black) in fractionated lignin showing lower values in fractions precipitated at higher pH, while aliphatic hydroxyl content (red) do not show any specific trend.

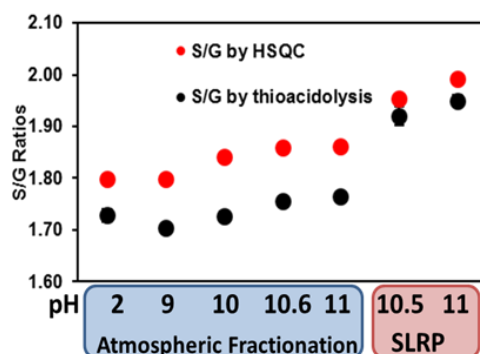


Figure B2. Trends of S/G ratios in fractionated lignin by HSQC NMR (red) and thioacidolysis (black) showing higher S/G values in fractions precipitated at higher pH and SLRP samples

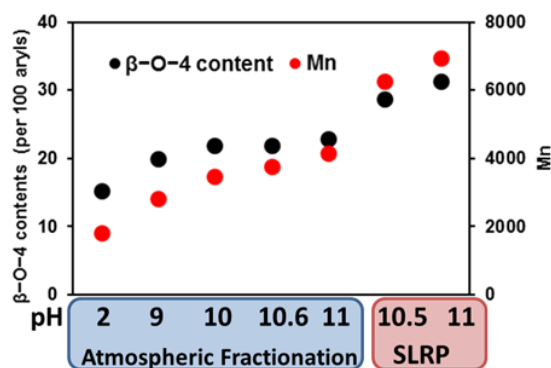


Figure B3. Trends of beta-O-4 content (black) as measured by <sup>13</sup>C-NMR and molecular weight among fractionated lignin showing similar increasing trend in fractions precipitated at higher pH and SLRP samples.

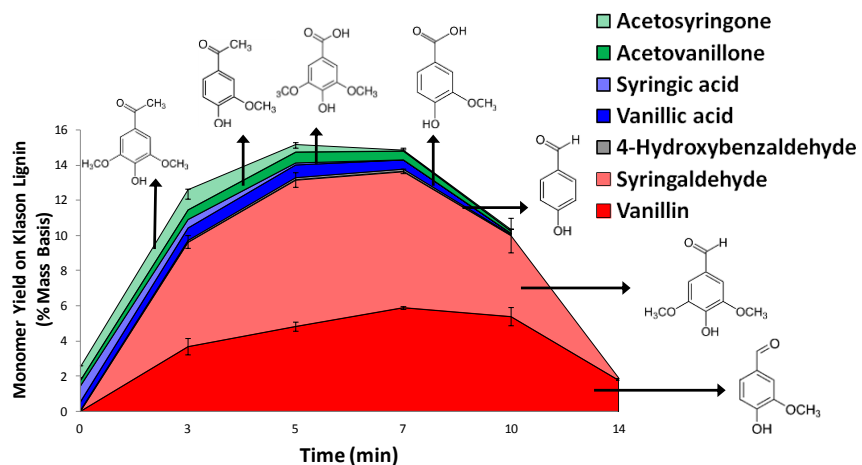


Figure B4. Kinetics of Cu-catalyzed oxidation reactions of lignin sample SLRP-2 showing time for optimal yield at the study condition is at 7 minutes.

## APPENDIX C: Supplementary Materials for Chapter 4

The isothermal isobaric ensemble (NPT) molecular dynamics was performed using COMPASS II force field with types similar to that described in the main manuscript. For each compound, 10 molecules of it was randomly packed in a cell with a volume of 4000 Å<sup>3</sup>. The cell was then relaxed and underwent NPT MD with 1000 ps equilibration time and 1000 ps production time, from which the cell volume was averaged over. Temperature coupling was performed with the Nose algorithm ( $Q = 0.01$ ) and Berendsen barostat was employed with a decay constant of 0.1 ps.

Table C1. Comparison between density calculated from NPT dynamics using COMPASS II force field and experimental density of compounds similar to the dimer.

	MD (g/cm <sup>3</sup> )	Exp. (g/cm <sup>3</sup> )	Error (%)
Benzoic acid	1.23	1.27	-3.15
1,3 Methoxy benzene	1.06	1.01	4.95
Phenyl Ethanol	0.99	1.02	-2.94
Guaiacol	1.19	1.11	7.21
Glucose	1.45	1.54	-5.84
guaiacylglycerol-beta-guaiacyl ether	1.27	-	-

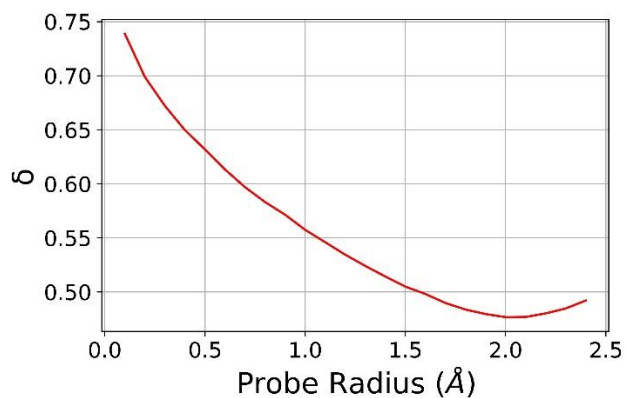


Figure C1. The change in fraction of surface accessible surface area (SASA) of the dimer in solvated adsorb in reference to fully solvated state ( $\delta$ ) as estimated by SASA as a function of probe radius.

## **BIBLIOGRAPHY**

## BIBLIOGRAPHY

1. *Generation of renewable energy in the U.S. from 2008 to 2017, by technology (in terawatt hours)*. (Bloomberg New Energy Finance. n.d.).
2. Ellabban, O., Abu-Rub, H. & Blaabjerg, F. Renewable energy resources: Current status, future prospects and their enabling technology. *Renew. Sustain. Energy Rev.* **39**, 748–764 (2014).
3. Wachsman, E. D. & Lee, K. T. Lowering the temperature of solid oxide fuel cells. *Science* **334**, 935–939 (2011).
4. Wachsman, E. D., Marlowe, C. A. & Lee, K. T. Role of solid oxide fuel cells in a balanced energy strategy. *Energy Environ. Sci.* **5**, 5498–5509 (2012).
5. Schutyser, W. *et al.* Chemicals from lignin: an interplay of lignocellulose fractionation, depolymerisation, and upgrading. *Chem. Soc. Rev.* **47**, 852–908 (2018).
6. Voelcker, J. Nissan takes a different approach to fuel cells: ethanol. *Green Car Reports* Available at: [https://www.greencarreports.com/news/1104467\\_nissan-takes-a-different-approach-to-fuel-cells-ethanol](https://www.greencarreports.com/news/1104467_nissan-takes-a-different-approach-to-fuel-cells-ethanol). (Accessed: 10th September 2018)
7. Nissan unveils world's first solid-oxide fuel cell e-NV200. Available at: <https://insideevs.com/nissan-unveils-worlds-first-solid-oxide-fuel-cell-vehicle-e-nv200-sofc/>. (Accessed: 19th September 2018)
8. Nissan SOFC powered vehicle system runs on bioethanol. *Fuel Cells Bull.* **2016**, 2–3 (2016).
9. Ahamer, C., Opitz, A. K., Rupp, G. M. & Fleig, J. Revisiting the temperature dependent ionic conductivity of yttria stabilized zirconia (YSZ). *J. Electrochem. Soc.* **164**, F790–F803 (2017).
10. Asadikiya, M. & Zhong, Y. Oxygen ion mobility and conductivity prediction in cubic yttria-stabilized zirconia single crystals. *J. Mater. Sci.* **53**, 1699–1709 (2018).
11. Mahato, N., Banerjee, A., Gupta, A., Omar, S. & Balani, K. Progress in material selection for solid oxide fuel cell technology: A review. *Prog. Mater. Sci.* **72**, 141–337 (2015).
12. Solid Oxide Fuel Cells (SOFCs). *Forschungszentrum Jülich*
13. Heather L. Trajano & Charles E. Wyman. Fundamentals of biomass pretreatment at low pH. in *Aqueous pretreatment of plant biomass for biological and chemical conversion to fuels and chemicals* (John Wiley & Sons Ltd).
14. D. Kärkäs, M., S. Matsuura, B., M. Monos, T., Magallanes, G. & J. Stephenson, C. R. Transition-metal catalyzed valorization of lignin: the key to a sustainable carbon-neutral future. *Org. Biomol. Chem.* **14**, 1853–1914 (2016).

15. Ammal, S. C. & Heyden, A. Combined DFT and microkinetic modeling study of hydrogen oxidation at the Ni/YSZ anode of solid oxide fuel cells. *J. Phys. Chem. Lett.* **3**, 2767–2772 (2012).
16. Cui, J. *et al.* Conversion of xylose to furfuryl alcohol and 2-methylfuran in a continuous fixed-bed reactor. *ChemSusChem* **9**, 1259–1262 (2016).
17. Zhang, L., Xi, G., Yu, K., Yu, H. & Wang, X. Furfural production from biomass-derived carbohydrates and lignocellulosic residues via heterogeneous acid catalysts. *Ind. Crops Prod.* **98**, 68–75 (2017).
18. Cui, J. *et al.* Conversion of carbohydrates to furfural via selective cleavage of the carbon–carbon bond: the cooperative effects of zeolite and solvent. *Green Chem.* **18**, 1619–1624 (2016).
19. Li, C., Zhao, X., Wang, A., Huber, G. W. & Zhang, T. Catalytic transformation of lignin for the production of chemicals and fuels. *Chem. Rev.* **115**, 11559–11624 (2015).
20. DeRose, A. J. *et al.* Inhibitor for prevention of braze migration in solid oxide fuel cells. (2010).
21. Smithells, C., Gale, W. & Totemeier, T. Smithells metals reference book. *ASM Mater. Inf. Soc.* (2004).
22. Kim, J. Y., Hardy, J. S. & Scott Weil, K. Effects of CuO Content on the wetting behavior and mechanical properties of a Ag–CuO braze for ceramic joining. *J. Am. Ceram. Soc.* **88**, 2521–2527 (2005).
23. Nikolopoulos, P. & Sotiropoulou, D. Wettability between zirconia ceramics and the liquid metals copper, nickel and cobalt. *J. Mater. Sci. Lett.* **6**, 1429–1430 (1987).
24. Hardy, J. S., Kim, J. Y. & Weil, K. S. Joining mixed conducting oxides using an air-fired electrically conductive braze. *J. Electrochem. Soc.* **151**, J43–J49 (2004).
25. Weil, K. S., Kim, J. Y. & Hardy, J. S. Reactive air brazing: A novel method of sealing sofc's and other solid-state electrochemical devices. *Electrochem. Solid-State Lett.* **8**, A133–A136 (2005).
26. Phongpreecha, T., Nicholas, J. D., Bieler, T. R. & Qi, Y. Computational design of metal oxides to enhance the wetting and adhesion of silver-based brazes on yttria-stabilized-zirconia. *Acta Mater.* **152**, 229–238 (2018).
27. Adler, E. Lignin chemistry—past, present and future. *Wood Sci. Technol.* **11**, 169–218 (1977).
28. Huang, X., Korányi, T. I., Boot, M. D. & Hensen, E. J. M. Catalytic depolymerization of lignin in supercritical ethanol. *ChemSusChem* **7**, 2276–2288 (2014).

29. Bouxin, F. P. *et al.* Catalytic depolymerisation of isolated lignins to fine chemicals using a Pt/alumina catalyst: part 1—impact of the lignin structure. *Green Chem.* **17**, 1235–1242 (2015).
30. Rahimi, A., Ulbrich, A., Coon, J. J. & Stahl, S. S. Formic-acid-induced depolymerization of oxidized lignin to aromatics. *Nature* **515**, 249–252 (2014).
31. Lu, J., Wang, M., Zhang, X., Heyden, A. & Wang, F. Cleavage mechanism for lignin model compounds over Pd catalysts identified by combination of first-principles calculations and experiments. *ACS Catal.* **6**, 5589–5598 (2016).
32. Si, X. *et al.* A strategy for generating high-quality cellulose and lignin simultaneously from woody biomass. *Green Chem.* **19**, 4849–4857 (2017).
33. Bosch, S. V. den *et al.* Integrating lignin valorization and bio-ethanol production: on the role of Ni-Al<sub>2</sub>O<sub>3</sub> catalyst pellets during lignin-first fractionation. *Green Chem.* **19**, 3313–3326 (2017).
34. Ferrini, P., Chesi, C., Parkin, N. & Rinaldi, R. Effect of methanol in controlling defunctionalization of the propyl side chain of phenolics from catalytic upstream biorefining. *Faraday Discuss.* **202**, 403–413 (2017).
35. Klein, I., Marcum, C., Kenttämä, H. & Abu-Omar, M. M. Mechanistic investigation of the Zn/Pd/C catalyzed cleavage and hydrodeoxygenation of lignin. *Green Chem.* **18**, 2399–2405 (2016).
36. Ye, Y., Zhang, Y., Fan, J. & Chang, J. Selective production of 4-ethylphenolics from lignin via mild hydrogenolysis. *Bioresour. Technol.* **118**, 648–651 (2012).
37. Parsell, T. *et al.* A synergistic biorefinery based on catalytic conversion of lignin prior to cellulose starting from lignocellulosic biomass. *Green Chem.* **17**, 1492–1499 (2015).
38. Konnerth, H., Zhang, J., Ma, D., Prechtel, M. H. G. & Yan, N. Base promoted hydrogenolysis of lignin model compounds and organosolv lignin over metal catalysts in water. *Chem. Eng. Sci.* **123**, 155–163 (2015).
39. Barta, K., Warner, G. R., Beach, E. S. & Anastas, P. T. Depolymerization of organosolv lignin to aromatic compounds over Cu-doped porous metal oxides. *Green Chem.* **16**, 191–196 (2013).
40. Wang, X. & Rinaldi, R. Solvent effects on the hydrogenolysis of diphenyl ether with Raney nickel and their implications for the conversion of lignin. *ChemSusChem* **5**, 1455–1466 (2012).
41. Gasson, J. R. *et al.* Modeling the lignin degradation kinetics in an ethanol/formic acid solvolysis approach. Part 1. Kinetic model development. *Ind. Eng. Chem. Res.* **51**, 10595–10606 (2012).

42. Forchheim, D., Gasson, J. R., Hornung, U., Kruse, A. & Barth, T. Modeling the lignin degradation kinetics in a ethanol/formic acid solvolysis approach. Part 2. Validation and transfer to variable conditions. *Ind. Eng. Chem. Res.* **51**, 15053–15063 (2012).
43. Wanmolee, W. *et al.* Catalytic conversion of organosolv lignins to phenolic monomers in different organic solvents and effect of operating conditions on yield with methyl isobutyl ketone. *ACS Sustain. Chem. Eng.* **6**, 3010–3018 (2018).
44. Li, Q. & Lopez, N. Chirality, rigidity and conjugation: a first principles study on the key molecular aspects in lignin depolymerization on Ni-based catalysts. *ACS Catal.* **8**, 4230–4240 (2018).
45. Horstemeyer, M. F. Multiscale modeling: A review. in *Practical aspects of computational chemistry: Methods, concepts and applications* (eds. Leszczynski, J. & Shukla, M. K.) 87–135 (Springer Netherlands, 2010). doi:10.1007/978-90-481-2687-3\_4
46. Jancar, J. *et al.* Current issues in research on structure–property relationships in polymer nanocomposites. *Polymer* **51**, 3321–3343 (2010).
47. Campbell, C. T. & Sellers, J. R. V. The entropies of adsorbed molecules. *J. Am. Chem. Soc.* **134**, 18109–18115 (2012).
48. Carrasco, J., Liu, W., Michaelides, A. & Tkatchenko, A. Insight into the description of van der Waals forces for benzene adsorption on transition metal (111) surfaces. *J. Chem. Phys.* **140**, 084704 (2014).
49. Liu, W. *et al.* Benzene adsorbed on metals: Concerted effect of covalency and van der Waals bonding. *Phys. Rev. B* **86**, 245405 (2012).
50. Carey, S. J., Zhao, W. & Campbell, C. T. Energetics of adsorbed benzene on Ni(111) and Pt(111) by calorimetry. *Surf. Sci.* **676**, 9–16 (2018).
51. Abild-Pedersen, F. *et al.* Scaling properties of adsorption energies for hydrogen-containing molecules on transition-metal surfaces. *Phys. Rev. Lett.* **99**, 016105 (2007).
52. Jacobsen, C. J. H. *et al.* Catalyst design by interpolation in the periodic table: Bimetallic ammonia synthesis catalysts. *J. Am. Chem. Soc.* **123**, 8404–8405 (2001).
53. Vojvodic, A. *et al.* Exploring the limits: A low-pressure, low-temperature Haber–Bosch process. *Chem. Phys. Lett.* **598**, 108–112 (2014).
54. Medford, A. J. *et al.* Activity and selectivity trends in synthesis gas conversion to higher alcohols. *Top. Catal.* **57**, 135–142 (2013).
55. Andersson, M. P. *et al.* Toward computational screening in heterogeneous catalysis: Pareto-optimal methanation catalysts. *J. Catal.* **239**, 501–506 (2006).

56. Greeley, J., Jaramillo, T. F., Bonde, J., Chorkendorff, I. & Nørskov, J. K. Computational high-throughput screening of electrocatalytic materials for hydrogen evolution. *Nat. Mater.* **5**, 909–913 (2006).
57. Studt, F. *et al.* Identification of non-precious metal alloy catalysts for selective hydrogenation of acetylene. *Science* **320**, 1320–1322 (2008).
58. Ferrin, P. *et al.* Modeling ethanol decomposition on transition metals: A combined application of scaling and Brønsted–Evans–Polanyi relations. *J. Am. Chem. Soc.* **131**, 5809–5815 (2009).
59. Montemore, M. M. & Medlin, J. W. Scaling relations between adsorption energies for computational screening and design of catalysts. *Catal. Sci. Technol.* **4**, 3748–3761 (2014).
60. Nørskov, J. K., Bligaard, T., Rossmeisl, J. & Christensen, C. H. Towards the computational design of solid catalysts. *Nat. Chem.* **1**, 37–46 (2009).
61. Nørskov, J. K., Studt, F., Abild-Pedersen, F. & Bligaard, T. Activity and selectivity maps. in *Fundamental concepts in heterogeneous catalysis* 97–113 (John Wiley & Sons, Inc, 2014).
62. Bull, S. J. & Berasetegui, E. G. An overview of the potential of quantitative coating adhesion measurement by scratch testing. *Tribol. Int.* **39**, 99–114 (2006).
63. Mittal, K. L. Adhesion measurement of thin films. *active and passive electronic components* (1976). doi:10.1155/APEC.3.21
64. Nahor, H., Meltzman, H. & Kaplan, W. D. Ni–YSZ(111) solid–solid interfacial energy. *J. Mater. Sci.* **49**, 3943–3950 (2014).
65. Li, H.-T. *et al.* Interfacial stoichiometry and adhesion at metal/ $\alpha$ -Al<sub>2</sub>O<sub>3</sub> Interfaces. *J. Am. Ceram. Soc.* **94**, s154–s159
66. Meltzman, H., Mordehai, D. & Kaplan, W. D. Solid–solid interface reconstruction at equilibrated Ni–Al<sub>2</sub>O<sub>3</sub> interfaces. *Acta Mater.* **60**, 4359–4369 (2012).
67. Zhang, Z., Li, L. & Yang, J. C. Adhesion of Pt Nanoparticles Supported on  $\gamma$ -Al<sub>2</sub>O<sub>3</sub> Single Crystal. *J. Phys. Chem. C* **117**, 21407–21412 (2013).
68. Si-Qi, S., Shingo, T. & Masanori, K. Effect of the stoichiometry on the electronic structure of the Ni(111)/ $\alpha$ -Al<sub>2</sub>O<sub>3</sub> (0001) interface: a first-principles investigation. *Chin. Phys. B* **17**, 2655 (2008).
69. Rose, J. H., Smith, J. R. & Ferrante, J. Universal features of bonding in metals. *Phys. Rev. B* **28**, 1835–1845 (1983).
70. Rose, J. H., Ferrante, J. & Smith, J. R. Universal binding energy curves for metals and bimetallic interfaces. *Phys. Rev. Lett.* **47**, 675–678 (1981).

71. Banerjea, A. & Smith, J. R. Origins of the universal binding-energy relation. *Phys. Rev. B* **37**, 6632–6645 (1988).
72. Rose, J. H., Smith, J. R., Guinea, F. & Ferrante, J. Universal features of the equation of state of metals. *Phys. Rev. B* **29**, 2963–2969 (1984).
73. Chabanet, O. *et al.* Predicting crack growth resistance of aluminium sheets. *Comput. Mater. Sci.* **26**, 1–12 (2003).
74. Elzas, A. & Thijsse, B. Cohesive law describing crack growth at iron/precipitate interfaces. *Comput. Mater. Sci.* **134**, 214–224 (2017).
75. Schlosser, H. & Ferrante, J. Universality relationships in condensed matter: Bulk modulus and sound velocity. *Phys. Rev. B* **37**, 4351–4357 (1988).
76. Guinea, F., Rose, J. H., Smith, J. R. & Ferrante, J. Scaling relations in the equation of state, thermal expansion, and melting of metals. *Appl. Phys. Lett.* **44**, 53–55 (1984).
77. Li, Y. J., Qi, W. H., Huang, B. Y., Wang, M. P. & Xiong, S. Y. Modeling the melting temperature of metallic nanowires. *Mod. Phys. Lett. B* **24**, 2345–2356 (2010).
78. Shu, G. G., Xu, Q. & Wu, P. Study of wetting on chemically softened interfaces by using combined solution thermodynamics and DFT calculations: Forecasting effective softening elements. *ACS Appl. Mater. Interfaces* **7**, 7576–7583 (2015).
79. Alfredsson, M., Richard, C. & Catlow, A. Predicting the metal growth mode and wetting of noble metals supported on c-ZrO<sub>2</sub>. *Surf. Sci.* **561**, 43–56 (2004).
80. Malijeviský, A. Does surface roughness amplify wetting? *J. Chem. Phys.* **141**, 184703 (2014).
81. Durov, A. V., Naidich, Y. V. & Kostyuk, B. D. Investigation of interaction of metal melts and zirconia. *J. Mater. Sci.* **40**, 2173–2178 (2005).
82. Peereboom, L., Koenigsnecht, B., Hunter, M., Jackson, J. E. & Miller, D. J. Aqueous-phase adsorption of glycerol and propylene glycol onto activated carbon. *Carbon* **45**, 579–586 (2007).
83. Zuo, Z., Huang, W., Han, P. & Li, Z. Solvent effects for CO and H<sub>2</sub> adsorption on Cu<sub>2</sub>O (111) surface: A density functional theory study. *Appl. Surf. Sci.* **256**, 2357–2362 (2010).
84. Zhang, R., Ling, L., Li, Z. & Wang, B. Solvent effects on Cu<sub>2</sub>O(111) surface properties and CO adsorption on Cu<sub>2</sub>O(111) surface: A DFT study. *Appl. Catal. Gen.* **400**, 142–147 (2011).
85. Garcia-Ratés, M. & López, N. Multigrid-based methodology for implicit solvation models in periodic DFT. *J. Chem. Theory Comput.* **12**, 1331–1341 (2016).

86. Steinmann, S. N., Sautet, P. & Michel, C. Solvation free energies for periodic surfaces: comparison of implicit and explicit solvation models. *Phys. Chem. Chem. Phys.* **18**, 31850–31861 (2016).
87. Nikolopoulos, P., Ondracek, G. & Sotiropoulou, D. Wettability and interfacial energies between zirconia ceramic and liquid metals. *Ceram. Int.* **15**, 201–206 (1989).
88. Laosiripojana, N. & Assabumrungrat, S. Catalytic steam reforming of methane, methanol, and ethanol over Ni/YSZ: The possible use of these fuels in internal reforming SOFC. *J. Power Sources* **163**, 943–951 (2007).
89. Khor, K. A., Dong, Z. L. & Gu, Y. W. Influence of oxide mixtures on mechanical properties of plasma sprayed functionally graded coating. *Thin Solid Films* **368**, 86–92 (2000).
90. Hong, H. S., Chae, U.-S., Choo, S.-T. & Lee, K. S. Microstructure and electrical conductivity of Ni/YSZ and NiO/YSZ composites for high-temperature electrolysis prepared by mechanical alloying. *J. Power Sources* **149**, 84–89 (2005).
91. Sasaki, T. *et al.* Atomic and electronic structures of Ni/YSZ(111) interface. *Mater. Trans.* **45**, 2137–2143 (2004).
92. Winterbottom, W. L. Equilibrium shape of a small particle in contact with a foreign substrate. *Acta Metall.* **15**, 303–310 (1967).
93. Meltzman, H., Chatain, D., Avizemer, D., Besmann, T. M. & Kaplan, W. D. The equilibrium crystal shape of nickel. *Acta Mater.* **59**, 3473–3483 (2011).
94. Tsoga, A. & Nikolopoulos, P. Surface and grain-boundary energies in yttria-stabilized zirconia (YSZ-8 mol%). *J. Mater. Sci.* **31**, 5409–5413 (1996).
95. Matsunaga, K. *et al.* Bonding nature of metal/oxide incoherent interfaces by first-principles calculations. *Phys. Rev. B* **74**, 125423 (2006).
96. Sawata, A., Tsuneyoshi, K., Mizusaki, J. & Tagawa, H. Oxygen chemical potential profile in a solid oxide fuel cell and simulation of electrochemical performance. *Solid State Ion.* **40**, 415–420 (1990).
97. Eremeev, S. V., Nemirovich-Danchenko, L. Y. & Kul'kova, S. E. Effect of oxygen vacancies on adhesion at the Nb/Al<sub>2</sub>O<sub>3</sub> and Ni/ZrO<sub>2</sub> interfaces. *Phys. Solid State* **50**, 543–552 (2008).
98. Eremeev, S. V., Schmauder, S., Hocker, S. & Kulkova, S. E. *Ab-initio* investigation of Ni(Fe)/ZrO<sub>2</sub>(0 0 1) and Ni–Fe/ZrO<sub>2</sub>(0 0 1) interfaces. *Surf. Sci.* **603**, 2218–2225 (2009).
99. Kasamatsu, S., Tada, T. & Watanabe, S. First principles study of oxygen vacancies near nickel/zirconia interface. *E-J. Surf. Sci. Nanotechnol.* **8**, 93–100 (2010).

100. Shishkin, M. & Ziegler, T. The oxidation of H<sub>2</sub> and CH<sub>4</sub> on an oxygen-enriched yttria-stabilized zirconia surface: A theoretical study based on density functional theory. *J. Phys. Chem. C* **112**, 19662–19669 (2008).
101. Hemmingson, S. L. & Campbell, C. T. Trends in adhesion energies of metal nanoparticles on oxide surfaces: Understanding support effects in catalysis and nanotechnology. *ACS Nano* **11**, 1196–1203 (2017).
102. Didier, F. & Jupille, J. The van der Waals contribution to the adhesion energy at metal-oxide interfaces. *Surf. Sci.* **314**, 378–384 (1994).
103. Li, J.-G. Wetting and Interfacial Bonding of Metals with Ionocovalent Oxides. *J. Am. Ceram. Soc.* **75**, 3118–3126 (1992).
104. Miedema, A. R. & Boom, R. Surface tension and electron density of pure liquid metals. *Z. Fuer Met.* **69**, 183–190 (1978).
105. Beltrán, J. I. & Muñoz, M. C. *Ab-initio* study of decohesion properties in oxide/metal systems. *Phys. Rev. B* **78**, 245417 (2008).
106. Chatain, D., Rivollet, I. & Eustathopoulos, N. Adhésion thermodynamique dans les systèmes non-réactifs métal liquide-alumine. *J. Chim. Phys.* **83**, 561–567 (1986).
107. Chatain, D., Coudurier, L. & Eustathopoulos, N. Wetting and interfacial bonding in ionocovalent oxide-liquid metal systems. *Rev. Phys. Appliquée* **23**, 1055–1064 (1988).
108. Peden, C. H. F., Kidd, K. B. & Shinn, N. D. Metal/metal-oxide interfaces: A surface science approach to the study of adhesion. *J. Vac. Sci. Technol. Vac. Surf. Films* **9**, 1518–1524 (1991).
109. Shaikhutdinov, S. K. & Weiss, W. Oxygen pressure dependence of the  $\alpha$ -Fe<sub>2</sub>O<sub>3</sub>(0001) surface structure. *Surf. Sci.* **432**, L627–L634 (1999).
110. Dai, Y., Lu, P., Cao, Z., Campbell, C. T. & Xia, Y. The physical chemistry and materials science behind sinter-resistant catalysts. *Chem. Soc. Rev.* **47**, 4314–4331 (2018).
111. Gerberich, W. W. & Cordill, M. J. Physics of adhesion. *Rep. Prog. Phys.* **69**, 2157 (2006).
112. Zhang, Z., Kawamura, M., Abe, Y. & Kim, K. H. Thermal stability of Ag films with various interface layers. *Jpn. J. Appl. Phys.* **53**, 048003 (2014).
113. Kriese, M. D., Moody, N. R. & Gerberich, W. W. Quantitative measurement of the effect of annealing on the adhesion of thin copper films using superlayers. *MRS Online Proc. Libr. Arch.* **505**, (1997).
114. Moody, N. R., Adams, D. P., Cordill, M. J., Yang, N. & Bahr, D. F. The effects of copper on the interfacial failure of gold films. *MRS Online Proc. Libr. Arch.* **695**, (2001).

115. Baron, C. H., Raabe, D., Korte-Kerzel, S. & Scheu, C. On the design of alloys and synthesis for composite steels. (RWTH Aachen Aachen, Germany, 2017).
116. Yoon, Y., Rousseau, R., Weber, R. S., Mei, D. & Lercher, J. A. First-principles study of phenol hydrogenation on Pt and Ni catalysts in aqueous phase. *J. Am. Chem. Soc.* **136**, 10287–10298 (2014).
117. Hensley, A. J. R., Wang, Y., Mei, D. & McEwen, J.-S. Mechanistic effects of water on the Fe-catalyzed hydrodeoxygenation of phenol. The role of Brønsted acid sites. *ACS Catal.* **8**, 2200–2208 (2018).
118. Garcia-Ratés, M., García-Muelas, R. & López, N. Solvation effects on methanol decomposition on Pd(111), Pt(111), and Ru(0001). *J. Phys. Chem. C* **121**, 13803–13809 (2017).
119. Kulig, W. Introduction to solvation models for theoretical chemistry. (2016).
120. Mennucci, B. & Tomasi, J. Continuum solvation models: A new approach to the problem of solute's charge distribution and cavity boundaries. *J. Chem. Phys.* **106**, 5151–5158 (1997).
121. Cramer, C. J. & Truhlar, D. G. Implicit Solvation Models: Equilibria, Structure, Spectra, and Dynamics. *Chem. Rev.* **99**, 2161–2200 (1999).
122. Sundararaman, R. & Schwarz, K. Evaluating continuum solvation models for the electrode-electrolyte interface: Challenges and strategies for improvement. *J. Chem. Phys.* **146**, 084111 (2017).
123. Gunceler, D., Letchworth-Weaver, K., Sundararaman, R., Schwarz, K. A. & Arias, T. A. The importance of nonlinear fluid response in joint density-functional theory studies of battery systems. *Model. Simul. Mater. Sci. Eng.* **21**, 074005 (2013).
124. Le, J., Cuesta, A. & Cheng, J. The structure of metal-water interface at the potential of zero charge from density functional theory-based molecular dynamics. *J. Electroanal. Chem.* **819**, 87–94 (2018).
125. Le, J., Fan, Q., Perez-Martinez, L., Cuesta, A. & Cheng, J. Theoretical insight into the vibrational spectra of metal–water interfaces from density functional theory based molecular dynamics. *Phys. Chem. Chem. Phys.* **20**, 11554–11558 (2018).
126. Iyemperumal, S. K. & Deskins, N. A. Evaluating solvent effects at the aqueous/Pt(111) interface. *ChemPhysChem* **18**, 2171–2190 (2017).
127. Saiz, E., Cannon, R. M. & Tomsia, A. P. High-temperature wetting and the work of adhesion in metal/oxide systems. *Annu. Rev. Mater. Res.* **38**, 197–226 (2008).
128. Fergus, J. W. Sealants for solid oxide fuel cells. *J. Power Sources* **147**, 46–57 (2005).
129. Braze alloy containing particulate material. (2005).

130. Method and apparatus for gasketing a fuel cell. (2004).
131. Le, S. *et al.* Effective Ag–CuO sealant for planar solid oxide fuel cells. *J. Alloys Compd.* **496**, 96–99 (2010).
132. Zhou, Q., Bieler, T. R. & Nicholas, J. D. Transient porous nickel interlayers for improved silver-based solid oxide fuel cell brazes. *Acta Mater.* **148**, 156–162 (2018).
133. Ueki, M., Naka, M. & Okamoto, I. Wettability of some metals against zirconia ceramics. *J. Mater. Sci. Lett.* **5**, 1261–1262 (1986).
134. Achievements in Reactive Air Brazing. *Adv. Eng. Mater.* **16**, 1413–1414 (2014).
135. Meier, A. M., Chidambaram, P. & Edwards, G. R. A comparison of the wettability of copper-copper oxide and silver-copper oxide on polycrystalline alumina. *J. Mater. Sci.* **30**, 4781–4786 (1995).
136. Kim, J. Y., Hardy, J. S. & Weil, K. S. Silver-copper oxide based reactive air braze for joining yttria-stabilized zirconia. *J. Mater. Res.* **20**, 636–643 (2005).
137. Chen, H. *et al.* Reactive air brazing for sealing mixed ionic electronic conducting hollow fibre membranes. *Acta Mater.* **88**, 74–82 (2015).
138. Hashimoto, S. *et al.* Oxygen nonstoichiometry and thermo-chemical stability of  $\text{La}_{0.6}\text{Sr}_{0.4}\text{Co}_{1-y}\text{Fe}_y\text{O}_{3-\delta}$  ( $y=0.2, 0.4, 0.6, 0.8$ ). *Solid State Ion.* **181**, 1713–1719 (2010).
139. Chen, Yu & Adler, S. B. Thermal and chemical expansion of Sr-doped lanthanum cobalt oxide ( $\text{La}_{1-x}\text{Sr}_x\text{CoO}_{3-\delta}$ ). *Chem. Mater.* **17**, 4537–4546 (2005).
140. Bishop, S. R., Duncan, K. L. & Wachsman, E. D. Thermo-chemical expansion in strontium-doped lanthanum cobalt iron oxide. *J. Am. Ceram. Soc.* **93**, 4115–4121 (2010).
141. Pfaff, E. M., Kaletsch, A. & Broeckmann, C. Design of a mixed ionic/electronic conducting oxygen transport membrane pilot module. *Chem. Eng. Technol.* **35**, 455–463 (2012).
142. Cao, J., Si, X., Li, W., Song, X. & Feng, J. Reactive air brazing of YSZ-electrolyte and  $\text{Al}_2\text{O}_3$ -substrate for gas sensor sealing: Interfacial microstructure and mechanical properties. *Int. J. Hydrog. Energy* **42**, 10683–10694 (2017).
143. Weil, K. S., Hardy, J. S. & Kim, J. Y. Oxidation ceramic to metal braze seals for applications in high temperature electrochemical devices and method of making. (2006).
144. Middelkoop, V. Reactive air brazing (RAB) for gas separation membranes. in *Encyclopedia of Membranes* (eds. Drioli, E. & Giorno, L.) 1710–1713 (Springer Berlin Heidelberg, 2016). doi:10.1007/978-3-662-44324-8\_1773

145. Chatzimichail, R., Triantafyllou, G., Tietz, F. & Nikolopoulos, P. Interfacial properties of (Ag + CuO) brazes used as sealing materials in SOFC stacks. *J. Mater. Sci.* **49**, 300–313 (2014).
146. Barin, I. Compilation of thermochemical data. in *Thermochemical Data of Pure Substances* 33–34 (Wiley-VCH Verlag GmbH, 1995). doi:10.1002/9783527619825.ch3
147. Zhou, Q., Bieler, T. R. & Nicholas, J. D. Reactive-element-free, silver-based brazes for SOFC applications. *ECS Trans.* **78**, 1759–1767 (2017).
148. Hu, J., Li, D., Lu, J. G. & Wu, R. Effects on electronic properties of molecule adsorption on CuO surfaces and nanowires. *J. Phys. Chem. C* **114**, 17120–17126 (2010).
149. Maimaiti, Y., Nolan, M. & Elliott, S. D. Reduction mechanisms of the CuO(111) surface through surface oxygen vacancy formation and hydrogen adsorption. *Phys. Chem. Chem. Phys.* **16**, 3036–3046 (2014).
150. Eichler, A. & Kresse, G. First-principles calculations for the surface termination of pure and yttria-doped zirconia surfaces. *Phys. Rev. B* **69**, 045402 (2004).
151. Takemoto, S. & Tada, T. Zirconium-peroxo embedded in non-stoichiometric yttria stabilized zirconia (110) from first-principles. *Solid State Ion.* **285**, 215–221 (2016).
152. Ding, H., Virkar, A. V. & Liu, F. Defect configuration and phase stability of cubic versus tetragonal yttria-stabilized zirconia. *Solid State Ion.* **215**, 16–23 (2012).
153. Pascual, C. & Durán, P. Subsolidus phase equilibria and ordering in the system ZrO<sub>2</sub>-Y<sub>2</sub>O<sub>3</sub>. *J. Am. Ceram. Soc.* **66**, 23–27 (1983).
154. Beltrán, J. I., Gallego, S., Cerdá, J., Moya, J. S. & Muñoz, M. C. Internal ceramic reconstruction weakens metal–ZrO<sub>2</sub> adhesion. *J. Phys. Chem. B* **108**, 15439–15442 (2004).
155. Kul'kova, S. E., Bakulin, A. V., Hocker, S. & Schmauder, S. Theoretical study of adhesion at the metal-zirconium dioxide interfaces. *Tech. Phys.* **58**, 325–334 (2013).
156. Malyi, O. I., Kulish, V. V., Bai, K., Wu, P. & Chen, Z. A computational study of the effect of alloying additions on the stability of Ni/c-ZrO<sub>2</sub> interfaces. *Surf. Sci.* **611**, 5–9 (2013).
157. Scott Weil, K., Coyle, C. A., Darsell, J. T., Xia, G. G. & Hardy, J. S. Effects of thermal cycling and thermal aging on the hermeticity and strength of silver–copper oxide air-brazed seals. *J. Power Sources* **152**, 97–104 (2005).
158. Skiera, E. *et al.* Mechanical properties of reactive air brazed (RAB) metal/ceramic joints. Part 1: Visco-plastic deformation of silver-based reactive air brazes. *Adv. Eng. Mater.* **16**, 1462–1467 (2014).
159. Kim, J. Y., Hardy, J. S. & Weil, S. Dual-atmosphere tolerance of Ag–CuO-based air braze. *Int. J. Hydrog. Energy* **32**, 3655–3663 (2007).

160. Pönicke, A., Schilm, J., Kusnezoff, M. & Michaelis, A. Aging behavior of reactive air brazed seals for SOFC. *Fuel Cells* **15**, 735–741 (2015).
161. Perdew, J. P., Burke, K. & Ernzerhof, M. Generalized gradient approximation made simple. *Phys. Rev. Lett.* **77**, 3865–3868 (1996).
162. Becke, A. D. Density-functional exchange-energy approximation with correct asymptotic behavior. *Phys. Rev. A* **38**, 3098–3100 (1988).
163. Kresse, G. & Joubert, D. From ultrasoft pseudopotentials to the projector augmented-wave method. *Phys. Rev. B* **59**, 1758–1775 (1999).
164. Dudarev, S. L., Botton, G. A., Savrasov, S. Y., Humphreys, C. J. & Sutton, A. P. Electron-energy-loss spectra and the structural stability of nickel oxide: An LSDA+U study. *Phys. Rev. B* **57**, 1505–1509 (1998).
165. Mosey, N. J., Liao, P. & Carter, E. A. Rotationally invariant ab initio evaluation of Coulomb and exchange parameters for DFT+U calculations. *J. Chem. Phys.* **129**, 014103 (2008).
166. Mansourian-Hadavi, N. *et al.* Transport and band structure studies of crystalline ZnRh<sub>2</sub>O<sub>4</sub>. *Phys. Rev. B* **81**, 075112 (2010).
167. Bengone, O., Alouani, M., Blöchl, P. & Hugel, J. Implementation of the projector augmented-wave LDA+U method: Application to the electronic structure of NiO. *Phys. Rev. B* **62**, 16392–16401 (2000).
168. Andersson, D. A., Simak, S. I., Johansson, B., Abrikosov, I. A. & Skorodumova, N. V. Modeling of CeO<sub>2</sub>, Ce<sub>2</sub>O<sub>3</sub>, and CeO<sub>2-x</sub> in the LDA+U formalism. *Phys. Rev. B* **75**, 035109 (2007).
169. Density functional theory analysis of dopants in cupric oxide. *J. Appl. Phys.* **111**, 103708 (2012).
170. Zhao, Z. *et al.* First-principles study on the doping effects of nitrogen on the electronic structure and optical properties of Cu<sub>2</sub>O. *RSC Adv.* **3**, 84–90 (2012).
171. Chevalier, J., Gremillard, L., Virkar, A. V. & Clarke, D. R. The tetragonal-monoclinic transformation in zirconia: Lessons learned and future trends. *J. Am. Ceram. Soc.* **92**, 1901–1920 (2009).
172. Idris, M. A., Bak, T., Li, S. & Nowotny, J. Effect of segregation on surface and near-surface chemistry of yttria-stabilized zirconia. *J. Phys. Chem. C* **116**, 10950–10958 (2012).
173. Winnubst, A. J. A., Kroot, P. J. M. & Burggraaf, A. J. AES/STEM grain boundary analysis of stabilized zirconia ceramics. *J. Phys. Chem. Solids* **44**, 955–960 (1983).
174. Kumikov, V. K. & Khokonov, K. B. On the measurement of surface free energy and surface tension of solid metals. *J. Appl. Phys.* **54**, 1346–1350 (1983).

175. Donnan, F. G. & Shaw, T. W. A. The solubility of oxygen in molten silver. *J. Soc. Chem. Ind.* **29**, 987–989 (1910).
176. Kirshenbaum, A. D., Cahill, J. A. & Grosse, A. V. The density of liquid silver from its melting point to its normal boiling point 2450°K. *J. Inorg. Nucl. Chem.* **24**, 333–336 (1962).
177. *Module, Forcite. 'Material Studio 6.0.'* (Accelrys Inc., 2011).
178. Sun, H. *et al.* COMPASS II: extended coverage for polymer and drug-like molecule databases. *J. Mol. Model.* **22**, 47 (2016).
179. Zhang, W. X. & He, C. Melting of cu nanowires: A study using molecular dynamics simulation. *J. Phys. Chem. C* **114**, 8717–8720 (2010).
180. Wagner, C. N. J., Ocken, H. & Joshi, M. L. Interference and radial distribution functions of liquid copper, silver, tin, and mercury. *Z. Für Naturforschung A* **20**, 325–335 (2014).
181. Darsell, J. T. & Weil, K. S. Experimental determination of phase equilibria in the silver–copper oxide system at high temperature. *Scr. Mater.* **56**, 1111–1114 (2007).
182. Tyson, W. R. & Miller, W. A. Surface free energies of solid metals: Estimation from liquid surface tension measurements. *Surf. Sci.* **62**, 267–276 (1977).
183. Sotiropoulou, D. & Nikolopoulos, P. Work of adhesion in ZrO<sub>2</sub>-liquid metal systems. *J. Mater. Sci.* **28**, 356–360 (1993).
184. Zhang, W. & Smith, J. R. Stoichiometry and adhesion of Nb/Al<sub>2</sub>O<sub>3</sub>. *Phys. Rev. B* **61**, 16883–16889 (2000).
185. Characterization of CuAlO<sub>2</sub> thin films prepared on sapphire substrates by reactive sputtering and annealing. *Jpn. J. Appl. Phys.* **47**, 592 (2008).
186. Shih, C. H. & Tseng, B. H. Formation mechanism of CuAlO<sub>2</sub> prepared by rapid thermal annealing of Al<sub>2</sub>O<sub>3</sub>/Cu<sub>2</sub>O/sapphire sandwich structure. *Phys. Procedia* **32**, 395–400 (2012).
187. Liu, Q.-J. & Liu, Z.-T. Theoretical insights into structural–electronic relationships and relative stability of the Cu-, Al- and O-terminated CuAlO<sub>2</sub>(0001) surfaces. *Vacuum* **107**, 90–98 (2014).
188. Hennings, D. Phase equilibria and thermodynamics of the double oxide phase Cu<sub>3</sub>TiO<sub>4</sub>. *J. Solid State Chem.* **31**, 275–279 (1980).
189. Derling, S., Müller, T., Abicht, H.-P., Felgner, K.-H. & Langhammer, H. T. Copper oxide as a sintering agent for barium titanate based ceramics. *J. Mater. Sci.* **36**, 1425–1431 (2001).
190. Jacob, K. T. & Alcock, C. B. Thermodynamics of CuAlO<sub>2</sub> and CuAl<sub>2</sub>O<sub>4</sub> and phase equilibria in the system Cu<sub>2</sub>O-CuO-Al<sub>2</sub>O<sub>3</sub>. *J. Am. Ceram. Soc.* **58**, 192–195 (1975).

191. Erskine, K. M., Meier, A. M. & Pilgrim, S. M. Brazing perovskite ceramics with silver/copper oxide braze alloys. *J. Mater. Sci.* **37**, 1705–1709 (2002).
192. Weil, K. S., Hardy, J. S., Rice, J. P. & Kim, J. Y. Brazing as a means of sealing ceramic membranes for use in advanced coal gasification processes. *Fuel* **85**, 156–162 (2006).
193. Souza, G. M., Victoria, R., Joly, C. & Verdade, L. *Bioenergy & Sustainability: Bridging the gaps*. (SCOPE Bioenergy, 2015).
194. Davison, B. H. *et al.* The impact of biotechnological advances on the future of US bioenergy. *Biofuels Bioprod. Biorefining* **9**, 454–467 (2015).
195. Himmel, M. E. *et al.* Biomass recalcitrance: Engineering plants and enzymes for biofuels production. *Science* **315**, 804–807 (2007).
196. Bruijninx, P. C. A. & Weckhuysen, B. M. Biomass conversion: Lignin up for break-down. *Nat. Chem.* **6**, 1035–1036 (2014).
197. Ragauskas, A. J. *et al.* Lignin valorization: Improving lignin processing in the biorefinery. *Science* **344**, 1246843 (2014).
198. Lora, J. H. & Glasser, W. G. Recent industrial applications of lignin: A sustainable alternative to nonrenewable materials. *J. Polym. Environ.* **10**, 39–48 (2002).
199. Mansouri, N.-E. E. & Salvadó, J. Structural characterization of technical lignins for the production of adhesives: Application to liginosulfonate, kraft, soda-anthraquinone, organosolv and ethanol process lignins. *Ind. Crops Prod.* **24**, 8–16 (2006).
200. Zakzeski, J., Jongerius, A. L., Bruijninx, P. C. A. & Weckhuysen, B. M. Catalytic lignin valorization process for the production of aromatic chemicals and hydrogen. *ChemSusChem* **5**, 1602–1609 (2012).
201. Holladay, J. E., White, J. F., Bozell, J. J. & Johnson, D. *Top value-added chemicals from biomass - Volume II—Results of screening for potential candidates from biorefinery lignin*. (2007).
202. Zheng, Y., Chen, D. & Zhu, X. Aromatic hydrocarbon production by the online catalytic cracking of lignin fast pyrolysis vapors using Mo<sub>2</sub>N/γ-Al<sub>2</sub>O<sub>3</sub>. *J. Anal. Appl. Pyrolysis* **104**, 514–520 (2013).
203. Yoshikawa, T. *et al.* Production of phenols from lignin via depolymerization and catalytic cracking. *Fuel Process. Technol.* **108**, 69–75 (2013).
204. Werhan, H., Mir, J. M., Voitl, T. & Rudolf von Rohr, P. Acidic oxidation of kraft lignin into aromatic monomers catalyzed by transition metal salts. *Holzforschung* **65**, 703–709 (2011).

205. Kelley, P., Lin, S., Edouard, G., Day, M. W. & Agapie, T. Nickel-mediated hydrogenolysis of C–O bonds of aryl ethers: What Is the Source of the Hydrogen? *J. Am. Chem. Soc.* **134**, 5480–5483 (2012).
206. Parsell, T. H. *et al.* Cleavage and hydrodeoxygenation (HDO) of C–O bonds relevant to lignin conversion using Pd/Zn synergistic catalysis. *Chem. Sci.* **4**, 806–813 (2013).
207. Sturgeon, M. R. *et al.* Lignin depolymerisation by nickel supported layered-double hydroxide catalysts. *Green Chem.* **16**, 824–835 (2014).
208. Jia, S., Cox, B. J., Guo, X., Zhang, Z. C. & Ekerdt, J. G. Cleaving the  $\beta$ -O-4 bonds of lignin model compounds in an acidic ionic liquid, 1-H-3-methylimidazolium chloride: An optional strategy for the degradation of lignin. *ChemSusChem* **3**, 1078–1084 (2010).
209. Wu, G., Heitz, M. & Chornet, E. Improved Alkaline oxidation process for the production of aldehydes (vanillin and syringaldehyde) from steam-explosion hardwood lignin. *Ind. Eng. Chem. Res.* **33**, 718–723 (1994).
210. Behling, R., Valange, S. & Chatel, G. Heterogeneous catalytic oxidation for lignin valorization into valuable chemicals: what results? What limitations? What trends? *Green Chem.* **18**, 1839–1854 (2016).
211. Azarpira, A., Ralph, J. & Lu, F. Catalytic alkaline oxidation of lignin and its model compounds: A pathway to aromatic biochemicals. *BioEnergy Res.* **7**, 78–86 (2014).
212. Stärk, K., Taccardi, N., Bösmann, A. & Wasserscheid, P. Oxidative depolymerization of lignin in ionic liquids. *ChemSusChem* **3**, 719–723 (2010).
213. Wu, G. & Heitz, M. Catalytic mechanism of  $\text{Cu}^{2+}$  and  $\text{Fe}^{3+}$  in alkaline  $\text{O}_2$  oxidation of lignin. *J. Wood Chem. Technol.* **15**, 189–202 (1995).
214. Jiang, Y.-Y., Yan, L., Yu, H.-Z., Zhang, Q. & Fu, Y. Mechanism of vanadium-catalyzed selective C–O and C–C cleavage of lignin model compound. *ACS Catal.* **6**, 4399–4410 (2016).
215. Sedai, B. *et al.* Comparison of copper and vanadium homogeneous catalysts for aerobic oxidation of lignin models. *ACS Catal.* **1**, 794–804 (2011).
216. Hoover, J. M. & Stahl, S. S. Highly practical copper(I)/TEMPO catalyst system for chemoselective aerobic oxidation of primary alcohols. *J. Am. Chem. Soc.* **133**, 16901–16910 (2011).
217. Bujanovic, B., Reiner, R. S., Ralph, S. A. & Atalla, R. H. Polyoxometalate delignification of birch kraft pulp and effect on residual lignin. *J. Wood Chem. Technol.* **31**, 121–141 (2011).
218. Hocking, M. B. Vanillin: Synthetic flavoring from spent sulfite liquor. *J. Chem. Educ.* **74**, 1055 (1997).

219. Dignum, M. J. W., Kerler, J. & Verpoorte, R. Vanilla production: technological, chemical, and biosynthetic aspects. *Food Rev. Int.* **17**, 119–120 (2001).
220. Fargues, C., Mathias, Á. & Rodrigues, A. Kinetics of vanillin production from kraft lignin oxidation. *Ind. Eng. Chem. Res.* **35**, 28–36 (1996).
221. Sergeev, A. G., Webb, J. D. & Hartwig, J. F. A Heterogeneous nickel catalyst for the hydrogenolysis of aryl ethers without arene hydrogenation. *J. Am. Chem. Soc.* **134**, 20226–20229 (2012).
222. Zhang, J. *et al.* A Series of NiM (M = Ru, Rh, and Pd) Bimetallic catalysts for effective lignin hydrogenolysis in water. *ACS Catal.* **4**, 1574–1583 (2014).
223. Zhang, J. *et al.* Highly efficient, NiAu-catalyzed hydrogenolysis of lignin into phenolic chemicals. *Green Chem.* **16**, 2432–2437 (2014).
224. He, J., Zhao, C. & Lercher, J. A. Ni-catalyzed cleavage of aryl ethers in the aqueous phase. *J. Am. Chem. Soc.* **134**, 20768–20775 (2012).
225. Onwudili, J. A. & Williams, P. T. Catalytic depolymerization of alkali lignin in subcritical water: influence of formic acid and Pd/C catalyst on the yields of liquid monomeric aromatic products. *Green Chem.* **16**, 4740–4748 (2014).
226. Song, Q. *et al.* Lignin depolymerization (LDP) in alcohol over nickel-based catalysts via a fragmentation–hydrogenolysis process. *Energy Environ. Sci.* **6**, 994–1007 (2013).
227. Bosch, S. V. den *et al.* Reductive lignocellulose fractionation into soluble lignin-derived phenolic monomers and dimers and processable carbohydrate pulps. *Energy Environ. Sci.* **8**, 1748–1763 (2015).
228. Barta, K. & Ford, P. C. Catalytic conversion of nonfood woody biomass solids to organic liquids. *Acc. Chem. Res.* **47**, 1503–1512 (2014).
229. Barta, K. *et al.* Catalytic disassembly of an organosolv lignin via hydrogen transfer from supercritical methanol. *Green Chem.* **12**, 1640–1647 (2010).
230. Song, Q., Wang, F. & Xu, J. Hydrogenolysis of lignosulfonate into phenols over heterogeneous nickel catalysts. *Chem. Commun.* **48**, 7019–7021 (2012).
231. Sun, S.-N., Li, M.-F., Yuan, T.-Q., Xu, F. & Sun, R.-C. Effect of ionic liquid/organic solvent pretreatment on the enzymatic hydrolysis of corncob for bioethanol production. Part 1: Structural characterization of the lignins. *Ind. Crops Prod.* **43**, 570–577 (2013).
232. Schutyser, W. *et al.* Influence of bio-based solvents on the catalytic reductive fractionation of birch wood. *Green Chem.* **17**, 5035–5045 (2015).

233. Gao, F., Webb, J. D., Sorek, H., Wemmer, D. E. & Hartwig, J. F. Fragmentation of lignin samples with commercial Pd/C under ambient pressure of hydrogen. *ACS Catal.* **6**, 7385–7392 (2016).
234. Yue, F., Lu, F., Sun, R.-C. & Ralph, J. Syntheses of lignin-derived thioacidolysis monomers and their uses as quantitation standards. *J. Agric. Food Chem.* **60**, 922–928 (2012).
235. Boerjan, W., Ralph, J. & Baucher, M. Lignin biosynthesis. *Annu. Rev. Plant Biol.* **54**, 519–546 (2003).
236. Aguayo, M. G., Ferraz, A., Elissetche, J. P., Masarin, F. & Mendonça, R. T. Lignin chemistry and topochemistry during kraft delignification of eucalyptus globulus genotypes with contrasting pulpwood characteristics. *Holzforschung* **68**, 623–629 (2013).
237. Alvira, P., Tomás-Pejó, E., Ballesteros, M. & Negro, M. J. Pretreatment technologies for an efficient bioethanol production process based on enzymatic hydrolysis: A review. *Bioresour. Technol.* **101**, 4851–4861 (2010).
238. Brodeur, G. *et al.* Chemical and Physicochemical Pretreatment of Lignocellulosic Biomass: A Review. *Enzyme Res.* **2011**, e787532 (2011).
239. Gellerstedt, G., Majtnerova, A. & Zhang, L. Towards a new concept of lignin condensation in kraft pulping. Initial results. *C. R. Biol.* **327**, 817–826 (2004).
240. Nakamura, T., Kawamoto, H. & Saka, S. Condensation reactions of some lignin related compounds at relatively low pyrolysis temperature. *J. Wood Chem. Technol.* **27**, 121–133 (2007).
241. Shimada, K., Hosoya, S. & Ikeda, T. Condensation reactions of softwood and hardwood lignin model compounds under organic acid cooking conditions. *J. Wood Chem. Technol.* **17**, 57–72 (1997).
242. Stoklosa, R. J. & Hodge, D. B. Fractionation and improved enzymatic deconstruction of hardwoods with alkaline delignification. *BioEnergy Res.* **8**, 1224–1234 (2015).
243. Velez, J. & Thies, M. C. Solvated liquid-lignin fractions from a Kraft black liquor. *Bioresour. Technol.* **148**, 586–590 (2013).
244. Gu, F. *et al.* Effect of complete dissolution in LiCl/DMSO on the isolation and characteristics of lignin from wheat straw internode. *Ind. Crops Prod.* **74**, 703–711 (2015).
245. Stoklosa, R. J. *et al.* Correlating lignin structural features to phase partitioning behavior in a novel aqueous fractionation of softwood Kraft black liquor. *Green Chem.* **15**, 2904–2912 (2013).
246. Balakshin, M. & Capanema, E. On the quantification of lignin hydroxyl groups with <sup>31</sup>P and <sup>13</sup>C NMR spectroscopy. *J. Wood Chem. Technol.* **35**, 220–237 (2015).

247. El Hage, R. *et al.* Characterization of milled wood lignin and ethanol organosolv lignin from miscanthus. *Polym. Degrad. Stab.* **94**, 1632–1638 (2009).
248. Kim, H. & Ralph, J. Solution-state 2D NMR of ball-milled plant cell wall gels in DMSO-d<sub>6</sub>/pyridine-d<sub>5</sub>. *Org. Biomol. Chem.* **8**, 576–591 (2010).
249. Li, Z. *et al.* Chemical and structural changes associated with Cu-catalyzed alkaline-oxidative delignification of hybrid poplar. *Biotechnol. Biofuels* **8**, 1–12 (2015).
250. Ralph, S. A. & Ralph, J. NMR database of lignin and cell wall model compounds.
251. Liitiä, T. M., Maunu, S. L., Hortling, B., Toikka, M. & Kilpeläinen, I. Analysis of technical lignins by two- and three-dimensional NMR spectroscopy. *J. Agric. Food Chem.* **51**, 2136–2143 (2003).
252. Toledano, A., Serrano, L., Garcia, A., Mondragon, I. & Labidi, J. Comparative study of lignin fractionation by ultrafiltration and selective precipitation. *Chem. Eng. J.* **157**, 93–99 (2010).
253. Mussatto, S. I., Fernandes, M. & Roberto, I. C. Lignin recovery from brewer's spent grain black liquor. *Carbohydr. Polym.* **70**, 218–223 (2007).
254. Klett, A. S., Chappell, P. V. & Thies, M. C. Recovering ultraclean lignins of controlled molecular weight from Kraft black-liquor lignins. *Chem. Commun.* **51**, 12855–12858 (2015).
255. Saito, T. *et al.* Methanol fractionation of softwood kraft lignin: Impact on the lignin properties. *ChemSusChem* **7**, 221–228 (2014).
256. Lake, M. A. & Blackburn, J. C. Process for recovering lignin. (2011).
257. Tomani, P. The lignoboost process. *Cellul. Chem. Technol.* **44**, 53–58
258. Kouisni, L., Holt-hindle, P., Maki, K. & Paleologou, M. The lignoforce system<sup>TM</sup>: A new process for the production of high-quality lignin from black liquor. *J. Sci. Technol. For. Prod. Process.* **2**, 6–10 (2012).
259. Zhang, L. & Gellerstedt, G. Quantitative 2D HSQC NMR determination of polymer structures by selecting suitable internal standard references. *Magn. Reson. Chem.* **45**, 37–45 (2007).
260. Faith, W. L., Keyes, D. B., Clark, R. L., Lowenheim, F. A. & Moran, M. K. Vanillin. in *Industrial chemicals* (Wiley New York, 1957).
261. Brunow, G., Lundquist, K. & Gellerstedt, G. Lignin. in *Analytical methods in wood chemistry, pulping, and papermaking* (eds. Sjöström, P. D. E. & Alén, P. D. R.) 77–124 (Springer Berlin Heidelberg, 1999). doi:10.1007/978-3-662-03898-7\_4
262. Hatfield, R. & Fukushima, R. S. Can lignin be accurately measured? *Crop Sci.* **45**, 832 (2005).

263. Constant, S., Robitzer, M., Quignard, F. & Di Renzo, F. Vanillin oligomerization as a model of side reactions in lignin fragmentation. *Catal. Today* **189**, 123–128 (2012).
264. Tarabanko, V. E., Petukhov, D. V. & Selyutin, G. E. New mechanism for the catalytic oxidation of lignin to vanillin. *Kinet. Catal.* **45**, 569–577 (2004).
265. Sedai, B. *et al.* Aerobic oxidation of  $\beta$ -1 lignin model compounds with copper and oxovanadium catalysts. *ACS Catal.* **3**, 3111–3122 (2013).
266. Bosch, S. V. den *et al.* Tuning the lignin oil OH-content with Ru and Pd catalysts during lignin hydrogenolysis on birch wood. *Chem. Commun.* **51**, 13158–13161 (2015).
267. Yan, N. *et al.* Selective degradation of wood lignin over noble-metal catalysts in a two-step process. *ChemSusChem* **1**, 626–629 (2008).
268. Evstigneev, E. I. Factors affecting lignin solubility. *Russ. J. Appl. Chem.* **84**, 1040–1045 (2011).
269. Crestini, C., Melone, F., Sette, M. & Saladino, R. Milled wood lignin: A linear oligomer. *Biomacromolecules* **12**, 3928–3935 (2011).
270. Yue, F., Lu, F., Ralph, S. & Ralph, J. Identification of 4–O–5 units in softwood lignins via definitive lignin models and NMR. *Biomacromolecules* **17**, 1909–1920 (2016).
271. Montroll, E. W. & Simha, R. Theory of depolymerization of long chain molecules. *J. Chem. Phys.* **8**, 721–726 (1940).
272. Feghali, E., Carrot, G., Thuéry, P., Genre, C. & Cantat, T. Convergent reductive depolymerization of wood lignin to isolated phenol derivatives by metal-free catalytic hydrosilylation. *Energy Environ. Sci.* **8**, 2734–2743 (2015).
273. Voitl, T. & Rudolf von Rohr, P. Oxidation of lignin using aqueous polyoxometalates in the presence of alcohols. *ChemSusChem* **1**, 763–769 (2008).
274. Huang, X., Korányi, T. I., Boot, M. D. & Hensen, E. J. M. Ethanol as capping agent and formaldehyde scavenger for efficient depolymerization of lignin to aromatics. *Green Chem.* **17**, 4941–4950 (2015).
275. Anderson, E. M. *et al.* Reductive catalytic fractionation of corn stover lignin. *ACS Sustain. Chem. Eng.* **4**, 6940–6950 (2016).
276. Galkin, M. V. & Samec, J. S. M. Selective route to 2-Propenyl aryls directly from wood by a tandem organosolv and palladium-catalysed transfer hydrogenolysis. *ChemSusChem* **7**, 2154–2158 (2014).
277. Shuai, L. *et al.* Formaldehyde stabilization facilitates lignin monomer production during biomass depolymerization. *Science* **354**, 329–333 (2016).

278. Luterbacher, J. S. *et al.* Lignin monomer production integrated into the  $\gamma$ -valerolactone sugar platform. *Energy Environ. Sci.* **8**, 2657–2663 (2015).
279. Rinaldi, R. *et al.* Paving the way for lignin valorisation: Recent advances in bioengineering, biorefining and catalysis. *Angew. Chem. Int. Ed.* **55**, 8164–8215 (2016).
280. Vanholme, R., Demedts, B., Morreel, K., Ralph, J. & Boerjan, W. Lignin biosynthesis and structure. *Plant Physiol.* **153**, 895–905 (2010).
281. Zakzeski, J., Bruijninx, P. C. A., Jongerius, A. L. & Weckhuysen, B. M. The catalytic valorization of lignin for the production of renewable chemicals. *Chem. Rev.* **110**, 3552–3599 (2010).
282. Qi, S.-C., Hayashi, J., Kudo, S. & Zhang, L. Catalytic hydrogenolysis of kraft lignin to monomers at high yield in alkaline water. *Green Chem.* **19**, 2636–2645 (2017).
283. Klein, I., Saha, B. & Abu-Omar, M. M. Lignin depolymerization over Ni/C catalyst in methanol, a continuation: effect of substrate and catalyst loading. *Catal. Sci. Technol.* **5**, 3242–3245 (2015).
284. Chen, J. *et al.* High yield production of natural phenolic alcohols from woody biomass using a nickel-based catalyst. *ChemSusChem* **9**, 3353–3360 (2016).
285. Anderson, E. M. *et al.* Flowthrough reductive catalytic fractionation of biomass. *Joule* **1**, 613–622 (2017).
286. Phongprecha, T. *et al.* Predicting lignin depolymerization yields from quantifiable properties using fractionated biorefinery lignins. *Green Chem.* **19**, 5131–5143 (2017).
287. Zhang, Y., He, H., Dong, K., Fan, M. & Zhang, S. A DFT study on lignin dissolution in imidazolium-based ionic liquids. *RSC Adv.* **7**, 12670–12681 (2017).
288. Zhu, Y., Yan, J., Liu, C. & Zhang, D. Modeling interactions between a  $\beta$ -O-4 type lignin model compound and 1-allyl-3-methylimidazolium chloride ionic liquid. *Biopolymers* **107**, (2017).
289. Silveira, R. L., Stoyanov, S. R., Gusarov, S., Skaf, M. S. & Kovalenko, A. Supramolecular interactions in secondary plant cell walls: effect of lignin chemical composition revealed with the molecular theory of solvation. *J. Phys. Chem. Lett.* **6**, 206–211 (2015).
290. Petridis, L., Schulz, R. & Smith, J. C. Simulation analysis of the temperature dependence of lignin structure and dynamics. *J. Am. Chem. Soc.* **133**, 20277–20287 (2011).
291. Galkin, M. V., Sawadjoon, S., Rohde, V., Dawange, M. & Samec, J. S. M. Mild heterogeneous palladium-catalyzed cleavage of  $\beta$ -O-4'-ether linkages of lignin model compounds and native lignin in air. *ChemCatChem* **6**, 179–184 (2014).

292. Galkin, M. V., Dahlstrand, C. & Samec, J. S. M. Mild and robust redox-neutral Pd/C-catalyzed lignol  $\beta$ -O-4' bond cleavage through a low-energy-barrier pathway. *ChemSusChem* **8**, 2187–2192 (2015).
293. Parthasarathi, R., Romero, R. A., Redondo, A. & Gnanakaran, S. Theoretical study of the remarkably diverse linkages in lignin. *J. Phys. Chem. Lett.* **2**, 2660–2666 (2011).
294. Beste, A. & Buchanan, A. C. Computational study of bond dissociation enthalpies for lignin model compounds. substituent effects in phenethyl phenyl ethers. *J. Org. Chem.* **74**, 2837–2841 (2009).
295. Kim, S. *et al.* Computational study of bond dissociation enthalpies for a large range of native and modified lignins. *J. Phys. Chem. Lett.* **2**, 2846–2852 (2011).
296. Grimme, S., Antony, J., Ehrlich, S. & Krieg, H. A consistent and accurate ab initio parametrization of density functional dispersion correction (DFT-D) for the 94 elements H-Pu. *J. Chem. Phys.* **132**, 154104 (2010).
297. Grimme, S., Ehrlich, S. & Goerigk, L. Effect of the damping function in dispersion corrected density functional theory. *J. Comput. Chem.* **32**, 1456–1465 (2011).
298. Dion, M., Rydberg, H., Schröder, E., Langreth, D. C. & Lundqvist, B. I. Van der Waals density functional for general geometries. *Phys. Rev. Lett.* **92**, 246401 (2004).
299. Klimeš, J., Bowler, D. R. & Michaelides, A. Chemical accuracy for the van der Waals density functional. *J. Phys. Condens. Matter* **22**, 022201 (2010).
300. Mathew, K. & Hennig, R. G. Implicit self-consistent description of electrolyte in plane-wave density-functional theory. *ArXiv160103346 Cond-Mat* (2016).
301. Mathew, K., Sundararaman, R., Letchworth-Weaver, K., Arias, T. A. & Hennig, R. G. Implicit solvation model for density-functional study of nanocrystal surfaces and reaction pathways. *J. Chem. Phys.* **140**, 084106 (2014).
302. Batsanov, S. S. Van der Waals Radii of Elements. *Inorg. Mater.* **37**, 871–885 (2001).
303. Fishman, M., Zhuang, H. L., Mathew, K., Dirschka, W. & Hennig, R. G. Accuracy of exchange-correlation functionals and effect of solvation on the surface energy of copper. *Phys. Rev. B* **87**, 245402 (2013).
304. Implicit solvation model for density-functional study of nanocrystal surfaces and reaction pathways. *J. Chem. Phys.* **140**, 084106 (2014).
305. Dannhauser, W. & Bahe, L. W. Dielectric Constant of Hydrogen Bonded Liquids. III. Superheated Alcohols. *J. Chem. Phys.* **40**, 3058 (2004).
306. Hinz, H.-J. *Thermodynamic Data for Biochemistry and Biotechnology*. (Springer Science & Business Media, 2012).

307. Rigby, D., Sun, H. & Eichinger, B. E. Computer simulations of poly(ethylene oxide): force field, pvt diagram and cyclization behaviour. *Polym. Int.* **44**, 311–330 (1997).
308. Yildirim, H., Greber, T. & Kara, A. Trends in adsorption characteristics of benzene on transition metal surfaces: Role of surface chemistry and van der waals interactions. *J. Phys. Chem. C* **117**, 20572–20583 (2013).
309. Lu, J. & Heyden, A. Theoretical investigation of the reaction mechanism of the hydrodeoxygenation of guaiacol over a Ru(0001) model surface. *J. Catal.* **321**, 39–50 (2015).
310. Benzene adsorption on Cu(111): Formation of a stable bilayer. *J. Chem. Phys.* **101**, 9122–9131 (1994).
311. Koschel, H., Held, G. & Steinrück, H.-P. The orientation of benzene on bimetallic surfaces. *Surf. Rev. Lett.* **06**, 893–901 (1999).
312. Ruiz, V. G., Liu, W., Zojer, E., Scheffler, M. & Tkatchenko, A. Density-functional theory with screened van der Waals interactions for the modeling of hybrid inorganic-organic systems. *Phys. Rev. Lett.* **108**, 146103 (2012).
313. Lee, K., Morikawa, Y. & Langreth, D. C. Adsorption of n-butane on Cu(100), Cu(111), Au(111), and Pt(111): Van der Waals density-functional study. *Phys. Rev. B* **82**, 155461 (2010).
314. Liu, W. *et al.* Structure and energetics of benzene adsorbed on transition-metal surfaces: density-functional theory with van der Waals interactions including collective substrate response. *New J. Phys.* **15**, 053046 (2013).
315. Mittendorfer, F. *et al.* Graphene on Ni(111): Strong interaction and weak adsorption. *Phys. Rev. B* **84**, 201401 (2011).
316. Lebègue, S. *et al.* Cohesive properties and asymptotics of the dispersion interaction in graphite by the random phase approximation. *Phys. Rev. Lett.* **105**, 196401 (2010).
317. Delle Site, L., Abrams, C. F., Alavi, A. & Kremer, K. Polymers near metal surfaces: selective adsorption and global conformations. *Phys. Rev. Lett.* **89**, 156103 (2002).
318. Xu, L. & Yang, X. Molecular dynamics simulation of adsorption of pyrene–polyethylene glycol onto graphene. *J. Colloid Interface Sci.* **418**, 66–73 (2014).
319. Besombes, S., Robert, D., Utille, J.-P., Tavel, F. R. & Mazeau, K. Molecular modeling of syringyl and p-hydroxyphenyl  $\beta$ -O-4 dimers. Comparative study of the computed and experimental conformational properties of lignin  $\beta$ -O-4 model compounds. *J. Agric. Food Chem.* **51**, 34–42 (2003).
320. Simon, J. P. & Eriksson, K.-E. L. The significance of intra-molecular hydrogen bonding in the  $\beta$ -O-4 linkage of lignin. *J. Mol. Struct.* **384**, 1–7 (1996).

321. Stolov, M. A., Zaitseva, K. V., Varfolomeev, M. A. & Acree, W. E. Enthalpies of solution and enthalpies of solvation of organic solutes in ethylene glycol at 298.15K: Prediction and analysis of intermolecular interaction contributions. *Thermochim. Acta* **648**, 91–99 (2017).
322. Stephens, T. W. *et al.* Enthalpy of solvation correlations for organic solutes and gases dissolved in 2-propanol, 2-butanol, 2-methyl-1-propanol and ethanol. *Thermochim. Acta* **523**, 214–220 (2011).
323. Saleheen, M. & Heyden, A. Liquid-phase modeling in heterogeneous catalysis. *ACS Catal.* **8**, 2188–2194 (2018).
324. DeLano, W. L. *PyMOL*. (2002).
325. Bernt, C. M., Manesewan, H., Chui, M., Boscolo, M. & Ford, P. C. Temperature tuning the catalytic reactivity of Cu-Doped porous metal oxides with lignin models. *ACS Sustain. Chem. Eng.* **6**, 2510–2516 (2018).
326. Besse, X., Schuurman, Y. & Guilhaume, N. Reactivity of lignin model compounds through hydrogen transfer catalysis in ethanol/water mixtures. *Appl. Catal. B Environ.* **209**, 265–272 (2017).
327. Pepper, J. M. & Lee, Y. W. Lignin and related compounds. I. A comparative study of catalysts for lignin hydrogenolysis. *Can. J. Chem.* **47**, 723–727 (1969).
328. Pepper, J. M. & Lee, Y. W. Lignin and related compounds. II. Studies using ruthenium and Raney nickel as catalysts for lignin hydrogenolysis. *Can. J. Chem.* **48**, 477–479 (1970).
329. Singh, S. K. & Ekhe, J. D. Cu–Mo doped zeolite ZSM-5 catalyzed conversion of lignin to alkyl phenols with high selectivity. *Catal. Sci. Technol.* **5**, 2117–2124 (2015).
330. Oregui-Bengoechea, M., Gandarias, I., Arias, P. L. & Barth, T. Unraveling the role of formic acid and the type of solvent in the catalytic conversion of lignin: A holistic approach. *ChemSusChem* **10**, 754–766 (2017).
331. Zanchet, D., Santos, J. B. O., Damyanova, S., Gallo, J. M. R. & C. Bueno, J. M. Toward understanding metal-catalyzed ethanol reforming. *ACS Catal.* **5**, 3841–3863 (2015).
332. Konsolakis, M. *et al.* Hydrogen production by ethanol steam reforming (ESR) over CeO<sub>2</sub> supported transition metal (Fe, Co, Ni, Cu) catalysts: Insight into the structure-activity relationship. *Catalysts* **6**, 39 (2016).
333. Hou, T., Zhang, S., Chen, Y., Wang, D. & Cai, W. Hydrogen production from ethanol reforming: Catalysts and reaction mechanism. *Renew. Sustain. Energy Rev.* **44**, 132–148 (2015).
334. Li, W., Wang, H., Ren, Z., Wang, G. & Bai, J. Co-production of hydrogen and multi-wall carbon nanotubes from ethanol decomposition over Fe/Al<sub>2</sub>O<sub>3</sub> catalysts. *Appl. Catal. B Environ.* **84**, 433–439 (2008).

335. Samuel, R., Pu, Y., Raman, B. & Ragauskas, A. J. Structural characterization and comparison of switchgrass ball-milled lignin before and after dilute acid pretreatment. *Appl. Biochem. Biotechnol.* **162**, 62–74 (2010).
336. Jiang, X. *et al.* Fractionation and characterization of kraft lignin by sequential precipitation with various organic solvents. *ACS Sustain. Chem. Eng.* **5**, 835–842 (2017).
337. Bhalla, A. *et al.* Engineered lignin in poplar biomass facilitates Cu-catalyzed alkaline-oxidative pretreatment. *ACS Sustain. Chem. Eng.* **6**, 2932–2941 (2018).
338. Li, Z. *et al.* Catalysis with CuII(bpy) improves alkaline hydrogen peroxide pretreatment. *Biotechnol. Bioeng.* **110**, 1078–1086 (2013).
339. Luterbacher, J. S. *et al.* Nonenzymatic Sugar Production from Biomass Using Biomass-Derived  $\gamma$ -Valerolactone. *Science* **343**, 277–280 (2014).
340. Das, A. *et al.* Lignin conversion to low-molecular-weight aromatics via an aerobic oxidation-hydrolysis sequence: Comparison of different lignin sources. *ACS Sustain. Chem. Eng.* **6**, 3367–3374 (2018).
341. Rinaldi, R. A Tandem for lignin-first biorefinery. *Joule* **1**, 427–428 (2017).
342. Huang, X., Zhu, J., Korányi, T. I., Boot, M. D. & Hensen, E. J. M. Effective release of lignin fragments from lignocellulose by lewis acid metal triflates in the lignin-first approach. *ChemSusChem* **9**, 3262–3267 (2016).
343. Zeng, Y., Zhao, S., Yang, S. & Ding, S.-Y. Lignin plays a negative role in the biochemical process for producing lignocellulosic biofuels. *Curr. Opin. Biotechnol.* **27**, 38–45 (2014).
344. Yang, B. & Wyman, C. E. Effect of xylan and lignin removal by batch and flowthrough pretreatment on the enzymatic digestibility of corn stover cellulose. *Biotechnol. Bioeng.* **86**, 88–98 (2004).
345. Öhgren, K., Bura, R., Saddler, J. & Zacchi, G. Effect of hemicellulose and lignin removal on enzymatic hydrolysis of steam pretreated corn stover. *Bioresour. Technol.* **98**, 2503–2510 (2007).
346. Crowe, J. D., Zarger, R. A. & Hodge, D. B. Relating nanoscale accessibility within plant cell walls to improved enzyme hydrolysis yields in corn stover subjected to diverse pretreatments. *J. Agric. Food Chem.* **65**, 8652–8662 (2017).
347. Williams, D. L., Crowe, J. D., Ong, R. G. & Hodge, D. B. Water sorption in pretreated grasses as a predictor of enzymatic hydrolysis yields. *Bioresour. Technol.* **245**, 242–249 (2017).
348. Bär, J. *et al.* Deconstruction of hybrid poplar to monomeric sugars and aromatics using ethanol organosolv fractionation. *Biomass Convers. Biorefinery* **1**, 1–12 (2018).

349. Pan, X. *et al.* Biorefining of softwoods using ethanol organosolv pulping: Preliminary evaluation of process streams for manufacture of fuel-grade ethanol and co-products. *Biotechnol. Bioeng.* **90**, 473–481 (2005).
350. Hames, Bonnie, *et al.* "Preparation of samples for compositional analysis." Laboratory Analytical Procedure (LAP) 1617 (2008).
351. Lan, T. Q., Lou, H. & Zhu, J. Y. Enzymatic saccharification of lignocelluloses should be conducted at elevated pH 5.2–6.2. *BioEnergy Res.* **6**, 476–485 (2013).
352. Williams, D. L. & Hodge, D. B. Impacts of delignification and hot water pretreatment on the water induced cell wall swelling behavior of grasses and its relation to cellulolytic enzyme hydrolysis and binding. *Cellulose* **21**, 221–235 (2014).
353. Phongpreecha, T., Liu, J., Qi, Y. & Hodge, D. A. Adsorption of lignin  $\beta$ -O-4 dimers on metal surfaces in vacuum and solvated environments. *In preparation*.
354. Macala, G. S. *et al.* Hydrogen transfer from supercritical methanol over a solid base catalyst: A Model for lignin depolymerization. *ChemSusChem* **2**, 215–217 (2009).
355. Selig, M. J. *et al.* Deposition of lignin droplets produced during dilute acid pretreatment of maize stems retards enzymatic hydrolysis of cellulose. *Biotechnol. Prog.* **23**, 1333–1339 (2007).
356. Piccinin, S., Stampfl, C. & Scheffler, M. First-principles investigation of Ag-Cu alloy surfaces in an oxidizing environment. *Phys. Rev. B* **77**, 075426 (2008).
357. Wang, J. & Wang, S.-Q. Surface energy and work function of fcc and bcc crystals: Density functional study. *Surf. Sci.* **630**, 216–224 (2014).
358. Mills, K. C. & Su, Y. C. Review of surface tension data for metallic elements and alloys: Part 1 – Pure metals. *Int. Mater. Rev.* **51**, 329–351 (2006).
359. Hong, S., Shin, Y.-H. & Ihm, J. Crystal shape of a nickel particle related to carbon nanotube growth. *Jpn. J. Appl. Phys.* **41**, 6142 (2002).
360. Abrikosov, I. A., Ruban, A. V., Skriver, H. L. & Johansson, B. Calculated orientation dependence of surface segregations in Pt<sub>50</sub>Ni<sub>50</sub>. *Phys. Rev. B* **50**, 2039–2042 (1994).
361. Tepesch, P. d. & Quong, A. a. First-Principles Calculations of  $\alpha$ -alumina (0001) surfaces energies with and without hydrogen. *Phys. Status Solidi B* **217**, 377–387 (2000).
362. McHale, J. M., Navrotsky, A. & Perrotta, A. J. Effects of increased surface area and chemisorbed H<sub>2</sub>O on the relative stability of nanocrystalline  $\gamma$ -Al<sub>2</sub>O<sub>3</sub> and  $\alpha$ -Al<sub>2</sub>O<sub>3</sub>. *J. Phys. Chem. B* **101**, 603–613 (1997).

363. Costa, D., Sharkas, K., Islam, M. M. & Marcus, P. *Ab initio* study of the chemical states of water on Cr<sub>2</sub>O<sub>3</sub>(0001): From the isolated molecule to saturation coverage. *Surf. Sci.* **603**, 2484–2493 (2009).
364. Rohr, F. *et al.* Strong relaxations at the Cr<sub>2</sub>O<sub>3</sub>(0001) surface as determined via low-energy electron diffraction and molecular dynamics simulations. *Surf. Sci.* **372**, L291–L297 (1997).
365. Wang, X.-G. *et al.* The hematite  $\alpha$ -Fe<sub>2</sub>O<sub>3</sub>(0001) surface: evidence for domains of distinct chemistry. *Phys. Rev. Lett.* **81**, 1038–1041 (1998).
366. Mazeina, L. & Navrotsky, A. Enthalpy of water adsorption and surface enthalpy of goethite ( $\alpha$ -FeOOH) and hematite ( $\alpha$ -Fe<sub>2</sub>O<sub>3</sub>). *Chem. Mater.* **19**, 825–833 (2007).
367. Scherson, Y. D., Aboud, S. J., Wilcox, J. & Cantwell, B. J. Surface structure and reactivity of rhodium oxide. *J. Phys. Chem. C* **115**, 11036–11044 (2011).
368. Broqvist, P., Grönbeck, H. & Panas, I. Surface properties of alkaline earth metal oxides. *Surf. Sci.* **554**, 262–271 (2004).
369. Brunauer, S., Kantró, D. L. & Weise, C. H. The surface energies of calcium oxide and calcium hydroxide. *Can. J. Chem.* **34**, 729–742 (1956).
370. Gilman, J. J. Direct measurements of the surface energies of crystals. *J. Appl. Phys.* **31**, 2208–2218 (1960).
371. Rohrbach, A., Hafner, J. & Kresse, G. Molecular adsorption on the surface of strongly correlated transition-metal oxides: A case study for CO/NiO(100). *Phys. Rev. B* **69**, 075413 (2004).
372. Skorodumova, N. V., Baudin, M. & Hermansson, K. Surface properties of CeO<sub>2</sub> from first principles. *Phys. Rev. B* **69**, 075401 (2004).
373. Hayun, S., Ushakov, S. V. & Navrotsky, A. Direct measurement of surface energy of CeO<sub>2</sub> by differential scanning calorimetry. *J. Am. Ceram. Soc.* **94**, 3679–3682 (2011).
374. Wang, G. *et al.* Density functional studies of zirconia with different crystal phases for oxygen reduction reaction. *RSC Adv.* **5**, 85122–85127 (2015).
375. Ballabio, G., Bernasconi, M., Pietrucci, F. & Serra, S. *Ab initio* study of yttria-stabilized cubic zirconia surfaces. *Phys. Rev. B* **70**, 075417 (2004).
376. Bendavid, L. I. & Carter, E. A. First-Principles predictions of the structure, stability, and photocatalytic potential of Cu<sub>2</sub>O Surfaces. *J. Phys. Chem. B* **117**, 15750–15760 (2013).
377. Evarestov, R. A., Bandura, A. V. & Proskurov, E. V. Plain DFT and hybrid HF-DFT LCAO calculations of SnO<sub>2</sub> (110) and (100) bare and hydroxylated surfaces. *Phys. Status Solidi B* **243**, 1823–1834 (2006).

378. Perron, H. *et al.* Optimisation of accurate rutile TiO<sub>2</sub>(110), (100), (101) and (001) surface models from periodic DFT calculations. *Theor. Chem. Acc.* **117**, 565–574 (2007).
379. Vittadini, A., Selloni, A., Rotzinger, F. P. & Grätzel, M. Structure and energetics of water adsorbed at TiO<sub>2</sub> Anatase (101) and (001) surfaces. *Phys. Rev. Lett.* **81**, 2954–2957 (1998).
380. Synthesis and crystal structure of 2H—CuAlO<sub>2</sub>: *Zeitschrift für Kristallographie - Crystalline Materials.* (1983). Available at: <https://www-degruyter-com.proxy2.cl.msu.edu/view/j/zkri.1983.165.issue-1-4/zkri.1983.165.14.313/zkri.1983.165.14.313.xml>. (Accessed: 28th July 2017)
381. Crystal structure of copper(I) chromium(III) oxide, 2H-CuCrO<sub>2</sub>: *Zeitschrift für Kristallographie - Crystalline Materials.* (1996). Available at: <https://www-degruyter-com.proxy2.cl.msu.edu/view/j/zkri.1996.211.issue-7/zkri.1996.211.7.481/zkri.1996.211.7.481.xml>. (Accessed: 28th July 2017)
382. Effenberger, H. Structure of hexagonal copper(I) ferrite. *Acta Crystallogr. C* **47**, 2644–2646 (1991).
383. Kandpal, H. C. & Seshadri, R. First-Principles electronic structure of the delafossites ABO<sub>2</sub> (A=Cu, Ag, Au; B=Al, Ga, Sc, In, Y): evolution of d10–d10 interactions. *Solid State Sci.* **4**, 1045–1052 (2002).
384. Jain, A. *et al.* Commentary: The Materials Project: A materials genome approach to accelerating materials innovation. *APL Mater.* **1**, 011002 (2013).
385. Mason, S. E., Iceman, C. R., Trainor, T. P. & Chaka, A. M. Density functional theory study of clean, hydrated, and defective alumina (1 $\bar{1}$ 02) surfaces. *Phys. Rev. B* **81**, 125423 (2010).
386. Lo, C. S., Tanwar, K. S., Chaka, A. M. & Trainor, T. P. Density functional theory study of the clean and hydrated hematite (1 $\bar{1}$ 02) surfaces. *Phys. Rev. B* **75**, 075425 (2007).
387. Batyrev, I., Alavi, A. & Finnis, M. W. Ab initio calculations on the Al<sub>2</sub>O<sub>3</sub> (0001) surface. *Faraday Discuss.* **114**, 33–43 (1999).
388. Rohrbach, A., Hafner, J. & Kresse, G. Ab initio study of the (0001) surfaces of hematite and chromia: Influence of strong electronic correlations. *Phys. Rev. B* **70**, 125426 (2004).
389. Barbier, A., Stierle, A., Kasper, N., Guittet, M.-J. & Jupille, J. Surface termination of hematite at environmental oxygen pressures: Experimental surface phase diagram. *Phys. Rev. B* **75**, 233406 (2007).
390. Batyrev, I. G. & Kleinman, L. In-plane relaxation of Cu(111) and Al(111)/ $\alpha$ -Al<sub>2</sub>O<sub>3</sub>(0001) interfaces. *Phys. Rev. B* **64**, 033410 (2001).
391. Guenard, P., Renaud, G., Barbier, A. & Gautier-Soyer, M. Determination of the  $\alpha$ -Al<sub>2</sub>O<sub>3</sub> (0001) surface relaxation and termination by measurements of crystal truncation rods. *MRS Online Proc. Libr. Arch.* **437**, (1996).

392. Wang, X.-G., Chaka, A. & Scheffler, M. Effect of the environment on  $\alpha$ -Al<sub>2</sub>O<sub>3</sub>(0001) surface structures. *Phys. Rev. Lett.* **84**, 3650–3653 (2000).
393. Filippetti, A. & Fiorentini, V. Magnetic ordering in CuO from first principles: A cuprate antiferromagnet with fully three-dimensional exchange interactions. *Phys. Rev. Lett.* **95**, (2005).
394. Song, Y.-Y. & Wang, G.-C. A DFT Study and microkinetic simulation of propylene partial oxidation on CuO (111) and CuO (100) surfaces. *J. Phys. Chem. C* **120**, 27430–27442 (2016).
395. Wang, Y. *et al.* Electronic structures of Cu<sub>2</sub>O, Cu<sub>4</sub>O<sub>3</sub>, and CuO: A joint experimental and theoretical study. *Phys. Rev. B* **94**, 245418 (2016).
396. Soon, A., Söhnel, T. & Idriss, H. Plane-wave pseudopotential density functional theory periodic slab calculations of CO adsorption on Cu<sub>2</sub>O(111) surface. *Surf. Sci.* **579**, 131–140 (2005).
397. Wang, Z. I. Nanobelts, nanowires, and nanodiskettes of semiconducting oxides—from materials to nanodevices. *Adv. Mater.* **15**, 432–436 (2003).
398. Burnside, S. D. *et al.* Self-Organization of TiO<sub>2</sub> nanoparticles in thin films. *Chem. Mater.* **10**, 2419–2425 (1998).
399. Vittadini, A., Casarin, M. & Selloni, A. Chemistry of and on TiO<sub>2</sub>-anatase surfaces by DFT calculations: a partial review. *Theor. Chem. Acc.* **117**, 663–671 (2007).
400. Christensen, A. & Carter, E. A. Adhesion of ultrathin ZrO<sub>2</sub>(111) films on Ni(111) from first principles. *J. Chem. Phys.* **114**, 5816–5831 (2001).
401. Muñoz, M. C., Gallego, S., Beltrán, J. I. & Cerdá, J. Adhesion at metal–ZrO<sub>2</sub> interfaces. *Surf. Sci. Rep.* **61**, 303–344 (2006).
402. Teufer, G. The crystal structure of tetragonal ZrO<sub>2</sub>. *Acta Crystallogr.* **15**, 1187–1187 (1962).
403. Ackermann, R. J., Rauh, E. G. & Alexander, C. A. Thermodynamic properties of ZrO<sub>2</sub>(g). *High Temp. Sci.* **7**, 304–316 (1975).
404. Bordier, G. & Noguera, C. Electronic structure of a metal-insulator interface: Towards a theory of nonreactive adhesion. *Phys. Rev. B* **44**, 6361–6371 (1991).
405. Nørskov, J. K., Studt, F., Abild-Pedersen, F. & Bligaard, T. The electronic factor in heterogeneous catalysis. in *Fundamental concepts in heterogeneous catalysis* 114–137 (John Wiley & Sons, Inc, 2014).
406. Goniakowski, J., Mottet, C. & Noguera, C. Non-reactive metal/oxide interfaces: from model calculations towards realistic simulations. *Phys. Status Solidi B* **243**, 2516–2532 (2006).